A Numerical Analysis of 3-D Inviscid Stator/Rotor Interactions Using Non-Reflecting Boundary Conditions

by

André P. Saxer

GTL Report #209

March 1992

GAS TURBINE LABORATORY
MASSACHUSETTS INSTITUTE OF TECHNOLOGY
CAMBRIDGE, MASSACHUSETTS

A Numerical Analysis of 3-D Inviscid Stator/Rotor Interactions Using Non-Reflecting Boundary Conditions

by

André P. Saxer

GTL Report #209 March 1992

Research funding for this work was provided by Rolls-Royce PLC under the supervision of Dr. Peter Stow. Additional funding was provided by the Swiss National Foundation for Scientific Research.

A NUMERICAL ANALYSIS OF 3-D INVISCID STATOR/ROTOR INTERACTIONS USING NON-REFLECTING BOUNDARY CONDITIONS

by
ANDRE PIERRE SAXER

This dissertation presents a method for the computation of three-dimensional inviscid, transonic steady and unsteady flows, primarily in axial flow turbines. The work is divided into two major contributions. The first is an algorithm for the solution of the 3-D Euler equations which incorporates a second-order accurate numerical smoothing for non-uniform grids and steady-state non-reflecting boundary conditions. Fourier analysis applied to the linearized Euler equations is used to develop novel quasi-3-D non-reflecting boundary conditions at the inflow/outflow and at the stator/rotor interface. The accuracy, effectiveness and robustness of the boundary condition formulation is demonstrated through several subsonic and transonic test cases and through comparison with the standard 1-D formulation.

The second contribution consists in the study of three specific flow phenomena occurring in an axial flow turbine. First, the steady-state effects of an inlet spanwise stagnation temperature gradient in a transonic stage are analyzed. The mechanism for the migration of the temperature as well as the extent of the non-uniformity are assessed. Then, the secondary flow produced by a combined thermal and vortical inlet distortion on a downstream moving rotor is studied. The extent of the radial mixing for steady and unsteady flow is assessed as a function of the strength of the inlet disturbance. The third case is an analysis of the steady, unsteady and time-averaged flow fields in a highly loaded industrial transonic turbine stage. In particular, the unsteady shock interaction due to the impact of the stator trailing edge shock wave off the downstream rotor is studied. From the last two cases it is concluded that in many aspects the time-averaged results are extremely close to the steady-state values, even with strong unsteady shock interaction. For each case the mechanisms for the creation of the secondary flow and deviations from a steady, uniform inlet conditions flow field are presented and analyzed.

Acknowledgments

I would like to thank everyone who, over the past $4\frac{1}{2}$ years, has helped me in one way or another to be successful in this project. I will not forget.

During this endeavor, the presence of some special people in my heart has helped me to overcome the gloomy times and to refocus on the important issues in life. One person in particular deserves to be cited here...she knows who.

Special thanks to Prof. Michael B. Giles for his guidance, support and always 'à propos' advice during the entire MIT experience. Mike is 'what a thesis advisor was meant to be'. I would like to thank the other members of my committee, Profs. Edward M. Greitzer, Mark Drela and Mårten T. Landahl for their good suggestions during this work, as well as the readers of this thesis, Profs. Alan H. Epstein and Manuel Martinez-Sanchez and Dr. Gerald R. Guenette for their helpful comments.
Also, I would like to acknowledge the support of Prof. I. L. Ryhming who was the first to encourage me to try my luck on the other side of the Atlantic, and at MIT in particular.
To you, all the members of the CFD Lab, past and present, thanks for all the 'little things' that helped so much.

Finally I would like to mention the entire crew of Star Trek the Next Generation for beaming me where no man has gone before every Saturday night for one hour.

Research funding for this work was provided by Rolls-Royce PLC under the supervision of Dr. Peter Stow. Additional funding to support my education was provided by the Swiss National Foundation for Scientific Research.

Contents

List of Figures

List of Tables

Nomenclature

c	speed of sound
c_p	specific heat at constant pressure
c_v	specific heat at constant volume
C	cost function
C_p	pressure coefficient ($C_p = \frac{p-p_{inl}}{\frac{1}{2}\rho_{inl}V_{inl}^2}$)
C_{p_t}	stagnation pressure coefficient ($C_{p_t} = \frac{p_t-p_{tinl}}{\frac{1}{2}\rho_{inl}V_{inl}^2}$)
$\vec{C}$	reduced velocity
D^2	pseudo-Laplacian operator
e	internal energy per unit mass
E	total rotary internal energy per unit mass
$\vec{F}$	force
F, G, H	fluxes in Cartesian coordinates
h	static enthalpy
H	height
$\hat{\imath}, \hat{\jmath}, \hat{k}$	unit vectors in the x, y and z directions, respectively
I	rothalpy
k, l	wave numbers in the x and y directions, respectively
l	typical grid spacing or cell length
L	blade chord length
$\dot{m}$	mass flow
M	Mach number
p	static pressure
$p_t^\star$	rotary stagnation pressure ($p_t^\star = p + \frac{1}{2}\rho((u^2+v^2+w^2)_{rel} - \Omega^2R^2)$)
P	pitch
Q	source term column vector
R	radius ($R = \sqrt{y^2+z^2}$)
$\hat{s}, \hat{n}, \hat{b}$	unit vectors in intrinsic coordinates
S_x	projected area of a cell face on the yz plane
S_y	projected area of a cell face on the xz plane
S_z	projected area of a cell face on the xy plane
T	static temperature
$\vec{T}$	torque
$\boldsymbol{u}^R, \boldsymbol{v}^L$	right and left eigenvectors
u, v, w	Cartesian velocity components
U	state vector
U_p	vector of primitive variables
$\vec{U}_w$	rotor wheel speed
V	cell volume

$\vec{V}$	velocity vector in absolute frame
$\vec{W}$	velocity vector in relative frame
x, y, z	Cartesian coordinates
x, θ, R	cylindrical coordinates

Greek:

γ	ratio of specific heats
Δt	local time-step
κ	artificial bulk viscosity
ν_2	second-difference smoothing coefficient
ν_4	fourth-difference smoothing coefficient
ρ	static density
σ	radius of curvature of the streamline
σ	under-relaxation factor
Φ	vector of linearized characteristic variables
ψ	grid weight function
$\vec{\omega}$	vorticity vector
Ω	angular speed

Superscripts:

n	time index
T	transposed vector

Subscripts:

abs	absolute frame
f	cell face index
i	cell index
inl, out	inlet, outlet
j	node index
max	maximum quantity
min	minimum quantity
P	pitch
rel	relative frame
R	radial component
r, s	rotor, stator
s	steady-state
s, n, b	streamwise, normal and binormal components
t	total (stagnation) conditions
v	vortex

x	x (axial) component
y	y component
z	z component
θ	tangential (circumferential) component
∞	uniform flow conditions

Accents:

$\bar{}$	arithmetic average
$\hat{}$	Fourier transformed quantity
$\tilde{}$	linearized perturbation
$\vec{}$	vector quantity

Chapter 1

Introduction

C'est pas demain la veille! Abraracourcix, chef gaulois.

The flow physics of a modern transonic turbine stage such as the one shown in Fig. 1.1 is extremely complex. The flow field is inherently unsteady due to the relative motion between the stationary blades (stator) and the rotating rotor blades. In fact several sources of unsteadiness are present in a turbomachine with frequency scales ranging from a fraction of the shaft speed to several times that of the highest blade-passing frequency, see for instance the reviews by Greitzer [43] and Giles [36]. Some of them are purely of inviscid nature such as potential stator/rotor interactions, flutter, inlet distortions. Others such as wake interactions with the subsequent blade row, vortex shedding, passage and tip vortices originate due to the viscous nature of the gas. Also, due to high Reynolds number and depending on the operating conditions, regions of laminar, transition and turbulent flow may occur. This means that the length scales can range from the circumference of the machine to a very small fraction of the blade chord.

The next two paragraphs are not intended to present an extensive list of all the studies previously done on turbine stator/rotor flow physics, but rather to expose review papers in this field of research. The thesis is organized such that additional, more specific references, are cited in the appropriate chapters.

Until recently, experimental study has formed the bulk of the research focussed on

turbine stator/rotor related flow physics. A good summary of the relevant effects can be found in the papers by Sharma et al. [96, 97] Joslyn et al. [62] and Joslyn and Dring [61]. References [96] and [97] focus on the effects of upstream wakes and temperature streaks on losses, heat loads and secondary flows. The effects of upstream streamwise vortices due to incoming endwall boundary-layer profiles has been experimentally investigated in terms of aerodynamic loading and heat transfer. The studies show that large variations in the size and strength of the rotor-relative secondary flow vortices occur which will alter the velocity profile of the subsequent stator, and affect the development of the boundary-layer. In general heat loads and losses on a turbine airfoil are increased by the unsteady interaction between the suction surface boundary-layer and the wakes and vortices from upstream rows. In References [62] and [61] aerodynamic data was acquired in one and a half stage axial turbine in order to assess the effects of secondary flows on radial transport, and analyze the three-dimensionality of the flow in terms of swirl angles, static, total and rotary stagnation pressure spanwise distributions.

Because of the additional shock wave interactions with the above phenomena, in the transonic regime things usually get worse. For instance extensive experimental research on wake/rotor as well as shock wave/rotor interaction in turbines, [5, 8, 18, 93, 58, 57], has shown that the passing upstream distortion (wake, shock wave) can cause an intermittent transition in the rotor's boundary-layer, causing the heat transfer to alternate between a low, laminar value and a high, turbulent value, which in turn affects the overall losses.

Confronted with a multiple-scale complex problem, it is extremely difficult to analyze 'as a whole' the flow occurring in an industrial transonic turbine stage. Hence, numerical analysis, the technique adopted in this project, offers an interesting and complementary (not alternative) approach towards the understanding of the flow physics occurring in axial flow turbomachinery. As shown below in the literature review, an interesting feature of computational fluid dynamics is its ability to 'segregate' different classes of flows and flow phenomena.

Numerical methods for calculating turbomachinery flow fields are reviewed by McNally and Sockol [77] and Giles [36]. McNally and Sockol's review is older and focusses on grid generation techniques, solution methods for the stream function equation, full potential equation, Euler and parabolized Navier-Stokes equations. At that time only a handful of codes for solving 3-D multi-stage flow fields were available. On the other hand Giles' review is more recent and concentrates on methods for unsteady flow using different levels of approximations, i.e. linear potential, linearized Euler, Euler and thin-shear-layer Navier-Stokes. In particular, the reviewer stresses the importance of boundary conditions such as inlet, outlet, periodic and stator/rotor interface. The emergence of linearized methods, and linearized Euler in particular is interesting. It indicates that although Navier-Stokes flow predictions are better in terms of matching local experimental data, Euler methods are well suited to predict first-order effects or trends. For instance, the Euler solvers of Ni [83] and Denton [17], which include modelling of the viscous effects through a body force term in the momentum equations [16], are currently being used in the turbine aero design process, whereas Navier-Stokes methods are still not computationally cheap enough.

In the last few years in addition to Ni and Denton's, several papers have been published in this area: Fourmaux [27] and Lewis [72], inviscid 2-D stator/rotor interaction; Jorgenson [60] quasi-three-dimensional thin-layer unsteady Navier-Stokes stator/rotor and Giles [37, 33] quasi-3-D inviscid/viscous unsteady stator/rotor interaction; Rai [87] and Chen [12] 3-D viscous unsteady stator/rotor interaction and Dawes [15] 3-D steady viscous. As opposed to experimental work, a majority of the papers on stator/rotor numerical analysis have concentrated on algorithm issues such as conservative versus non-conservative, ability to cope with arbitrary stator-to-rotor pitch ratios, boundary conditions, and proof-of-concept demonstrations. Today, however, the emphasis seems to turn towards applications in a search for better flow physics understanding. In that respect, one important objective of this thesis is to isolate and investigate separately some of the flow characteristics typically occurring in a (first) transonic turbine stage. Surprisingly, although the genesis of the above mentioned problems is sometimes due to viscosity (wakes, passage vortex for instance), the dynamics of the subsequent flow in-

teractions is mainly driven by inviscid mechanisms. Hence, this work is entirely focussed on inviscid flow phenomena.

1.1 Objectives of the thesis

This dissertation involves two distinct, though complementary, major objectives. The first goal is to develop an efficient numerical algorithm solving the 3-D inviscid equations of motion for turbomachinery flows. The Euler equations expressing the conservation of mass, momentum and energy of an inviscid, compressible gas offer a suitable model system for the numerical study of stator/rotor interactions. However, a major problem associated with any numerical procedure is the handling of the boundary conditions. The boundary conditions have to be formulated in order to avoid spurious reflections that may contaminate the global solution. This is particularly important in a transonic stage with small axial gaps, such as the one studied here, where shock waves propagate indefinitely and can be be reflected by improper boundary conditions. Moreover, the boundary condition formulation needs to be able to accurately represent details of the flow field since the flow problems analyzed here involve variations from a current steady-state, i.e. the steady as well as unsteady secondary flow must be a true representation of a physical phenomenon.

To achieve this, a novel *quasi-3-D non-reflecting boundary conditions* formulation is introduced. The theory is based upon Fourier analysis and eigenvectors applied to the linearized Euler equations, and is implemented for transonic and subsonic axial flow turbomachine calculations. The technique is designed to avoid numerical reflections and ensures conservation of mass, momentum and energy when applied at the stator/rotor interface.

The second major objective of this dissertation is to add flow physics understanding to the body of research mentioned in the introductory section. This is accomplished in

the second part of the thesis by applying the newly developed CFD tool to three specific types of 3-D turbine stator/rotor interactions. The first case concerns the secondary radial transport in the rotor due to a stator inlet non-uniform total temperature. This is a typical problem encountered in a modern first turbine stage, because the requirement of high operating temperatures in order to increase the cycle performance creates severe heat loads. The flow leaving the combustor of a gas turbine is not temporally or spatially uniform. The mean flow temperature is usually well above the limit supported by the surrounding material. Cooling of the walls and the blades of the first stage is thus usually necessary. Consequently, midspan streaks of hot, less dense gas pass through the first stator row and become hot jets of fluid. A second-order non-linear effect causes this fluid to preferentially migrate towards the pressure surface of the first rotor row. This increases the mean temperature of the fluid at the edge of the boundary-layer, and so increases the mean heat transfer, which can in turn lead to blade failure.

The second case involves thermal and shear flow driven secondary flow in a rotor due to an incoming passage vortex coupled with a spanwise non-uniform temperature distribution. It is well known that in three dimensions the blade rows interact with the passage vortices generated by the upstream endwall boundary-layer and also with the tip vortices. For highly loaded turbines a significant secondary flow is generated in the blade passage due to the large turning. These secondary flows leave the blade rows as organized streamwise vortices, which then interact with the following blade row, affecting both the boundary-layer development and the heat transfer. Hence, with respect to first turbine stages, both thermal and velocity gradients effects are important in the development of secondary flow, and should be assessed from a steady and an unsteady point of view.

The final case consists of comparing and analyzing the steady, unsteady and time-averaged transonic flow fields in a highly loaded first turbine stage. For a supersonic vane exit, a system of oblique shocks is generated at the trailing edge of the stator. For small axial gaps, the shock extends to the rotor and impinges on the suction and pressure sides. This causes unsteady rotor loading as well as unsteady shock/boundary-

layer interactions. Relative to the time-averaged solution, it is important to assess the extent of the unsteadiness due to the inviscid shock interaction in terms of secondary flow and stator and rotor loadings, for instance.

The demand for improved performance of today's gas turbines requires the designer to account for 3-D steady as well as unsteady effects. For example, the thermal analysis of a turbine airfoil requires the knowledge of local heat loads, which means that the knowledge of the average driving temperature in the blade passage is not sufficient to optimally design the cooling system. Hence time-accurate values are required as well as deviations from the average. Hence, the computation of steady and unsteady flow fields in a complete industrial first turbine stage under different, though realistic inlet conditions, will serve to evaluate the extent of the changes that may occur with respect to the design conditions, i.e. uniform inlet conditions and steady flow field which rely heavily on through-flow techniques [1, 110].

Another motivation for analyzing and comparing the steady and the time-averaged unsteady flow solution stems from the emergence of methods that incorporate 'corrections' to the baseline steady flow in order to account for deterministic periodic unsteadiness, see for instance References [2] and [38]. In [2], Adamczyk derived a set of average-passage flow equations for a multi-stage turbomachine by sequentially applying an ensemble-averaging, a time-averaging and a passage-to-passage averaging operator to the governing equations. In [38], Giles proposed an asymptotic approach for multi-stage unsteady flow computations in which the effect of periodic unsteadiness on the steady flow is included through quadratic terms. Compared tρ the full non-linear unsteady flow methods, these techniques offer potentially great savings in computer time, though still retaining the global effects of unsteadiness. However, the use of these improved 'mean-flow' solution procedures needs to be justified by evaluating the extent of the changes resulting from unsteadiness. These are examined here in the second (subsonic) and third (transonic) flow cases which involve a combined vortical and thermal disturbance entering a moving downstream rotor, and a stator/rotor shock wave interaction, respectively.

1.2 Thesis outline

An important feature of the numerical procedure is that absolute and relative variables are used, i.e. stator quantities are defined in an inertial frame of reference whereas rotor quantities are defined relative to the rotating frame of reference. In Chapter 2 of this thesis, the so-called Euler equations governing the motion of an inviscid compressible gas are presented in a Cartesian system of reference rotating at a constant angular speed. From this form, the equations in the absolute frame (stator) are easily derived. Also presented in Chapter 2 are the reference quantities used to non-dimensionalize the equations, and a system of cylindrical coordinates particularly useful when implementing the boundary conditions. Circumferential periodicity is assumed throughout this thesis, so that calculations can be performed on a single blade-passage. This is usually a good assumption for turbine flow fields as opposed to compressor flows where inlet distortions can lead to severe instabilities such as rotating stall, see for instance [42].

The discretization procedure is presented in Chapter 3. The Ni-Lax-Wendroff algorithm implemented on an unstructured grid formed by an ensemble of hexahedral cells is discussed together with the properties of accuracy and consistency. Then, the implementation of this scheme on a multi-processor machine together with the periodic and wall boundary conditions are presented.

The numerical algorithm adopted in this work requires the addition of a so-called numerical smoothing, whose purpose is to ensure both stability and shock capturing. It has the form of a combined fourth- and second-difference operator acting on the state vector. The fourth-difference smoothing used in this work is designed to ensure second-order accuracy for shock-free solutions even in the presence of grid irregularities. This property is important when comparing different solutions. It is an extension to 3-D of a method introduced by Holmes and Connell [54]. This matter is discussed in Chapter 4.

The *quasi-3-D non-reflecting boundary conditions* for steady-state flows are presented in Chapter 5. The objective of this formulation is to allow calculations to be performed

on truncated domains such as the ones encountered in a numerical simulation of a turbomachine flow field, without the generation of spurious non-physical reflections at the far-field boundaries. The theoretical aspect of the quasi-3-D approach using Fourier analysis performed upon the linearized Euler equations is presented and linked to the standard 1-D formulation. The quasi-3-D non-reflecting boundary conditions can also be used to match together a stator and a rotor computation so that the interface is treated in an average conservative manner. The importance of the interface treatment becomes crucial when simulating flows in turbines with small axial gaps where shocks must cross the boundary without being reflected. Chapter 5 concludes by presenting results showing the effectiveness of the quasi-3-D boundary conditions by comparing them to the standard 1-D formulation for several cases.

Validation of a 3-D unsteady inviscid solver is not a trivial task. The results presented in Chapter 6 attempt to achieve this by using an analytical and an experimental test case. Another way of validating the code is to check upon certain integral quantities that have to be conserved in the computational domain.

The 3-D applications of the Euler solver to stator/rotor interactions are presented in Chapters 7 through 9.

In Chapter 7, the present method is used to analyze the effects of an inlet radial temperature distribution coming out of the combustor of a gas turbine onto the first turbine stage. In this simulation, the Munk and Prim [80] substitution principle is used to show that no 3-D secondary flow associated with the spanwise temperature gradient occurs in the vane. However, a significant secondary flow is generated in the relative frame of reference, which is a consequence of the rotor relative non-uniform inlet total pressure distribution as well as the rotor-relative inlet angle. The effect of the rotor-relative secondary flow on the upstream stator is also discussed. The results of this chapter are analyzed with respect to the flow field occurring in the stage with uniform inlet conditions.

In Chapter 8, an attempt is made to assess the effects of thermally and shear flow driven secondary flows on a downstream rotor. In particular, a model for a passage vortex is proposed and then coupled to a spanwise temperature profile. This combined vortex/temperature flow field is set as inlet conditions of a partial vane which is connected downstream to a moving rotor. Steady-state results are presented and compared with the unsteady computation. For unsteady computations, a simple stator/rotor interface boundary condition which uses 1-D characteristics theory is employed. This algorithm, also presented in Chapter 8, restricts the stator-to-rotor pitch ratio to 1.

In Chapter 9, a full unsteady calculation of a highly loaded transonic first turbine stage is presented together with the steady-state results. The flow physics of the steady-state and the unsteady shocks motion are discussed, and a comparison between the time-averaged and the steady-state solutions is presented. As will be seen, the unsteady shock system produces a secondary flow of vortical nature absent in the steady-state calculation.

Finally in Chapter 10, the major contributions of this work are outlined, some extensions for future research are proposed and some conclusions are drawn about the utility of the present approach.

It is worthwhile to outline the material presented in Appendices A through E.

The mesh generation technique is discussed in Appendix A. It describes how a set of simple 2-D profiles from industrial data can be manipulated to define second-order continuous surfaces such as the blade and the upper and lower annulus walls that are then used to generate a structure suitable for 3-D numerical grid generation. Chosen for its robustness and relative ease of implementation, the distribution of the field mesh points is found by solving a set of elliptic partial differential equations. The source terms are automatically evaluated in the iterative solution procedure to produce a control of cell size and skewness at the blade boundary.

The derivation of the cell volume as well as the areas of the cell faces is presented in Appendix B.

For explicit time-marching methods such as the Ni-Lax-Wendroff scheme, the allowable time-step is restricted by the so-called Courant-Friedrichs-Levy (CFL) stability limit, which states that the numerical domain of dependence must contain the complete domain of dependence of the original hyperbolic differential equation. The stability analysis is performed in Appendix C.

In Appendix D, the implementation of the quasi-3-D non-reflecting boundary conditions are discussed. Subsonic, as well as supersonic, inflow and outflow conditions are presented.

Finally, Appendix E contains a discussion of the effects of scaling the rotor blade in order to get a stator-to-rotor pitch ratio equal to 1, which compares to 1.69 in the actual geometry.

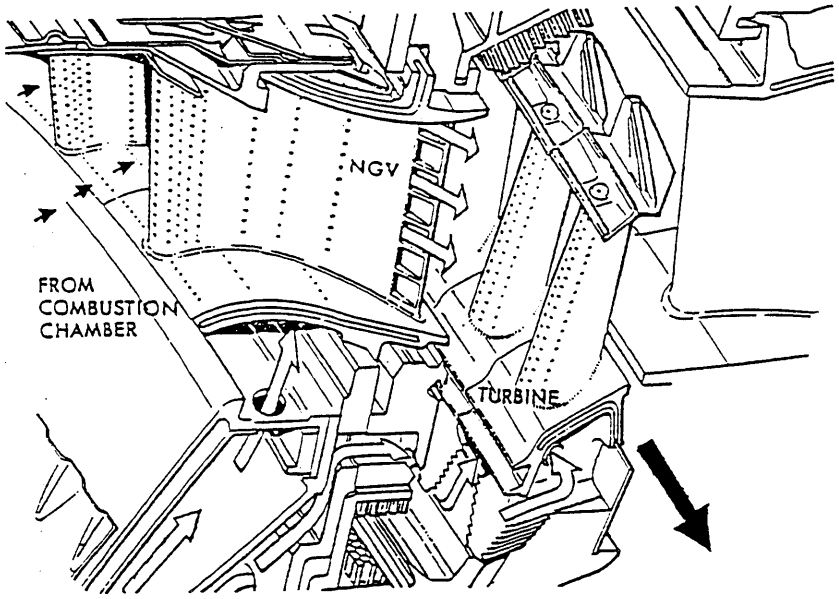

Figure 1.1: Transonic turbine stage.

Chapter 2

Governing Relations

2.1 Three-dimensional Euler equations

Reynolds and Prandtl numbers of the order of a million and unity, respectively are typical values encountered in a gas turbine engine. This means that the viscous and thermal effects are confined to thin shear layers. This is particularly true in the turbine section in which the fluid does not have to work against a mean adverse pressure gradient as in the compressor section. Outside these regions, the gas is assumed to be non heat-conducting, inviscid and compressible. By applying the fundamental principles of conservation of mass, momentum and energy to this kind of fluid, the so-called Euler equations of fluid dynamics are obtained. Integral forms of the conservation laws are presented in several books, see for instance Ryhming [91], Anderson [4], Liepmann & Roshko [73] and Kuethe & Chow [67].

The conservation laws can be derived for either a fixed or moving control volume in space. The differential form is usually obtained from the integral form by shrinking the control volume to a point and applying the divergence theorem. As mentioned earlier, a relative motion between the blade rows is inherent to a stator/rotor interaction. The algorithm developed in this thesis solves the flow fields associated with a non-rotating and rotating row in their own Cartesian coordinate systems. Thus, the conservation laws for a fixed control volume can be used. Absolute values subscripted $_{abs}$ are used

in the stator, fixed frame of reference, whereas rotor-relative quantities subscripted $_{rel}$ are used in the rotating coordinate system[1]. Appropriate transformations are then performed at the interface to match the two flow fields. Also, the subscripts $_{inl}$ and $_{out}$ are used to indicate an inlet and outlet quantity, respectively. Thus, in a combined stator/rotor computation, these subscripts refer to the stator inlet and the rotor outlet, respectively.

The flow field is modelled by the Euler equations for an inviscid, adiabatic compressible gas. Used in a conservative formulation, the resulting system correctly accounts for the formation of shocks and their associated entropy and vorticity production. In a Cartesian coordinate system rotating at constant speed Ω around the x axis, see Figure 2.1, the Euler equations can be expressed as

$$\frac{\partial U}{\partial t} + \frac{\partial F}{\partial x} + \frac{\partial G}{\partial y} + \frac{\partial H}{\partial z} = Q, \tag{2.1}$$

where U is the state vector in the relative frame defined as $U = (\rho, \rho u, \rho v, \rho w, \rho E)^T_{rel}$. The fluxes F, G, H of mass, momentum and energy are given by

$$F = \begin{pmatrix} \rho u \\ \rho u^2 + p \\ \rho uv \\ \rho uw \\ \rho uI \end{pmatrix}, \; G = \begin{pmatrix} \rho v \\ \rho uv \\ \rho v^2 + p \\ \rho vw \\ \rho vI \end{pmatrix}, \; H = \begin{pmatrix} \rho w \\ \rho uw \\ \rho vw \\ \rho w^2 + p \\ \rho wI \end{pmatrix}. \tag{2.2}$$

The source term Q, representing the centripetal and Coriolis forces per unit volume, acting on a fluid particle at radius $R = \sqrt{y^2+z^2}$ is defined as

[1]The subscripts $_{abs}$ and $_{rel}$ are used only when a confusion may occur and so are otherwise dropped.

$$Q = \begin{pmatrix} 0 \\ 0 \\ \rho(\Omega^2 y - 2\Omega w) \\ \rho(\Omega^2 z + 2\Omega v) \\ 0 \end{pmatrix}. \tag{2.3}$$

E is the total rotary internal energy per unit mass, i.e.

$$E = e + \frac{1}{2}(u^2+v^2+w^2)_{rel} - \frac{1}{2}\Omega^2 R^2, \tag{2.4}$$

where e is the internal energy per unit mass, defined as $e = c_v T$ for a calorically perfect gas. c_v is the specific heat at constant volume and T the static temperature. The static pressure p and the rothalpy I are related to the density ρ, relative velocity components u, v and w, and E by the following two equations which assume a perfect gas with constant specific heat ratio $\gamma = c_p/c_v$.

$$p = (\gamma - 1)\rho\left(E - \frac{1}{2}(u^2+v^2+w^2)_{rel} + \frac{1}{2}\Omega^2 R^2\right), \tag{2.5}$$

$$I = E + \frac{p}{\rho} = \frac{\gamma}{\gamma - 1}\frac{p}{\rho} + \frac{1}{2}(u^2+v^2+w^2)_{rel} - \frac{1}{2}\Omega^2 R^2. \tag{2.6}$$

Using absolute velocities and total energy, the above relations are also valid in the absolute frame (stator, $\Omega = 0$) in which case Q is set to zero and the rothalpy is replaced by the stagnation enthalpy h_t,

$$h_t = h + \frac{1}{2}(u^2+v^2+w^2)_{abs}, \tag{2.7}$$

where h is the static enthalpy defined as $h = c_p T$ and c_p is the specific heat at constant pressure.

The derivation of the equations from the absolute frame of reference to the rotating frame is elegantly presented in Reference [39] using tensor analysis and is not reported

here.

2.2 Non-dimensionalization

It is useful to rewrite the above equations in non-dimensional form. Using non-dimensional variables allows an easier comparison between different flow cases, by avoiding unit conversion factors. Also, the scaling laws that may appear in the flow fields are explicit in dimensionless quantities. The inlet stagnation density, $(\rho_t)_{inl}$, stagnation speed of sound, $(c_t)_{inl}$, and the blade axial chord at the hub, L_{hub}, are chosen as reference values. In the case of a combined stator/rotor calculation, the axial chord of the stator (first row) is used as the length of reference. Introducing these quantities gives the following non-dimensional variables,

$$
\begin{aligned}
x' &= \frac{x}{L_{hub}} & y' &= \frac{y}{L_{hub}} & z' &= \frac{z}{L_{hub}} \\
u' &= \frac{u}{(c_t)_{inl}} & v' &= \frac{v}{(c_t)_{inl}} & w' &= \frac{w}{(c_t)_{inl}} \\
\rho' &= \frac{\rho}{(\rho_t)_{inl}} & p' &= \frac{p}{(\rho_t)_{inl}(c_t^2)_{inl}} & t' &= \frac{t}{L_{hub}/(c_t)_{inl}} \\
\Omega' &= \frac{\Omega}{(c_t)_{inl}/L_{hub}} & e' &= \frac{e}{(c_t^2)_{inl}} & h' &= \frac{h}{(c_t^2)_{inl}}.
\end{aligned}
\tag{2.8}
$$

With this procedure, the form of the non-dimensional governing equations becomes identical to that of the dimensional equations. Thus, for convenience the primes are dropped and reference is henceforth made to the non-dimensional variables only. For

instance, the stator inlet state vector written in terms of dimensionless variables is

$$U_{inl} = \frac{1}{(1+\frac{\gamma-1}{2}M_{inl}^2)^{\frac{1}{\gamma-1}}} \begin{pmatrix} 1 \\ \frac{(M_x)_{inl}}{(1+\frac{\gamma-1}{2}M_{inl}^2)^{\frac{1}{2}}} \\ \frac{(M_y)_{inl}}{(1+\frac{\gamma-1}{2}M_{inl}^2)^{\frac{1}{2}}} \\ \frac{(M_z)_{inl}}{(1+\frac{\gamma-1}{2}M_{inl}^2)^{\frac{1}{2}}} \\ \frac{1}{\gamma(\gamma-1)} \end{pmatrix}. \tag{2.9}$$

Using the definition of the local speed of sound c,

$$c = \sqrt{\frac{\gamma p}{\rho}}, \tag{2.10}$$

and the shorthand notation

$$V = (\sqrt{u^2 + v^2 + w^2})_{abs}, \tag{2.11}$$

the inlet Mach number M_{inl} is defined as

$$M_{inl} = \left(\frac{V}{c}\right)_{inl} = \sqrt{(M_x^2)_{inl} + (M_y^2)_{inl} + (M_z^2)_{inl}}. \tag{2.12}$$

In addition, the following inlet stagnation quantities are found.

$$(h_t)_{inl} = \frac{1}{\gamma-1}, \quad (\rho_t)_{inl} = 1, \quad (p_t)_{inl} = \frac{1}{\gamma}. \tag{2.13}$$

2.3 Cylindrical coordinate system

As mentioned earlier, the 3-D Euler equations are solved in a Cartesian coordinate system, that is either fixed as in the stator frame, or rotating at constant angular speed Ω in the case of the rotor. However, it is more natural to apply boundary conditions in

a turbomachinery environment using a cylindrical coordinate system. Thus, a relation between the Cartesian and the cylindrical coordinates is needed. With reference to Figure 2.1 the following relations apply,

$$y = R\cos\theta, \tag{2.14}$$

$$z = R\sin\theta, \tag{2.15}$$

$$R = \sqrt{y^2 + z^2}, \tag{2.16}$$

$$\theta = \arctan\left(\frac{z}{y}\right), \tag{2.17}$$

$$\hat{e}_\theta = \sin\theta\,\hat{j} - \cos\theta\,\hat{k}, \tag{2.18}$$

$$\hat{e}_R = \cos\theta\,\hat{j} + \sin\theta\,\hat{k}. \tag{2.19}$$

Both coordinate systems are right-handed if thought of as (x, y, z) and (x, θ, R).

Using the cylindrical coordinates, the absolute velocity $\vec{V} = (u_x, u_\theta, u_R)_{abs}$ in the stator frame of reference is related to the relative velocity $\vec{W} = (u_x, u_\theta, u_R)_{rel}$ in the rotor by

$$\vec{V} = \vec{W} + \vec{U}_w, \tag{2.20}$$

where $\vec{U}_w$ is the rotor wheel speed defined as

$$\vec{U}_w = \Omega R\,\hat{e}_\theta. \tag{2.21}$$

Rotation around the x axis is defined as

$$\vec{\Omega} = -\Omega\hat{\imath}. \tag{2.22}$$

Hence,

$$(u_x)_{abs} = (u_x)_{rel}, \tag{2.23}$$

$$(u_\theta)_{abs} = (u_\theta)_{rel} + \Omega R, \tag{2.24}$$

$$(u_R)_{abs} = (u_R)_{rel}. \tag{2.25}$$

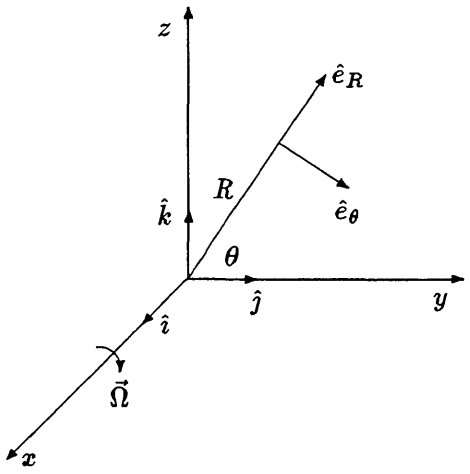

Figure 2.1: Cartesian and cylindrical coordinate systems.

The two prescribed flow angles needed as inlet boundary conditions in Chapter 5 are defined in Figure 2.2. With respect to the cylindrical coordinate system the following relations apply to any vector $\vec{V} = (u_x, u_\theta, u_R)$.

$$u_x = V \cos\alpha_\theta \sin\alpha_R, \tag{2.26}$$

$$u_\theta = V \sin\alpha_\theta \sin\alpha_R, \tag{2.27}$$

$$u_R = V \cos\alpha_R. \tag{2.28}$$

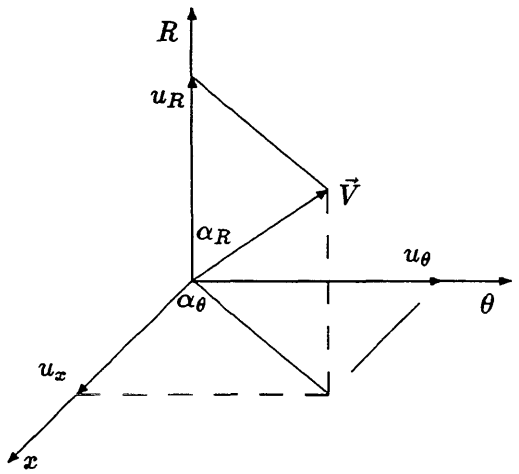

Figure 2.2: Prescribed inlet angles.

Chapter 3

Discretization Procedure

3.1 Lax-Wendroff algorithm on unstructured hexahedral cells

An explicit time-marching numerical algorithm of Lax-Wendroff type is used to solve the Euler Equations (2.1). The flow variables are located at the vertices of the hexahedral cells and are assigned according to an initial condition. For each node the governing equations are then integrated in time and, subject to adequate boundary conditions, a steady-state or periodic unsteady solution can be obtained.

The flux across each cell face is based upon the average of the fluxes F, G, and H at the corner nodes. The flux residual is evaluated by summing the fluxes through the six faces, and adding the source term for the cell. From this residual, the changes in the flow variables are distributed back to the eight corners, according to the Lax-Wendroff algorithm which guarantees numerical stability, subject to the Courant-Friedrichs-Levy time-step limit. The basic integration scheme is similar to that introduced by Ni [81], re-cast by Hall [46] and then extended to 3-D by Ni and Bogoian [82]. However, it differs from the other formulations in precise details for non-uniform grids and it is here described to be used in a flow solver that handles unstructured grids. The derivation is valid for any arbitrary grid defined only by the coordinates (x, y, z) of its grid nodes in a Cartesian space.

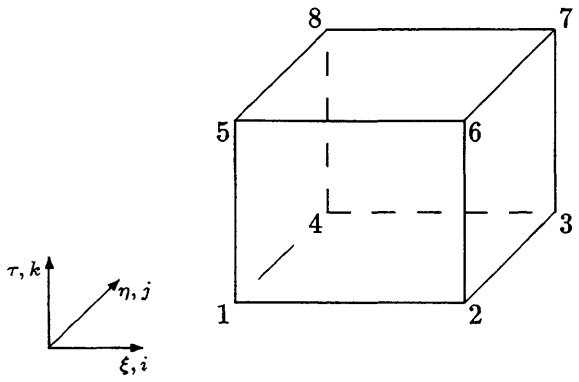

face	nodes
1	2376
2	1485
3	3487
4	1562
5	5678
6	1234

Figure 3.1: Hexahedral cell nomenclature.

Formally the Lax-Wendroff algorithm starts by considering the second-order Taylor series expansion for $U^{n+1} = U((n+1)\Delta t)$, where the superscript ^{n} denotes the time level and $\Delta t \equiv t^{n+1} - t^n$.

$$U^{n+1} = U^n + \Delta t \left(\frac{\partial U}{\partial t}\right)^n + \frac{1}{2}\Delta t^2 \left(\frac{\partial^2 U}{\partial t^2}\right)^n . \tag{3.1}$$

Substituting from Eq. (2.1) and changing the order of differentiation yields,

$$U^{n+1} = U^n - \Delta t \left(\frac{\partial F}{\partial x} + \frac{\partial G}{\partial y} + \frac{\partial H}{\partial z} - Q\right)^n - \frac{\Delta t}{2}\left(\frac{\partial}{\partial x}\Delta F^n + \frac{\partial}{\partial y}\Delta G^n + \frac{\partial}{\partial z}\Delta H^n - \Delta Q^n\right), \tag{3.2}$$

where

$$\Delta F^n = \Delta t \frac{\partial F}{\partial t}, \quad \Delta G^n = \Delta t \frac{\partial G}{\partial t}, \quad \Delta H^n = \Delta t \frac{\partial H}{\partial t}, \quad \Delta Q^n = \Delta t \frac{\partial Q}{\partial t}. \tag{3.3}$$

It is easier to explain the construction of the Lax-Wendroff algorithm on unstructured grids by considering the Figures 3.1 and 3.2. The grid nodes are numbered and the cells are referred to by capital letters. Surrounding node 1 are the eight nearest neighboring mesh cells denoted A, B, C, D, E, F, G, H. The state vector change at node 1 is defined as $\delta U_1 \equiv U_1^{n+1} - U_1^n$. This residual is found by integrating Equation (3.2) over

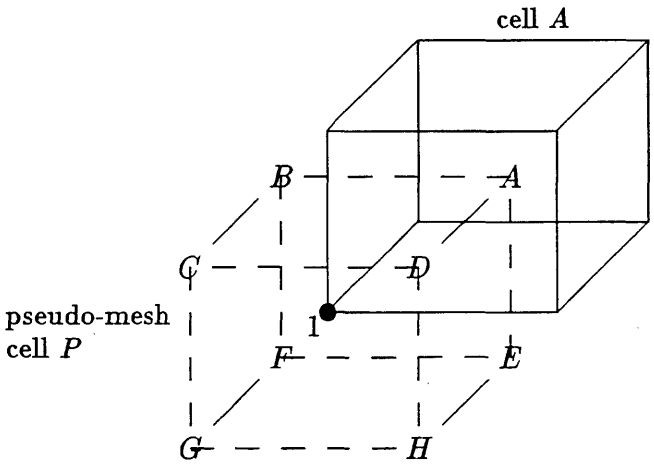

Figure 3.2: Control volume of pseudo-mesh cell P (dashed) surrounding node 1, with cell neighbor A. The center of the adjacent cells marked by capital letters are located at the corners of P.

the pseudo-mesh cell P of finite volume V_1 and by applying Gauss' theorem, i.e.

$$\delta U_1 = \frac{1}{V_1}\Big(\; - \; \Delta t \iint_{cell\,P} (F,G,H)(n_x,n_y,n_z)dS \; + \; \Delta t V_1 Q_1$$
$$- \; \frac{\Delta t}{2} \iint_{cell\,P} (\Delta F, \Delta G, \Delta H)(n_x,n_y,n_z)dS \; + \; \frac{\Delta t}{2} V_1 \Delta Q_1 \Big). \quad (3.4)$$

$\vec{n} = (n_x, n_y, n_z)$ is the unit normal vector directed outside the surface element dS and the notation

$$(F,G,H)(n_x,n_y,n_z) = Fn_x + Gn_y + Hn_z \quad (3.5)$$

is used. The residual δU_1 is now expressed as a function of the changes occurring in the eight cells of which node 1 is a corner, i.e.

$$\delta U_1 = \sum_{i=1}^{8\,cells} \delta U_{1i} = \delta U_{1A} + \delta U_{1B} + \delta U_{1C} + \delta U_{1D} + \delta U_{1E} + \delta U_{1F} + \delta U_{1G} + \delta U_{1H}. \quad (3.6)$$

Thus all of the cells surrounding node 1 contribute to the change δU_1.

The two integrals in Equation (3.4) are considered separately. The first integral, rep-

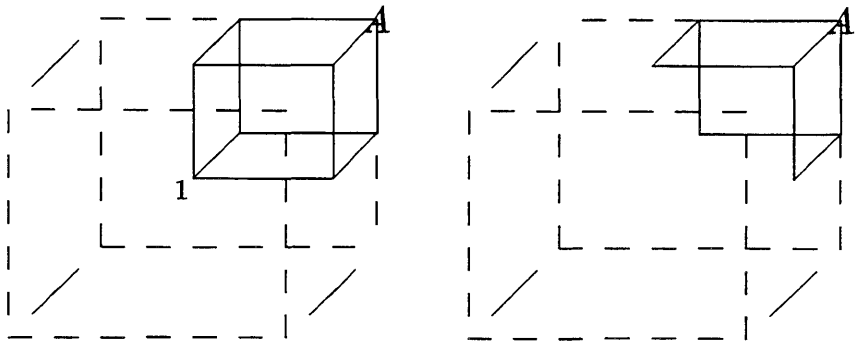

Figure 3.3: Contributions of cell A to the first-order, left, and second-order, right, flux integration.

resenting the first-order flux contribution at node 1, can be split into eighth independent closed surface integrals, each of these being approximated as one eight of the surface integral over the larger cells $A, \ldots, H$. Also an average value of the first-order source term is defined at each center of the larger cells $A, \ldots, H$ and contribute equivalently to node 1. The second-order flux contribution to node 1 uses the same control volume V_1 as the first-order terms but is approximated as a sum of open surface integrals, see Figure 3.3. For instance, the first- and second-order contributions of cell A to node 1 are given by

$$\begin{aligned}\delta U_{1A} = \frac{1}{V_1}\Big(\; - \; & \frac{\Delta t}{8}\iint_{cell\,A}(F,G,H)(n_x,n_y,n_z)dS \; + \; \frac{\Delta t_A}{8}V_A Q_A \\ & - \; \frac{\Delta t}{2\cdot 4}\iint_{faces\,(1-3-5)_A}(\Delta F,\Delta G,\Delta H)(n_x,n_y,n_z)dS \\ & + \; \frac{\Delta t_A}{2\cdot 8}V_A \Delta Q_A \Big). \end{aligned} \tag{3.7}$$

The average first-order change in U for the whole cell A in the time-step Δt_A is denoted ΔU_A and written as

$$\Delta U_A \;=\; -\left(\frac{\Delta t}{V}\right)_A \iint_{cell\,A}(F,G,H)(n_x,n_y,n_z)dS \; + \; \Delta t_A Q_A$$

$$= -\left(\frac{\Delta t}{V}\right)_A \left(\sum_{f=1}^{6\,faces} (\bar{F}S_x + \bar{G}S_y + \bar{H}S_z)_f \right)_{cell\,A} + \Delta t_A Q_A + O(l^4), \quad (3.8)$$

where the superscript $^-$ denotes an arithmetic average over the four grid nodes defining the face f of cell A. S_x, S_y and S_z are the projected areas on the yz, xz and xy planes of the face f, respectively. The derivation of the areas as well as the volume for a cell is given in Appendix B. Note that the sum in Eq. (3.8) represents a flux balance for the cell A. With this, Eq. (3.7) is re-written as

$$\delta U_{1A} = \frac{1}{8}\left(\frac{\Delta t}{V}\right)_1 \left\{ \left(\frac{V}{\Delta t}\right)_A \Delta U_A - \sum_{f=1,3,5} (\Delta F_A \bar{S}_x + \Delta G_A \bar{S}_y + \Delta H_A \bar{S}_z)_f + \frac{V_A}{2}\Delta Q_A \right\}, \quad (3.9)$$

where $\bar{S}_x$, $\bar{S}_y$ and $\bar{S}_z$ refer to the averaged projection areas of opposite faces and thus represent the faces of the pseudo-cell P sketched in Fig. 3.2. Note that according to the cell nomenclature defined in Figure 3.1, the second-order fluxes of cell A contribute to the state vector change of node 1 only through the (average) faces 1, 3 and 5.

For a time-marching calculation the convergence to steady-state flow is accelerated by using variable time-steps, see Appendix C. The arrangement of the Δt terms in Equation (3.9) ensures that conservation is independent of the local time-step.

The second-order flux terms ΔF_A, ΔG_A and ΔH_A are obtained from

$$\Delta F_A = \left(\frac{\partial F}{\partial U}\right)_A \Delta U_A, \quad \Delta G_A = \left(\frac{\partial G}{\partial U}\right)_A \Delta U_A, \quad \Delta H_A = \left(\frac{\partial H}{\partial U}\right)_A \Delta U_A, \quad (3.10)$$

whereas the second-order source term ΔQ_A is given by

$$\Delta Q_A = \left(\frac{\partial Q}{\partial U}\right)_A \Delta U_A. \quad (3.11)$$

In Eqs. (3.10) and (3.11) the Jacobians are evaluated using U_A, the cell-average of the eight nodes. For computational efficiency it is best not to actually form the Jacobian matrix and perform the matrix-vector multiplication. Instead the following equations are used.

$$\Delta F_1 = \Delta(\rho u)$$

$$
\begin{aligned}
\Delta F_2 &= \bar{u}\Delta(\rho u) + \bar{\rho}\bar{u}\Delta u + \Delta p \\
\Delta F_3 &= \bar{u}\Delta(\rho v) + \bar{\rho}\bar{v}\Delta u \\
\Delta F_4 &= \bar{u}\Delta(\rho w) + \bar{\rho}\bar{w}\Delta u \\
\Delta F_5 &= \bar{u}(\Delta(\rho E)+\Delta p) + \bar{\rho}\bar{I}\Delta u
\end{aligned}
\tag{3.12}
$$

$$
\begin{aligned}
\Delta G_1 &= \Delta(\rho v) \\
\Delta G_2 &= \bar{v}\Delta(\rho u) + \bar{\rho}\bar{u}\Delta v \\
\Delta G_3 &= \bar{v}\Delta(\rho v) + \bar{\rho}\bar{v}\Delta v + \Delta p \\
\Delta G_4 &= \bar{v}\Delta(\rho w) + \bar{\rho}\bar{w}\Delta v \\
\Delta G_5 &= \bar{v}(\Delta(\rho E)+\Delta p) + \bar{\rho}\bar{I}\Delta v
\end{aligned}
\tag{3.13}
$$

$$
\begin{aligned}
\Delta H_1 &= \Delta(\rho w) \\
\Delta H_2 &= \bar{w}\Delta(\rho u) + \bar{\rho}\bar{u}\Delta w \\
\Delta H_3 &= \bar{w}\Delta(\rho v) + \bar{\rho}\bar{v}\Delta w \\
\Delta H_4 &= \bar{w}\Delta(\rho w) + \bar{\rho}\bar{w}\Delta w + \Delta p \\
\Delta H_5 &= \bar{w}(\Delta(\rho E)+\Delta p) + \bar{\rho}\bar{I}\Delta w
\end{aligned}
\tag{3.14}
$$

$$
\begin{aligned}
\Delta Q_1 &= 0 \\
\Delta Q_2 &= 0 \\
\Delta Q_3 &= \Omega^2\bar{y}\Delta\rho - 2\Omega\Delta(\rho w) \\
\Delta Q_4 &= \Omega^2\bar{z}\Delta\rho + 2\Omega\Delta(\rho v) \\
\Delta Q_5 &= 0,
\end{aligned}
\tag{3.15}
$$

where

$$
\begin{aligned}
\Delta u &= (\Delta(\rho u) - \bar{u}\Delta\rho)/\bar{\rho} \\
\Delta v &= (\Delta(\rho v) - \bar{v}\Delta\rho)/\bar{\rho} \\
\Delta w &= (\Delta(\rho w) - \bar{w}\Delta\rho)/\bar{\rho} \\
\Delta p &= (\gamma-1)\left(\Delta(\rho E) - \bar{u}\Delta(\rho u) - \bar{v}\Delta(\rho v) - \bar{w}\Delta(\rho w) + \frac{\Delta\rho}{2}(\bar{u}^2+\bar{v}^2+\bar{w}^2+\Omega^2R^2)\right).
\end{aligned}
\tag{3.16}
$$

Now that the contribution of cell A to node 1 has been defined, the same procedure applies to the other cells $B,\ldots,H$ according to Equation (3.6) and

$$
\begin{aligned}
\delta U_{1B} &= \frac{1}{8}\left(\frac{\Delta t}{V}\right)_1\left\{\left(\frac{V}{\Delta t}\right)_B \Delta U_B - \sum_{f=2,3,5}(\Delta F_B\bar{S}_x+\Delta G_B\bar{S}_y+\Delta H_B\bar{S}_z)_f + \frac{V_B}{2}\Delta Q_B\right\}, \\
\delta U_{1C} &= \frac{1}{8}\left(\frac{\Delta t}{V}\right)_1\left\{\left(\frac{V}{\Delta t}\right)_C \Delta U_C - \sum_{f=2,4,5}(\Delta F_C\bar{S}_x+\Delta G_C\bar{S}_y+\Delta H_C\bar{S}_z)_f + \frac{V_C}{2}\Delta Q_C\right\}, \\
\delta U_{1D} &= \frac{1}{8}\left(\frac{\Delta t}{V}\right)_1\left\{\left(\frac{V}{\Delta t}\right)_D \Delta U_D - \sum_{f=1,4,5}(\Delta F_D\bar{S}_x+\Delta G_D\bar{S}_y+\Delta H_D\bar{S}_z)_f + \frac{V_D}{2}\Delta Q_D\right\}, \\
\delta U_{1E} &= \frac{1}{8}\left(\frac{\Delta t}{V}\right)_1\left\{\left(\frac{V}{\Delta t}\right)_E \Delta U_E - \sum_{f=1,3,6}(\Delta F_E\bar{S}_x+\Delta G_E\bar{S}_y+\Delta H_E\bar{S}_z)_f + \frac{V_E}{2}\Delta Q_E\right\}, \\
\delta U_{1F} &= \frac{1}{8}\left(\frac{\Delta t}{V}\right)_1\left\{\left(\frac{V}{\Delta t}\right)_F \Delta U_F - \sum_{f=2,3,6}(\Delta F_F\bar{S}_x+\Delta G_F\bar{S}_y+\Delta H_F\bar{S}_z)_f + \frac{V_F}{2}\Delta Q_F\right\}, \\
\delta U_{1G} &= \frac{1}{8}\left(\frac{\Delta t}{V}\right)_1\left\{\left(\frac{V}{\Delta t}\right)_G \Delta U_G - \sum_{f=2,4,6}(\Delta F_G\bar{S}_x+\Delta G_G\bar{S}_y+\Delta H_G\bar{S}_z)_f + \frac{V_G}{2}\Delta Q_G\right\}, \\
\delta U_{1H} &= \frac{1}{8}\left(\frac{\Delta t}{V}\right)_1\left\{\left(\frac{V}{\Delta t}\right)_H \Delta U_H - \sum_{f=1,4,6}(\Delta F_H\bar{S}_x+\Delta G_H\bar{S}_y+\Delta H_H\bar{S}_z)_f + \frac{V_H}{2}\Delta Q_H\right\}.
\end{aligned}
\tag{3.17}
$$

3.2 Conservation and accuracy

A numerical algorithm that solves the non-linear inviscid equations ought to be conservative, since this property guarantees the correct Rankine-Hugoniot shock jump relations and the correct treatment of other discontinuities such as slip lines. Analytically conservation is expressed by

$$\frac{d}{dt}\iiint U\,dx\,dy\,dy + \iint (F,G,H)(n_x,n_y,n_z)dS = \iiint Q\,dx\,dy\,dz. \tag{3.18}$$

The Lax-Wendroff scheme decomposes the domain into cells and approximates the above analytical equation by a discrete equation. Conservation is ensured as well as consistency if the discrete solution approaches the analytic solution as the grid is refined. As mentioned in [34] the Lax-Wendroff algorithm is proven to be conservative if

$$\sum_{j\,nodes}\left(\frac{V}{\Delta t}\delta U\right)_j = \sum(\text{boundary fluxes}) + (\text{source terms}), \tag{3.19}$$

where δU_j is equal to the sum of the contributions from all of the cells of which node j is a corner. The sum of the boundary fluxes and the source terms can be replaced by the sum of the contributions to the corner nodes from all the cells, i.e.

$$\sum_{j\,nodes}\left(\frac{V}{\Delta t}\delta U\right)_j = \sum_{i\,cells}(\text{sum of contributions to corner nodes})_i, \tag{3.20}$$

which in turn can be divided into sums of contributions from the first-, the second-order, the smoothing and the source terms.

$$\sum_{j\,nodes}\left(\frac{V}{\Delta t}\delta U\right)_j = \sum_{i\,cells}(1^{st}\text{-order})_i + (2^{nd}\text{-order})_i + (\text{smoothing})_i + (\text{source terms})_i. \tag{3.21}$$

The second-order flux terms are written in a way such that the sum of their contributions to the corner nodes of a cell is zero. This feature holds also for the second- and fourth-difference smoothing operators (see Chapter 4). Thus, the only contributions to the right-hand side of Equation (3.19) is given by the first-order inviscid fluxes and the source terms. As already pointed out, the first-order terms represent a flux balance for the cell, i.e. the scheme is written such that the flux out of a particular cell across a

particular face is equal an opposite to the flux out of the neighboring cell across the same face. Hence all the interior fluxes cancel leaving only the boundary flux terms.

Using the discretization procedure of Section 3.1 the solution for steady flows is formally spatially second-order accurate even for non-uniform grids that have metrics discontinuities. Indeed, Hall [46] observed that as steady-state is approached, that is $\delta U \rightarrow 0$, the first-order change ΔU behaves similarly, i.e. $\Delta U \rightarrow 0$ (in an inertial frame of reference, i.e. $Q = 0$). This is consistent with Eqs. (3.9) and (3.17) since the second-order terms ΔF, ΔG, ΔH and ΔQ are zero for $\Delta U = 0$. Hence, the essential term to be considered for accuracy is the flux balance for a single cell as expressed by Eq. (3.8). This is locally fourth-order accurate and thus integrating over the entire domain composed of the order of $1/l^2$ boundary cells results in a global flux balance which is second-order accurate. This is an advantage over the cell-averaged finite-volume schemes such as that of Jameson et al. [56], in which second-order spatial accuracy is obtained only on smooth grids.

For a combined stator/rotor calculation, conservation ultimately depends on the data transfer algorithm used at the interface. This is discussed in Section 5.5 for steady flows and Section 8.3 for unsteady flows.

The second-order terms introduce an effect similar to upwinding or downwinding, which is necessary to ensure the proper domain of dependence. Thus, the Lax-Wendroff algorithm is consistent with the local wave propagation. Also, these terms stabilize the numerical procedure and make the overall scheme second-order time-accurate. Additional details can be found in References [81, 46, 104, 3].

3.3 Unstructured meshes and implementation

As opposed to the mesh generation technique described in Appendix A, the implementation of the solution method uses an unstructured grid. This technique offers the advantage of effectively uncoupling the mesh generation from the flow solver, see Reference [75].

In this method, a one-dimensional array is used in which each index is associated with a grid coordinate. The flow variables associated with each node together with some cell-related variables are also defined in a one-dimensional array. One set of cell variables is defined as pointers giving the indices of the grid nodes which form the corners of the cell. The pointer system is required because the Lax-Wendroff algorithm sweeps through the list of cells from which corner nodes information is gathered to calculate the fluxes and the source terms and then distributes appropriate changes to the flow variables back to the corner nodes.

The implementation of the Lax-Wendroff scheme on unstructured grids is briefly outlined here. The first pass calculates the fluxes F, G and H at all nodes. The second pass calculates on a cell-by-cell basis the ΔU, ΔF, ΔG, ΔH and ΔQ and then the contributions to the changes at each of its nodes. The contributions to the node changes from the second- and fourth-difference smoothing terms are also evaluated in this pass together with the changes at the boundary nodes due to the inlet/outlet/interface and wall boundary conditions. The third pass adds the changes onto the flow variables at each node and evaluates the convergence checks.

The numerical scheme is implemented such that one simultaneously calculates the flow in both the stator and the rotor, with interface boundary conditions implemented to couple the two calculations together. A system of cell coloring, designed to eliminate data dependencies at the cell corners, makes it possible to take full advantage of vector and concurrent arithmetic. By construction, no two cells of the same color touch each other, so computations on one color can be performed simultaneously on either a vector

pipeline or multi-processor machine. This coloring system is used in the second pass and makes it also possible to compute, in the same loop, the rotating and non-rotating fluxes. A set of 16 colors is used in each of the two frame of references. Half of the 16 colors are assigned to cells connected to the blade, hub and tip solid surfaces which are then used in the implementation of the wall boundary condition. The remaining 8 colors are assigned to the field cells.

Periodic and solid wall boundary conditions are discussed in the next two sections. Inlet/outlet and stator/rotor interface boundary conditions are the subject of Chapter 5.

3.4 Periodic boundary condition

For steady-state turbomachinery axisymmetric flow calculations it is possible to reduce the size of the computational domain from multiple blade passages to one blade-to-blade passage, even if the rotor pitch does not match the stator pitch. The calculation is then performed with suitably defined boundary conditions at periodic surfaces. Using the Lax-Wendroff algorithm this is easily implemented by adding the update contributions that one periodic node on one side of the boundary surface (say lower) obtains from its contributing cells C, D, G and H to the contributions that the corresponding upper periodic node obtains from its cells A, B, F and E. In the axisymmetric case (as opposed to the linear cascade), the third and fourth Cartesian components of the changes in the state vector U on one side of the periodic surface have to be rotated by the pitch angle θ_P before they can be added to their counterparts on the other periodic surface. For instance, the changes on the lower periodic surface are expressed as

$$\begin{aligned}
\delta U_{1lower} &= \delta U_{1lower} + \delta U_{1upper} \\
\delta U_{2lower} &= \delta U_{2lower} + \delta U_{2upper} \\
\delta U_{3lower} &= \delta U_{3lower} + \delta U_{3upper}\cos(\theta_P) - \delta U_{4upper}\sin(\theta_P)
\end{aligned} \tag{3.22}$$

$$\delta U_{4lower} = \delta U_{4lower} + \delta U_{3upper} \sin(\theta_P) + \delta U_{4upper} \cos(\theta_P)$$

$$\delta U_{5lower} = \delta U_{5lower} + \delta U_{5upper},$$

where

$$\theta_P = \frac{2\pi}{\text{number of blades}}. \tag{3.23}$$

The sum of the upper and lower contributions is then used to update the flow variables at both nodes.

For unsteady stator/rotor computations this same periodic boundary condition is used, which means that the stator-to-rotor pitch ratio has to equal 1. For non-equal pitches the stator/rotor interface boundary conditions as well as the periodic conditions get more complicated (although conceptually not much more difficult) and are not considered in this thesis.

3.5 Wall boundary condition

A solid wall boundary condition is applied at the hub, the tip and the blade surface. The wall boundary condition states that there is no normal flow relative to the surface. This is analytically expressed by

$$\vec{V} \cdot \vec{n} = 0 \quad \text{stationary frame,} \tag{3.24}$$

and

$$\vec{W} \cdot \vec{n} = 0 \quad \text{rotating frame.} \tag{3.25}$$

$\vec{n}$ is the unit vector normal to the boundary surface and $\vec{V}$, $\vec{W}$ are the absolute and relative velocity vectors, respectively. An equivalent statement is that there is no flux of mass through the wall, and so the only contribution from the wall faces to the fluxes is through the pressure.

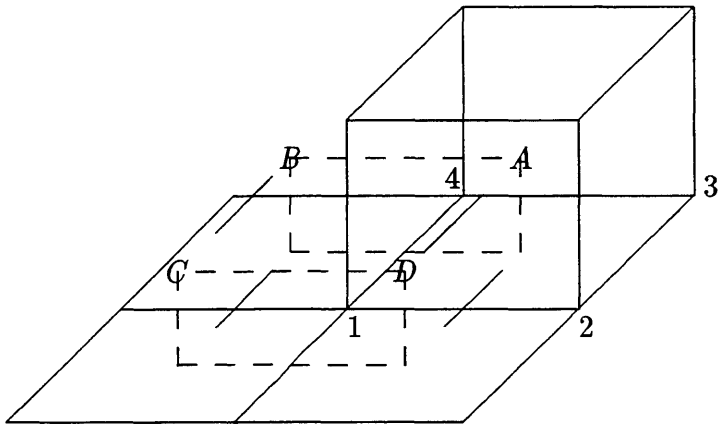

Figure 3.4: Wall boundary cells with modified control volume (dashed). Wall face 6 of cell A is defined by the edge nodes 1234.

The solid surface algorithm is implemented in the overall procedure after the Lax-Wendroff changes δU have been distributed to all the nodes, including the nodes at the walls. Assume that nodes 1 to 4 of cell A lie on a solid wall that is also defined by the bottom faces of cells B, C and D, see Figure 3.4. Since the mesh cells E, F, G and H do not exist and thus do not contribute to the fluxes, the control volume of the pseudo-mesh cell P is altered. The algorithm sweeps through the list of wall-colored cells and corrects the Lax-Wendroff changes of the eight corner nodes, using the wall faces fluxes. For instance, the contribution of cell A to δU_{1A} is modified as

$$(\delta U_{1A})_{wall} = (\delta U_{1A})_{field} + \frac{1}{8}\left(\frac{\Delta t}{V}\right)_1 (\Delta U_A)_{wall\,correction}, \tag{3.26}$$

where

$$(\Delta U_A)_{wall\,correction} = \left(\bar{F}S_x + \bar{G}S_y + \bar{H}S_z\right)_{f=6} - \begin{pmatrix} 0 \\ \bar{p}S_x \\ \bar{p}S_y \\ \bar{p}S_z \\ 0 \end{pmatrix}_{f=6} . \tag{3.27}$$

The first term on the right-hand-side of the above equation represents the flux error introduced in the field calculation, whereas the second term is the actual pressure contribution from face number 6 of Figs. 3.1 and 3.4.

Chapter 4

Numerical Smoothing

The Numerical smoothing consists of a damping operator which is added to numerical schemes in order to stabilize them by preventing unwanted high-frequency waves in smooth flow regions. In the Lax-Wendroff algorithm the second-order flux term is analogous to a dissipative operator of upwind type. This feature renders the scheme stable for the calculation of smooth flow fields. However it can be shown, see for instance [104] and [109], that the Lax-Wendroff finite difference approximation of the model wave equation introduces a third-order dispersion (and a fourth-order dissipation) error. Dispersion is a phenomenon in which waves of different frequencies travel at different speeds and arises because of the non-linear relation between wave number and frequency in the discrete approximation to the differential equation. As a result steady-state oscillatory modes known as odd-even decoupling modes are allowed as part of the solution in the basic scheme. Hence, a so-called *background* or *freestream* smoothing is necessary to damp out these non-physical oscillations.

Numerical smoothing is also required to capture discontinuities such as shocks. In the mechanism of creation of a shock, it is known that viscosity as well as heat conduction play a dominant role. These effects allow smooth variations of pressure and density (as well as other flow quantities such as Mach number and velocity) so that the shock thickness remains finite. It is thus only in the limit of no heat conduction and no viscosity that the variations approach the discontinuous values given by the Rankine-Hugoniot theory. Hence, a dissipative operator is required in order for a shock capturing technique to give a thickness to the shock. This layer is usually of the order of a few mesh cells

characteristic length. The *shock* smoothing is usually obtained by a second-difference operator.

While its presence is essential, it is important that the numerical smoothing terms be kept as small as possible to minimize degradation of the solution accuracy.

In this work, the numerical smoothing is constructed as a combination of a fourth- and a second-difference damping operator. Though the structure of the smoothing operators vary, this is a standard approach adopted by many researchers, see for instance References [56, 90], and which conceptually corresponds to adding terms of the form

$$-(SF)_{smo4}\nabla\cdot\left(l\nabla(l^2\nabla^2 U)\right)+(SF)_{smo2}\nabla\cdot(\kappa(l\nabla U)), \tag{4.1}$$

to the right-hand-side of Equation (2.1). $(SF)_{smo4}$ and $(SF)_{smo2}$ are scaling factors for the fourth- and second-difference operators, respectively. l is a length comparable in magnitude to the local grid size, and κ is an artificial bulk viscosity. Numerically, the damping terms are both added to the basic Lax-Wendroff scheme when evaluating the changes in the state vector variables. The following sections discuss these two types of damping.

4.1 Fourth-difference smoothing

Acting at node 1, the change in the state vector U due to the fourth-difference smoothing operator is

$$(\delta U_1)_{smo4}=\left(\frac{\Delta t}{V}\right)_1\sum_{i=1}^{8\,cells}-\nu_4\left(\frac{V}{\Delta t_{max}}\right)_i(\bar{D}_i^2-D_1^2). \tag{4.2}$$

This contribution is added to the right-hand-side of Equation (3.6), and the eight cells refer to the neighboring cells $A,\ldots,H$ of Figure 3.2. D_1^2 is a pseudo-Laplacian based on the six edge nodes surrounding node 1, see Fig. 4.1, and defined by Holmes and Connell

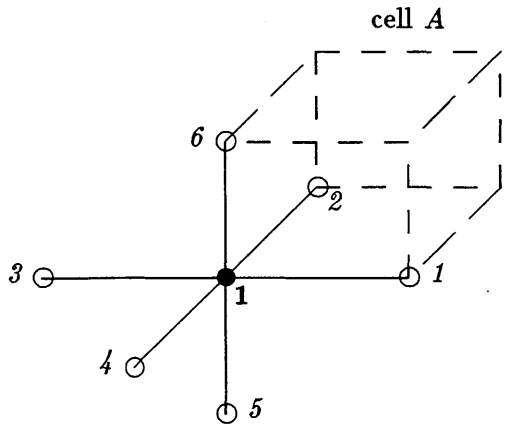

Figure 4.1: Stencil for pseudo-Laplacian. For clarity cells $B, \ldots, H$ are not represented.

[54] as

$$D_1^2 = \sum_{j=1}^{6\,nodes} \psi_j \, (U_j - U_1). \tag{4.3}$$

Notice that this technique is not restricted to using the stencil shown in Figure 4.1. U_1 and U_j represent nodal values of the state vector, whereas $\bar{D}_i^2$ is the discrete representation of a cell-averaged pseudo-Laplacian, i.e.

$$\bar{D}_i^2 = \sum_{j=1}^{8\,corner\ nodes} \frac{1}{8} D_j^2. \tag{4.4}$$

In Eq. (4.3), ψ_j is a grid dependent weight which is designed to be close to unity to ensure an even dependence on all of the neighboring nodes. This is achieved by defining $\psi_j = 1 + \Delta\psi_j$ and using Lagrange multipliers to minimize the cost function C_1,

$$L \equiv C_1 = \sum_{j=1}^{6\,nodes} (\Delta\psi_j)^2, \tag{4.5}$$

under the constraints that linear functions in x, y and z produce a pseudo-Laplacian with zero value, that is

$$\begin{aligned} f(\Delta\psi_j) &\equiv D_1^2(x) = \sum_{j=1}^{6\,nodes} \psi_j (x_j - x_1) = 0, \\ g(\Delta\psi_j) &\equiv D_1^2(y) = \sum_{j=1}^{6\,nodes} \psi_j (y_j - y_1) = 0, \end{aligned} \tag{4.6}$$

$$h(\Delta\psi_j) \equiv D_1^2(z) = \sum_{j=1}^{6\,nodes} \psi_j(z_j - z_1) = 0.$$

According to the Lagrange multiplier technique, see for instance [52], this is equivalent to specify that the 'auxiliary function',

$$\phi = L - \lambda_x f - \lambda_y g - \lambda_z h \tag{4.7}$$

attains a relative maximum or minimum at node 1, when no constraints are imposed. Thus,

$$\frac{\partial \phi}{\partial(\Delta\psi_j)} = 0 \tag{4.8}$$

$$\Longrightarrow \quad \Delta\psi_j = \lambda_x(x_j - x_1) + \lambda_y(y_j - y_1) + \lambda_z(z_j - z_1). \tag{4.9}$$

Replacing Eq. (4.9) into Eqs. (4.6) and solving the resulting system using Cramer's rule, the following relations are obtained for the unknowns λ_x, λ_y and λ_z.

$$\begin{aligned}
\lambda_x &= \frac{-R_x(I_{yy}I_{zz} - I_{yz}^2) + R_y(I_{xy}I_{zz} - I_{xz}I_{yz}) - R_z(I_{xy}I_{yz} - I_{yy}I_{xz})}{I_{xx}(I_{yy}I_{zz} - I_{yz}^2) - I_{xy}(I_{xy}I_{zz} - I_{xz}I_{yz}) + I_{xz}(I_{xy}I_{yz} - I_{yy}I_{xz})}, \\
\lambda_y &= \frac{R_x(I_{xy}I_{zz} - I_{xz}I_{yz}) - R_y(I_{xx}I_{zz} - I_{xz}^2) + R_z(I_{xx}I_{yz} - I_{xy}I_{xz})}{I_{xx}(I_{yy}I_{zz} - I_{yz}^2) - I_{xy}(I_{xy}I_{zz} - I_{xz}I_{yz}) + I_{xz}(I_{xy}I_{yz} - I_{yy}I_{xz})}, \\
\lambda_z &= \frac{-R_x(I_{xy}I_{yz} - I_{yy}I_{xz}) + R_y(I_{xx}I_{yz} - I_{xy}I_{xz}) - R_z(I_{xx}I_{yy} - I_{xy}^2)}{I_{xx}(I_{yy}I_{zz} - I_{yz}^2) - I_{xy}(I_{xy}I_{zz} - I_{xz}I_{yz}) + I_{xz}(I_{xy}I_{yz} - I_{yy}I_{xz})},
\end{aligned} \tag{4.10}$$

where

$$R_x = \sum_{j=1}^{6\,nodes} (x_j - x_1), \quad R_y = \sum_{j=1}^{6\,nodes} (y_j - y_1), \quad R_z = \sum_{j=1}^{6\,nodes} (z_j - z_1), \tag{4.11}$$

$$I_{xx} = \sum_{j=1}^{6\,nodes} (x_j - x_1)^2, \quad I_{yy} = \sum_{j=1}^{6\,nodes} (y_j - y_1)^2, \quad I_{zz} = \sum_{j=1}^{6\,nodes} (z_j - z_1)^2, \tag{4.12}$$

$$\begin{aligned}
I_{xy} &= \sum_{j=1}^{6\,nodes} (x_j - x_1)(y_j - y_1), \quad I_{xz} = \sum_{j=1}^{6\,nodes} (x_j - x_1)(z_j - z_1), \\
I_{yz} &= \sum_{j=1}^{6\,nodes} (y_j - y_1)(z_j - z_1).
\end{aligned} \tag{4.13}$$

The purpose of the constraints is to ensure that the smoothing term does not corrupt a linear solution on an irregular mesh. The importance of this was first established by Lindquist [74] and Giles [31] but their approach is computationally more expensive and complicated to implement in 3-D since it would require division of the cells into tetrahedra. Note that this procedure for computing the weights does not require a special treatment of the weights at the mesh boundaries. The branches of the pseudo-Laplacian stencil located outside the computational domain are simply cut-off and the weights adjust themselves accordingly.

$(\Delta t/V)_1$ is the (time-step/volume) ratio associated with the grid node 1, whereas $(V/\Delta t_{max})_i$ is the (volume/maximum time-step) ratio for cell i. The use of the local maximum time-step in the smoothing terms (2^{nd} and 4^{th}) ensures that steady and unsteady calculations use the same (time-step/volume ratio). This is important when comparing steady to time-averaged unsteady solutions, see Chapters 8 and 9.

In Eq. (4.2), ν_4 is a coefficient whose typical value is 0.002. However, to accelerate convergence in a steady-state calculation a value of order 0.01 can be employed.

Conservation is ensured by defining $\bar{D}_i$ as in Eq. (4.4), i.e. the sum of the smoothing contributions to the corner nodes of a cell is zero. By operating a conservative second-difference with the second-order pseudo-Laplacian, one ensures that neither mass, momentum or energy is produced by this smoothing nor that the effects of inlet distortions on the flow field are smoothing dependent, except for second-order effects. As noticed by Holmes and Connell [54], the optimum weights for some distorted grids may differ significantly from unity. For stability reasons, they elect to clip the weights in the range (0,2). However, although a slower convergence rate has been observed, some of the results presented in this work have been calculated without clipping.

4.2 Shock smoothing

As mentioned earlier, the purpose of the shock smoothing is to stabilize shocks calculations. Conceptually, it consists of a second-difference operator acting on the state vector U. It is written as

$$(\delta U_1)_{smo2} = \left(\frac{\Delta t}{V}\right)_1 \sum_{i=1}^{8\,cells} \kappa_i \left(\frac{V}{\Delta t_{max}}\right)_i (\bar{U}_i - U_1). \tag{4.14}$$

As for the fourth-difference smoothing term, Eq. (4.14) is added to the right-hand-side of Equation (3.6). $\bar{U}_i$ is the cell-averaged state vector as defined by Eq. (4.4) and κ_i is a cell-defined artificial bulk viscosity tailored by the local flow divergence and Mach number to avoid large shock overshoots and not to alter the global accuracy of the scheme in smooth flow regions. The derivation of the bulk viscosity stems from an idea of von Neumann and Richtmeyer and is discussed in the following paragraph.

The internal structure of a physical shock is determined by the balance of the inviscid flux and the flux due to the bulk viscosity of the fluid. For instance, the Navier-Stokes solution for a 1-D normal shock layer can be found in Reference [111]. The idea of von Neumann and Richtmeyer [89] is to introduce a purely artificial dissipative mechanism into the momentum equation of an otherwise inviscid fluid so that the shocks could be captured as part of the solution. For 1-D flow, the modified equation[1] in conservative form is

$$\frac{\partial \rho u}{\partial t} + \frac{\partial \rho u^2}{\partial x} = -\frac{\partial p}{\partial x} - \frac{\partial}{\partial x}\left(-\kappa \frac{\partial u}{\partial x}\right). \tag{4.15}$$

With ordinary viscosity, in which the stress is proportional to the rate of shear, the thickness of the transition layer varies with the shock strength, approaching zero for a very strong shock and infinity for a very weak one. However, one wishes to ensure that the shock width remains nearly the same, i.e. of the order of the local grid spacing, regardless of the shock strength. For that reason, von Neumann and Richtmeyer

[1]This momentum equation in this form is dimensional, and so is κ. All the other equations in this chapter are in non-dimensional form, and thus so is κ_i.

proposed the following definition for a variable 'pseudo-viscous' coefficient κ,

$$\kappa = \begin{cases} \rho\, l^2 \left|\frac{\partial u}{\partial x}\right|, & \frac{\partial u}{\partial x} < 0 \\ 0, & \frac{\partial u}{\partial x} \geq 0 \end{cases} \tag{4.16}$$

Setting κ to zero when the flow divergence (or volumetric dilatation) is positive prevents smoothing of expansion regions. The variable l represents the shock width and is proportional to the local mesh spacing.

Applying this concept to 3-D flows requires the definition of a scaled flow divergence for a given cell i. With reference to Figure 3.1 this is defined as

$$\begin{aligned} div(\vec{v})_i &\approx \frac{1}{V_i^{2/3}} \iint_{cell\, i} (\vec{v} \cdot \vec{n})\, dS \\ &= \frac{1}{V_i^{2/3}} \sum_{f=1}^{6\, faces} \vec{v}_f \cdot \vec{S}_f \\ &= \frac{1}{V_i^{2/3}} \sum_{f=1}^{6\, faces} (\text{surface fluxes})_f \\ &= \frac{1}{V_i^{2/3}} \sum_{f=1}^{6\, faces} (\bar{u}S_x + \bar{v}S_y + \bar{w}S_z)_f. \end{aligned} \tag{4.17}$$

$\vec{v} = \vec{V}$ in the absolute frame and $\vec{v} = \vec{W}$ in the rotating frame. S_x, S_y and S_z are the projected areas on the yz, xz and xy planes of a face cell, respectively, see Appendix B. $\bar{u}$, $\bar{v}$ and $\bar{w}$ represent the face-averaged values from the four corner nodes. For instance $\bar{u}$ on $face$ 1 is given by

$$(\bar{u})_1 = \frac{1}{4}(u_2 + u_3 + u_7 + u_6). \tag{4.18}$$

$\bar{v}$ and $\bar{w}$ are defined similarly. In particular, the total volume flux out of the cell in the y direction is given by

$$\sum_{f=1}^{6\, faces} (\bar{v}S_y)_f = (\bar{v}S_y)_1 + (\bar{v}S_y)_2 + (\bar{v}S_y)_3 + (\bar{v}S_y)_4 + (\bar{v}S_y)_5 + (\bar{v}S_y)_6. \tag{4.19}$$

In the x and z directions, the summations are obtained by replacing $(\bar{v}S_y)$ by $(\bar{u}S_x)$ and $(\bar{w}S_z)$, respectively.

Then, the local cell-defined artificial bulk viscosity κ_i is defined as

$$\kappa_i = \begin{cases} \nu_2 \, \bar{\rho}_i \, \bar{M}_i^2 \, |div(\vec{v})_i|, & div(\vec{v})_i < 0 \\ 0, & div(\vec{v})_i \geq 0 \end{cases} \tag{4.20}$$

The definition of $div(\vec{v})_i$ means that in smooth flow regions it is approximately the flow divergence multiplied by a cell length, and in regions with a discontinuity due to a shock it is approximately the velocity jump across the shock. Thus the shock smoothing is second-order accurate in smooth flow region and consistent with the basic scheme. The coefficient ν_2 has a value of approximately 0.1. The local cell-averaged Mach number is introduced in the artificial bulk viscosity variable in order to prevent excessive smoothing of decelerating flow near stagnation points. Note that unlike von Neumann and Richtmeyer's approach, the shock smoothing used here applies to the variables in conservation form and is employed in the mass, momentum and energy equation. Finally, notice that if κ_i was taken to be a small positive uniform value, then this smoothing would be very similar to Ni's original smoothing as described in Reference [81].

Chapter 5

Quasi-3-D Non-Reflecting Boundary Conditions

5.1 Overview

One typical difficulty occurring in a numerical simulation of a turbomachine flow field is the handling of the boundary conditions (b.c.'s). This is because in an internal flow environment the computation has to be performed on truncated domains, whose far-field boundaries do not represent an undisturbed known flow field as in external aerodynamics. Typically, most of the codes available today are not capable of preventing spurious, non-physical reflections at inflow and outflow boundaries. This leads to erroneous performance predictions, since the calculated flow field is dependent on the position of the far-field boundary condition. Also for secondary flow calculations accurate boundary conditions are needed since using the standard 1-D approach corrupts the solution locally, as shown later in the results section.

The theoretical foundations of non-reflecting boundary conditions for model initial boundary value problems have been established by mathematicians specializing in the analysis of partial differential equations, see for instance [65] and [20]. Some applications involving the Euler equations of fluid dynamics have been done. For 2-D steady-state flow, exact non-reflecting boundary conditions for the solution of the linearized Euler equations can be derived using Fourier expansion in the direction along the inlet and the exit boundaries. This has been done by Ferm and Gustafsson for an airfoil and

a channel flow [25, 26]. Hirsch and Verhoff [53] used a similar approach for cascade flows, though expanding the characteristic variables instead of the primitive ones used by Ferm and Gustafsson. In [35] Giles presented a unified theory on the formulation of non-reflecting boundary conditions and the application to the Euler equations. In particular, he derived different types of boundary conditions. These include exact 1-D and 2-D as well as approximate 2-D boundary conditions to be used for steady and unsteady flows. A different approach has been proposed by Bayliss and Turkel [7]. They used the asymptotic behavior of the wave equation to derive a boundary condition formulation for external flows.

The purpose of this chapter is to present a quasi-three-dimensional non-reflecting boundary condition formulation that can be used in a numerical simulation of steady-state inviscid flow fields. The objective in formulating the non-reflecting boundary conditions is to prevent non physical reflections at inflow and outflow boundaries as well as at stator/rotor interfaces. The method is an adaptation of the exact 2-D steady non-reflecting boundary conditions of Giles [35] to three dimensions. The theoretical approach, based upon Fourier analysis and eigenvectors is presented here as well as the extensions required for the linearized Euler equations. Implemented in a turbomachinery environment, the approach assumes that the solution at the boundary is circumferentially decomposed into Fourier modes, the 0^{th} mode corresponding to the average solution. The average mode is treated according to the standard 1-D boundary condition formulation, which allows the user to specify certain physical quantities at the boundaries. The features of the 1-D approach as well as some of its limitations are discussed in Sections 5.2 and 5.3. The remaining part of the solution, represented by the sum of the harmonics is treated according to the exact 2-D theory and prevents spurious reflections at the boundaries. A very brief summary of the theory is that upstream and downstream of the blade row in an infinite duct which produces no incoming modes, the steady-state perturbations in the density, velocity and pressure must satisfy certain linear relationships. These relationships are found by analyzing the propagation of eigenmodes that are solutions of the linearized Euler equations and vary sinusoidally in the pitchwise direction. Enforcing these relationships at the in-

flow and outflow boundaries imposes steady-state non-reflecting boundary conditions which ensure that no incoming modes are generated. This approach together with its implementation in a 3-D context is discussed in Section 5.4.

The stator/rotor interface treatment is discussed in Section 5.5.

The circumferential Fourier decomposition (versus radial decomposition) is motivated by the fact that in an axial flow turbomachine the pitchwise variations are usually larger than the radial variations. The results presented in Section 5.6 show clearly that using this quasi-3-D non-reflecting boundary condition formulation improves the accuracy.

A very brief summary of this chapter together with the essential conclusions is given in Section 5.7.

Finally note that while this chapter discusses the theoretical aspect of non-reflecting boundary conditions, the reader may refer to Appendix D for the implementation procedure.

5.2 1-D non-reflecting boundary conditions

The usual 1-D approach is to assume perturbations travelling normal to the boundary in the x-direction, see for instance [113]. Hence, the linearized Euler equations written in primitive form reduce to

$$\frac{\partial U_p}{\partial t} + \bar{A}\frac{\partial U_p}{\partial x} = 0, \tag{5.1}$$

where

$$U_p = \begin{pmatrix} \rho - \bar{\rho} \\ u - \bar{u} \\ v - \bar{v} \\ w - \bar{w} \\ p - \bar{p} \end{pmatrix} = \begin{pmatrix} \tilde{\rho} \\ \tilde{u} \\ \tilde{v} \\ \tilde{w} \\ \tilde{p} \end{pmatrix}, \quad \bar{A} = \begin{pmatrix} \bar{u} & \bar{\rho} & 0 & 0 & 0 \\ 0 & \bar{u} & 0 & 0 & \frac{1}{\bar{\rho}} \\ 0 & 0 & \bar{u} & 0 & 0 \\ 0 & 0 & 0 & \bar{u} & 0 \\ 0 & \gamma\bar{p} & 0 & 0 & \bar{u} \end{pmatrix}. \tag{5.2}$$

The elements of the vector U_p represent perturbations from a uniform flow, and the Jacobian matrix $\bar{A}$ is evaluated using those same uniform flow conditions. Notice that this represents only a local linearization of the flow, i.e. within one mesh cell, since when concerned with turbomachinery applications the coefficients of $\bar{A}$ may still vary with radius for instance.

$\bar{A}$ can be diagonalized by the similarity transformation,

$$T^{-1}\bar{A}T = \begin{pmatrix} \bar{u} & 0 & 0 & 0 & 0 \\ 0 & \bar{u} & 0 & 0 & 0 \\ 0 & 0 & \bar{u} & 0 & 0 \\ 0 & 0 & 0 & \bar{u}+\bar{c} & 0 \\ 0 & 0 & 0 & 0 & \bar{u}-\bar{c} \end{pmatrix} = \Lambda, \tag{5.3}$$

where $\bar{c} = \sqrt{\gamma\bar{p}/\bar{\rho}}$ is the mean flow speed of sound. The diagonal components of Λ represent the speed of propagation of five characteristic waves, called the entropy, the two vorticity, and for subsonic flow, the upstream and the downstream irrotational pressure waves, respectively. Multiplication of Eq. (5.1) by T^{-1} yields,

$$\frac{\partial \Phi}{\partial t} + \Lambda \frac{\partial \Phi}{\partial x} = 0, \tag{5.4}$$

where $\Phi = T^{-1}U_p$. Φ is referred to as the vector of linearized characteristic variables,

and in detail the five variables are,

$$\begin{pmatrix} \phi_1 \\ \phi_2 \\ \phi_3 \\ \phi_4 \\ \phi_5 \end{pmatrix} = \begin{pmatrix} -\bar{c}^2 & 0 & 0 & 0 & 1 \\ 0 & 0 & \bar{\rho}\bar{c} & 0 & 0 \\ 0 & 0 & 0 & \bar{\rho}\bar{c} & 0 \\ 0 & \bar{\rho}\bar{c} & 0 & 0 & 1 \\ 0 & -\bar{\rho}\bar{c} & 0 & 0 & 1 \end{pmatrix} \begin{pmatrix} \widetilde{\rho} \\ \widetilde{u} \\ \widetilde{v} \\ \widetilde{w} \\ \widetilde{p} \end{pmatrix}. \tag{5.5}$$

The transformation from the 1-D characteristic variables is given by $U_p = T\Phi$, i.e.

$$\begin{pmatrix} \widetilde{\rho} \\ \widetilde{u} \\ \widetilde{v} \\ \widetilde{w} \\ \widetilde{p} \end{pmatrix} = \begin{pmatrix} \frac{-1}{\bar{c}^2} & 0 & 0 & \frac{1}{2\bar{c}^2} & \frac{1}{2\bar{c}^2} \\ 0 & 0 & 0 & \frac{1}{2\bar{\rho}\bar{c}} & \frac{-1}{2\bar{\rho}\bar{c}} \\ 0 & \frac{1}{\bar{\rho}\bar{c}} & 0 & 0 & 0 \\ 0 & 0 & \frac{1}{\bar{\rho}\bar{c}} & 0 & 0 \\ 0 & 0 & 0 & \frac{1}{2} & \frac{1}{2} \end{pmatrix} \begin{pmatrix} \phi_1 \\ \phi_2 \\ \phi_3 \\ \phi_4 \\ \phi_5 \end{pmatrix}. \tag{5.6}$$

At a subsonic inlet the correct unsteady, non-reflecting boundary conditions would be

$$\begin{pmatrix} \phi_1 \\ \phi_2 \\ \phi_3 \\ \phi_4 \end{pmatrix} = 0, \tag{5.7}$$

while at an outlet the correct non-reflecting boundary condition would be

$$\phi_5 = 0. \tag{5.8}$$

The standard numerical method for implementing these would be to calculate or extrapolate the outgoing characteristic values from the interior domain, and then use Eq. (5.6) to reconstruct the solution on the boundary.

5.3 1-D steady-state reflecting b.c.'s

For calculations of steady-state external flows, these one-dimensional boundary conditions may be applied without modification. In these types of calculations the far-field represents uniform conditions in which the inlet flow corresponds to the outlet one. That is, the steady-state perturbations in the density, velocity and pressure are zero. Hence, setting the incoming characteristics to zero is consistent with uniform flow conditions, so that this boundary condition formulation is non-reflecting.

For time-marching calculations of steady-state internal flows, however, the one-dimensional (unsteady) non-reflecting boundary conditions require modification. In a typical turbomachinery application one wishes to specify certain physical quantities at the boundaries. For example, at the outflow boundary one usually specifies the static pressure. This means that the incoming characteristic variable ϕ_5, instead of being zero, must have the value required to give the correct exit pressure. This is now a reflective boundary condition, since an outgoing unsteady pressure wave will produce an incoming pressure wave to keep the exit pressure constant. Similar unsteady reflections are generated at the inflow boundary through the specification of particular physical quantities.

The numerical implementation of the boundary conditions is dependent on the numerical algorithm being used for the interior equations. Using a Lax-Wendroff type algorithm to time-march the solution to the steady-state, the changes in the boundary values from time level n to time level $n+1$ are required. Thus the characteristic variables are defined in terms of perturbations to the average inflow or outflow at the time level n.

At the inflow, the average characteristic changes are calculated from the requirement that the average entropy, radial and tangential flow angles, and stagnation enthalpy have

certain values.

$$\begin{aligned}
(\bar{s})^{n+1} &= \bar{s}_{inl}, \\
(\bar{\alpha}_\theta)^{n+1} &= \alpha_{\theta\, inl}, \\
(\bar{\alpha}_R)^{n+1} &= \alpha_{R\, inl}, \\
(\bar{h}_t)^{n+1} &= \bar{h}_{t\, inl}.
\end{aligned} \tag{5.9}$$

$\bar{s}$ is an entropy-related function defined by

$$\bar{s} = \overline{\log(\gamma p) - \gamma \log \rho}, \tag{5.10}$$

and $\bar{h}_t$ is the mean total enthalpy. $\alpha_{\theta\, inl}$ and $\alpha_{R\, inl}$ together with $\bar{s}_{inl}$ and $\bar{h}_{t\, inl}$ are user-specified average inflow angles, entropy and total enthalpy, respectively, which are usually function of the radius.

For an axially subsonic outflow, the first four characteristics are outgoing, so only the fifth characteristic variable needs to be set. The average change in the characteristic is determined to achieve the user-specified average exit pressure $\bar{p}_{out}$ at a certain radius together with the requirement that the outflow is in radial equilibrium. The latter condition is expressed by

$$\frac{\partial \bar{p}(R)_{out}}{\partial R} = \bar{\rho} \frac{\bar{u}_\theta^2}{R}, \tag{5.11}$$

together with the specification of $\bar{p}_{out}$ at some particular radius.

A detailed description of the implementation procedure is given in Appendix D.

The standard one-dimensional boundary conditions are also 'reflective' in a steady-state sense. This is most clearly understood at the outflow boundary where a circumferentially uniform exit pressure has been specified. If the outflow is supersonic there will be an oblique shock extending from the trailing edge to the outflow boundary. The uniform pressure condition forces the generation of a reflected expansion wave at the boundary. This expansion wave extends upstream to the blade row, and can produce

significant errors. The objective of the new boundary conditions presented in the next section is to prevent this reflection, and similar reflections at the inflow boundary.

5.4 Quasi-3-D approach

5.4.1 Outline

By the principle of linear superposition it is possible to split a general solution into a sum of different frequencies, and calculate their contributions independently, each with its own forcing terms and boundary conditions. Here we are concerned with axial turbomachines in which the flow variations are usually larger in the circumferential than in the radial direction. Hence, by assuming a periodic solution in the pitchwise direction it is quite natural to perform a Fourier decomposition of the flow at the boundary into a sum of a mean and circumferential components.

In this approach, the 0^{th} Fourier mode corresponds to the circumferential solution average and is treated according to the standard 1-D characteristics theory. Specifically, this allows the user to specify the value of the circumferential average characteristics, but this quantity may be radius dependent. For instance, this is how the average inlet tangential, radial flow angles, stagnation enthalpy and entropy can be specified, as well as the outlet radial equilibrium condition.

The remaining part of the solution, represented by the sum of the harmonics, is treated according to Giles' 2-D non-reflecting boundary conditions theory [35]. Implemented in 3-D, this part of the formulation uncouples the tangential flow variation from the radial variation. However, the advantage of this improved approach over the standard 1-D formulation is that when sweeping along the span, exact 2-D non-reflecting boundary conditions can be imposed on each Fourier mode in the tangential direction.

Section 5.5 describes how the same boundary condition approach can be used to match together a stator and a rotor calculations, so that the interface is treated in an average, conservative manner. Since this method considers radial flow variations in the average mode only, it is called *quasi-3-D non-reflecting boundary conditions.*

Note that in the absence of any radial variations, the boundary conditions are exact within the 2-D linear theory.

5.4.2 Fourier analysis: dispersion relation

The boundary condition treatment is approached by assuming that the flow is governed by the linearized Euler equations, which, written in primitive form for two-dimensional steady-state variations are

$$\bar{A}\frac{\partial U_p}{\partial x} + \bar{B}\frac{\partial U_p}{\partial y} = 0, \tag{5.12}$$

where U_p and $\bar{A}$ are given by Eqs. (5.2) and $\bar{B}$ represents the following matrix

$$\bar{B} = \begin{pmatrix} \bar{v} & 0 & \bar{\rho} & 0 & 0 \\ 0 & \bar{v} & 0 & 0 & 0 \\ 0 & 0 & \bar{v} & 0 & \frac{1}{\bar{\rho}} \\ 0 & 0 & 0 & \bar{v} & 0 \\ 0 & 0 & \gamma\bar{p} & 0 & \bar{v} \end{pmatrix}. \tag{5.13}$$

Fourier analysis considers wave-like solutions which are equal to a scalar wave function multiplying a constant column vector.

$$U_p(x,y) = e^{i(kx+ly)}\boldsymbol{u}^R. \tag{5.14}$$

Substituting this into the differential equation gives

$$(k\bar{A} + l\bar{B})\boldsymbol{u}^R = 0, \tag{5.15}$$

which has non-trivial solutions provided that

$$\det(k\bar{A} + l\bar{B}) = 0. \tag{5.16}$$

Evaluating Eq. (5.16) gives the dispersion relation, which is a polynomial equation of degree 5 in each of k and l.

$$(\bar{u}k + \bar{v}l)^3 \left((\bar{u}k + \bar{v}l)^2 - \bar{c}^2(k^2 + l^2)\right) = 0. \tag{5.17}$$

We will be concerned with the roots k_n of this equation for given values of l.

Three of the five roots are clearly identical.

$$k_{1,2,3} = \frac{-\bar{v}l}{\bar{u}}. \tag{5.18}$$

The other two roots are given by

$$\left(\bar{c}^2 - \bar{u}^2\right) k^2 - 2\bar{u}\bar{v}kl - (\bar{v}l)^2 + (\bar{c}l)^2 = 0. \tag{5.19}$$

Hence the fourth and the fifth roots are defined by,

$$k_4 = \frac{(\bar{u}\bar{v}l + \bar{c}\beta l)}{\bar{c}^2 - \bar{u}^2}, \tag{5.20}$$

$$k_5 = \frac{(\bar{u}\bar{v}l - \bar{c}\beta l)}{\bar{c}^2 - \bar{u}^2}, \tag{5.21}$$

where

$$\beta = \begin{cases} i\,\mathrm{sign}(l)\sqrt{\bar{c}^2 - (\bar{u}^2 + \bar{v}^2)}\,, & (\bar{u}^2 + \bar{v}^2) < \bar{c}^2 \\ -\mathrm{sign}(\bar{v})\sqrt{(\bar{u}^2 + \bar{v}^2) - \bar{c}^2}\,, & (\bar{u}^2 + \bar{v}^2) > \bar{c}^2. \end{cases} \tag{5.22}$$

Notice that for supersonic flow, β does not depend on l. The two relations for β reflect the difference in the behavior of a perturbation propagating in subsonic or supersonic flow. In subsonic flow, the perturbation decays exponentially, whereas in supersonic flow it propagates indefinitely. The appearance of two values for β is further discussed in Reference [32].

5.4.3 Fourier analysis: eigenvectors

A critical step in the construction and analysis of boundary conditions is to separate the waves into incoming and outgoing modes. This is accomplished by looking at the velocity of energy propagation, i.e. the group velocity [112] of the five dispersive propagating waves. This would require to introduce the time dependent term in Eqs. (5.12), but the direction of propagation is already known from the analysis given in Section 5.2.

The column vector $\boldsymbol{u}^R$ is the right null-vector of the singular matrix $(kI + l\bar{A}^{-1}\bar{B})$.

$$(kI + \bar{A}^{-1}l\bar{B})\boldsymbol{u}^R = \bar{A}^{-1}(k\bar{A} + l\bar{B})\boldsymbol{u}^R = 0, \tag{5.23}$$

i.e. $\boldsymbol{u}^R$ is a right eigenvector of $l\bar{A}^{-1}\bar{B}$ with eigenvalue $-k$. The construction of the non-reflecting boundary conditions requires also the row vector $\boldsymbol{v}^L$ which is the left null-vector of the singular matrix $\bar{A}^{-1}(k\bar{A} + l\bar{B})$.

$$\boldsymbol{v}^L\bar{A}^{-1}(k\bar{A} + l\bar{B}) = 0. \tag{5.24}$$

The important feature of this left null-vector is its orthogonality to $\boldsymbol{u}^R$. If k_m and k_n are two different solutions of the dispersion relation for the same values of l, and if $\boldsymbol{u}_m^R$ and $\boldsymbol{v}_n^L$ are the corresponding right and left eigenvectors, then

$$\boldsymbol{v}_n^L\bar{A}^{-1}(k_m\bar{A} + l\bar{B})\boldsymbol{u}_m^R = 0, \tag{5.25}$$

and

$$\boldsymbol{v}_n^L\bar{A}^{-1}(k_n\bar{A} + l\bar{B})\boldsymbol{u}_m^R = 0. \tag{5.26}$$

Subtracting one from the other gives

$$(k_m - k_n)\boldsymbol{v}_n^L\boldsymbol{u}_m^R = 0 \;\Rightarrow\; \boldsymbol{v}_n^L\boldsymbol{u}_m^R = 0. \tag{5.27}$$

This orthogonality condition will be used later in the next section.

Root 1: entropy wave

$$k_1 = \frac{-\bar{v}l}{\bar{u}}. \tag{5.28}$$

After some algebra, it can be shown that appropriate right and left orthonormal eigenvectors are

$$\boldsymbol{u}_1^R = \begin{pmatrix} -1/\bar{c}^2 \\ 0 \\ 0 \\ 0 \\ 0 \end{pmatrix}, \tag{5.29}$$

and

$$\boldsymbol{v}_1^L = \begin{pmatrix} -\bar{c}^2 & 0 & 0 & 0 & 1 \end{pmatrix}. \tag{5.30}$$

This choice of eigenvectors corresponds to the entropy wave. This can be verified by noting that the only non-zero term in the right eigenvector is the density, so that the wave has varying entropy, no vorticity and constant pressure. Also, the left eigenvector 'measures' entropy in the sense that $\boldsymbol{v}_1^L U_p$ is equal to the linearized entropy, $\tilde{p} - \bar{c}^2\tilde{\rho}$.

Root 2: first vorticity wave

$$k_2 = \frac{-\bar{v}l}{\bar{u}}. \tag{5.31}$$

The second set of right and left eigenvectors for the multiple root is given by

$$\boldsymbol{u}_2^R = \frac{1}{\bar{\rho}\bar{c}} \begin{pmatrix} 0 \\ -l^2/\bar{u}k_2^2 \\ l/\bar{u}k_2 \\ 0 \\ 0 \end{pmatrix} = \frac{1}{\bar{\rho}\bar{c}} \begin{pmatrix} 0 \\ -\bar{u}/\bar{v}^2 \\ -1/\bar{v} \\ 0 \\ 0 \end{pmatrix}, \tag{5.32}$$

and

$$\boldsymbol{v}_2^L = \bar{\rho}\bar{c}(\ 0 \quad -\bar{u} \quad -\bar{v} \quad 0 \quad -1/\bar{\rho} \ ). \tag{5.33}$$

This root corresponds to a vorticity wave, which can be verified by noting that the right eigenvector gives a wave with vorticity, but uniform entropy and pressure.

Root 3: second vorticity wave

$$k_3 = \frac{-\bar{v}l}{\bar{u}}. \tag{5.34}$$

The third set of right and left eigenvectors for the multiple root is given by

$$\boldsymbol{u}_3^R = \frac{1}{\bar{\rho}\bar{c}} \begin{pmatrix} 0 \\ 0 \\ 0 \\ l/\bar{u}k_3 \\ 0 \end{pmatrix} = \frac{1}{\bar{\rho}\bar{c}} \begin{pmatrix} 0 \\ 0 \\ 0 \\ -1/\bar{v} \\ 0 \end{pmatrix}, \tag{5.35}$$

and

$$\boldsymbol{v}_3^L = \bar{\rho}\bar{c}(\ 0 \quad 0 \quad 0 \quad -\bar{v} \quad 0 \ ). \tag{5.36}$$

As with root 2, this set of eigenvectors corresponds to a vorticity wave.

Since the first three roots are a multiple root we must check that the chosen right and left eigenvectors satisfy the necessary orthogonality relations.

$$\boldsymbol{v}_n^L \boldsymbol{u}_m^R = 0, \quad n,m = 1,2,3, \quad n \neq m. \tag{5.37}$$

It is easily verified that these are correct.

Root 4: downstream running pressure wave

$$k_4 = \frac{\bar{u}\bar{v}l + \bar{c}\beta l}{\bar{c}^2 - \bar{u}^2}. \tag{5.38}$$

The eigenvectors are

$$\boldsymbol{u}_4^R = \frac{\bar{c}+\bar{u}}{2\bar{\rho}\bar{c}} \begin{pmatrix} \frac{\bar{\rho}}{\bar{c}^2}(-\bar{u}k_4/l - \bar{v}) \\ k_4/l \\ 1 \\ 0 \\ \bar{\rho}(-\bar{u}k_4/l - \bar{v}) \end{pmatrix} = \frac{1}{2\bar{\rho}\bar{c}(\bar{c}-\bar{u})} \begin{pmatrix} -\frac{\bar{\rho}}{\bar{c}}(\bar{c}\bar{v} + \bar{u}\beta) \\ \bar{c}\beta + \bar{u}\bar{v} \\ \bar{c}^2 - \bar{u}^2 \\ 0 \\ -\bar{\rho}\bar{c}(\bar{c}\bar{v} + \bar{u}\beta) \end{pmatrix}, \tag{5.39}$$

and

$$\boldsymbol{v}_4^L = \bar{\rho}\bar{c}(\ 0 \quad -\bar{v} \quad \bar{u} \quad 0 \quad \beta/\bar{\rho}\bar{c} \ ). \tag{5.40}$$

This root corresponds to an isentropic, irrotational pressure wave, travelling downstream.

Root 5: upstream running pressure wave

$$k_5 = \frac{\bar{u}\bar{v}l - \bar{c}\beta l}{\bar{c}^2 - \bar{u}^2}. \tag{5.41}$$

The eigenvectors are

$$\boldsymbol{u}_5^R = \frac{\bar{c}-\bar{u}}{2\bar{\rho}\bar{c}} \begin{pmatrix} \frac{\bar{\rho}}{\bar{c}^2}(-\bar{u}k_5/l-\bar{v}) \\ k_5/l \\ 1 \\ 0 \\ \bar{\rho}(-\bar{u}k_5/l-\bar{v}) \end{pmatrix} = \frac{1}{2\bar{\rho}\bar{c}(\bar{c}+\bar{u})} \begin{pmatrix} -\frac{\bar{\rho}}{\bar{c}}(\bar{c}\bar{v}-\bar{u}\beta) \\ -\bar{c}\beta+\bar{u}\bar{v} \\ \bar{c}^2-\bar{u}^2 \\ 0 \\ -\bar{\rho}\bar{c}(\bar{c}\bar{v}-\bar{u}\beta) \end{pmatrix}, \tag{5.42}$$

and

$$\boldsymbol{v}_5^L = \bar{\rho}\bar{c}(\; 0 \quad \bar{v} \quad -\bar{u} \quad 0 \quad \beta/\bar{\rho}\bar{c} \;). \tag{5.43}$$

This root corresponds to an isentropic, irrotational pressure wave, travelling upstream provided $\bar{u} < \bar{c}$.

Note that the above defined eigenvectors are only determined to within an arbitrary factor.

5.4.4 Ideal 2-D steady non-reflecting b.c.'s

Suppose that the differential equation is to be solved in the domain $x > 0$, and one wants to construct non-reflecting boundary conditions at $x = 0$ to minimize or ideally prevent the reflection of outgoing waves. At the boundary at $x = 0$, U_p can be decomposed into a sum of Fourier modes with different values of l, so the analysis begins by considering just one particular choice of l. In this case the most general form for U_p is

$$U_p(x,y) = \left[\sum_{n=1}^{5} a_n \boldsymbol{u}_n^R e^{ik_n x} \right] e^{ily}. \tag{5.44}$$

k_n is the n^{th} root of the dispersion relation for the given value of l, and $\boldsymbol{u}_n^R$ is the corresponding right eigenvector.

The ideal non-reflecting boundary conditions would be to specify that $a_n = 0$ for

each n that corresponds to an incoming wave. Because of orthogonality,

$$\begin{aligned} \boldsymbol{v}_n^L U_p &= \boldsymbol{v}_n^L \left[\sum_{m=1}^{5} a_m \boldsymbol{u}_m^R e^{ik_m x} \right] e^{ily} \\ &= a_n (\boldsymbol{v}_n^L \boldsymbol{u}_n^R) e^{ik_n x} e^{ily} \end{aligned} \tag{5.45}$$

and so an equivalent specification of non-reflecting boundary conditions is

$$\boldsymbol{v}_n^L U_p = 0, \tag{5.46}$$

for each n corresponding to an incoming mode, i.e. $n = 1, 2, 3, 4$ at the inflow and $n = 5$ at the outflow.

Both the right, $\boldsymbol{u}^R$, and left, $\boldsymbol{v}^L$, eigenvectors as defined in Sections 5.4.2 and 5.4.3 have a physical significance. As used in Eq. (5.44), the right eigenvector shows the variation in the primitive variables caused by a particular wave mode. Due to the orthogonality relations, the left eigenvector provides a measure of the amplitude of a particular wave component when applied to a general solution.

5.4.5 Extension to 3-D

As mentioned earlier, the construction of the quasi-three-dimensional non-reflecting boundary conditions starts by performing a Fourier decomposition of the flow field at the boundary. We begin by considering a linear cascade with pitch P in the y-direction and a boundary at $x = 0$. The perturbation U_p can be written as

$$U_p(0, y, z, t) = \bar{U}_p(z, t) + \sum_{-\infty, m \neq 0}^{\infty} \widehat{U_{p_m}}(z, t) e^{il_m y}, \tag{5.47}$$

where $\bar{U}_p(z, t)$ represents the pitchwise solution average at the boundary that has been constructed according to the standard 1-D approach. It also corresponds to the $m = 0$ Fourier mode, whereas the harmonics are defined by

$$\widehat{U_{p_m}}(z, t) = \frac{1}{P} \int_0^P U_p(0, y, z, t) e^{-il_m y} \, dy, \tag{5.48}$$

where

$$l_m = \frac{2\pi m}{P}. \tag{5.49}$$

At each spanwise location, ideal 2-D steady-state non-reflecting boundary conditions can now be constructed for each Fourier mode m, $(m \neq 0)$, according to Section 5.4.4.

The boundary conditions for $(m \neq 0)$ are

$$\boldsymbol{v}_n^L \widehat{U}_{pm} = 0 \tag{5.50}$$

for each incoming wave n. Using the eigenvectors defined in Section 5.4.3 the non-reflecting boundary conditions are,

$$\begin{pmatrix} -\bar{c}^2 & 0 & 0 & 0 & 1 \\ 0 & -\bar{\rho}\bar{c}\bar{u} & -\bar{\rho}\bar{c}\bar{v} & 0 & -\bar{c} \\ 0 & 0 & 0 & -\bar{\rho}\bar{c}\bar{v} & 0 \\ 0 & -\bar{\rho}\bar{c}\bar{v} & \bar{\rho}\bar{c}\bar{u} & 0 & \beta \end{pmatrix} \widehat{U}_{pm} = 0, \tag{5.51}$$

at the inflow and at the outflow the boundary condition is

$$\begin{pmatrix} 0 & \bar{\rho}\bar{c}\bar{v} & -\bar{\rho}\bar{c}\bar{u} & 0 & \beta \end{pmatrix} \widehat{U}_{pm} = 0. \tag{5.52}$$

The non-reflecting boundary conditions are now expressed in terms of the spatial Fourier transform of the one-dimensional characteristic variables.

$$\widehat{U}_{pm} = \begin{pmatrix} \frac{-1}{\bar{c}^2} & 0 & 0 & \frac{1}{2\bar{c}^2} & \frac{1}{2\bar{c}^2} \\ 0 & 0 & 0 & \frac{1}{2\bar{\rho}\bar{c}} & \frac{-1}{2\bar{\rho}\bar{c}} \\ 0 & \frac{1}{\bar{\rho}\bar{c}} & 0 & 0 & 0 \\ 0 & 0 & \frac{1}{\bar{\rho}\bar{c}} & 0 & 0 \\ 0 & 0 & 0 & \frac{1}{2} & \frac{1}{2} \end{pmatrix} \begin{pmatrix} \widehat{\phi}_1 \\ \widehat{\phi}_2 \\ \widehat{\phi}_3 \\ \widehat{\phi}_4 \\ \widehat{\phi}_5 \end{pmatrix}. \tag{5.53}$$

Hence the inflow boundary condition becomes

$$\begin{pmatrix} 1 & 0 & 0 & 0 & 0 \\ 0 & -\bar{v} & 0 & -\frac{1}{2}(\bar{c}+\bar{u}) & -\frac{1}{2}(\bar{c}-\bar{u}) \\ 0 & 0 & \bar{v} & 0 & 0 \\ 0 & \bar{u} & 0 & \frac{1}{2}(\beta-\bar{v}) & \frac{1}{2}(\beta+\bar{v}) \end{pmatrix} \begin{pmatrix} \widehat{\phi}_1 \\ \widehat{\phi}_2 \\ \widehat{\phi}_3 \\ \widehat{\phi}_4 \\ \widehat{\phi}_5 \end{pmatrix} = 0, \tag{5.54}$$

and the outflow equation becomes

$$\begin{pmatrix} 0 & -\bar{u} & 0 & \frac{1}{2}(\beta+\bar{v}) & \frac{1}{2}(\beta-\bar{v}) \end{pmatrix} \begin{pmatrix} \widehat{\phi}_1 \\ \widehat{\phi}_2 \\ \widehat{\phi}_3 \\ \widehat{\phi}_4 \\ \widehat{\phi}_5 \end{pmatrix} = 0. \tag{5.55}$$

Unlike the standard 1-D approach in which the harmonics of the incoming characteristics are set to zero, this improved method defines the incoming characteristics to be function of the outgoing ones by using Eqs. (5.54) and (5.55). This gives

$$\begin{pmatrix} \widehat{\phi}_1 \\ \widehat{\phi}_2 \\ \widehat{\phi}_3 \\ \widehat{\phi}_4 \end{pmatrix} = \begin{pmatrix} 0 \\ -\left(\frac{\beta+\bar{v}}{\bar{c}+\bar{u}}\right)\widehat{\phi}_5 \\ 0 \\ \left(\frac{\beta+\bar{v}}{\bar{c}+\bar{u}}\right)^2 \widehat{\phi}_5 \end{pmatrix}, \tag{5.56}$$

and

$$\widehat{\phi}_5 = \left(\frac{2\bar{u}}{\beta-\bar{v}}\right)\widehat{\phi}_2 - \left(\frac{\beta+\bar{v}}{\beta-\bar{v}}\right)\widehat{\phi}_4. \tag{5.57}$$

These algebraic relations are then lagged, see References [35] and [32] to ensure the well-posedness of the pseudo-time evolution process, so that finally the exact (in a two-dimensional sense), steady b.c.'s. turn out to be,

at inflow:

$$\frac{\partial}{\partial t}\begin{pmatrix}\widehat{\phi}_1\\ \widehat{\phi}_2\\ \widehat{\phi}_3\\ \widehat{\phi}_4\end{pmatrix} = \sigma\begin{pmatrix} -\widehat{\phi}_1 \\ -\left(\frac{\beta+\bar{v}}{\bar{c}+\bar{u}}\right)\widehat{\phi}_5 - \widehat{\phi}_2 \\ -\widehat{\phi}_3 \\ \left(\frac{\beta+\bar{v}}{\bar{c}+\bar{u}}\right)^2\widehat{\phi}_5 - \widehat{\phi}_4\end{pmatrix}. \tag{5.58}$$

At outflow:

$$\frac{\partial\widehat{\phi}_5}{\partial t} = \sigma\left(\left(\frac{2\bar{u}}{\beta-\bar{v}}\right)\widehat{\phi}_2 - \left(\frac{\beta+\bar{v}}{\beta-\bar{v}}\right)\widehat{\phi}_4 - \widehat{\phi}_5\right). \tag{5.59}$$

Numerical experience indicates that a suitable choice for σ is $\bar{c}/P$.

Boundary conditions for an annular cascade with many blades are obtained from these linear cascade b.c.'s by substituting (θ, R) for (y, z) and (u_θ, u_R) for (v, w). This approximation implicitly assumes that the blade pitch is much smaller than the tip radius, which is true for many turbomachine applications. The error associated with this approximation is believed to be smaller than the error arising because of the uncoupled radial and tangential modes.

5.5 Stator/rotor interface

In a steady stator/rotor interaction calculation, time-averaged rotor data and spatially-averaged stator data are being transferred from one row to another. This raises the question of what is the correct way in which to perform the averaging procedure. A rigorous definition is based upon the 'mixed-out' flow field and can be described as follows. If one assumes that sufficiently far upstream or downstream the flow is circumferentially uniform, then the flux F based upon this uniform value U_F must be equal to the average flux $\bar{F}$ at the boundary under consideration. As illustrated in Figure 5.1, the following

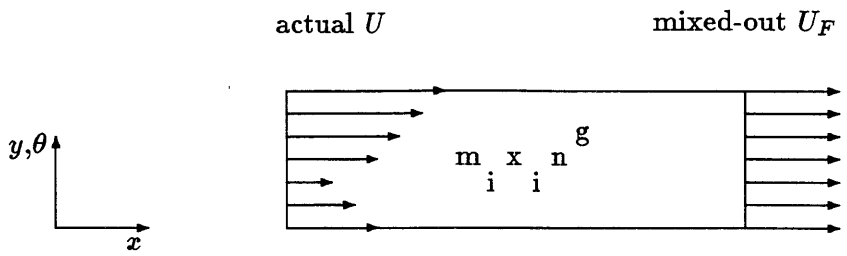

Figure 5.1: Flux averaging procedure.

definition is used.

$$\bar{F}(U) = F(U_F), \tag{5.60}$$

where

$$\bar{F} = \frac{1}{P}\int_0^P F(U)\,dy. \tag{5.61}$$

This gives the following set of equations for U_F.

$$\begin{aligned}
\rho_F\, u_{xF} &= \bar{F}_1, \\
\rho_F\, u_{xF}^2 + p_F &= \bar{F}_2, \\
\rho_F\, u_{xF}\, u_{\theta F} &= \bar{F}_3, \\
\rho_F\, u_{xF}\, u_{RF} &= \bar{F}_4, \\
\rho_F\, u_{xF}\, I_F &= \bar{F}_5.
\end{aligned} \tag{5.62}$$

Together with the equation

$$I_F = \frac{\gamma}{\gamma-1}\frac{p_F}{\rho_F} + \frac{1}{2}(u_{xF}^2 + u_{\theta F}^2 + u_{RF}^2) - \frac{1}{2}\Omega^2 R^2 \tag{5.63}$$

these can be solved to obtain,

$$p_F = \frac{1}{\gamma+1}\left(\bar{F}_2 + \sqrt{\bar{F}_2^2 + (\gamma^2-1)(\bar{F}_2^2 + \bar{F}_3^2 + \bar{F}_4^2 - 2\bar{F}_1\bar{F}_5 - (\bar{F}_1\Omega R)^2)}\right),$$

$$
\begin{aligned}
u_{xF} &= \frac{\bar{F}_2 - p_F}{\bar{F}_1}, \\
u_{\theta F} &= \frac{\bar{F}_3}{\bar{F}_1}, \\
u_{RF} &= \frac{\bar{F}_4}{\bar{F}_1}, \\
\rho_F &= \frac{\bar{F}_1}{u_{xF}}
\end{aligned}
\tag{5.64}
$$

Note that in Eqs. (5.62), (5.63) and (5.64) a cylindrical coordinate system has been used, where u_{xF}, $u_{\theta F}$ and u_{RF} are the axial, circumferential and radial flux-averaged velocity components, respectively. Based on these quantities, 'mixed-out' values of all other flow variables can be defined, and will be denoted by the subscript $_F$. An important point to note is that the physical mixing process implied in this procedure will generate viscous losses, and will result in a flow with higher entropy level. Hence, when applied to a flow at the outlet boundary this averaging procedure will tend to produce higher 'measured' losses than other averaging methods, such as averaging the outgoing entropy. Further discussion of this point for an arbitrary spatially non-uniform and unsteady flow is contained in a study by Fritsch [28].

At the stator/rotor interface, mass, momentum and energy have to be conserved, so that the objective is to make the flux of these out of the stator equal to the flux into the rotor. Using the flux-averaging technique an equivalent objective is to match the average flow quantities.

$$
\begin{aligned}
\rho_{F\,stator} &= \rho_{F\,rotor}, \\
u_{xF\,stator} &= u_{xF\,rotor}, \\
u_{\theta F\,stator} &= u_{\theta F\,rotor} + \Omega R, \\
u_{RF\,stator} &= u_{RF\,rotor}, \\
p_{F\,stator} &= p_{F\,rotor}.
\end{aligned}
\tag{5.65}
$$

Note that because of the use of relative flow variables, the rotor wheel speed ΩR has to be introduced into the condition of matching circumferential velocities.

If the current computed solution does not satisfy these matching conditions then it can be interpreted as a jump in the characteristic values.

$$\begin{pmatrix} \Delta\bar{\phi}_1 \\ \Delta\bar{\phi}_2 \\ \Delta\bar{\phi}_3 \\ \Delta\bar{\phi}_4 \\ \Delta\bar{\phi}_5 \end{pmatrix} = \begin{pmatrix} -\bar{c}^2 & 0 & 0 & 0 & 1 \\ 0 & 0 & \bar{\rho}\bar{c} & 0 & 0 \\ 0 & 0 & 0 & \bar{\rho}\bar{c} & 0 \\ 0 & \bar{\rho}\bar{c} & 0 & 0 & 1 \\ 0 & -\bar{\rho}\bar{c} & 0 & 0 & 1 \end{pmatrix} \begin{pmatrix} \rho_{Fstator} - \rho_{Frotor} \\ u_{xFstator} - u_{xFrotor} \\ u_{\theta Fstator} - u_{\theta Frotor} - \Omega R \\ u_{RFstator} - u_{RFrotor} \\ p_{Fstator} - p_{Frotor} \end{pmatrix} . \tag{5.66}$$

The average characteristic changes at the stator outflow and rotor inflow are now set to eliminate each of these characteristic jumps, taking note of the direction of propagation of each characteristic. Once this is done for both sides of the interface, the remainder of the boundary condition treatment is exactly the same as for a standard inflow and outflow boundary.

This stator/rotor interface treatment has been implemented such that the number of nodes (in both the tangential and the radial direction) on one side of the interface is not required to be the same as on the other side. This is achieved using a local flux transfer scheme that ensures flux conservation, see Appendix D.

5.6 Results

The effectiveness of the steady-state quasi-3-D non-reflecting boundary conditions is demonstrated in this section by presenting results for the high-turning turbine stage represented in Figs. 5.2 and 5.3. The design of this stage was performed by Rolls-Royce and is representative of a high pressure, cooled aircraft turbine operating in the transonic regime. In particular the small axial gap between the stator trailing edge and the rotor

leading edge (approximately 30% of the vane axial chord) is typical for this kind of turbine. For these closely spaced blades the formulation of the boundary conditions at the stator/rotor interface becomes a key point in the numerical simulation.

Firstly, results are presented for computations performed on the inlet guide vane alone, i.e. no rotor row attached downstream. The midspan flow fields shown in Fig. 5.4 have been calculated for supersonic outflow conditions (but still axially subsonic), with two different locations of the far-field boundaries. Notice that the location of the small domain exit boundary corresponds to the stator/rotor interface position in the computations of the complete stage reported later in this section. The solutions look very similar, although not identical due to the second-order non-linear effects caused by the presence of two weak oblique shocks extending from the trailing edge. Indeed, the linearization of the Euler equations at the boundaries introduces an error which is proportional to the square of the steady-state perturbation at the inflow and the outflow. However, the error is unnoticeable at the inflow and very much smaller at the outflow than the error introduced in the solution by using the standard boundary conditions, which impose uniform exit pressure, see Fig. 5.5. Using non-reflecting boundary conditions, the local maximum mismatch in pressure between the two solutions of Figure 5.4 is less than 4% of the vane exit dynamic head. Clearly, the formulation of the quasi-3-D non-reflecting boundary conditions allows the flow to adjust circumferentially (and also radially as seen later on) to account for the presence of the stator trailing edge. On the other hand, using the standard 1-D b.c.'s the outgoing shocks produce reflected expansion waves which greatly contaminate the solution on the blade, see Fig. 5.6. These spurious reflections produce a local error in pressure (compared to the solution with quasi-3-D b.c.'s) which accounts for up to 43% of the vane average exit dynamic head. Hence the non-reflecting boundary conditions give a major improvement in accuracy.

The midspan blade surface pressure computed by using the quasi-3-D and the 1-D formulations on the small and the large domain are compared in Fig. 5.6, where the inlet stagnation pressure $p_{t\,inl}$ is used as a reference. Notice that the disturbances produced by the outlet reflecting boundary do not propagate ahead of the choked throat, which is

consistent with inviscid flow theory. Due to the strong shock/exit boundary interaction in the 1-D formulation the location of the outlet surface affects the shocks' reflections, i.e. the solutions on the two domains are different with multiple wave reflections on the small one. This local behavior also produces average changes. For instance, the 1-D boundary condition formulation leads to a change in the flux-average turning angle compared to the quasi-3-D b.c.'s, as seen in Fig. 5.7. In a stator/rotor interaction this average change in the stator swirl angle can lead to a change in the rotor relative incidence angle of several degrees, and thus significantly affect the rotor loading.

The steady-state results for four coupled transonic stator/rotor calculations are summarized in Figs. 5.8, 5.9 and 5.10. To achieve an accurate basis for comparison, the small domain results were computed using circumferentially averaged exit pressures $p_F(R)$ obtained from the large domain calculations. Notice that in a full stage computation the matching of the stator and the rotor flow at the interface is done automatically without any user intervention. In these four computations, the quasi-3-D b.c.'s have been used at the stator inlet and outlet as well as at the rotor inlet. Thus, relative to the calculations using the quasi-3-D formulation at all inlets/outlets, the introduction of the 1-D b.c.'s at the rotor outlet does not visibly affect the vane flow field. However, the rotor field is affected through the trailing edge reflected shock which is clearly apparent. It should be pointed out that in the case of a calculation performed with 1-D b.c.'s implemented at the stator inlet, at the interface and at the rotor exit, the discrepancies between the 1-D and the 3-D formulations would be much larger. As mentioned in the preceding section, the use of 1-D b.c.'s at the stator outlet does affect the rotor inlet conditions. Thus, the rotor flow field in turn produces a change in the average stator/rotor interface pressure.

Fig. 5.9 indicates that the quasi-3-D formulation performs well at all radii, whereas the pressure plots in Fig. 5.10 demonstrate that as far as the blade loading is concerned, the use of the quasi-3-D formulation gives good results. The rotor-relative exit Mach number is very close to unity. It has been numerically observed that while the flow is converging to a steady-state solution, the exit boundary condition 'switches' from

subsonic to supersonic and vice versa, until the flow at lower radii settles to an average supersonic exit Mach number while the flow closer to the tip is subsonic. This point is important to notice, for the implementation of the non-reflecting boundary conditions requires a Fourier transform in the subsonic case, but none in the supersonic case.

The rotor results point out that by extending the computational domain sufficiently far downstream, the results calculated using the 1-D formulation tend to match the quasi-3-D b.c.'s solution, see Figs. 5.8 and 5.10. This is consistent with both the quasi-3-D and the 1-D b.c.'s formulations since these two techniques give the same results when applied to a uniform flow as it develops here in the constant area duct downstream of the rotor. However, as mentioned earlier this is true only because the rotor exit boundary condition alone is altered from being either quasi-3-D or 1-D.[1] Hence, only minor differences in pressure exist (i.e. less than 2% of the vane pressure drop) between the solutions computed with non-reflecting b.c.'s and the solution using the 1-D b.c. formulation on the large domain, see Fig. 5.10. This type of behavior is not apparent in the isolated stator computations of Figures 5.4 and 5.5 partly due to the downstream duct area change and the location of the large domain exit boundary which is still too close to the stator trailing edge. The 1-D b.c. formulation applied on the small domain produces errors up to 17% of the vane average pressure drop. In an actual turbine environment, it is not possible to extend the limits of the boundaries far upstream and far downstream. In particular, the axial gap between the stator and the rotor of Figures 5.2 and 5.3 is typical of a modern aircraft turbine. Hence, the use of accurate non-reflecting boundary conditions in a multi-stage environment is necessary in order to assess the performance of the whole engine.

The results for the subsonic flow in a linear turbine cascade are presented in Fig. 5.11. In this case no radial variations exist and the quasi-3-D formulation reduces to the exact 2-D non-reflecting boundary conditions where only second-order non-linear errors can arise. However, in this shock-free flow these are very small as shown by the virtual

[1] In order to show the effects of imposing the standard 1-D b.c.'s at one particular location, the full stage calculations presented here were computed with only the rotor exit boundary condition formulation modified to be either quasi-3-D non-reflecting or 1-D.

perfect match of the pressure contours between the small and the extended domain calculations (the discrepancy in pressure between the two solutions is smaller than 0.001 times the exit dynamic head).

5.7 Conclusions

A theory for the construction of steady-state quasi-3-D non-reflecting boundary conditions has been developed and applied to the Euler equations. The boundary condition formulation is derived using Fourier analysis applied to the linearized equations. A fundamental approximation is that radial effects are accounted for in the average mode only. In the absence of any radial variations, the boundary conditions are exact within the linear theory.

The quasi-3-D formulation has been implemented for transonic and subsonic axial flow turbomachine calculations with realistic operating conditions and for standard designs. In the transonic case where a shock wave crosses the computational boundary, the solution is virtually independent of the position of the computational domain limits with local discrepancies in pressure less than 2% of the vane average pressure drop, which compares to 24% when using the standard 1-D formulation. Hence, the second-order non-linear errors together with the error due to the uncoupling of the radial and tangential variations are very much smaller than the ones introduced in the solution when using the standard one-dimensional approach. In the subsonic case the solution is completely independent of the position of the far-field boundaries.

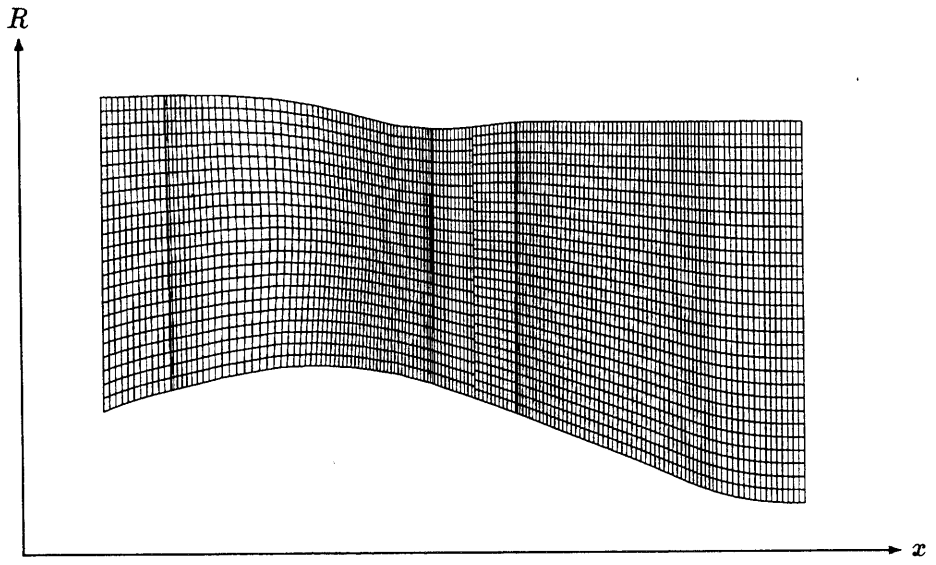

Figure 5.2: Side view of a transonic first turbine stage including stator suction and rotor pressure sides.

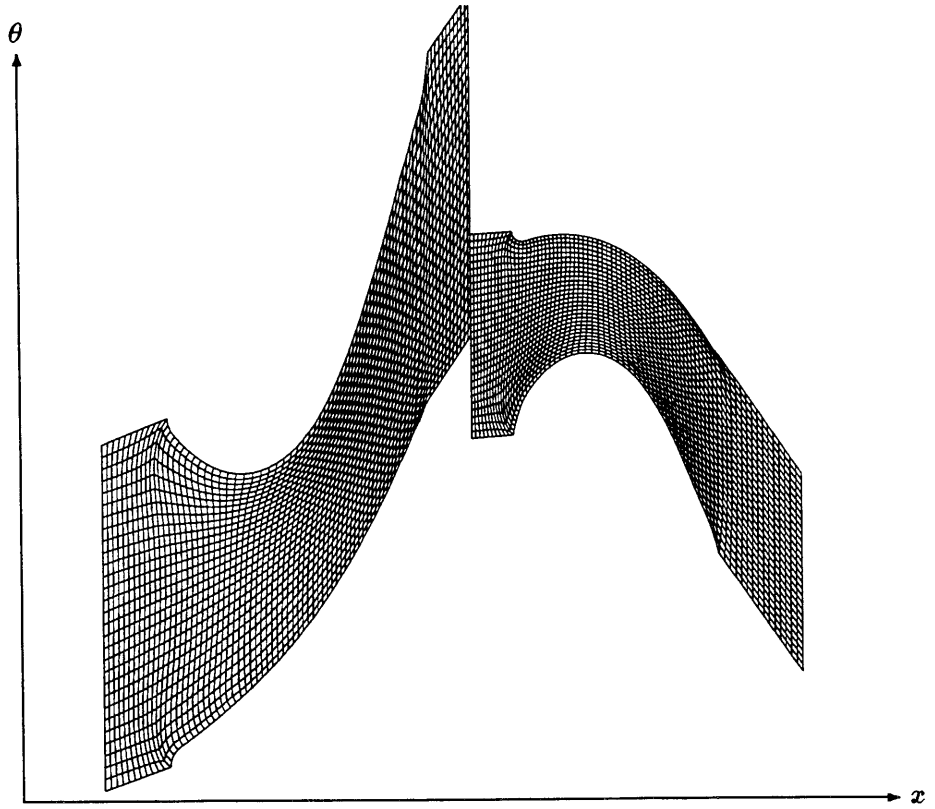

Figure 5.3: Mean height blade-to-blade mesh (stator: $80 \times 30 \times 24$, rotor: $77 \times 30 \times 30$ nodes). The stator and the rotor grids shown here are used in the small domain calculations.

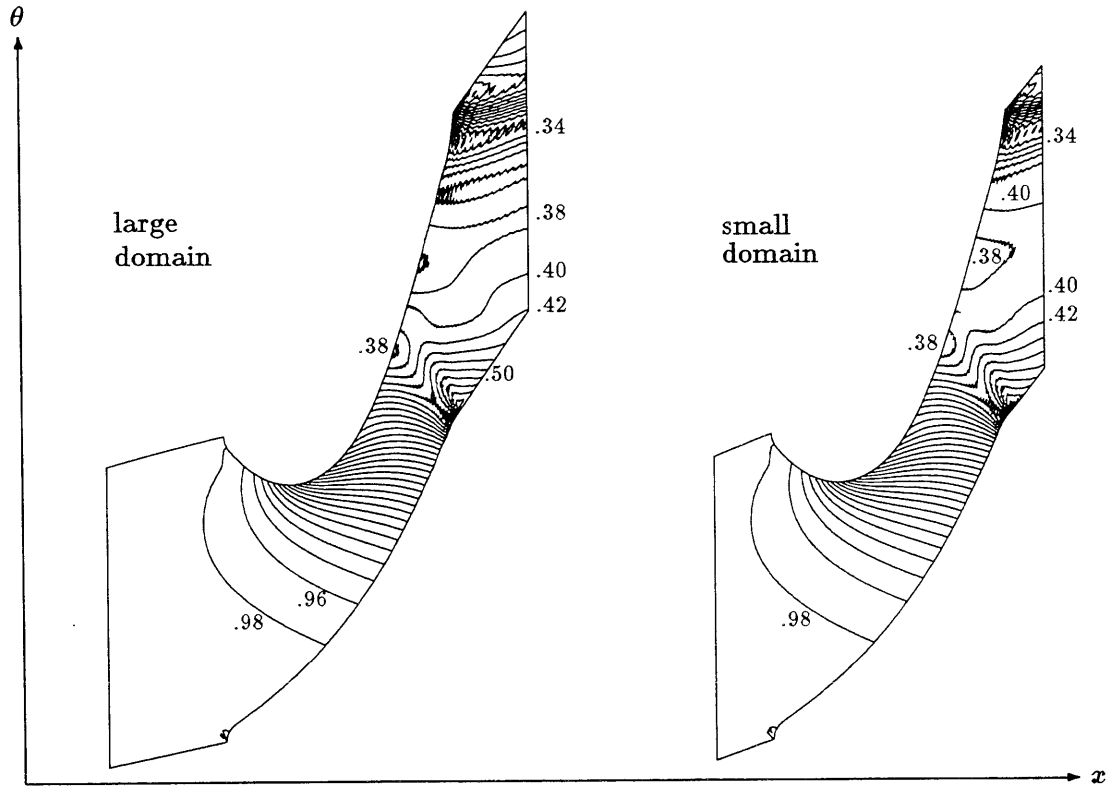

Figure 5.4: Stator midspan pressure contours ($p/p_{t\,inl}$) using quasi-3-D non-reflecting boundary conditions, $M_{exit} = 1.2$. Isolated stator calculations.

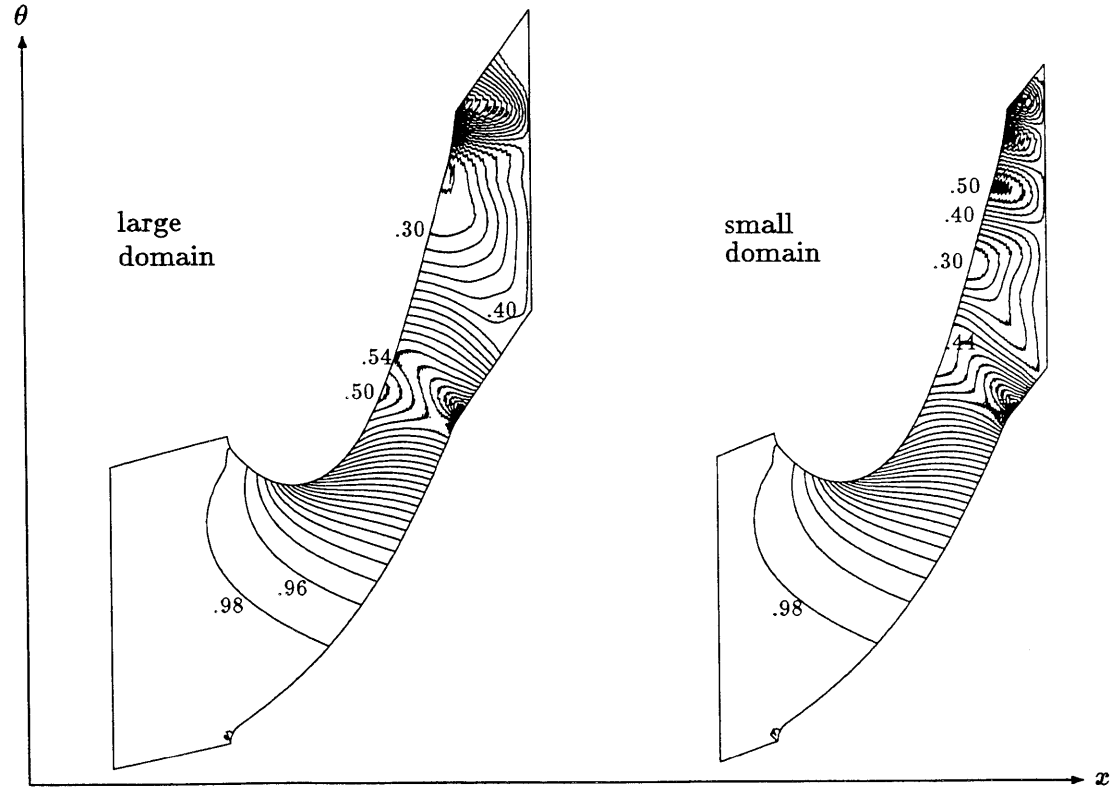

Figure 5.5: Stator midspan pressure contours ($p/p_{t\,inl}$) using reflecting boundary conditions at the outflow, $M_{exit} = 1.2$. Isolated stator calculations.

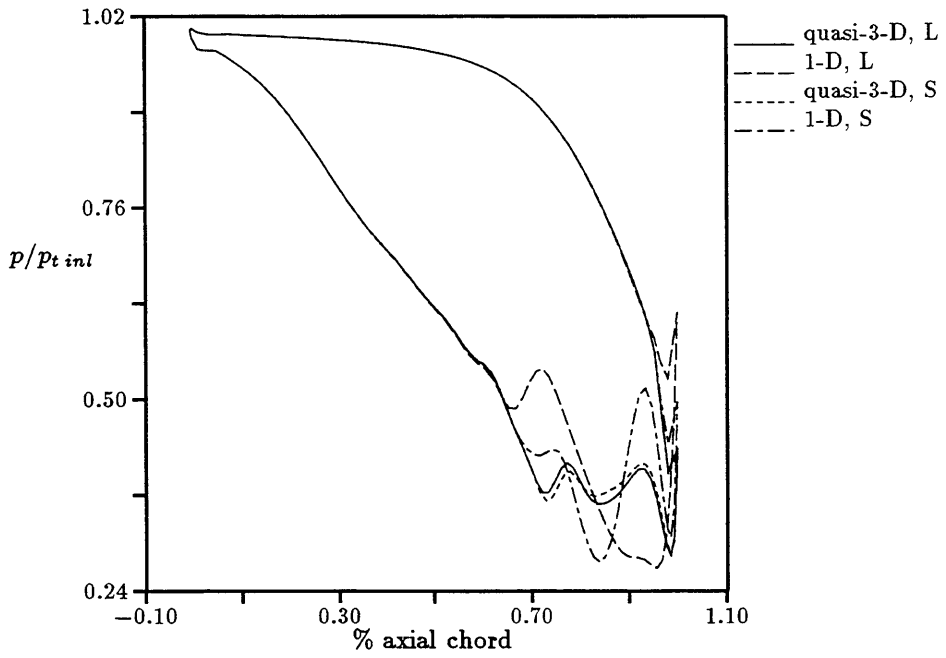

Figure 5.6: Midspan stator blade surface pressure using non-reflecting and reflecting b.c.'s. Isolated stator calculations. L: large domain, S: small domain.

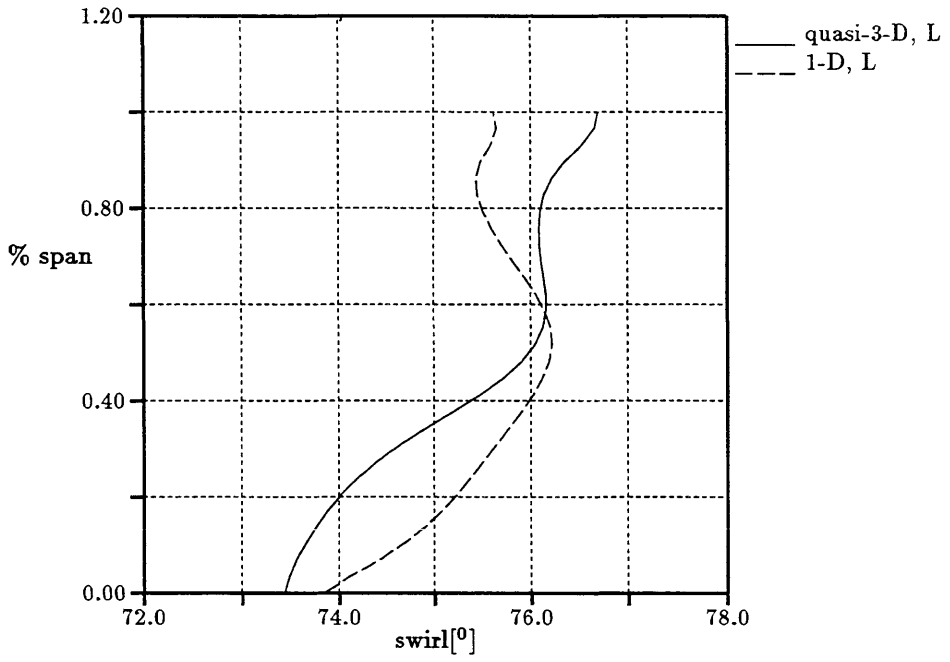

Figure 5.7: Flux-averaged turning angle at the large domain stator exit using non-reflecting and reflecting b.c.'s. Isolated stator calculations.

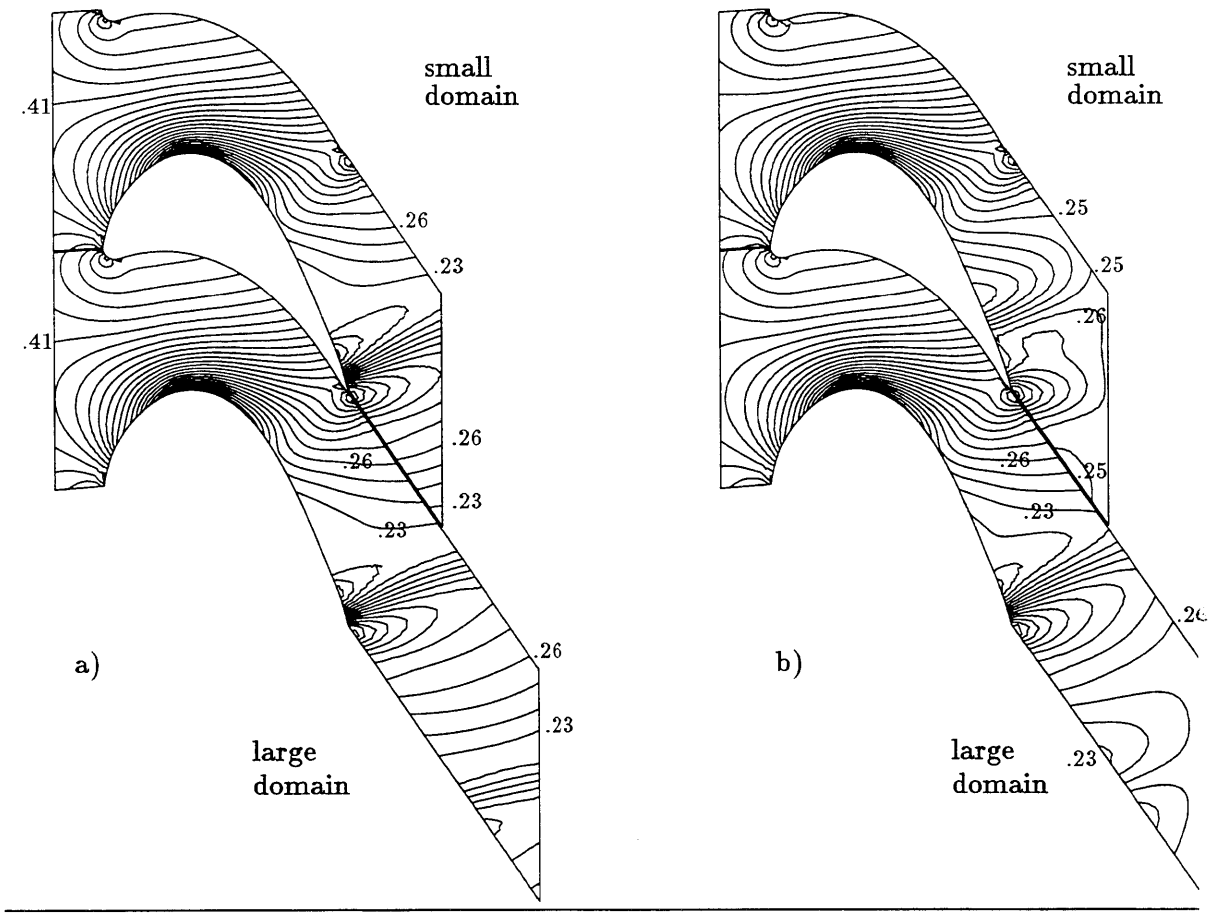

Figure 5.8: Rotor midspan pressure contours ($p/p_{t\,inl}$), $M_{exit} = 1.1$. Coupled stator/rotor calculations.
a) Quasi-3-D non-reflecting b.c.'s.
b) Standard 1-D reflecting b.c.'s. at rotor outlet.

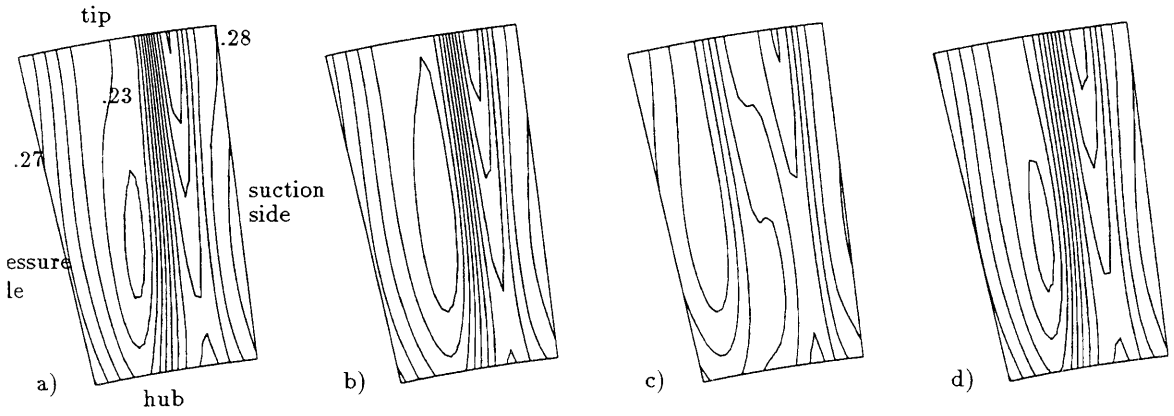

Figure 5.9: Rotor blade-to-blade and hub-to-tip pressure contours ($p/p_{t\,inl}$) at 20% chord downstream the trailing edge (equals half way between trailing edge and small domain exit). Coupled stator/rotor calculations. Increments = 0.01.
a) Quasi-3-D non-reflecting b.c.'s small domain and b) large domain.
c) Standard 1-D reflecting b.c.'s. small domain and d) large domain.

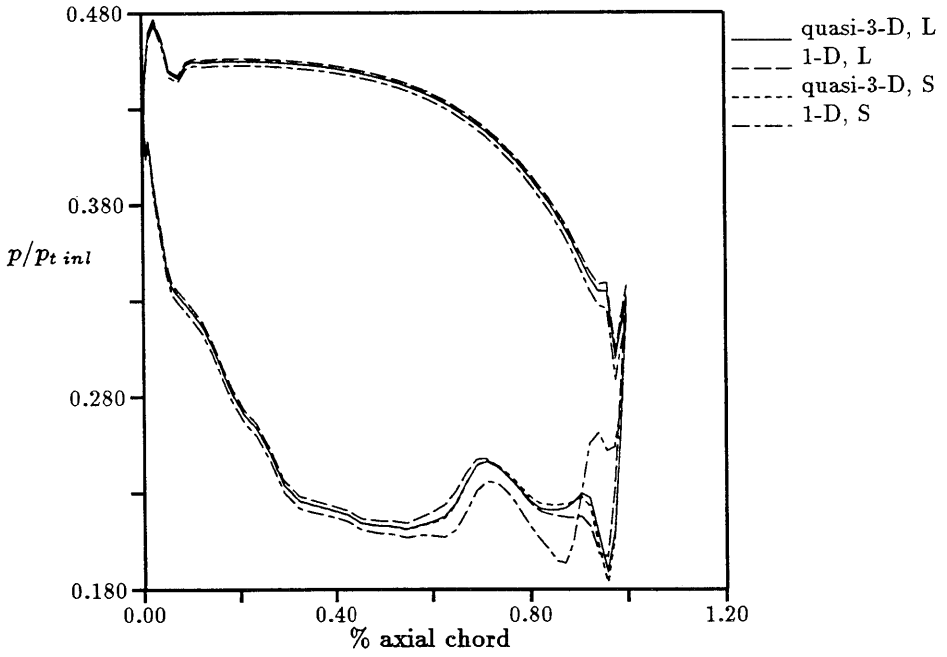

Figure 5.10: Midspan rotor blade surface pressure using non-reflecting and reflecting b.c.'s. Coupled stator/rotor calculations. L: large domain, S: small domain.

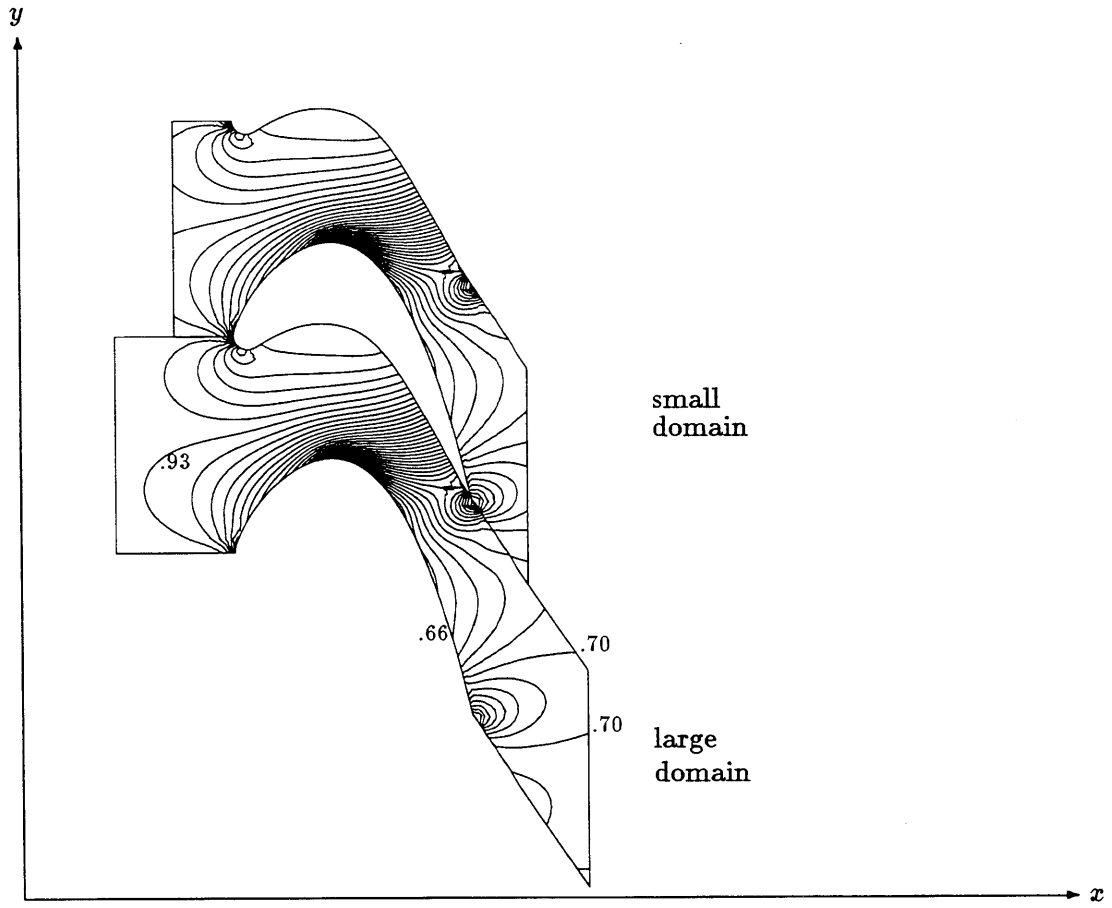

Figure 5.11: Pressure contours ($p/p_{t\,inl}$) using quasi-3-D non-reflecting boundary conditions, $M_{exit} = 0.75$. Linear cascade. Increments = 0.01.

Chapter 6

Code Validation

An essential ingredient in the development of a CFD code is the validation itself. This can be a large time-consuming process especially for three-dimensional unsteady cases, so naturally the definition of validation has to be clarified in some sense.

The first step is to show that the numerical method converges to the solution of the discretized equations. For steady-state this is usually accomplished by looking at iteration histories. These consist of the maximum and root mean square values of the changes δU at each Lax-Wendroff iteration, and should tend to machine accuracy. All the steady-state calculations presented in this thesis were converged to an absolute maximum residual below 5×10^{-6}, which means that the mean residual is between five to ten times smaller. For unsteady turbomachinery flow in which the unsteadiness arises solely from the relative motion between the rotor and the stator, the convergence is achieved once periodic flow is obtained, see Chapters 8 and 9.

This chapter is mostly devoted to steady-state flow, because the implementation procedure is exactly the same for steady and unsteady flow except for two fundamental differences. The first resides in the definition of the time-step. For unsteady computations, the time-step is taken to be the same for all the computational cells, whereas local time-stepping is used to compute steady solutions, see also Appendix C. The second difference appears in the handling of the stator/rotor interface boundary condition, which is discussed in Sections 5.5 and 8.3 for steady and unsteady flow, respectively. Hence, the additional validation work for unsteady flow is merely a check of data transfer at

the interface.

The most difficult part of the validation is to show that the discrete solution of the Euler equations is an accurate approximation to the analytical equations. Since analytic solutions are known for simple cases only, different approaches are used. The first approach consists of defining two test cases for which either analytical or experimental values are available for comparison with the computed solution. In both cases, the amount of discretization errors is indicated by the stagnation pressure changes. These should analytically be zero since the flows are subsonic and were computed using uniform inlet conditions. The two cases refer to 2-D flows in cascades which are artificially extended to 3-D. The first case is discussed in Section 6.1 and involves the incompressible flow within the Gostelow cascade [41] for which there is an analytic solution. The second calculation is performed upon a high subsonic, large turning cascade for which experimental blade surface data are available, see Section 6.2. In both cases the comparisons are good.

The Munk and Prim substitution principle [80] can be used as a means for checking 3-D solutions for steady inviscid flows in an actual non-rotating turbomachinery component. It can be shown that because of the decoupling of the energy equation from the mass and momentum equations, certain physical quantities have to remain the same for different flow solutions satisfying this principle. This is discussed in Chapter 7.

Another way of examining the solution is to check upon certain integral quantities that have to be conserved within the computational domain. This is the subject of Section 6.3.

6.1 Gostelow cascade

In this section, the present method is used to calculate the steady flow through the Gostelow cascade. In [41], Gostelow used a conformal mapping transformation to derive

the analytic incompressible solution.

Since the flow is inherently 2-D, it is appropriate to construct a 3-D cascade by stacking a few grid planes along the span. For that purpose, a modified version of the ISES elliptic grid generator [30] is used to define the 2-D mesh. The calculation involves a single blade passage of 120 nodes along the streamwise direction and 30 nodes from blade-to-blade, as seen in Fig. 6.1. 5 of these planes were then used to define the span. The stagger angle is 37.5^0 and the solidity 1.248.

There are two main problems associated with the Gostelow case. Firstly, the present method is not well suited for the calculation of incompressible flow, since the pressure waves associated with the time-marching procedure take a long time to damp out. Thus the convergence rate is low.

The computed Mach number contours are plotted in Figure 6.2. Note that the maximum Mach number is approximately 0.182, so that the compressibility effects are very small. Gostelow's tabulated results together with the computed surface pressure coefficients are compared in Fig. 6.3. The agreement is nearly perfect.

The second difficulty arises due to the analytic square-root pressure singularity at the trailing edge of the blade that sets the Kutta condition. To capture this effect as well as the large gradients in the flow solution around the leading edge, grid nodes clustering is required at both the leading edge and the trailing edge, see Figures 6.4 and 6.5, respectively. A product of a cubic and a sine function is used to get this kind of blade node spacing.

The prescribed inlet flow angle is 53.5^0 relative to the axial direction. The outlet angle is dependent upon the Kutta condition. Using the present method it has been established to 30.23^0, which compares to the analytic value of 30.025^0 indicating an error of the order of 1% in the tangential force. Finally, since the flow is nominally isentropic, the variations in stagnation pressure through the domain highlight the amount

of numerical errors. For this low Mach number flow these are best quantified by looking at the stagnation pressure coefficient defined as

$$C_{p_t} = \frac{p_t - p_{t\,inl}}{\frac{1}{2}\rho_{inl} V_{inl}^2}. \tag{6.1}$$

The C_{p_t} contours are plotted in Figure 6.6. Errors occur essentially around the blade with the larger values in magnitude concentrated at the leading edge where the truncation errors are the highest. Except for the leading edge region, the blade stagnation pressure error represents less than than 8% of the inlet dynamic head.

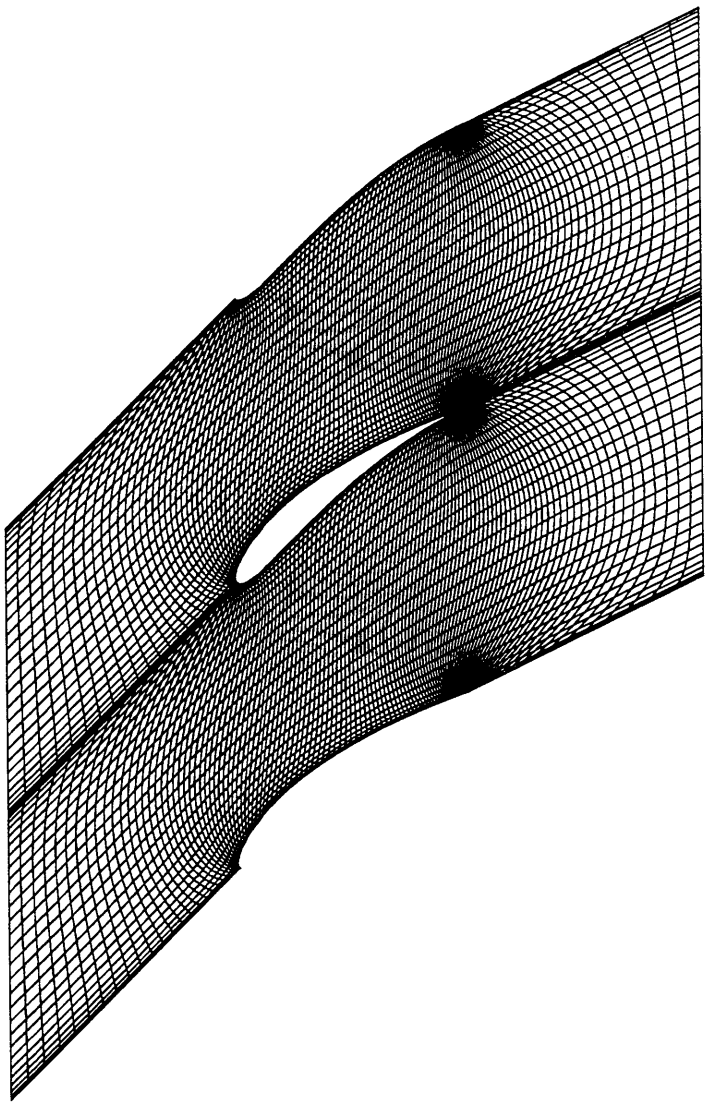

Figure 6.1: Blade and grid geometry for the Gostelow cascade. 120×30 ($\times 5$) nodes.

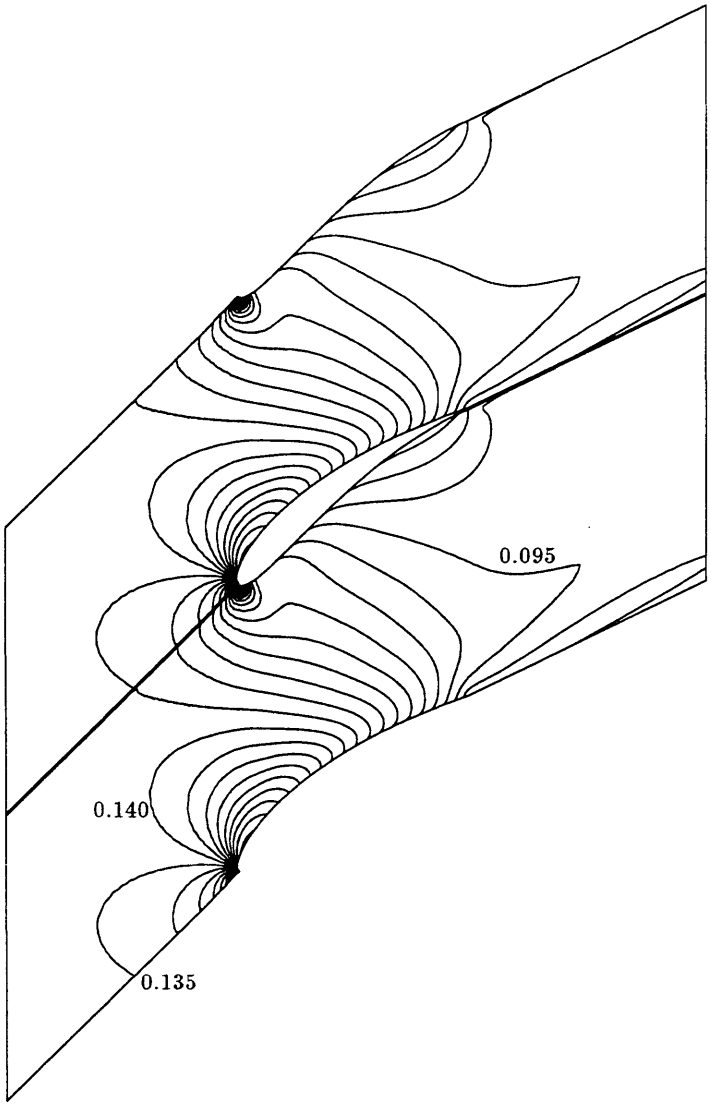

Figure 6.2: Mach number contours for the Gostelow cascade. Increments = 0.005.

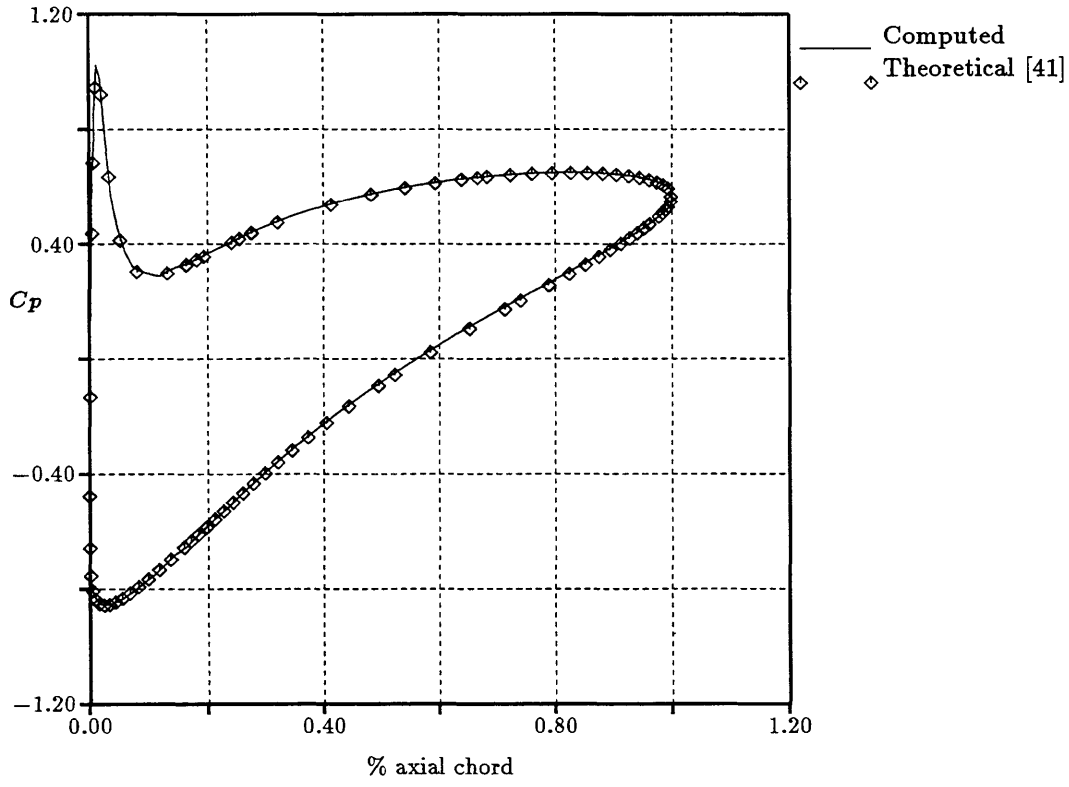

Figure 6.3: Computed and analytic pressure coefficient distributions on the Gostelow blade.

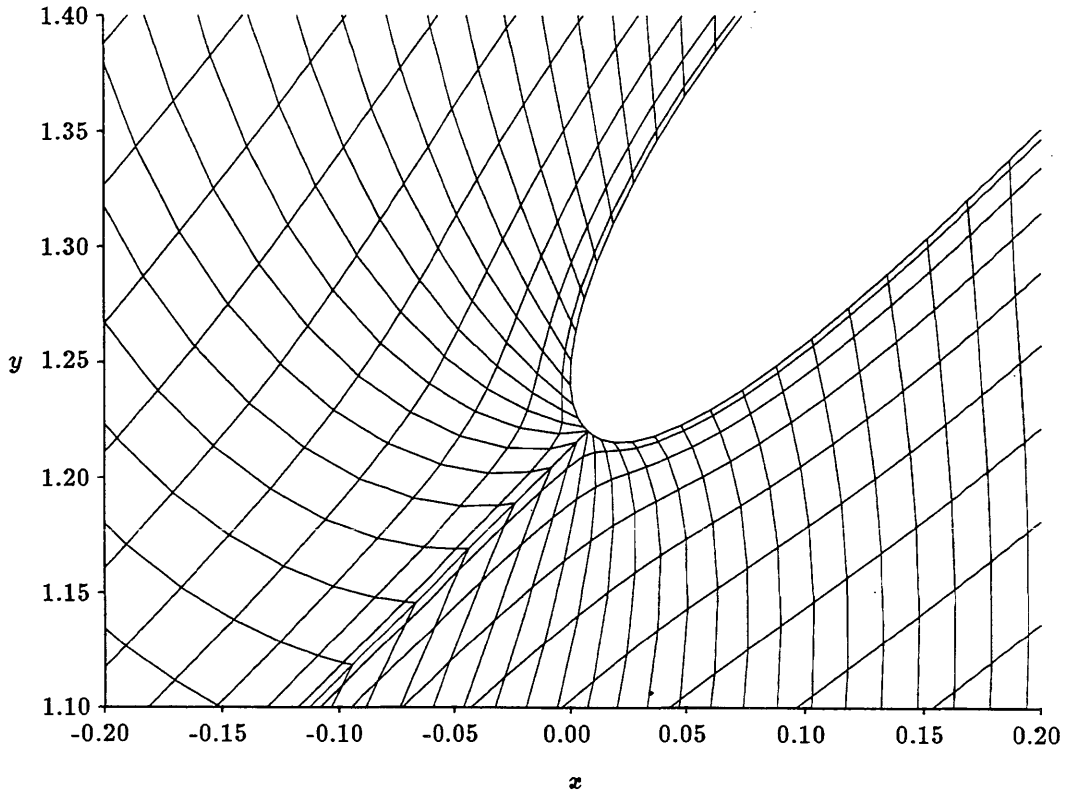

Figure 6.4: Blow-up of the Gostelow mesh near the leading edge.Axial chord = 1.

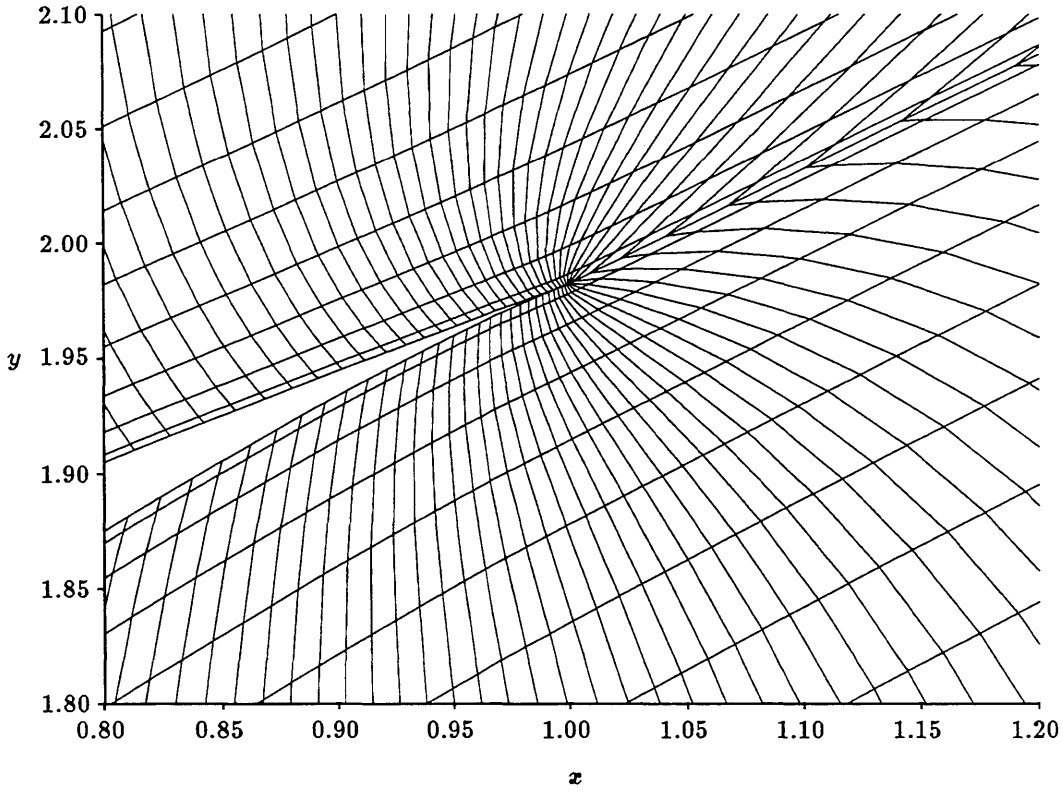

Figure 6.5: Blow-up of the Gostelow mesh near the trailing edge.

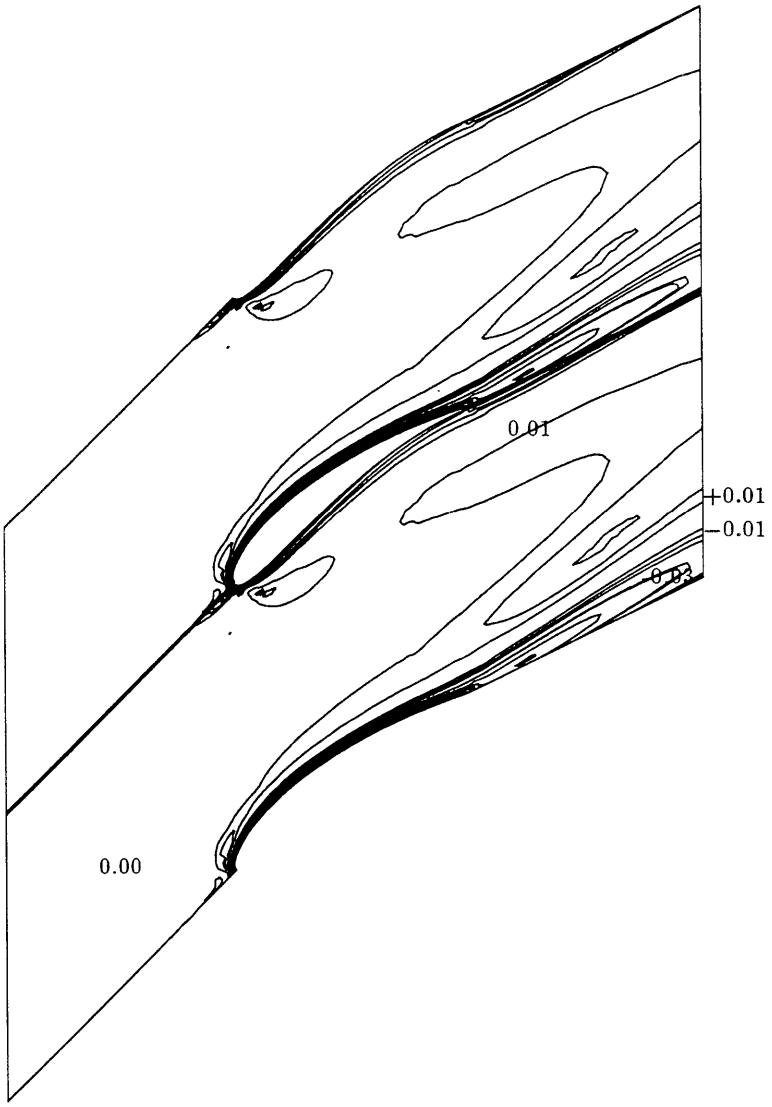

Figure 6.6: Stagnation pressure coefficient contours (C_{p_t}) for the Gostelow cascade. Increments = 0.01.

6.2 $T7$ turbine cascade

The $T7$ turbine nozzle is a subsonic high-turning linear cascade designed by Rolls-Royce and for which blade surface pressures are available. These were compared to numerical solutions in References [107] and [30].

As with the Gostelow cascade, a 2-D elliptic grid is first generated and then stacked along the span. One of the five blade-to-blade grid planes is shown in Fig. 6.7. Note that in contrast to the Gostelow grid, this mesh defines cells of nearly constant volumes, which allows the use of larger time-steps.

This case has an inlet flow angle of 52.8^0 and an exit angle of -72.7^0. It is thus a useful test case to determine the effects of grid shear on the algorithm. Figure 6.8 presents the Mach number contours. The maximum Mach number in the field is 0.817 whereas the exit Mach number is 0.75. The numerical errors are assessed by plotting the stagnation pressure contours, see Fig. 6.9. The maximum error in total pressure is 3.6 % of the inlet stagnation value, and accounts for 13% of the exit dynamic head. The maximum error is generated at the cusped trailing edge due to the lack of mesh resolution and part of it is convected downstream. Except for the leading and the trailing edge region, the blade surface stagnation pressure is within 1.5% of the exit dynamic head. The calculated and the measured surface pressures converted to isentropic Mach numbers using the inlet total pressure are compared in Fig. 6.10. The agreement is good except towards the trailing edge on the suction side, where viscous effects become more important.

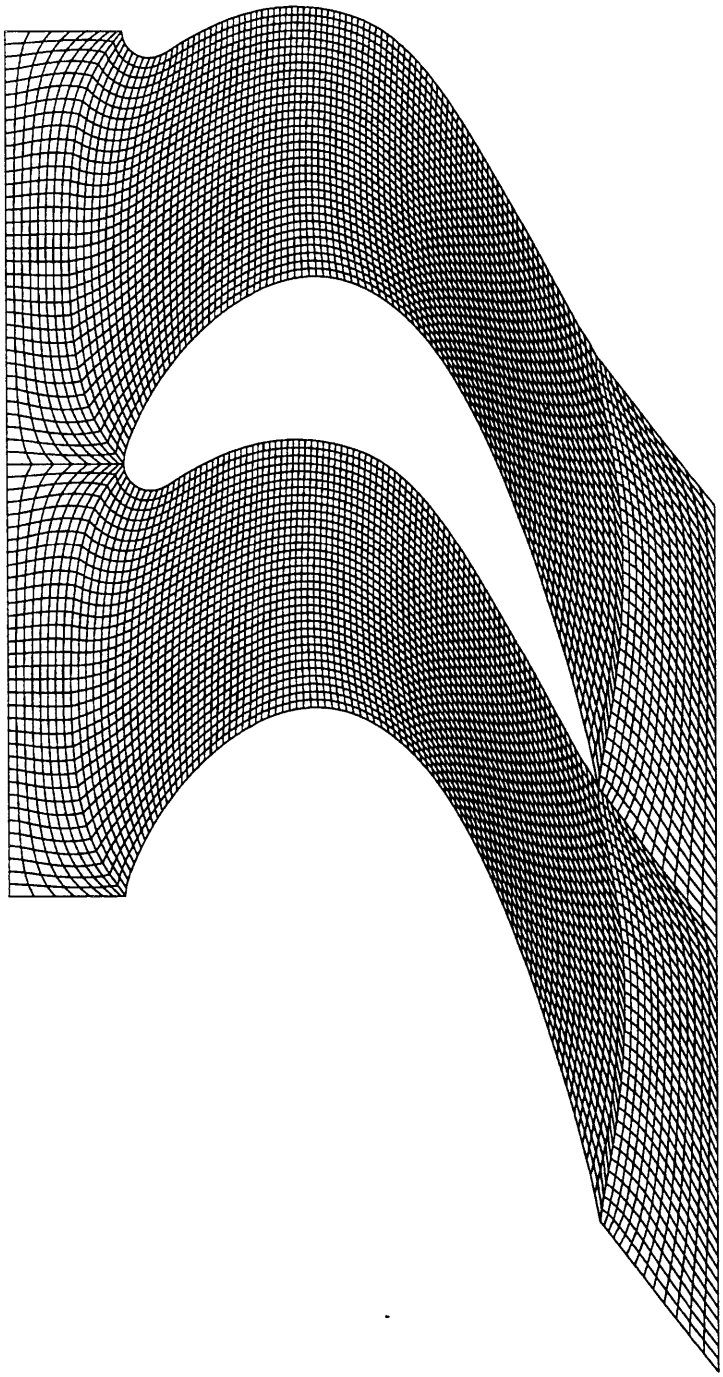

Figure 6.7: Blade and grid geometry for the turbine $T7$. $110 \times 35(\times 5)$ nodes.

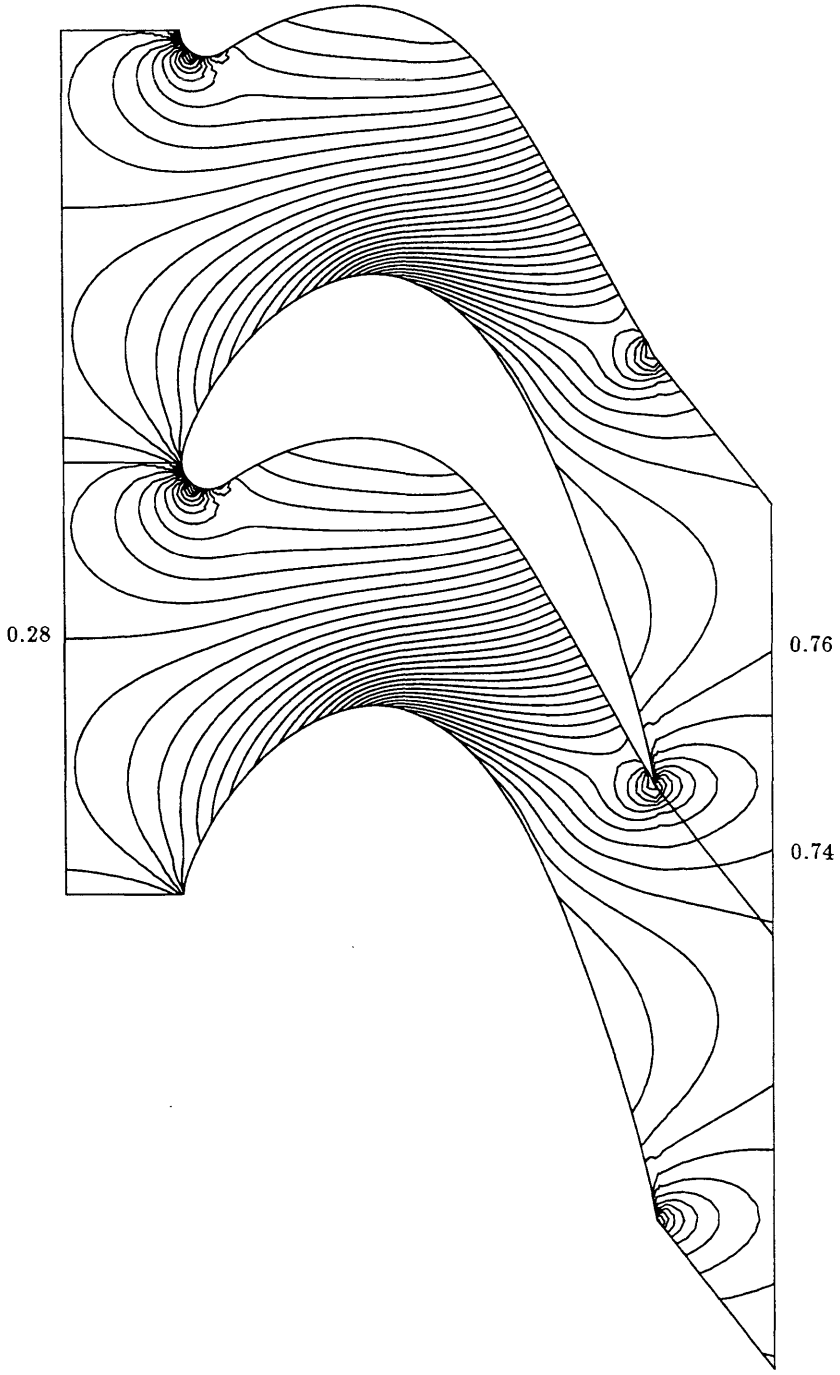

Figure 6.8: Isentropic Mach number contours for the turbine $T7$.
Increments = 0.02, $M_{max} = 0.82$.

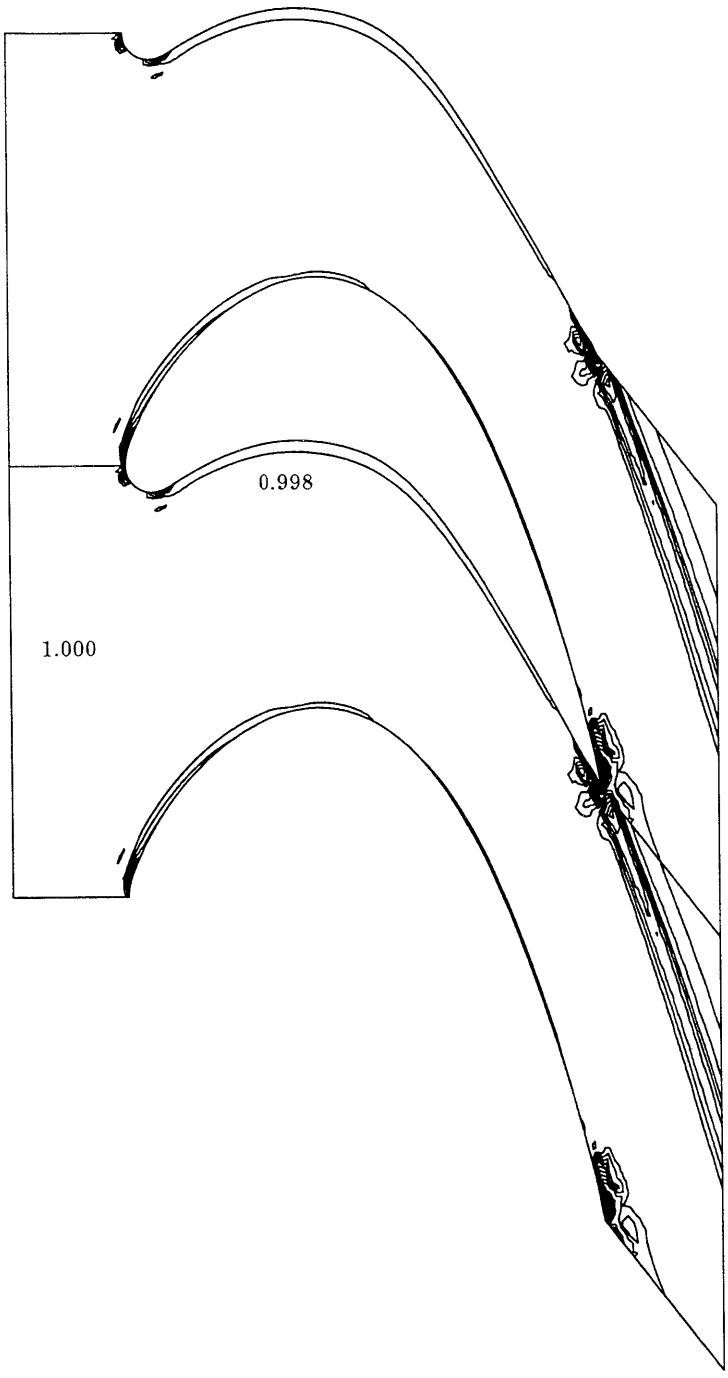

Figure 6.9: Total pressure contours ($p_t/p_{t\,inl}$) for the turbine $T7$.
Increments = 0.002, max = 1.017, min = 0.964.

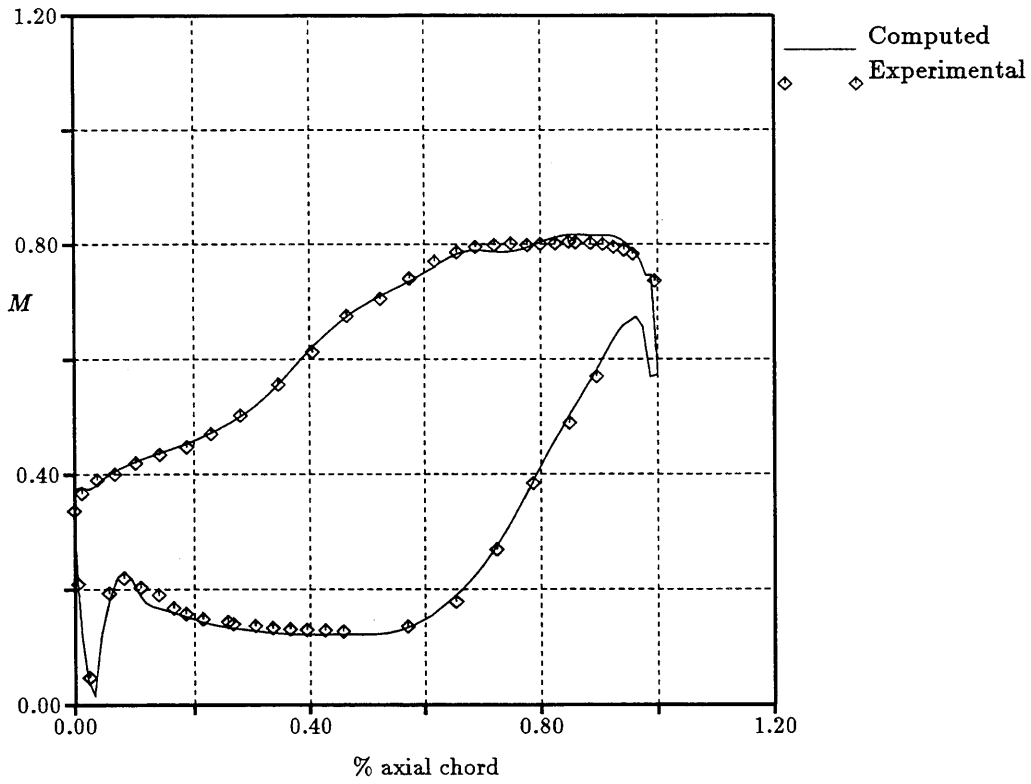

Figure 6.10: Computed and measured Mach number distributions around $T7$ blade. The Mach number is calculated from the blade surface pressure and the inlet stagnation pressure.

6.3 Integral quantities

As mentioned earlier, the purpose of this section is to validate the 3-D Euler solver with respect to integral quantities that have to be conserved within the computational domain. These are mass flow, angular momentum and power. Numerically conservation of mass, momentum and energy is expressed (and implemented) on a cell-by-cell basis. Also, as mentioned in Section 3.2 the flux contributions from the interior cell faces cancel out leaving only the boundary flux terms. Thus, errors expressing an unbalance of mass, angular momentum and power for the blade row and which are solely based upon quantitites at the domain boundary (inlet/outlet and solid walls) provide a check on the interior domain implementation procedure. In addition, an important aspect to notice is that the Euler code does *not* directly solve for the conservation of angular momentum and power on a cell-by-cell basis, though analytically these can be replaced by conservation of momentum and energy. For instance, if mistakes were made in the implementation of the source terms, they would show up in the angular momentum and power errors.

The errors for different steady-state stator/rotor calculations are presented in Table 6.1.

The error in mass flux balance is expressed by

$$E_{\dot{m}} = \frac{\dot{m}_j - \dot{m}_{inl}}{\dot{m}_{inl}}, \quad j = s\,out \;\; or \;\; r\,inl. \tag{6.2}$$

$\dot{m}_{inl}$ is the stage inlet mass flow, whereas $\dot{m}_{s\,out}$ and $\dot{m}_{r\,inl}$ represent the stator exit and the rotor inlet mass flow, respectively.

For an axisymmetric geometry, conservation of momentum is replaced by the conservation of angular momentum. For a spatially fixed control volume V surrounded by the surface S this is expressed as

$$\iiint_V \frac{\partial}{\partial t}(\rho\vec{v} \times \vec{r})\, dV + \iint_S (\rho\vec{v} \cdot \vec{n})(\vec{v} \times \vec{r})\, dS = \sum \vec{F} \times \vec{r} = \sum \vec{T}. \tag{6.3}$$

This equation states that the changes in angular momentum due to the unsteady fluctuations within the control volume plus the change in the flux of angular momentum across the control surface equals the sum of the externally applied torques. For turbomachinery applications, the axial component of the torque (due to the tangential force, or lift) is particularly important because it is used to derive the power delivered by the fluid to the blades. Thus the axial component of Equations (6.3) applied for a steady flow (in the frame of the blade row) is

$$\iint_{row} u_\theta R\, \rho u_x\, dS = \sum_{blade} F_\theta R = T_x. \tag{6.4}$$

That is the the difference between the angular momentum flowing into the blade row in all the inlet streamtubes and that flowing out in the downstream tubes plus the torque T_x acting on the blade due to the streamtubes sum to zero. The torque $T_{x,\,s,r}$ for a given stator or rotor blade row is defined as

$$T_{x\,s,r} = \sum_{blade_{s,r}} \bar{p}(\bar{y}S_z - \bar{z}S_y), \tag{6.5}$$

where the sum is taken over all the cell faces composing the blade surface. The change in angular momentum within the control volume is defined as

$$\Delta^{s,r\ out}_{s,r\ inl} T_x = \left(\sum_{hub}^{tip} \rho_F u_{xF}\, R u_{\theta F}\, S_x\right)_{s,r\ out} - \left(\sum_{hub}^{tip} \rho_F u_{xF}\, R u_{\theta F}\, S_x\right)_{s,r\ inl}. \tag{6.6}$$

Using this relation, the error in angular momentum conservation is defined as

$$E_\theta = \frac{\Delta^{s,r\ out}_{s,r\ inl} T_x - T_{x\,s,r}}{T_{x\,s,r}}. \tag{6.7}$$

Conservation of energy requires that the power delivered to the fluid by the rotating blades must be balanced by the power received by all the streamtubes in the turbine row. The latter one is expressed by

$$\Delta^{s,r\ out}_{s,r\ inl} P = P_{s,r\ out} - P_{s,r\ inl} = \left(\sum_{hub}^{tip} \rho_F u_{xF}\, h_{tF}\, S_x\right)_{r\ out} - \left(\sum_{hub}^{tip} \rho_F u_{xF}\, h_{tF}\, S_x\right)_{r\ inl}, \tag{6.8}$$

where

$$h_{tF} = \frac{\gamma}{\gamma-1}\frac{p_F}{\rho_F} + \frac{1}{2}(u_{xF}^2 + u_{\theta F}^2 + u_{RF}^2). \tag{6.9}$$

Therefore the integrated error function E_P for the rotor

$$E_P = \frac{\Delta_{r\,inl}^{r\,out} P - \Omega T_{xr}}{\Omega T_{xr}} \quad \text{rotor,} \tag{6.10}$$

in which ΩT_{xr} is the power delivered by the rotor blade to the fluid represents a lack of conservation of energy. For a non-rotating row, E_P indicates an error in the the conservation of stagnation enthalpy flux and is defined as

$$E_P = \frac{\Delta_{s\,inl}^{s\,out} P}{P_{s\,inl}} \quad \text{stator.} \tag{6.11}$$

Notice the use of circumferentially flux-averaged quantities in Eqs. (6.6) and (6.8).

case	$E_{\dot{m}}$	E_θ	E_P	*comments*
*sr*922	0.0085	0.0077	0.0080	Stator, see Section 5.6
	0.0230	0.0057	-0.0094	Rotor, quasi-3-D long domain
*sr*921	0.0048	0.0069	0.0053	Stator, see Section 5.6
	0.0058	0.0040	0.0310	Rotor, 1-D long domain
*sr*772	0.0096	0.0077	0.0090	Stator, see Section 5.6
	0.0221	0.0090	-0.0035	Rotor, quasi-3-D short domain
*sr*771	0.0091	0.0078	0.0088	Stator, see Section 5.6
	0.0180	0.0056	0.0033	Rotor, 1-D short domain
*sr*80	0.0056	0.0008	0.0027	Stator, see Section 7.4
	0.0025	0.0009	0.0058	Rotor, $h_{t\,inl} = const$ case
*sr*80*T*	-0.0026	0.0043	-0.0043	Stator, see Section 7.4
	-0.0333	0.0024	-0.0349	Rotor, variable $h_{t\,inl} = h_t(R)$ case

Table 6.1: Errors in mass flow ($E_{\dot{m}}$), angular momentum (E_θ) and power (E_P) for steady-state cases. The errors are in %.

Chapter 7

Steady-State Temperature Migration in a Transonic Turbine Stage

It is well known that the temperature coming out of the combustor of a gas turbine is spatially (and often temporally) non-uniform. The walls and the blades of the first stage of a modern gas turbine are cooled in order to protect the material from melting. Thus the stage inlet temperature is higher at midspan than at the hub and the tip walls. Pitchwise variations may also exist but are not considered here. The effects of temperature gradients are important in turbomachinery flow and in a turbine in particular, because they generate thermal wakes, affect the loading of the blades by creating secondary flows and modify the wall heat transfer.

The purpose of this chapter is to analyze the effects of a spanwise non-uniform inlet temperature distribution on the aerodynamics of a highly loaded transonic first turbine stage. Specifically, one is looking for 3-D secondary flow in the stage due to the migration of the total temperature. To enhance the understanding of the flow physics involved in the temperature migration process and to assess the magnitude of the secondary flow, the results are analyzed relative to the case of constant inlet stagnation enthalpy, see Figure 7.1. Notice that in both cases the inlet stagnation pressure is constant. The assumption of uniform stage inlet stagnation pressure is justified by the fact that at the combustor exit the Mach number is small (≈ 0.1) and the flow is in radial equilibrium so that the stage inlet pressure is constant and equal to the total pressure. As seen later in the analysis, the mechanisms driving the secondary flow are based on vorticity and

simple dynamics derived from steady-state velocity/vorticity triangle arguments as well as inviscid steady-state secondary flow theory. Hence, although the unsteady potential field is lost in the time-averaged solution, the steady result captures the major effects associated with temperature migration since it is primarily an inviscid steady process.

Cattafesta [10] performed an experiment in the MIT Blowdown Turbine Facility Scaling to assess the effects of inlet radial temperature profiles on the efficiency of a transonic turbine stage. This facility allows to simulate the continuous operation of a full scale high performance turbine [21]. In the present work, computations were performed on the same turbine stage. It consists of a highly loaded first turbine stage designed by Rolls-Royce for transonic flow. The overall geometry and the grid used for the calculations are shown in Figs. 7.2 and 7.3. The actual geometry consists of 36 stator blades and 61 rotor blades but the computational domain has been reduced to one blade-to-blade passage using periodic boundaries.

The numerical analysis of temperature migration in the stage is decomposed in two major parts. In the first part, a set of two computations with different inlet stagnation temperature distributions were performed on the isolated vane (no rotor downstream) of Figures 7.2 and 7.3. The purpose of the isolated stator calculations is double. Firstly, this case allows to introduce the the Munk and Prim [80] substitution principle, a concept that is extremely useful to explain the differences occurring between the two flow solutions. In addition to its practical application in this work, I think that it offers a very interesting approach towards the understanding of inviscid, steady-state compressible flow. Since it is usually not discussed in the basic fluid mechanics courses although it originally appeared in 1947, I feel that not only the description of this concept but also its derivation is appropriate.

Briefly summarized the Munk and Prim principle states that if a steady isentropic flow field is determined for a specified geometry and total pressure distribution, then the streamlines pattern, Mach number, static and total pressure fields remain unchanged for any stagnation temperature distribution. Clearly, the second reason for performing

the isolated vane computations is to check the implementation of the Euler solver since the two solutions should match perfectly for certain physical quantities according to the Munk and Prim principle. In addition, the application of this concept to the stage flow explains why no 3-D secondary flow associated with the spanwise temperature gradient occurs in the vane.

In the second part of this chapter, the results for a complete stage computation with the two different inlet stagnation temperature conditions are presented. The comparison of these flows clearly demonstrate that a secondary flow occurs in the rotor frame of reference. The secondary flow, which shows up as a strong radial flow primarily on the rotor pressure surface, is explained using velocity/vorticity triangles arguments and simple dynamics. The full stage computations also allow to determine the effects associated with the temperature migration of one row onto the other, effects which would not appear in the case of an isolated vane.

This chapter is structured as follows. A brief literature review on the subject of temperature distortions in turbines is presented in Section 7.1 followed in Section 7.2 by the derivation and consequences of the Munk and Prim substitution principle. This concept is then applied in Section 7.3 to analyze the flow in an isolated vane for two different inlet stagnation temperature distributions. The results for the coupled stator/rotor are presented in Section 7.4. Finally, the essential conclusions are summarized in Section 7.5.

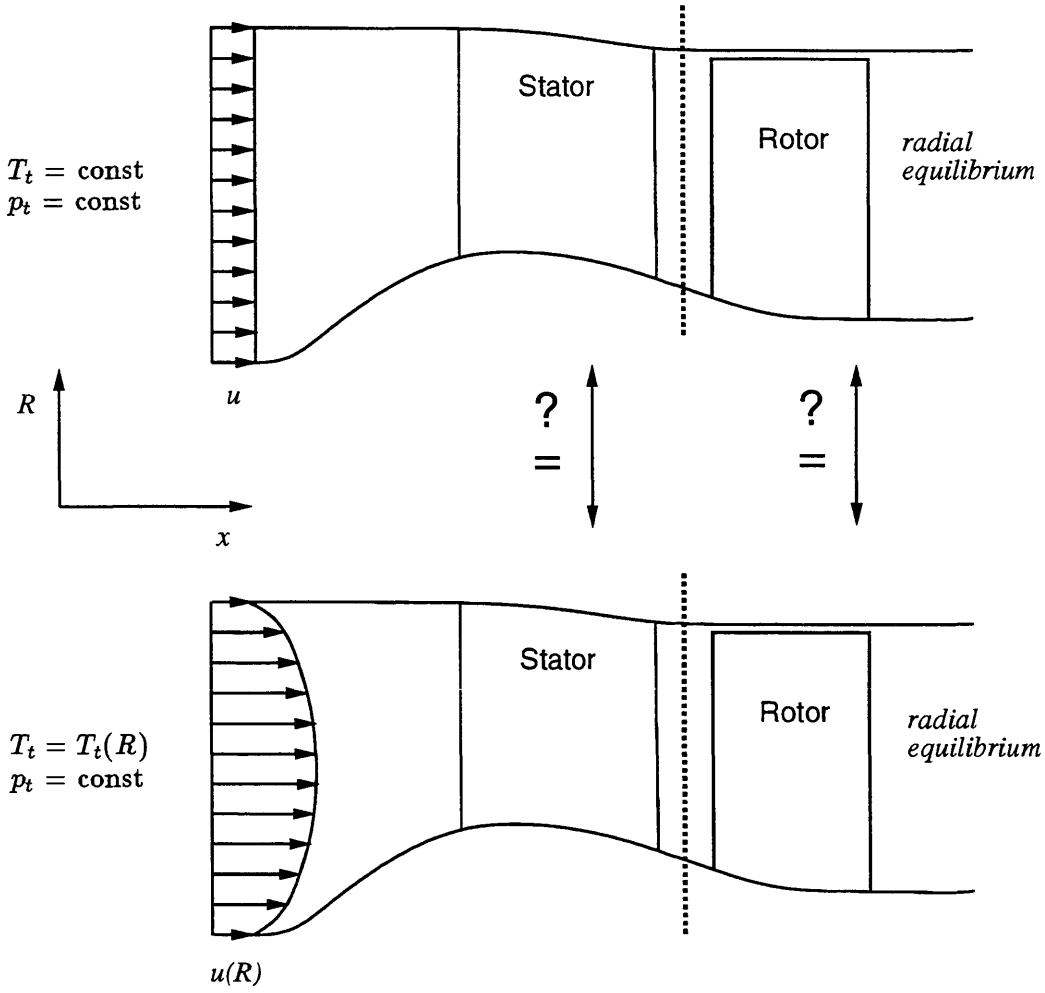

Figure 7.1: The radial temperature migration problem.

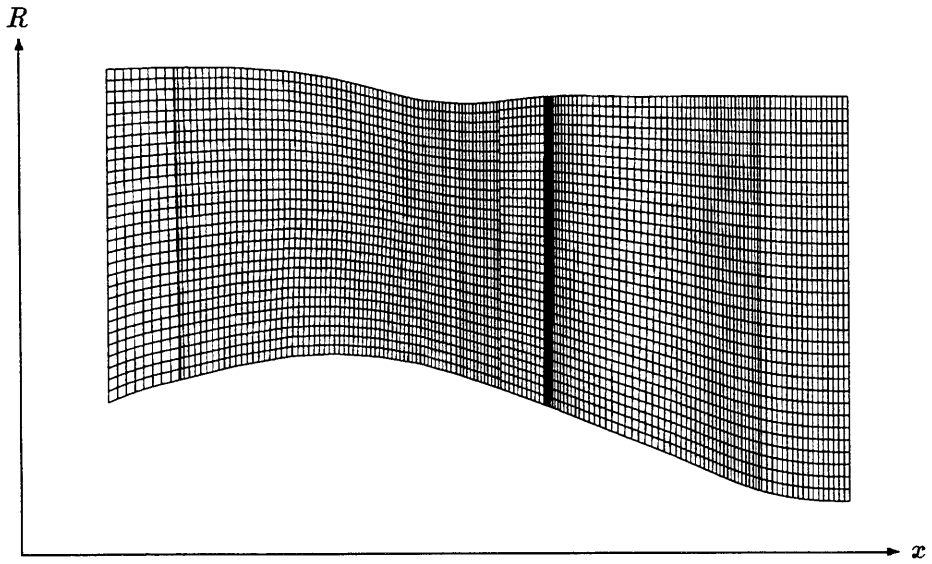

Figure 7.2: Side view of a transonic first turbine stage including stator pressure and rotor suction sides.

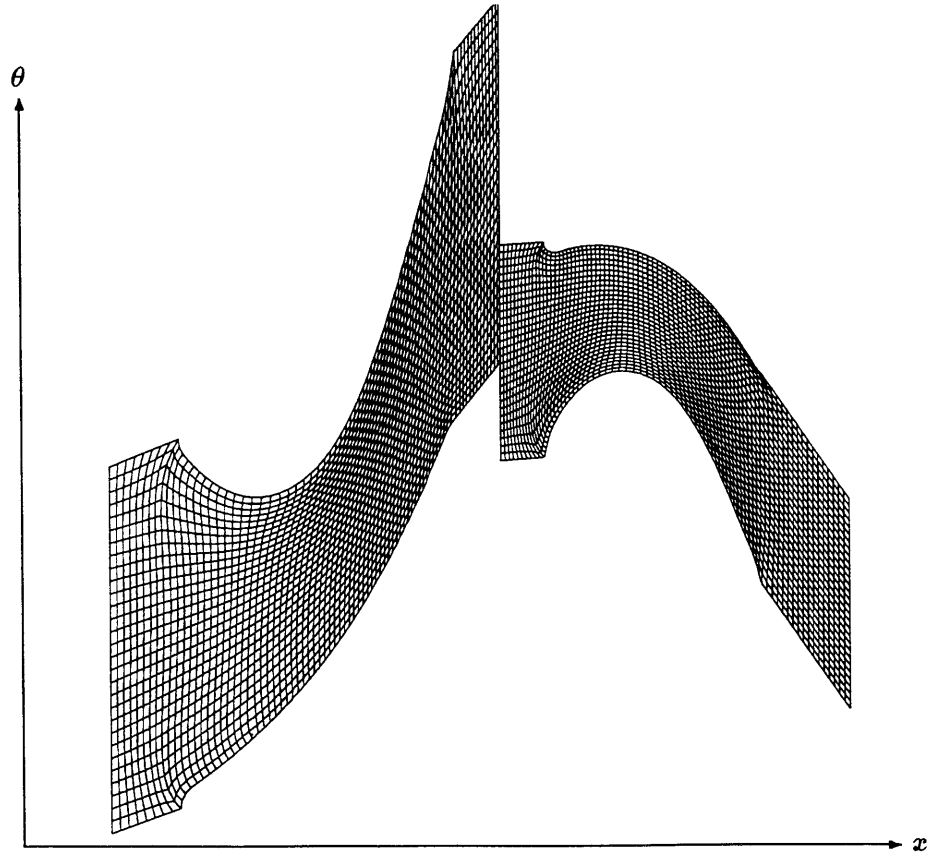

Figure 7.3: Mean height blade-to-blade mesh (stator: $80 \times 30 \times 30$, rotor: $80 \times 30 \times 34$ nodes).

7.1 A brief literature review

The effects of temperature distortions in an axial flow turbine have been investigated both experimentally and computationally.

Butler et al. [9] conducted an experiment in which hot air seeded with CO_2 was introduced at the inlet of a subsonic axial turbine stage. The temperature distortion consisted of a hot spot centered at 40% span at one circumferential location with a ratio of hot to cold air set to 2. A secondary flow was measured in the rotor frame of reference, but none in the stator row. Rai and Dring [88] carried out a 2-D analysis of the redistribution of an inlet temperature distortion in a turbine stage by solving the thin-layer Navier-Stokes equations. Also in 2-D, Krouthén and Giles [66] performed a numerical simulation of the effects of hot streaks in a turbine rotor. The domain was decomposed into a inviscid core region, where the Euler equations are solved, and a viscous region where the Reynolds-averaged, thin-layer Navier-Stokes equations are solved. Both 2-D studies presented unsteady temperature contours and predicted the migration of the hot gas towards the pressure surface, which is consistent with experimental observations.

More recently, Harasgama [47], Takahashi and Ni [105] and Dorney et al. [19] performed numerical simulations with inlet temperature distortions. In [47] the 3-D Navier-Stokes solver of Dawes [14] was used to analyze the rotor-relative flow field under the influence of a uniform, radially parabolic and radially skewed parabolic rotor inflow temperature profile. Takahashi and Ni used an Euler solver (with viscous modelling) to predict the rotor temperature redistribution resulting from the effects of circular hot jets as modelled in Butler's experiment. Periodic unsteady and steady 2- and 3-D results were presented. Among other conclusions, this study indicates that the steady and the time-averaged rotor pressure distribution agree well. However, the steady solution underestimates the temperatures. In a concurrent paper [19], 3-D unsteady Navier-Stokes computations were performed with similar inlet conditions. Both computations show similar trends, with the Navier-Stokes technique providing more detailed agreement with the experimental data. In addition, these studies clearly indicate that by

comparing the rotor surface temperature distribution to the 2-D simulations and the experiments, 3-D effects are essential in the temperature migration process of circular hot streaks. Notice that in all the above mentioned studies the turbine operated under subsonic flow conditions.

Lakshminarayana [68] carried out an analysis to predict thermally driven secondary flow in a nozzle and a rotor that is based upon Helmholtz's vorticity equation for inviscid compressible flow. He derived approximate relations relating the rotation of the isothermal surfaces to the gradient in stagnation temperature and provided expressions for the strength of the secondary vorticity and for predicting the temperature profiles at the exit at the exit of the blade row. These expressions were derived from the equation for the growth of secondary vorticity (streamwise) written in intrinsic coordinates.

7.2 Munk and Prim substitution principle

The derivation of the Munk and Prim substitution principle starts by considering the equations of motion of an inviscid, steady and adiabatic perfect gas of constant specific heats[1]. Also, there must be no body forces, hence this principle cannot be applied in a rotating frame of reference.

$$\nabla \cdot (\rho \vec{V}) = 0, \tag{7.1}$$

$$(\vec{V} \cdot \nabla)\vec{V} = -\frac{\nabla p}{\rho}, \tag{7.2}$$

$$\vec{V} \cdot \nabla h_t = 0. \tag{7.3}$$

The last equation indicates that the total enthalpy h_t is constant along a streamline, although h_t may vary from one streamline to another. The goal of the following derivation is to express the equations for the conservation of mass and momentum in terms of

[1]Note that an extension of this principle to account for viscous stresses and heat transfer has been proposed by Greitzer et al. [44]. The extended principle, however, is only approximate.

variables where the density and stagnation enthalpy do not explicitly appear. For that purpose, it is useful to replace the stagnation enthalpy h_t by the "maximum" velocity V_{max}. This velocity is defined as

$$h_t = \frac{1}{2}V_{max}^2 \tag{7.4}$$

and represents the velocity of the gas at the state where the energy is completely transformed into kinetic energy, i.e. $T = h = 0$. Also, define

$$\vec{C} = \frac{\vec{V}}{V_{max}} \tag{7.5}$$

as the reduced velocity vector. Hence, the energy equation along a streamline for a perfect gas of constant specific heat becomes

$$h_t = c_p T_t = h + \frac{1}{2}V^2 = \frac{h}{1 - C^2} \tag{7.6}$$

The continuity Equation (7.1) is now written in terms of the reduced velocity $\vec{C}$.

$$\begin{aligned} \nabla \cdot (\rho \vec{V}) &= \nabla \cdot \left((\rho_t \sqrt{2h_t})(\frac{\rho}{\rho_t})\vec{C} \right) \\ &= \rho_t \sqrt{2h_t}\, \nabla \cdot \left((\frac{\rho}{\rho_t})\vec{C} \right) + (\frac{\rho}{\rho_t})\vec{C} \cdot \nabla(\rho_t \sqrt{2h_t}) = 0. \end{aligned} \tag{7.7}$$

The second term to the right of the above equation is zero. This is because the quantity $\rho_t \sqrt{2h_t}$ is constant along a streamline[2], so that its gradient must be perpendicular to $\vec{V}$ or $\vec{C}$. Thus

$$\nabla \cdot \left((\frac{\rho}{\rho_t})\vec{C} \right) = 0. \tag{7.8}$$

The density term is replaced by a reduced velocity function using isentropic relations and Eq. (7.6).

$$\frac{\rho}{\rho_t} = \left(\frac{T}{T_t} \right)^{\frac{1}{\gamma - 1}} = \left(\frac{h}{h_t} \right)^{\frac{1}{\gamma - 1}} = (1 - C^2)^{\frac{1}{\gamma - 1}}. \tag{7.9}$$

Thus, the continuity equation becomes

$$\nabla \cdot [(1 - C^2)^{\frac{1}{\gamma - 1}} \vec{C}] = 0. \tag{7.10}$$

[2] Although ρ_t changes discontinuously across a shock, the argument is still valid ahead and downstream of the discontinuity.

The momentum Equation (7.2) is also rewritten in terms of the reduced velocity $\vec{C}$.

$$\rho(V_{max}\vec{C}\cdot\nabla)(V_{max}\vec{C})+\nabla p=0$$

$$\Longrightarrow\quad \rho V_{max}^2\vec{C}\cdot\nabla\vec{C}+\rho V_{max}\vec{C}(\vec{C}\cdot\nabla V_{max})+\nabla p=0 \tag{7.11}$$

Notice that $\nabla V_{max}=0$ along a streamtube. Apply Eq. (7.4) to get

$$\rho h\,2\frac{h_t}{h}(\vec{C}\cdot\nabla)\vec{C}+\nabla p=0. \tag{7.12}$$

For a perfect gas ρh can be defined as

$$\rho h=\rho c_pT=\rho\frac{\gamma R}{\gamma-1}T=\frac{\gamma}{\gamma-1}p. \tag{7.13}$$

Thus the momentum equation expressed in terms of pressure and reduced velocity vector alone is

$$\frac{2\gamma}{\gamma-1}\frac{p}{1-C^2}(\vec{C}\cdot\nabla)\vec{C}+\nabla p=0, \tag{7.14}$$

which can be rewritten as

$$(\vec{C}\cdot\nabla)\vec{C}+\frac{\gamma-1}{2\gamma}(1-C^2)\,\nabla(\ln p)=0. \tag{7.15}$$

The continuity Equation (7.10) and the dynamic Equation (7.15) form a system of two equations for the two unknowns $\vec{C}$ and p.

The fact that the stagnation enthalpy (or total temperature) does not explicitly appear in the equations of motion expressed in terms of the reduced velocity $\vec{C}$ and static pressure p, indicates that the energy equation is effectively uncoupled from the other equations of motion. Thus a solution of Eqs. (7.10) and (7.15) really consists of a family of solutions corresponding to different assignments of the total enthalpy to streamtubes. However, for each solution the pressure field p and the streamtubes area are the same, independent of the assignment of h_t. To express the relations between the solutions in terms of total pressure, Mach number, mass flow, and so on as a function of the given stagnation temperature distribution, it is best to focus on two single solutions determined for a specific geometry.

Consider for instance two steady-state flow fields occurring in the isolated stator of Figs. 7.2 and 7.3. The inlet and outlet conditions relative to these two flows are the same except for the inlet stagnation enthalpy distribution among the streamtubes. Focusing on one particular streamtube characterized by $h_{t_{cold}}$ in one solution and $h_{t_{hot}}$ in the other, it is readily seen that due to the invariance of $\vec{C}$ the two velocity fields are related by the following relations

$$\frac{\vec{V}_{cold}}{\vec{V}_{hot}} = \sqrt{\frac{h_{t_{cold}}}{h_{t_{hot}}}} = \sqrt{\frac{T_{t_{cold}}}{T_{t_{hot}}}}. \tag{7.16}$$

In addition the same pressure field will keep the flow in equilibrium, i.e.

$$p_{cold} = p_{hot} \tag{7.17}$$

and the streamline pattern is the same in both solutions. The following relations are then easy to demonstrate.

$$\frac{T_{cold}}{T_{hot}} = \frac{T_{t_{cold}}}{T_{t_{hot}}} \implies M_{cold} = M_{hot} \tag{7.18}$$

$$\frac{\rho_{cold}}{\rho_{hot}} = \frac{T_{t_{hot}}}{T_{t_{cold}}} \tag{7.19}$$

$$\rho_{cold} V_{cold}^2 = \rho_{hot} V_{hot}^2 \implies p_{t_{cold}} = p_{t_{hot}} \tag{7.20}$$

$$\frac{\dot{m}_{cold}}{\dot{m}_{hot}} = \sqrt{\frac{T_{t_{hot}}}{T_{t_{cold}}}} \tag{7.21}$$

7.3 Isolated vane

The stator inlet radial temperature profile is typical for a high performance combustor and consists of a parabolic shape with 20.8% over-temperature at midspan compared to the hub and tip walls, see for instance [10]. In Figure 7.4 the vane outlet mass-averaged total temperature is plotted as a function of percent span for the cases without and with inlet radial stagnation temperature variation. All other boundary conditions are the same for the two cases. Note that the subscript $_{cold}$ is used to describe a quantity related to the flow of constant inlet stagnation temperature whereas the subscript $_{hot}$ refers to the case with spanwise temperature gradient. The third curve plotted in Fig. 7.4 represents the prescribed inlet temperature profile for the '*hot*' flow case. Note also that $T_{t_{cold\ inlet}} = T_{t_{cold\ outlet}} = 1/(\gamma-1)$, which is correct since each streamtube conserves its stagnation temperature. In the '*hot*' flow case the the maximum over-temperature is well conserved at midspan but the minima at the hub and the tip are slightly higher at the exit than at the inlet indicating an effect of the numerical dissipation.

It is important to realize that in the '*hot*' flow case vorticity is being introduced as part of the inlet boundary condition as sketched in Fig. 7.1. This is done while keeping $p_{t_{cold\ inlet}} = p_{t_{hot\ inlet}} = \text{const}$. Hence, according to Eqs. (7.16) to (7.21), the '*hot*' flow case (rotational) may be substituted for the '*cold*' flow case (irrotational) without affecting the local values of static and total pressure, as well as Mach number. Consequently, no streamwise vorticity associated with the spanwise temperature gradient occurs in the vane.

Another way of checking this statement is to use Hawthorne's secondary flow theory [48, 50, 51]. He showed that, within the frame of the above mentioned assumptions, the secondary circulation formation is driven by a gradient in total pressure but not stagnation enthalpy. Since the total pressure is constant in both cases, the additional vortex lines introduced in the '*hot*' case have to remain perpendicular to the flow, i.e. no streamwise vorticity is generated. This can be verified by using the relations for the

growth of streamwise vorticity written in natural coordinates.

$$\frac{\partial}{\partial s}\left(\frac{\omega_s}{\rho V}\right) = \frac{2\omega_n}{\rho V \sigma} + \frac{1}{\rho^2 V^2 T}\frac{\partial T}{\partial b}\frac{\partial p}{\partial n}$$

$$= \frac{2}{\rho \rho_t V^2 \sigma}\frac{\partial p_t}{\partial b}. \tag{7.22}$$

Equation (7.22), taken from Reference [55], was derived from the Helmholtz equation that governs the generation and growth of vorticity for an inviscid compressible flow and in the absence of body forces. Using intrinsic coordinates, the vorticity is written as

$$\vec{\omega} = \hat{s}\omega_s + \hat{n}\omega_n + \hat{b}\omega_b, \tag{7.23}$$

where ω_s, ω_n and ω_b are the components of vorticity in the streamwise ($\hat{s}$), principal normal ($\hat{n}$) and binormal ($\hat{b}$) directions, respectively, and σ is the local radius of curvature of the streamline, see Fig. 8.12. Note that this theory is more extensively used in Chapter 8 to discuss the secondary flow occurring in a 3-D linear cascade due to a vortex and temperature gradient.

The important point to notice here is that the constancy of the stagnation pressure implies that the growth of secondary flow in the vane is zero. Hence, in the '*hot*' flow case and according to Eq. (7.22), the secondary flow developed by the turning of the inlet normal vorticity ω_n is exactly balanced by the secondary flow induced by the temperature gradient ($\partial T/\partial b$). Consequently, since no inlet streamwise vorticity is present in the '*cold*' and '*hot*' cases and none is generated along the passage, the solutions exhibit the Munk and Prim similarity. Indeed this shows up in the numerical simulation as indicated by Figures 7.5, 7.6 and 7.7, i.e. the two solutions lay on top of each other.

As shown in the next section, in the coupled stator/rotor calculation and compared to uniform inlet total enthalpy, the radial temperature variation indirectly affects the vane flow field region downstream of the choked throat, through the rotor flow field.

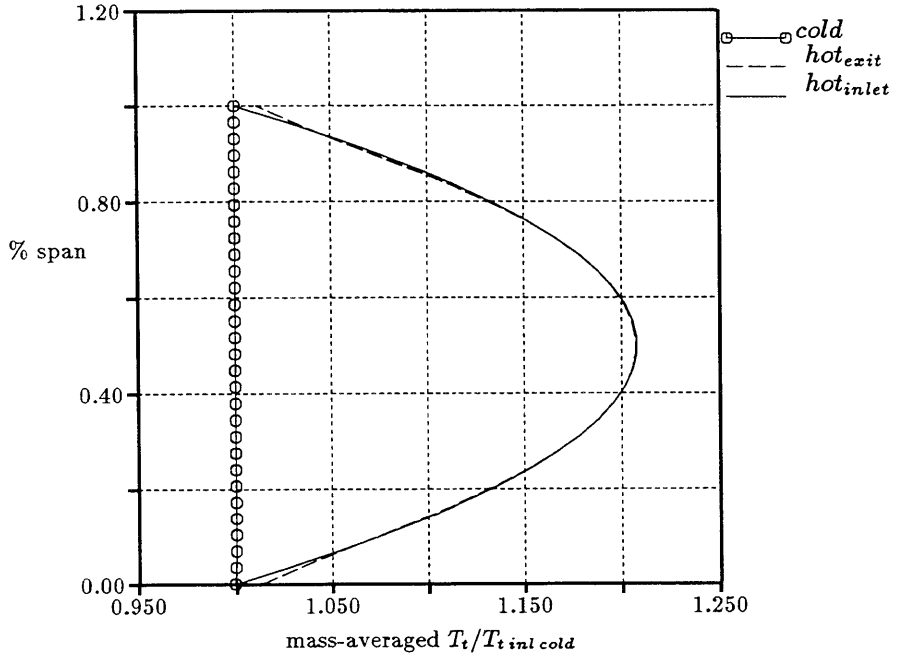

Figure 7.4: Isolated vane: mass-averaged stagnation temperature at vane inlet and exit.

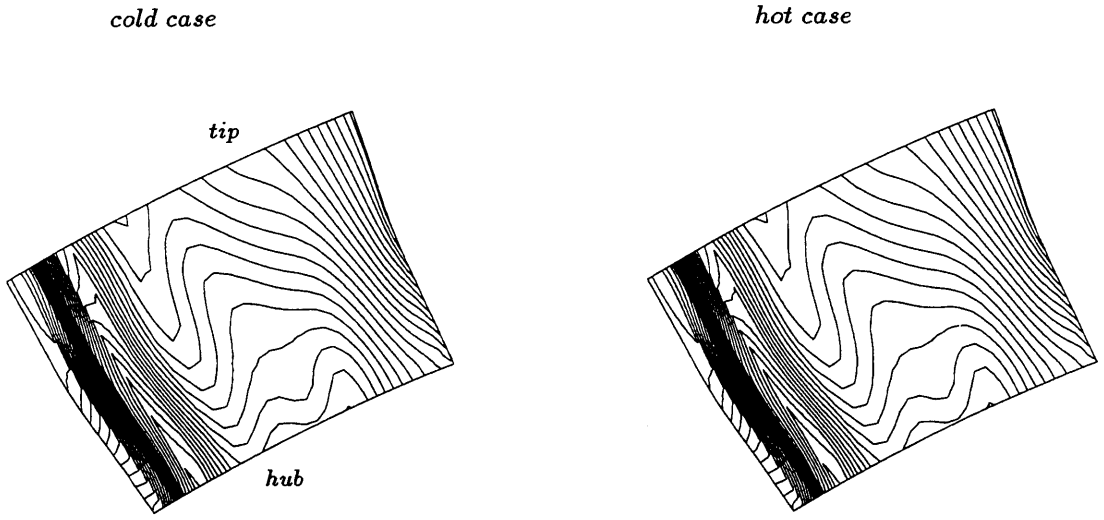

Figure 7.5: Munk and Prim test: vane pressure at 8% axial chord downstream trailing edge.

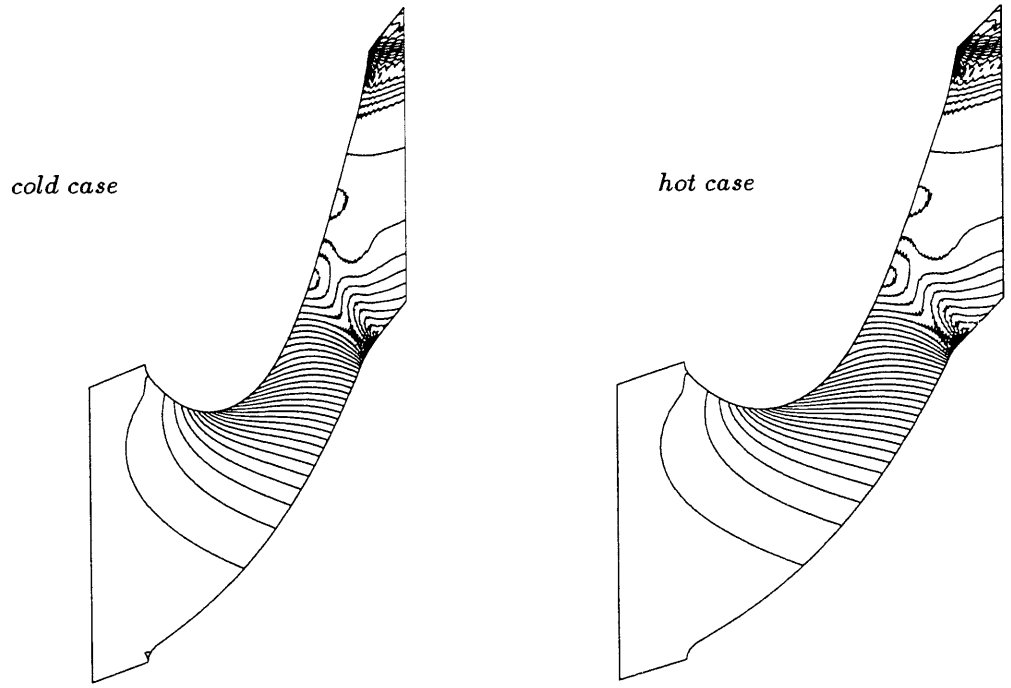

Figure 7.6: Munk and Prim test: midspan vane pressure ($p/p_{t\,inl}$). Increments = 0.02.

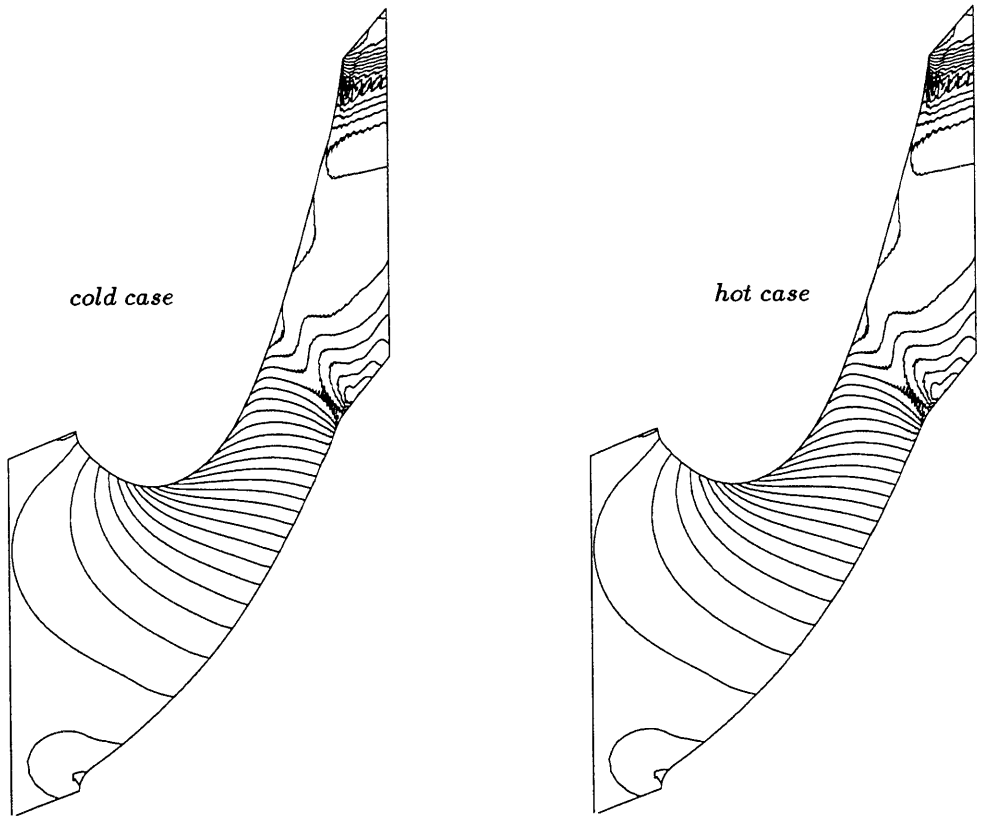

Figure 7.7: Munk and Prim test: midspan vane Mach number. $M_{exit} = 1.2$. Increments = 0.05.

7.4 Coupled stator/rotor results

The pressure fields at the hub wall and at a constant radius ($\approx$ midheight) are represented in Figures 7.8 and 7.9 for the '*cold*' case. The discussion of the flow features of the transonic stage operating under constant inlet conditions ('*cold*' case) is postponed until Chapter 9. Instead, this section focusses on the effects of the non-uniform inlet stagnation temperature profile and the resulting secondary flow occuring in the rotor frame.

For convenience, the flux-averaged flow parameters for the two cases are summarized in Table 7.1.

In the rotor frame of reference, both the inlet velocity and the tangential angle have larger values at midspan than they would have in the case of no radial variation. This can easily be demonstrated by subtracting the rotor tangential speed from the stator radial velocity shear, see Figure 7.10. Figure 7.10 is to be considered as representative of two velocity triangles drawn at midspan of the stator exit (or rotor inlet) and where V_{cold}/V_{hot} is given by Eq. (7.16). The rotor-relative flux-averaged inlet angles for the two cases are displayed in Figure 7.11.

The first consequence of this is that the rotor relative total pressure is affected as well by the introduction of the stagnation temperature variation, see Figure 7.12. The static pressure and relative stagnation pressure (on the pressure side of the blade) are shown on Figures 7.13 and 7.14 for the '*cold*' and '*hot*' flow cases, respectively. Relative to the ($T_{t_{cold\,inlet}}$ = const) calculation case, the '*hot*' flow case result shows a total pressure excess at midspan, and a deficit at the hub and the tip. This produces a radial pressure gradient on the pressure surface, which is comparable in magnitude to the axial pressure gradient, and generates a secondary flow from midspan towards the hub and the tip. This effect, can more clearly be seen by looking at the blade streamlines plotted on Figs. 7.15 and 7.16. Another way of visualizing the secondary flow is to look at the relative velocity vectors, see Reference [92] or the surface tufts plotted on the pressure

side, see Fig. 7.17. Note that the surface streamlines and tufts were generated using VISUAL3, the graphic visualization package developed at MIT by Giles and Haimes [40].

An important factor in determining the boundary-layer heat flux is the inviscid relative total temperature shown here on the pressure and suction sides for the '*hot*' flow case, see Fig. 7.19. By transforming the velocity vectors from the stator absolute to the rotor relative frame of reference, a spanwise difference in rotor relative inlet angle and velocity magnitude occurs, see Fig. 7.10. At this point, Fig. 7.10[3] represents the stator/rotor interface velocity triangles at midspan and at the hub (or tip) for the '*hot*' flow case only. The subscripts $_{cold}$ and $_{hot}$ are now referred to quantities at the endwalls and midspan, respectively.

The hot midspan fluid is oriented more towards the rotor pressure side and moves at a higher relative speed as compared to the cold endwall gas. Thus, as the two streams (hot midspan and cold endwalls) move through the rotor, the hot fluid migrates towards the pressure side relative to the cold fluid as seen in Figure 7.18. This segregation effect is based upon arguments inferred from the velocity triangles drawn at midspan and endwall. In their 2-D analysis of the collection of high temperature compressor rotor wakes on the pressure side of the downstream stators, Kerrebrock and Mikolajczak [63] used a similar velocity triangle argument to explain the segregation between wake fluid and inviscid fluid. Here, the segregation effect seems to be enhanced by the rotor relative secondary flow in the sense that the hot midspan gas spreads out, on the pressure side, towards the upper and lower walls of the channel. On the suction side, however, the cold fluid tends to move towards midspan, see Figure 7.19. This is consistent with the experimental observations of Butler et al. [9]. Also, Figures 7.19 and 7.20 indicate that the rotor trailing edge, on the pressure side, is over-heated along its entire span. In the '*cold*' flow case, however, the stagnation temperature remains approximately constant on the blade. Compared to the case with no stagnation temperature variation,

[3]Actually the wheel speed varies along the span, and in that respect Fig. 7.10 is more representative of a 3-D linear stator/rotor cascade. However, this does not affect the conclusions.

it becomes evident that rotor relative inviscid secondary flow has been induced by the stator inlet total temperature radial gradient.

Another way of understanding these results is to look at the vorticity field. In Figure 7.10, a vector representative of the hub vorticity in the absolute frame $\vec{\omega}$ is decomposed into a rotor relative streamwise component ω_s and a normal component ω_n. Note that the tip vorticity if drawn, would have opposite direction. According to the results of Section 7.3, no streamwise vorticity is generated in the vane, hence the stator exit absolute vorticity is perpendicular to the flow. However, it is readily seen that a negative component of streamwise vorticity is present at the rotor inlet and thus contributes to the development of secondary flow. As the fluid particles move through the lower half of the rotor passage, this streamwise vorticity tends to develop a radially upward component of velocity on the suction side and a downward velocity on the pressure side. On the upper half of the channel where fluid particles with positive streamwise vorticity enter the rotor, this mechanism is reversed inducing a radially upward motion on the pressure side and a downward velocity component on the suction surface. This is only a qualitative argument since the rotor inlet fluid vorticity is intensified or weakened according to secondary flow theory applied to a rotating duct. For an inviscid non-isentropic compressible flow rotating at constant angular speed Ω, it is not possible to derive for the growth of streamwise vorticity a simple expression such as the second form of Eq. (7.22). In general the gradient of two quantities such as the entropy and the rotary stagnation pressure $p_t^\star$,

$$p_t^\star = p + \frac{1}{2}\rho\left((u^2+v^2+w^2)_{rel} - \Omega^2 R^2\right), \tag{7.24}$$

are required, see for instance [51, 100, 50]. Only in particular instances such as incompressible or homentropic flow, expressions for the growth of streamwise vorticity can be written as a function of the gradient of rotary stagnation pressure only.

In the full stage calculations analyzed here, though the rotor exit pressure is the same, the stator/rotor interface pressure in the '*hot*' case differs from the '*cold*' case. Relative to the case with uniform inlet total temperature, the calculation with varying

total temperature shows a lower flux-averaged stator exit pressure that can be expressed as

$$\frac{(p_{F_{cold}} - p_{F_{hot}})_{hub\ vane\ exit}}{p_{t_{inl}}} \approx 0.365 - 0.349 = 0.016, \tag{7.25}$$

where $p_{t_{inl}} = 1/\gamma$. This pressure change represents 4% of the vane exit dynamic head (based on a hub Mach number of 1.31). This is different from the isolated vane results discussed in Section 7.3 in which two flows were compared with different inlet stagnation temperature profiles but the same exit pressure so that the Munk an Prim principle could be used. As explained earlier, one of the consequences of increasing the inlet stagnation temperature is to increase the rotor relative inlet angle at midspan. For a fixed mass flow, this results in larger midspan tangential velocity, hence larger total velocity and Mach number, see Figure 7.21. The flux-averaged pressure is thus reduced but, on account of the radial equilibrium coupling, this occurs not only at midspan but also at the endwalls. Consequently, for the same inlet total pressure, the stator exit velocity and hence the Mach number are also increased at the hub and the tip walls, see Fig. 7.22. Notice that the influence of the rotor flow field does not extend upstream of the choked stator throat. In the relative frame of reference, and compared to the case of constant inlet total temperature, higher incidence angles are now expected over the entire span, see Figure 7.11. This forces a shock, otherwise not present in the constant stagnation enthalpy calculation, to develop at the suction side of the rotor root, see Figures 7.23 and 7.24.

The generation of the rotor-relative secondary flow influences both the rotor heat transfer and boundary-layer development. In [95] Sharma and Graziani analyzed the influence of cross-flow on the development of the midspan suction surface boundary-layer in a turbine cascade. They showed that the effect of the endwall flow is to generate a cross-flow velocity gradient which drives endwall fluid towards midspan. Also, they demonstrated that the overall mass in the boundary-layer is greater than the 2-D value. This produces a thickening of the midspan suction surface boundary-layer and consequently an increase of the midheight losses, decrease in the Reynolds shear stress, skin friction and Stanton number. This is a general secondary flow mechanism that can be

applied to the flow treated here. In this application, however, the secondary flow is particularly strong on the pressure side of the rotor with a cross-flow driving midspan fluid towards the endwalls. It is expected that under the influence of the radial flow, a thinning of the midspan pressure surface boundary-layer would occur accompanied by an enhanced rotor blade heat transfer.

Another set of computations[4] involving a spanwise temperature variation in the stage was set up in order to compare the solutions using the present Euler solver and the results obtained by Pappas [84] running Denton's solver (inviscid version) [17]. Though the contraction of the annulus was the same, the stator and the rotor blade geometries used in the two calculations differed. For instance, different radial cuts were used to define the stator geometry. This affects both the thickness of the blade which, at the crown, varies about 20% from the tip (thicker) to the hub, and the twist, especially at the tip were differences in the exit swirl angle of 3^0 (relative to an average vane exit angle of 72^0 at the hub) appear between the two solver solutions. Pappas' trailing edge cusps (both stator and rotor) are much more elongated and slender than the ones defined in this work (about 5 times longer). Also, in Pappas' work, the rotor leading edge has been altered from rounded to cusped. These changes decrease the blade aspect ratio by increasing the axial chord (estimated at +10%) and affect the loading at the leading and the trailing edge.

In general, a qualitative agreement has been observed between the two sets of computations, with similar trends for the secondary flow consistent with the analysis given above. For instance, relative to the uniform inlet flow solution, the predicted magnitude of the midpsan excess in stagnation pressure and deficit at the hub (and the tip) is the same in the two computations with a value equal to 34% of the rotor-relative inlet dynamic head at the hub (based on Pappas' predicted hub Mach number of 0.45). Thus, both codes were able to predict the temperature migration in the rotor passage

[4]The set involved a calculation with a constant inlet temperature and another one with a 30% increase in stagnation temperature at midspan compared to the hub and tip values. The corrected speeds are the same with and without temperature variations. These computations were performed with an exit pressure 20% lower than the exit pressure of the cases summarized in Table 7.1.

and in particular on the blade surface, with the strongest effects occurring at the tip on the pressure side near the trailing edge. However, the predicted level of temperatures on the blade surface is different, see Figure 7.25. For instance, compared to 5% in Pappas' solution, the present method predicts a heating of the tip on the pressure side corresponding to 8.5% of the rotor-relative inlet stagnation temperature at midspan.

7.5 Conclusions

The effects of an inlet spanwise non-uniform stagnation temperature distribution in an industrial transonic first turbine stage have been analyzed. Computations on the vane alone and on the combined stator/rotor geometry were performed with an inlet radial temperature profile (21% over-heated flow at midspan compared to the hub and the tip wall, and parabolic spanwise variation) typical for these kind of axial flow turbines. To assess the importance of the resulting secondary flow (both in terms of magnitude and direction), computations with a uniform inlet stagnation temperature were also performed.

The isolated vane solutions computed with and without inlet temperature variations but the same stagnation pressure, exhibit an invariance of Mach number and pressure which is in accordance with the Munk and Prim subsitution principle. Also, the calculations show that no secondary flow is generated by the introduction of the stagnation temperature distortion as predicted by secondary flow theory. Hence, the isolated stator computations provided a useful test case for the Euler solver.

The solutions for the complete stage indicate that a significant secondary flow occurs in the rotor row. The introduction of the stator inlet temperature gradient results in general in the collection of hotter gas on the rotor pressure side than on the suction side. On the pressure side, the hot fluid is spreading from midspan towards the hub and the tip walls resulting in the heating of the upper and lower walls. At the tip on

the pressure side near the trailing edge, the heating reaches 8% of the inlet stagnation temperature reference value, which almost corresponds to one-half of the inlet midspan distortion.

The segregation effect between hot and cold fluid with the hot midspan gas oriented more towards the pressure side of the rotor blade (an increase of 6^0 in rotor inlet angle compared to the uniform inlet conditions solution) is explained from the stator/rotor interface velocity triangle. Relative to the uniform inlet conditions solution, the temperature distortion calculation exhibits an excess of rotor-relative inlet stagnation pressure at midspan and a deficit at the hub and the tip of about 12% of the rotor inlet dynamic head (based on a rotor-relative Mach number at the hub of 0.63), which contributes to the generation of secondary flow and the migration of hot fluid from midspan towards the upper and lower walls on the pressure side.

Relative to the solution with a uniform stagnation temperature at the inlet, the stator/rotor interface pressure is reduced (17% of the rotor inlet dynamic head), which in turn produces an increase in both the stator exit and rotor inlet Mach numbers and also the rotor inlet angle, see Table 7.1. This is sufficient to trigger a shock a the rotor root. This feature, together with the stagnation temperature migration indicates that the rotor-relative secondary flow is significant in the case examined.

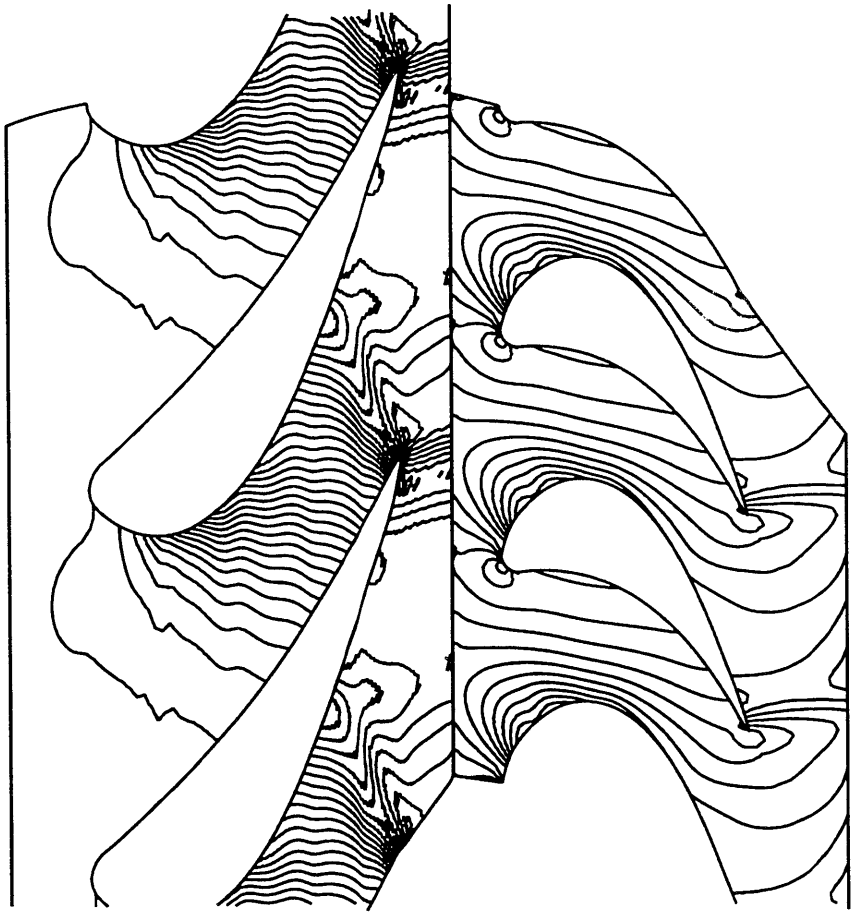

Figure 7.8: Cold case: pressure contours at the hub wall.

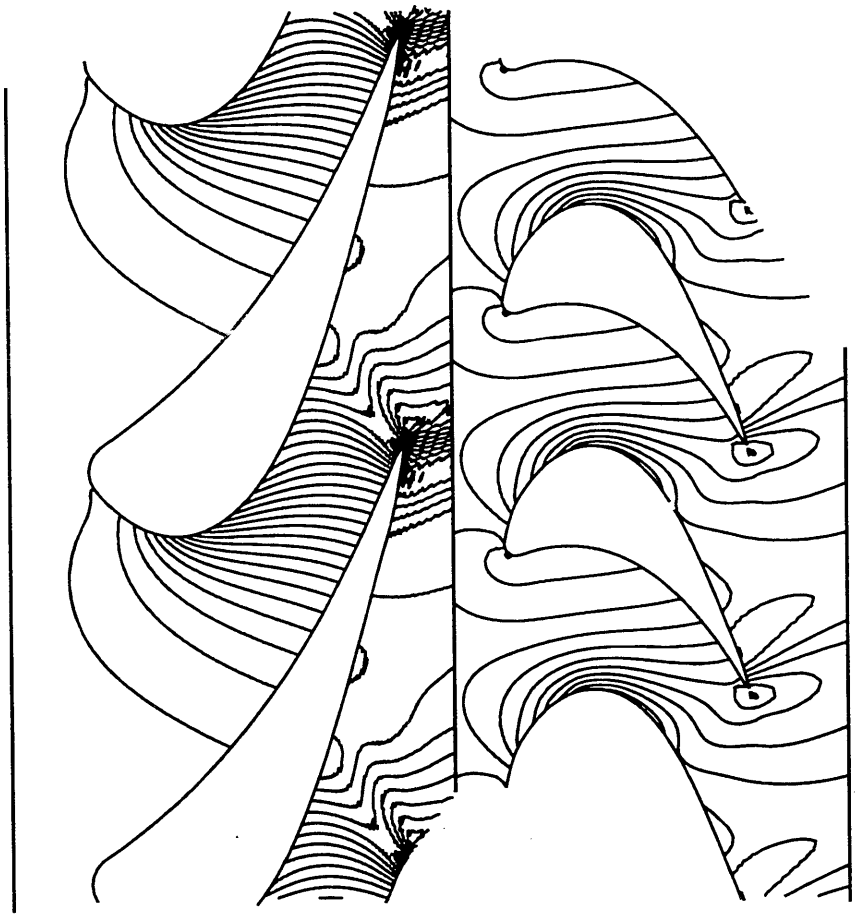

Figure 7.9: Cold case: pressure contours at constant radius ($R \approx$ midspan rotor leading edge).

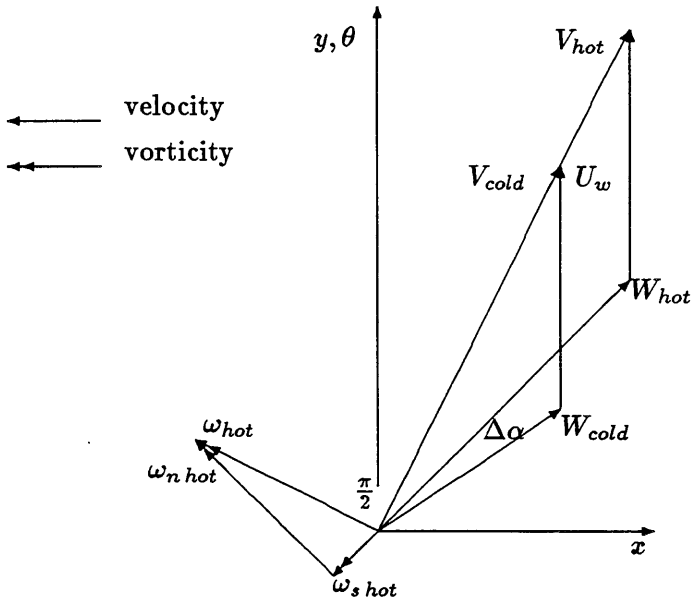

Figure 7.10: Velocity and vorticity triangles at stator/rotor interface.

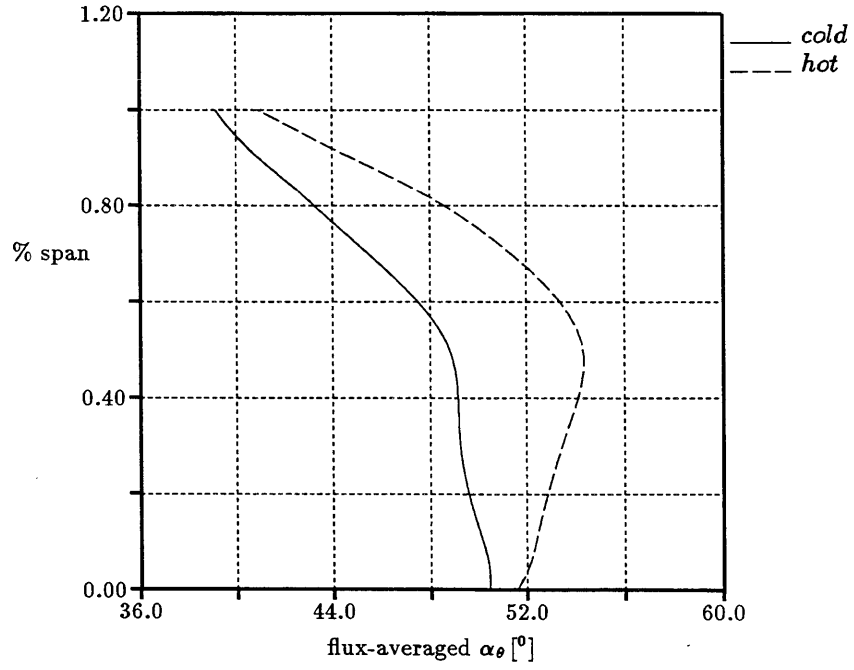

Figure 7.11: Rotor-relative flux-averaged inlet angles.

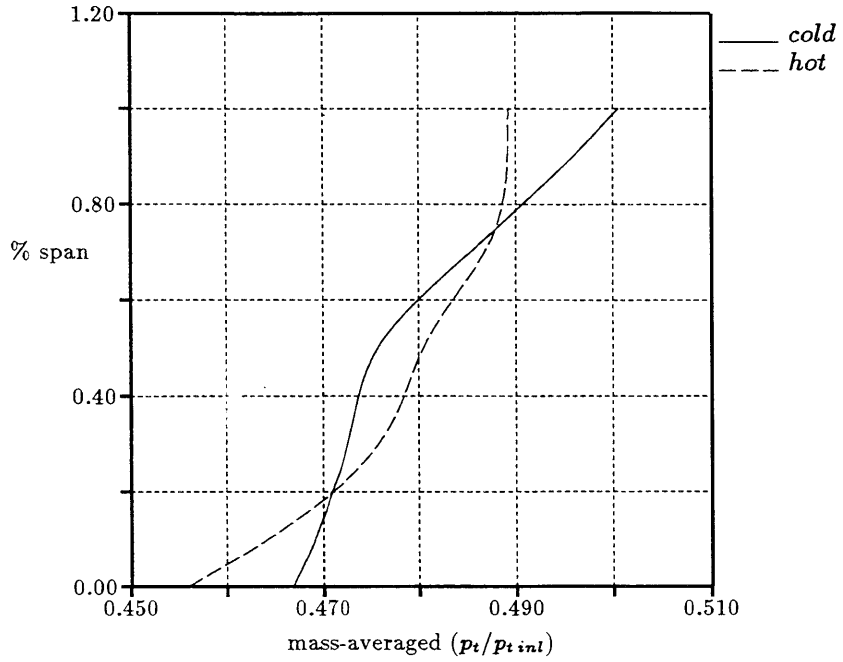

Figure 7.12: Rotor-relative mass-averaged inlet stagnation pressure.

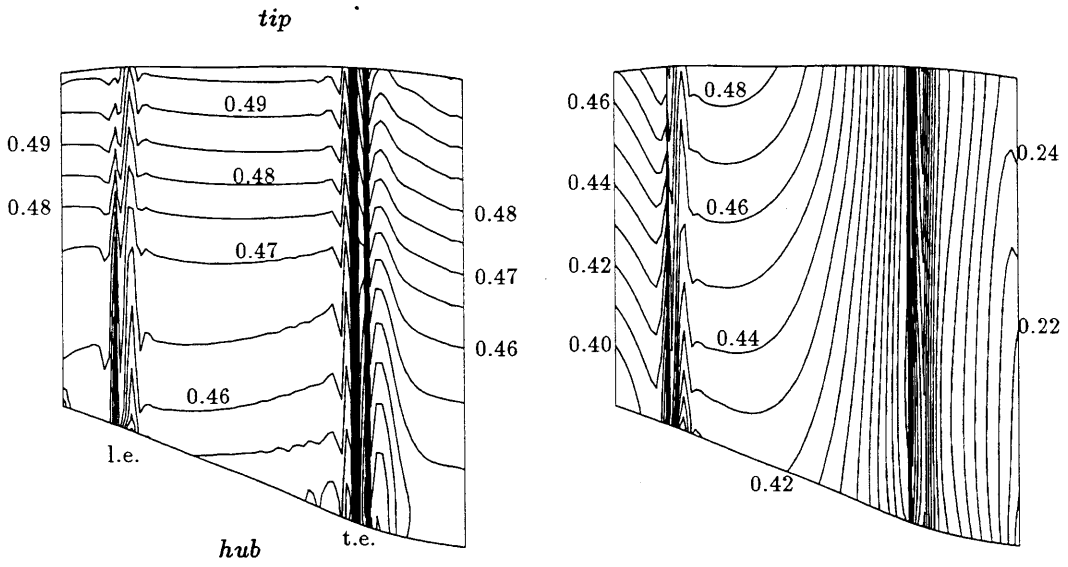

Figure 7.13: Cold case: rotor-relative stagnation pressure (p_t/p_{tinl}) (left) and static pressure (p/p_{tinl}) (right) contours on pressure side, and periodic surfaces ahead of leading edge and downstream of trailing edge.

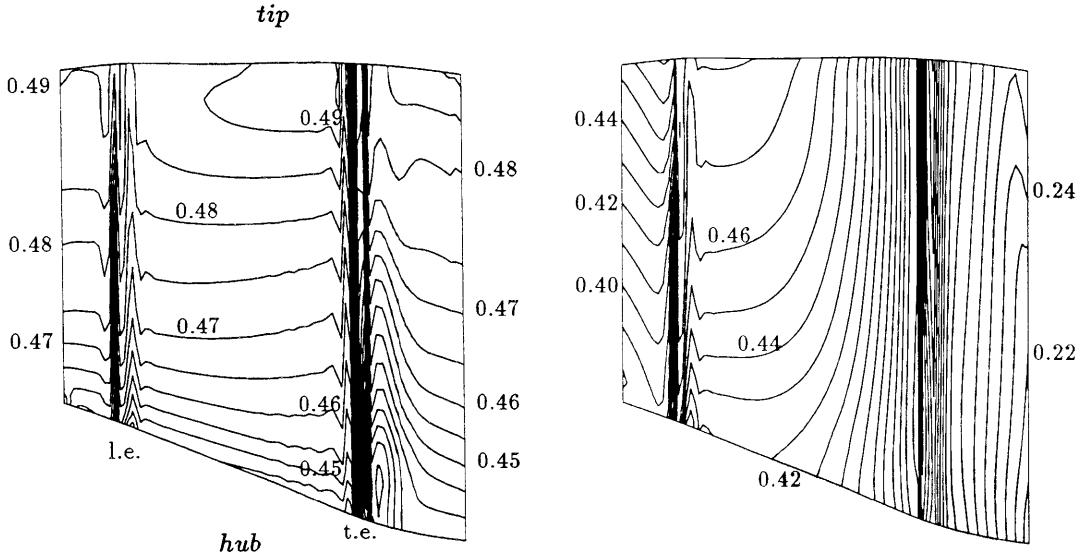

Figure 7.14: Hot case: rotor-relative stagnation pressure ($p_t/p_{t\,inl}$) (left) and static pressure ($p/p_{t\,inl}$) (right) contours on pressure side, and periodic surfaces ahead of leading edge and downstream of trailing edge.

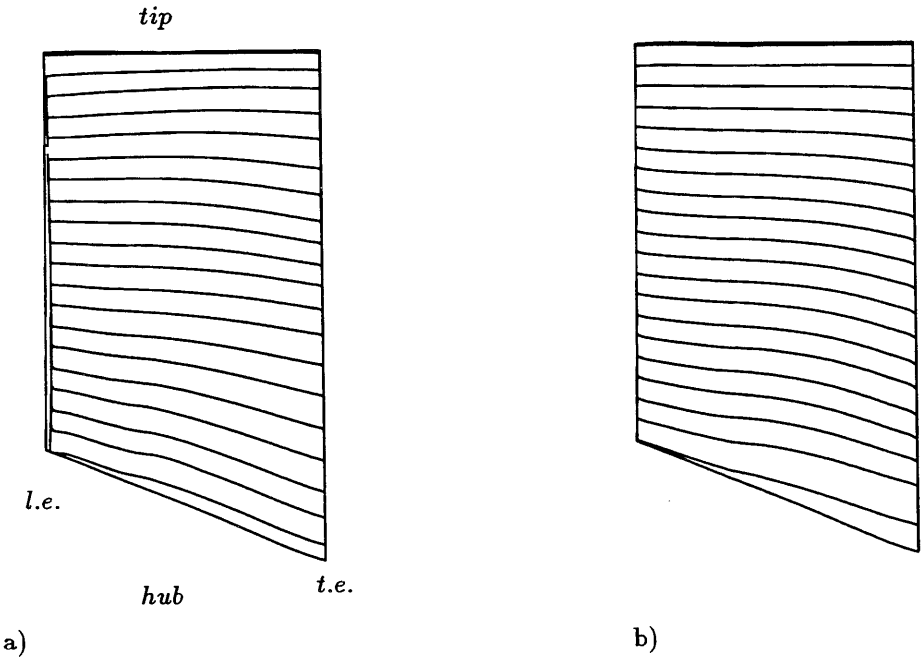

Figure 7.15: Cold case: streamlines on rotor blade; a) pressure side, b) suction side.

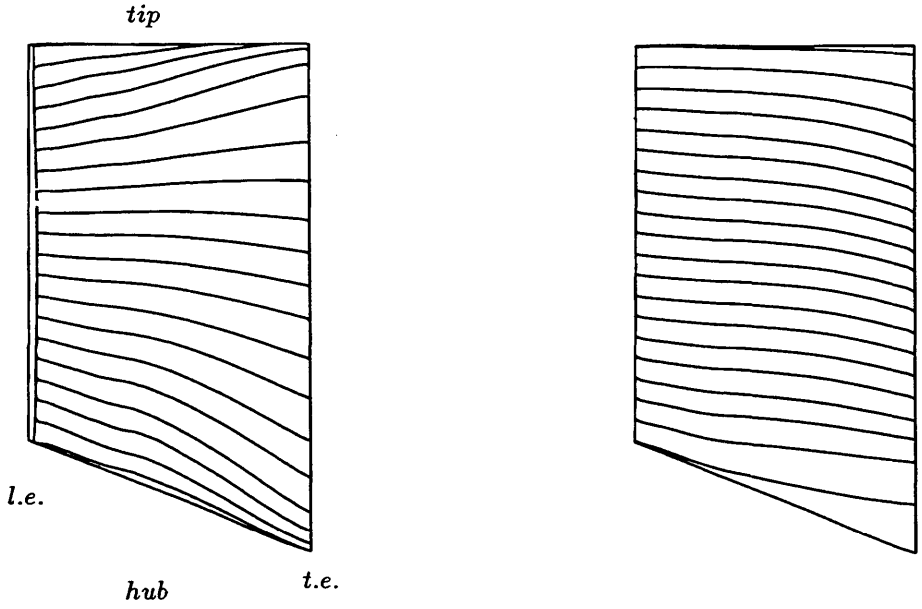

Figure 7.16: Hot case: streamlines on rotor blade; a) pressure side, b) suction side.

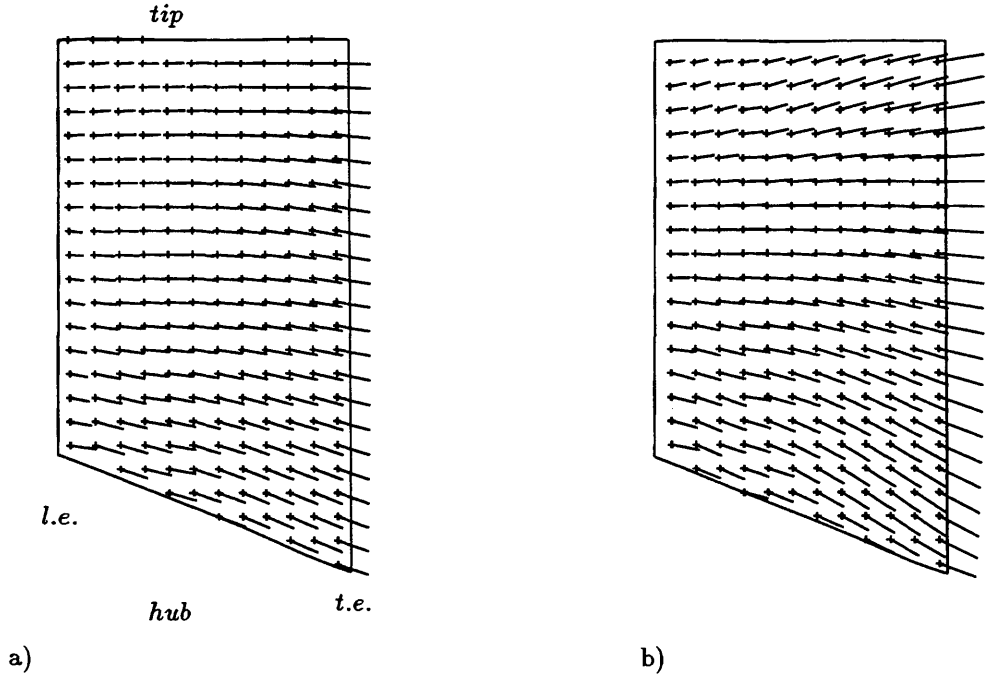

Figure 7.17: Tufts on rotor pressure side; a) cold case, b) hot case.

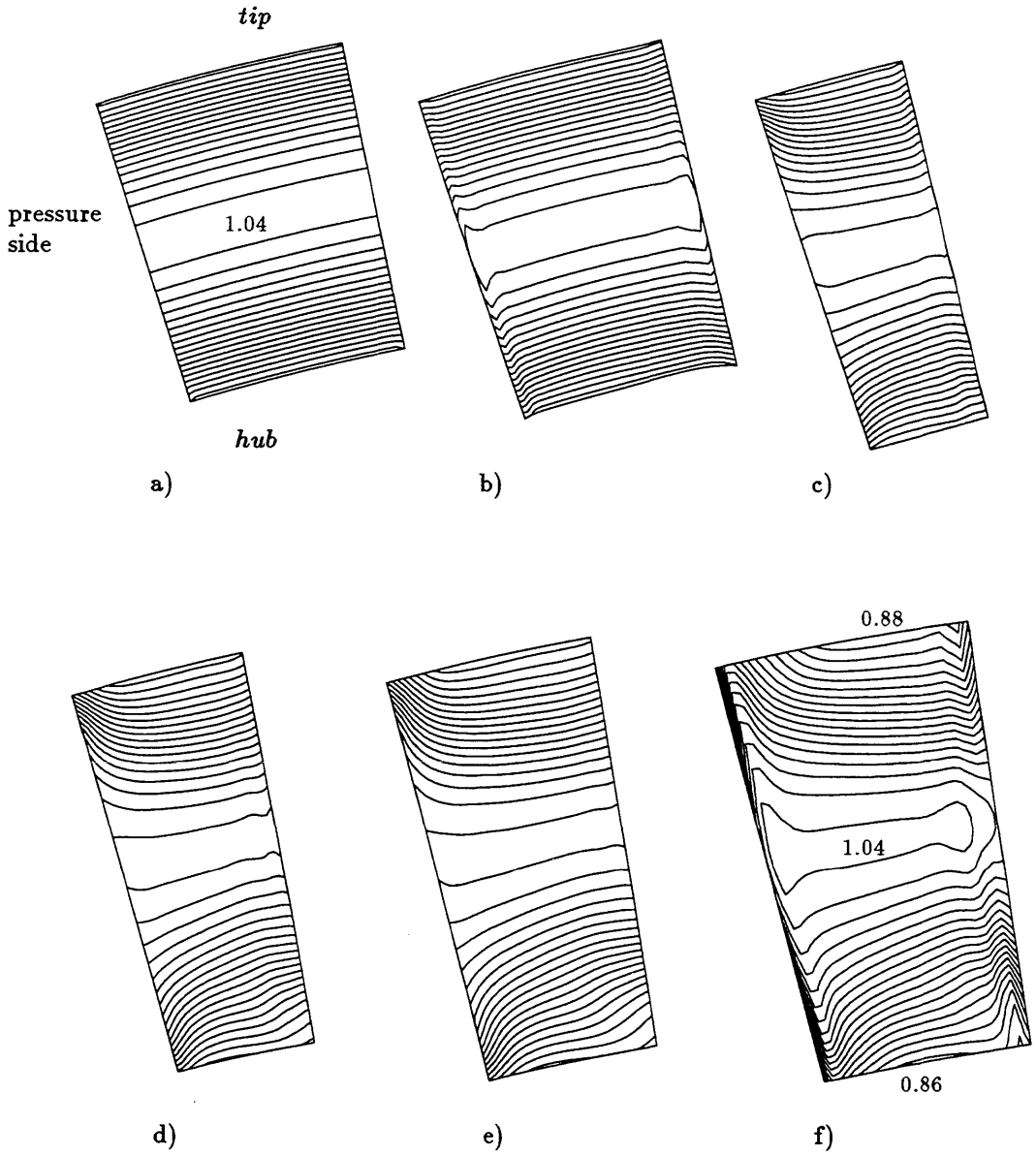

Figure 7.18: Migration of rotor-relative stagnation temperature (T_t/T_{tinl}) in blade-to-blade passage.
a) Inlet, b) leading edge, c), d), e), axial chord = 33%, 66%, 83%, f) trailing edge. Increments = 0.01.

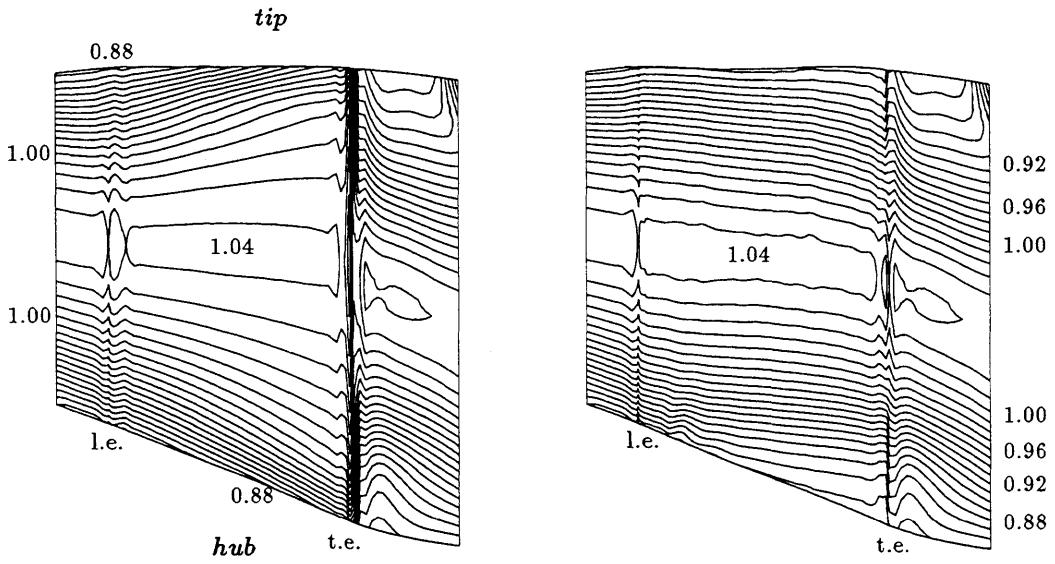

Figure 7.19: Hot case: rotor-relative stagnation temperature contours (T_t/T_{tinl}) on pressure side (left), suction side (right), and periodic surfaces ahead of leading edge and downstream of trailing edge. Increments = 0.01.

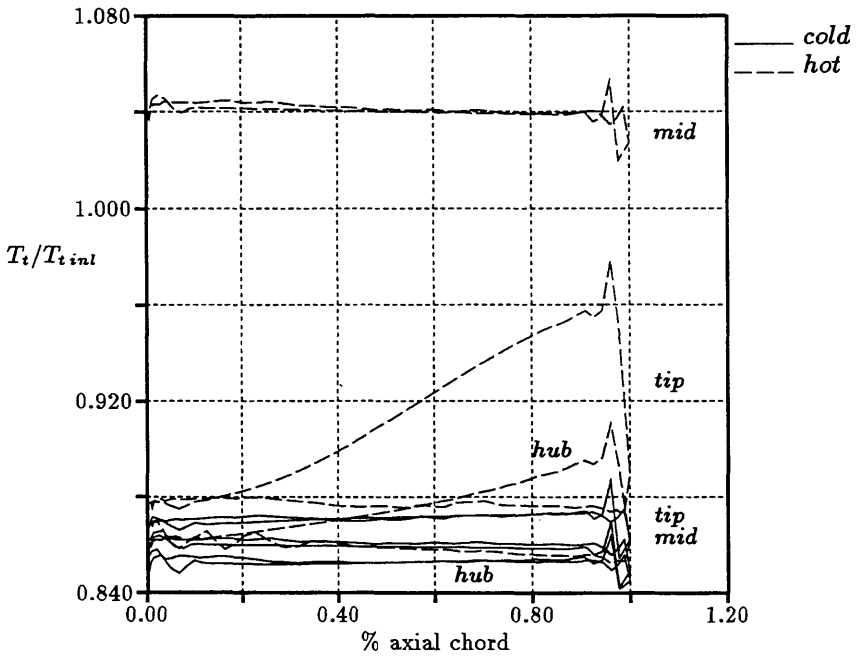

Figure 7.20: Relative stagnation temperature around the rotor blade.

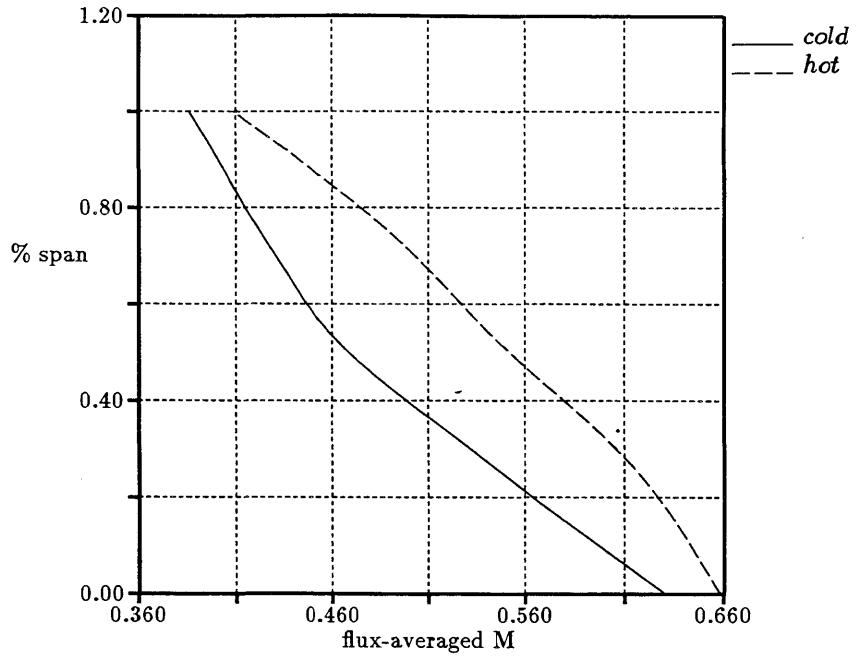

Figure 7.21: Rotor-relative flux-averaged inlet Mach number.

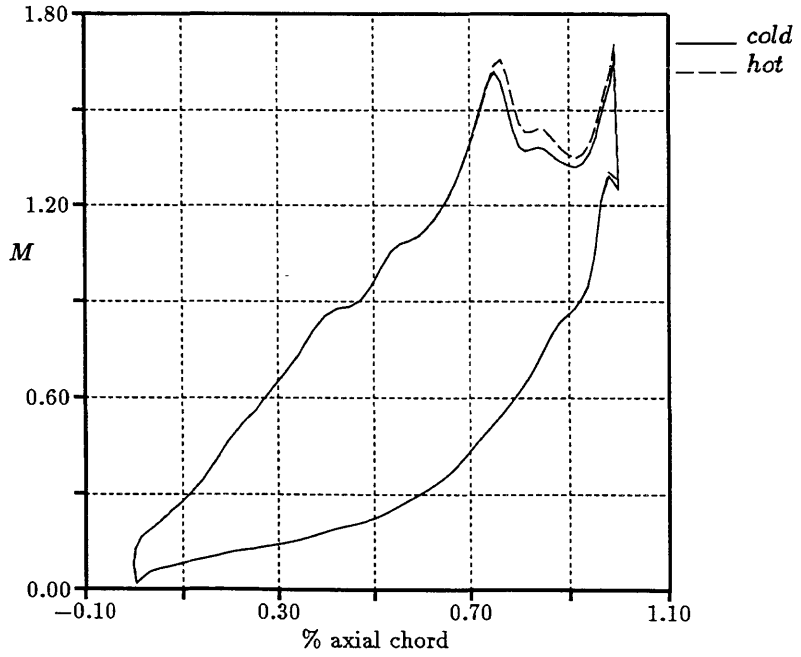

Figure 7.22: Stator Mach number around the blade root.

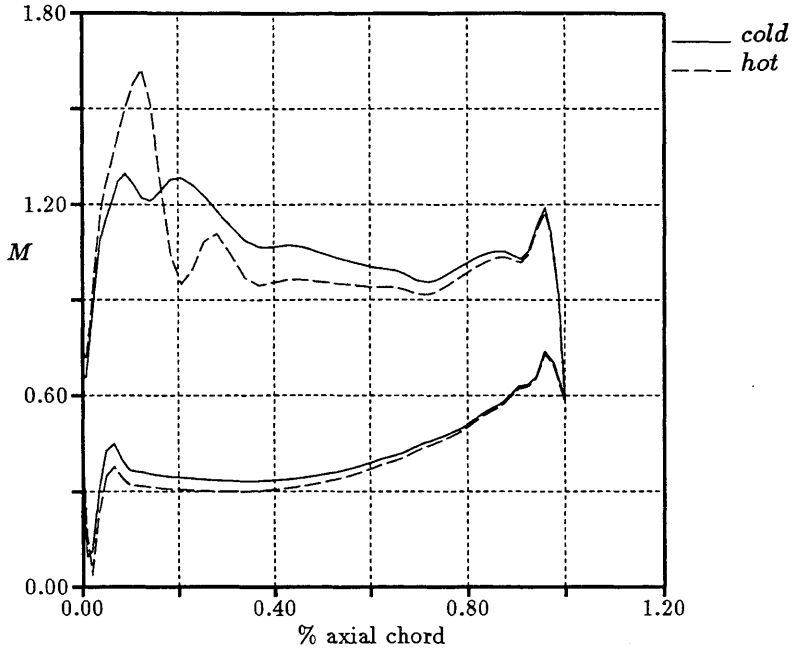

Figure 7.23: Rotor-relative Mach number around the blade root.

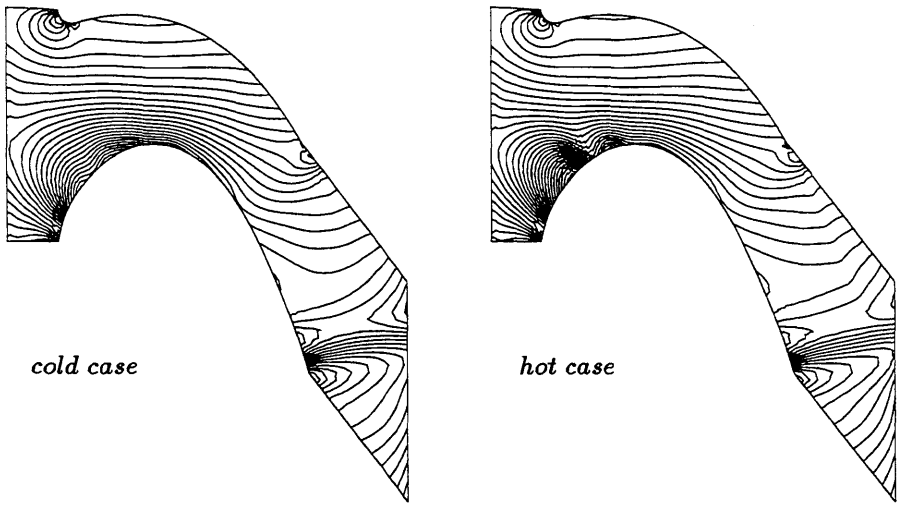

Figure 7.24: Pressure contours ($p/p_{t_{inl}}$) at the rotor root. Increments = 0.01.

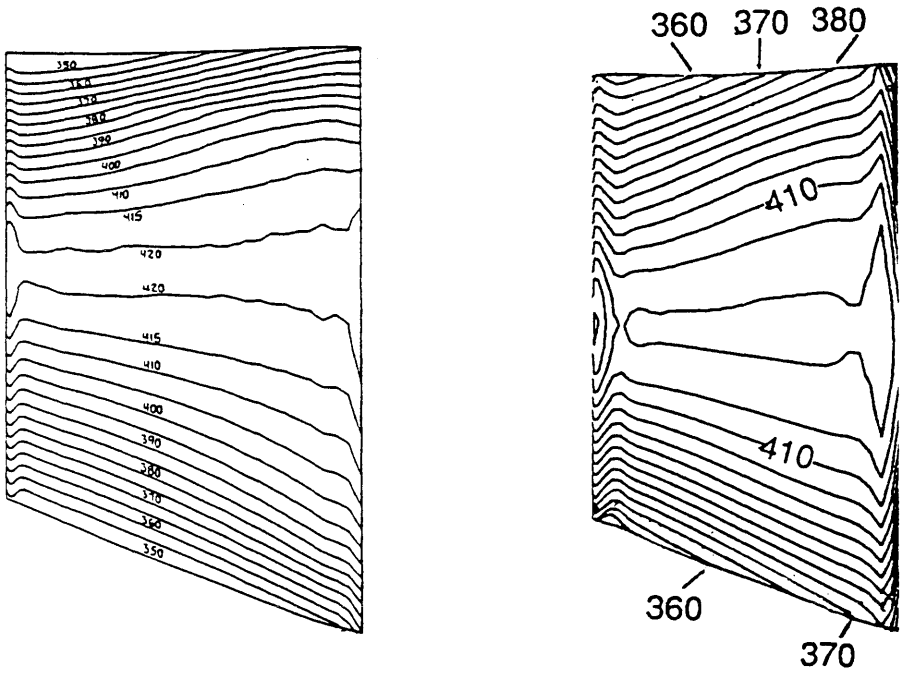

Pappas [84]

Present method

Figure 7.25: Rotor-relative stagnation temperature contours on pressure side with $(T_{t\,mid}/T_{t\,hub})_{inl} = 1.30$.

parameter		$sr80(cold)$	$sr80T\ (hot)$
Ratio of inlet mass flow $\left(\frac{\dot{m}_{cold}}{\dot{m}_{hot}}\right) = 1.061$		-	-
Ratio of inlet stagnation temperature $\left(\frac{T_{t\,mid}}{T_{t\,hub}}\right)$		1.000 (cst)	1.208 (parabolic)
Stator inlet tangential angle	hub	0.0^0	0.0^0
	mid	0.0^0	0.0^0
	tip	0.0^0	0.0^0
Stator outlet tangential angle	hub	72.5^0	72.5^0
	mid	75.2^0	74.9^0
	tip	74.8^0	74.6^0
Rotor-relative inlet tangential angle	hub	50.5^0	51.6^0
	mid	48.8^0	54.3^0
	tip	39.2^0	40.9^0
Rotor-relative outlet tangential angle	hub	-55.2^0	-57.3^0
	mid	-69.2^0	-68.4^0
	tip	-76.6^0	-81.3^0
Stator inlet Mach number	hub	0.15	0.15
	mid	0.13	0.13
	tip	0.13	0.13
Stator outlet Mach number	hub	1.31	1.33
	mid	1.20	1.23
	tip	1.14	1.16
Rotor-relative inlet Mach number	hub	0.63	0.66
	mid	0.47	0.55
	tip	0.39	0.41
Rotor-relative outlet Mach number	hub	1.06	1.05
	mid	1.00	1.01
	tip	0.97	0.96
Rotor Mach number	hub	0.76	0.75
	mid	0.81	0.74
	tip	0.85	0.85
Rotor wheel speed $\left(\frac{\Omega}{c_{t\,inl}/L_{hub}}\right)$		0.097	0.097
Ratio of specific heats γ		1.27	1.27

Table 7.1: Flow parameters for transonic turbine stage with and without inlet stagnation enthalpy gradient.

Chapter 8

Effect of a Stator Embedded Vortex and Temperature Gradient on a Downstream Rotor Flow Field

The appearance of streamwise vorticity downstream of a cascade due to the turning of the vortex filaments of the inlet boundary-layer can be understood by considering the classical secondary flow theory introduced originally by Squire and Winter [102] and Hawthorne [48]. It is also well known that the endwall boundary-layer present in front of a cylinder on a flat plate rolls up into a vortical motion, called the horseshoe vortex due to its shape as it flows on both sides of the cylinder. As discussed by Sieverding [99] in a survey paper, both phenomena are present in turbine blade passages and contribute to the formation of secondary flows. An important point to extract from this survey is that endwall streamsurfaces gradually rotate and develop into what is called a passage vortex, see Figure 8.1. This type of secondary flow has been extensively studied experimentally, see for instance References [6, 76, 71, 79].

The genesis of vorticity in the passage vortex is due to viscous effects. However, the dynamics of the subsequent flow interactions with the downstream rotor is driven primarily by inviscid mechanisms. In addition to shear flow interactions, most of the turbines operate with non-uniformities in the temperature at the inlet. In particular, radial temperature gradients are present at the combustion chamber exit. As discussed in Chapter 7 this generates secondary flow. In that respect, the objective of this chapter

is to investigate the combined effects of thermally and velocity driven secondary flows occurring in a downstream rotor. In an actual engine, two vortices usually of equal an opposite strength are present close to the hub and the tip endwall. For the flow in the first turbine row, this is combined with a radial temperature profile representing cool flow at the endwalls and heated gas at midspan. In this study only one vortex, located at midspan is present and combined with a linear spanwise temperature gradient. This avoids grid resolution issues, which is known to affect numerical solutions of vortical flows. However, the strength of the vortex and the magnitude of the temperature variation are chosen in accordance with experimental observations. Hence, though more academic than the flow discussed in Chapter 7, this case provides an upper bound for the magnitude of a disturbance entering a subsonic high-turning rotor, that combines both a shear flow and a temperature gradient. The analysis of the resulting secondary flow in the rotor (steady and unsteady) is important for several reasons. First, this allows to evaluate the strength of the rotor-relative secondary flow, relative to uniform inlet flow conditions. Second, the comparison of the steady flow solution to the time-average of the unsteady flow shows the effect of the steady-state stator/rotor interface averaging procedure described in Section 5.5. Finally, by setting the temperature gradient to zero, but allowing for the vortex-induced shear flow to enter the rotor, it is possible to reveal which one of the two disturbances, i.e. vortex or temperature gradient, creates a stronger secondary flow.

The generation of the passage vortex itself is not computed in this study. Instead, an analytical model is proposed to define it. The vortex is then inserted at a suitable location in the vane (stator). According to several experimental observations see for instance [99, 76, 71, 79], it is reasonable to assume that the secondary flow develops into a vortical structure in a region close to the trailing edge. Thus, the computational procedure uses a stationary row (vane) which has no blades and in which the inlet boundary corresponds to the trailing edge region of an actual cascade, see Figure 8.2.

In a turbomachine environment the rows consist of multiple blade passages, hence multiple passage vortices are formed due to the turning of the endwall boundary-layer.

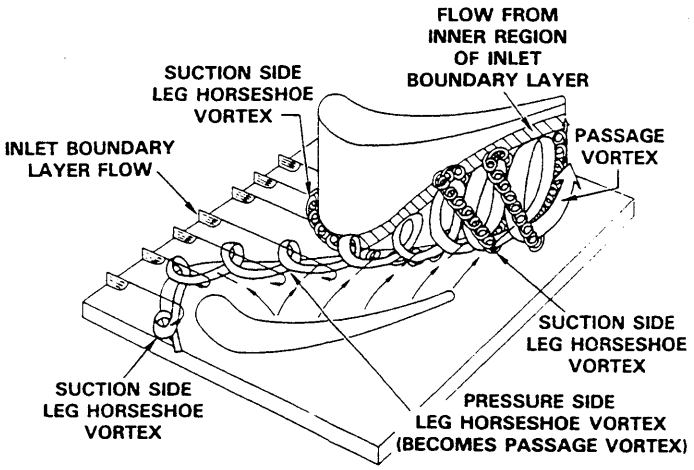

Figure 8.1: Cascade endwall flow structure, from Ref. [94].

The analytical model used for the passage vortices is discussed in Section 8.1. This model assumes that the secondary flows leave the vane row as organized streamwise vortices with combined finite size cores and free vortex structures, which is consistent with the experimental observations of Moore and Adhye [79], and Langston et al. [71]. It is designed to satisfy both periodic and wall boundary conditions.

The stationary row inlet boundary conditions are described in Section 8.2. The entrance velocity and stagnation temperature distributions result as the superposition of the vortical flow onto a uniform flow with a radially linear temperature gradient. These conditions are imposed using the standard 1-D boundary conditions approach. Then in Section 8.3 the unsteady stator/rotor interface boundary conditions are discussed.

The results for both steady and unsteady secondary flow effects in the rotor are discussed in Section 8.4. The unsteadiness is caused by the relative motion between the stationary vane and the moving rotor, while the inlet and exit conditions are kept fixed in time. As mentioned earlier, to understand the effects of the secondary flow, steady-state and time-averaged results with vortex and temperature gradient are compared to the flow results for uniform inlet conditions. This allows to quantify the secondary flow effects in the rotor with respect to the strength of the inlet vortex and the spanwise

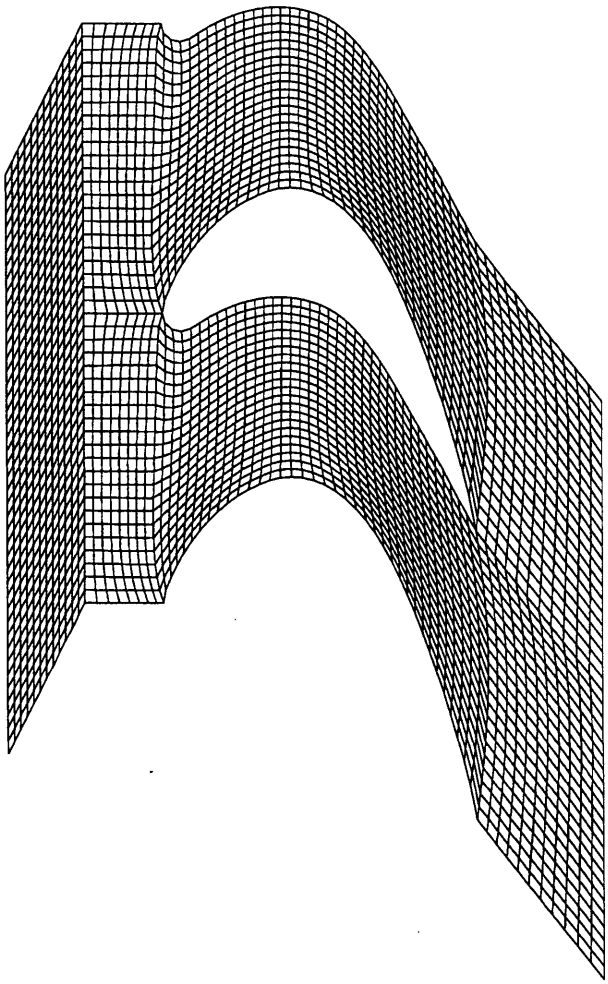

Figure 8.2: Grid geometry and blade $T7$ for vortex-temperature interaction. Vane: $13 \times 23 \times (13)$ nodes, rotor: $57 \times 23 \times (13)$ nodes.

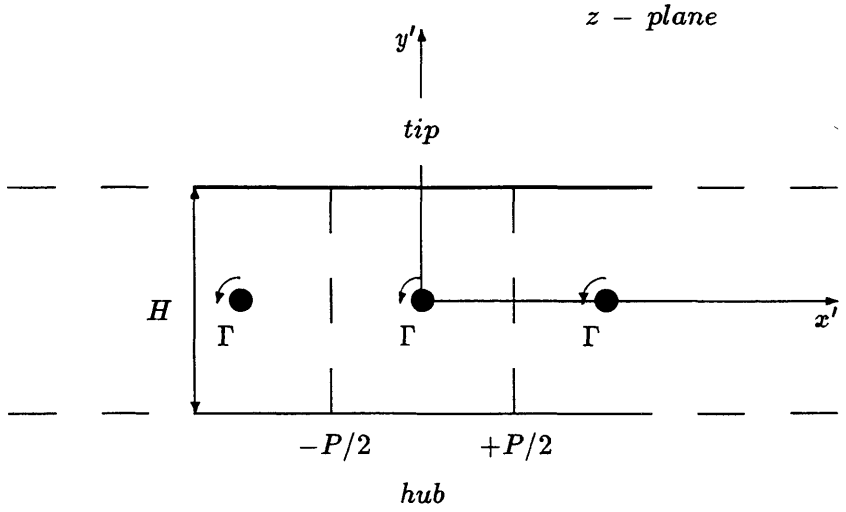

Figure 8.3: Periodic vortices between parallel plates.

temperature variation. Then, the unsteady effects are assessed.

Finally, in Section 8.5, some general conclusions are drawn from this study.

8.1 Passage vortex model

As mentioned earlier, the generation of the passage vortices in the vane is not calculated. Instead a model for these vortices is proposed using conformal mapping and potential theory, see for instance [78, 91]. To ensure correct wall and periodic boundary conditions the model starts by considering a row of periodic vortices, each of them of strength Γ, separated by a horizontal distance P and placed midway between parallel plates. This constitutes the physical ($z = x' + iy'$) plane, see Fig. 8.3. Then, following Milne-Thompson's procedure [78] for a single vortex between parallel planes, the velocity field induced by an infinite row of vortices is found by using the transformation $\zeta = i\, e^{\pi z/H}$. This transformation maps the strip between the plates on the upper half of the ($\zeta = \xi + i\eta$) plane, see Fig. 8.4. The top wall ($y' = H/2$) is mapped into the segment

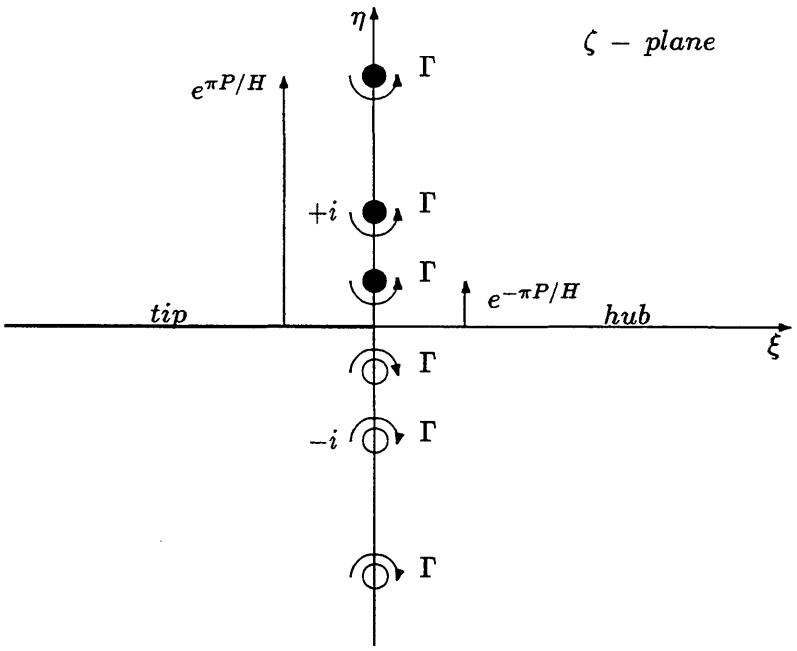

Figure 8.4: Periodic and image vortices in transformed complex plane, $\zeta = i\,e^{\pi z/H}$.

($\xi < 0, \eta = 0$) whereas the bottom wall ($y' = -H/2$) corresponds to ($\xi > 0, \eta = 0$). The vortices located in the physical plane at $z = nP$, $n = 0, \pm 1, \pm 2, \ldots$ correspond to $\zeta = i\,e^{\frac{nP\pi}{H}}$ and are all located in the ($\eta > 0$) portion of the ζ plane. Thus, to impose the wall tangency condition, image vortices of strength $-\Gamma$ are now placed at $\zeta = -i\,e^{\frac{nP\pi}{H}}$, $n = \pm 1, \pm 2, \ldots$.

The complex potential of a line vortex located at the origin is defined as $i\Gamma \log \zeta$. By superposition, the complex potential $G(\zeta)$ of all the vortices in the ζ plane is found by summing the potential of all the individual vortices, i.e.

$$G(\zeta) = i\Gamma \left(\sum_{n=-\infty}^{+\infty} \log(\zeta - ie^{\frac{nP\pi}{H}}) - \sum_{n=-\infty}^{+\infty} \log(\zeta + ie^{\frac{nP\pi}{H}}) \right). \tag{8.1}$$

After some algebra and noticing that the complex potential $F(z)$ in the z plane can be written as

$$F(z) = F(z(\zeta)) \equiv G(\zeta), \tag{8.2}$$

the following expression is obtained.

$$F(z) = i\Gamma \sum_{n=-\infty}^{+\infty} \log\left(\tanh(\frac{\pi}{2H}(z-nP))\right). \tag{8.3}$$

The complex velocity $w(z)$ in the physical plane is defined as

$$w(z) = \frac{dF}{dz} = u' - iv'. \tag{8.4}$$

Thus,

$$w(z) = i\Gamma\frac{\pi}{H} \sum_{n=-\infty}^{+\infty} \frac{1}{\sinh(\frac{\pi}{H}(z-nP))}, \tag{8.5}$$

from which the u' and v' velocity components can be found as

$$u' = \Gamma\frac{\pi}{H} \sum_{n=-\infty}^{+\infty} \frac{\sin(\frac{\pi}{H}y')\cosh(\frac{\pi}{H}(x'-nP))}{(\sin(\frac{\pi}{H}y')\cosh(\frac{\pi}{H}(x'-nP)))^2 + (\cos(\frac{\pi}{H}y')\sinh(\frac{\pi}{H}(x'-nP)))^2} \tag{8.6}$$

$$v' = \Gamma\frac{\pi}{H} \sum_{n=-\infty}^{+\infty} \frac{-\cos(\frac{\pi}{H}y')\sinh(\frac{\pi}{H}(x'-nP))}{(\sin(\frac{\pi}{H}y')\cosh(\frac{\pi}{H}(x'-nP)))^2 + (\cos(\frac{\pi}{H}y')\sinh(\frac{\pi}{H}(x'-nP)))^2} \tag{8.7}$$

This velocity field is now modified using Lamb's correction [70] in order to define vortices with finite size cores, i.e.

$$u_v = \left(1-e^{-\left(\frac{(x')^2+(y')^2}{a^2}\right)}\right) \times Eq.(8.6), \tag{8.8}$$

$$v_v = \left(1-e^{-\left(\frac{(x')^2+(y')^2}{a^2}\right)}\right) \times Eq.(8.7), \tag{8.9}$$

in which a is the vortex core radius and the subscript $_v$ denotes a velocity induced by the vortices.

8.2 Inlet conditions

The stationary row consists of a truncated stator in which no blades are present, see Figure 8.2. It models the aft part of an actual row extending from the trailing edge to

the interface. The axis of rotation of the vortices is aligned with the vane inlet uniform flow denoted u_∞, see Figure 8.5. The inlet velocity profile is found by superposing u_∞, which is oriented at an angle α_∞ with respect to the x direction, on the vortical flow described in the above section. Thus in a Cartesian coordinate system the inlet velocity components are defined as

$$\begin{aligned} u_{inl} &= u_\infty \cos\alpha_\infty + u_v \sin\alpha_\infty, \\ v_{inl} &= u_\infty \sin\alpha_\infty - u_v \cos\alpha_\infty, \\ w_{inl} &= v_v. \end{aligned} \tag{8.10}$$

For this particular application, the inlet boundary condition is implemented according to the 1-D boundary condition theory, see Appendix D. It is briefly outlined here. One wishes to study the effect of the vortical motion introduced as an inlet condition, and the requirement that the inlet temperature varies linearly from the hub to the tip, onto the downstream moving rotor. Hence, local values of the velocity and stagnation temperature are implemented as inlet boundary conditions at the time level $n+1$ in the Lax-Wendroff algorithm.

$$\begin{aligned} (|\vec{V}_{inl}|)^{n+1} &= |\vec{V}_{inl}|, \\ (\alpha_\theta)^{n+1} &= \alpha_{\theta\, inl}, \\ (\alpha_R)^{n+1} &= \alpha_{R\, inl}, \\ (h_t)^{n+1} &= h_{t\, inl}. \end{aligned} \tag{8.11}$$

$|\vec{V}_{inl}| = \sqrt{u_{inl}^2 + v_{inl}^2 + w_{inl}^2}$, α_θ and α_R are defined in Section 2.3. This is implemented using the same Newton-Raphson procedure as in Section D.1. However, instead of imposing average inlet entropy, average radial and tangential angles and average stagnation temperature at the inlet, local values of the velocity profile as given by the passage vortex model and the temperature profile are imposed. This is achieved by driving to zero

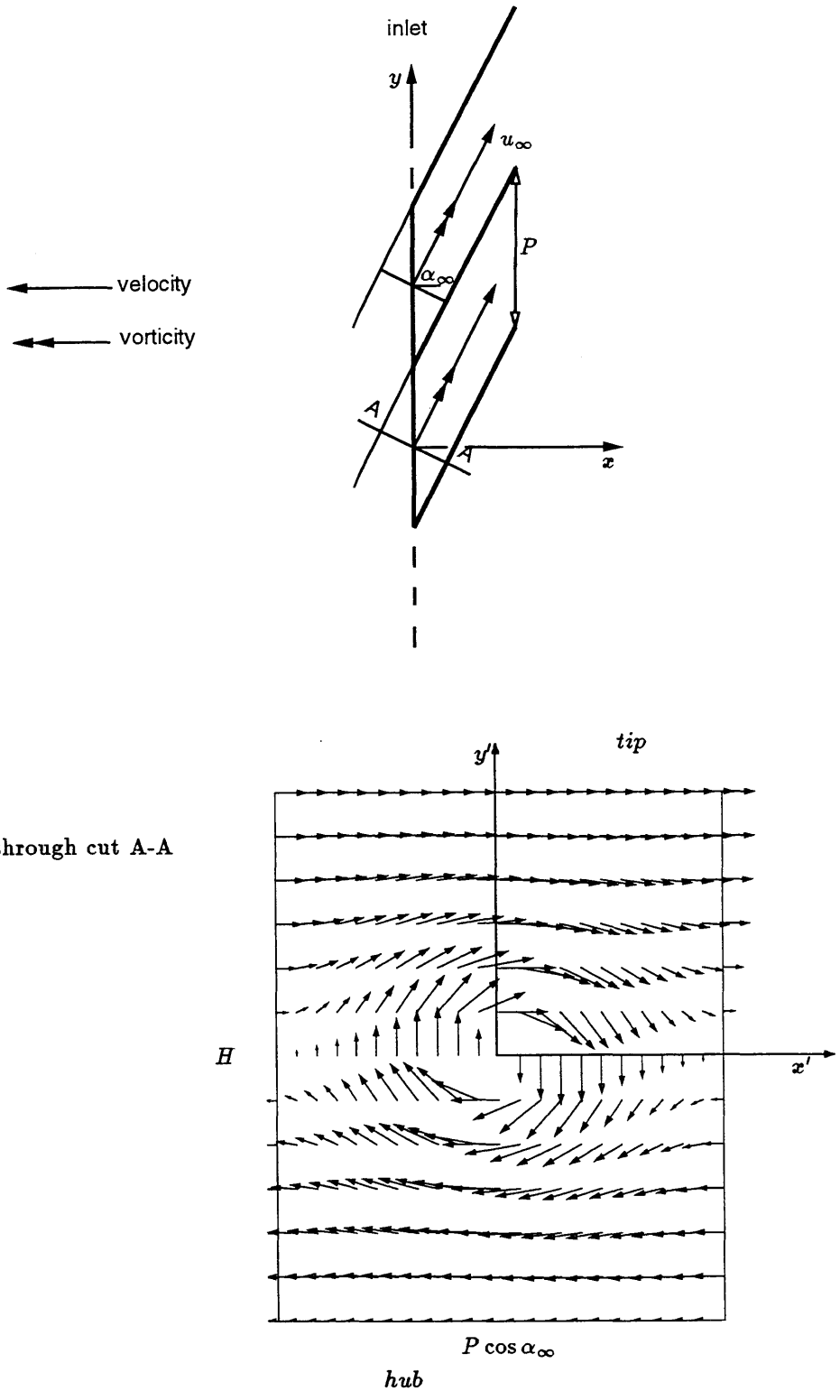

Figure 8.5: Row of vortices at vane inlet.

the following four residuals.

$$\begin{aligned} R_1^n &= \rho^n c^n (u_x^n - |\vec{V}_{inl}^n|), \\ R_2^n &= \rho^n c^n \left(u_\theta^n - |\vec{V}_{inl}^n| \sin(\alpha_{\theta inl}) \sin(\alpha_{R inl}) \right), \\ R_3^n &= \rho^n c^n \left(u_R^n - |\vec{V}_{inl}^n| \cos(\alpha_{R inl}) \right), \\ R_4^n &= \rho^n (h_t^n - h_{t inl}). \end{aligned} \tag{8.12}$$

The rest of the procedure is very similar to that given in Section D.1. Using the 1-D characteristics theory, the changes in the incoming characteristic variables are obtained by linearizing the residuals from the current time level through a one-step Newton-Raphson procedure.

$$\begin{pmatrix} R_1 \\ R_2 \\ R_3 \\ R_4 \end{pmatrix}^{n+1} \simeq \begin{pmatrix} R_1 \\ R_2 \\ R_3 \\ R_4 \end{pmatrix}^{n} + \left(\frac{\partial(R_1, R_2, R_3, R_4)}{\partial(\phi_1, \phi_2, \phi_3, \phi_4)} \right)^n \begin{pmatrix} \delta\phi_1 \\ \delta\phi_2 \\ \delta\phi_3 \\ \delta\phi_4 \end{pmatrix} = 0. \tag{8.13}$$

The values of the Jacobian matrix are found to be

$$J = \frac{\partial(R_1, R_2, R_3, R_4)}{\partial(\phi_1, \phi_2, \phi_3, \phi_4)} = \begin{pmatrix} 0 & 0 & 0 & \frac{1}{2} \\ 0 & 1 & 0 & 0 \\ 0 & 0 & 1 & 0 \\ \frac{1}{\gamma - 1} & \frac{v}{c} & \frac{w}{c} & \frac{1}{2}\left(1 + \frac{u}{c}\right) \end{pmatrix}. \tag{8.14}$$

Thus, the following changes in the incoming characteristics are found.

$$\begin{pmatrix} \delta\phi_1 \\ \delta\phi_2 \\ \delta\phi_3 \\ \delta\phi_4 \end{pmatrix} = -J^{-1} \begin{pmatrix} R_1 \\ R_2 \\ R_3 \\ R_4 \end{pmatrix}. \tag{8.15}$$

The outgoing fifth characteristic variable is given by the Lax-Wendroff algorithm,

$$\delta\phi_5 = \delta\phi_{5LW}. \tag{8.16}$$

The combined five characteristic changes calculated in physical space are then trans-

formed into changes in the primitive variables, and hence in conservation variables. This is done for all inlet nodes before the flow field can be updated. Notice that with this procedure, the inlet stagnation temperature is imposed.

8.3 Unsteady stator/rotor interface

The algorithm developed for transferring information through the stator/rotor interface while the rotor is moving is valid for equal pitches only. Moreover, the tangential as well as the radial nodes distribution has to be the same on both sides of the interface. At each time-step, the basic procedure uses the 1-D characteristics to update every stator and every rotor node that belongs to the interface. The local 1-D characteristic changes at the stator outflow and the rotor inflow are found as follows.

$$\begin{pmatrix} \Delta\phi_1 \\ \Delta\phi_2 \\ \Delta\phi_3 \\ \Delta\phi_4 \\ \Delta\phi_5 \end{pmatrix} = \begin{pmatrix} -\bar{c}^2 & 0 & 0 & 0 & 1 \\ 0 & 0 & \bar{\rho}\bar{c} & 0 & 0 \\ 0 & 0 & 0 & \bar{\rho}\bar{c} & 0 \\ 0 & \bar{\rho}\bar{c} & 0 & 0 & 1 \\ 0 & -\bar{\rho}\bar{c} & 0 & 0 & 1 \end{pmatrix} \begin{pmatrix} \rho_s - \rho_r \\ u_{xs} - u_{xr} \\ u_{\theta s} - u_{\theta r} - U_w \\ u_{Rs} - u_{Rr} \\ p_s - p_r \end{pmatrix}, \tag{8.17}$$

where the subscripts $_s$ and $_r$ represent stator- and rotor-relative quantities, respectively. Because of the use of relative flow variables, the rotor wheel speed $U_w = \Omega R$ has to be introduced. Notice that in Equation (8.17) local primitive variables are used instead of the flux-averaged ones of the steady stator/rotor interface boundary condition (Section 5.5). According to the direction of propagation of the characteristics, the stator outflow change is

$$\delta\phi_5 = -\Delta\phi_5 = \bar{\rho}\bar{c}(u_{xs} - u_{xr\,int}) - (p_s - p_{r\,int}), \tag{8.18}$$

while at the rotor inlet the changes are

$$\delta\phi_1 = \Delta\phi_1 = -\bar{c}^2(\rho_{s\,int} - \rho_r) + (p_{s\,int} - p_r),$$

$$\delta\phi_2 = \Delta\phi_2 = \bar{\rho}\bar{c}(u_{\theta s\,int} - u_{\theta r} - U_w),$$

$$\delta\phi_3 = \Delta\phi_3 = \bar{\rho}\bar{c}(u_{Rs\,int} - u_{Rr}),$$

$$\delta\phi_4 = \Delta\phi_4 = \bar{\rho}\bar{c}(u_{xs\,int} - u_{xr}) + (p_{s\,int} - p_r). \tag{8.19}$$

The subscript $_{int}$ represents an interpolated value. At a stator outflow node, the two closest rotor-relative nodes are used to linearly interpolate primitive variable values needed to calculate the changes. Similarly, for a rotor inflow node, the two closest stator nodes are used. The outgoing characteristic changes are taken from the changes calculated by the Lax-Wendroff algorithm. The combined five characteristic changes on both sides of the interface are then converted back to primitive and finally conservative variables before the flow field is updated.

Note that this procedure does not guarantee flux conservation across the interface. However, in all the simulations presented in this thesis this has not posed a problem. The maximum instantaneous error in mass flow across the interface is only about six times greater than the corresponding error in a steady-state computation. Unsteady convergence is reached when a periodic solution has been obtained. This typically takes ten rotor-passage periods, which is comparable to the number of periods needed for UNSFLO [34][1] to converge. This stator/rotor interface algorithm is also used in the unsteady computation of Chapter 9.

8.4 Results

The 3-D linear partial-vane/rotor geometry used to investigate the effects of the vortex-temperature secondary driven flow in a turbine stage is shown in Fig. 8.2. The rotor geometry, made of $T7$ blades, is similar to the 3-D linear cascade tested in Section 6.2. The 3-D mesh was generated by stacking along the span 13 of the planes shown in Fig. 8.2. The solidity is 0.94 and the aspect ratio 0.5. In order to distinguish one

[1]UNSFLO is a 2-D solver for unsteady inviscid flows in turbomachinery, designed to ensure flux conservation in both steady and unsteady modes.

endwall from the other and to aid the discussion of the results, one endwall is referred to as the hub and the other as the tip. It should be pointed out that this definition is arbitrary, i.e. for the case examined here (untwisted blades, absence of Coriolis and centrifugal effects), '*hub*' can be replaced by '*tip*' and conversely in all the figures. This means that for an observer looking downstream the cascade with the rotor moving from right to left the set up of the inlet conditions can be considered from two viewpoints: a clockwise vortex (see Fig. 8.5) combined with higher temperature at the hub than at the tip (see Fig. 8.6) *or* a counter-clockwise vortex with lower temperature at the hub compared to the tip. The results are explained according to the former point of view.

Table 8.1 lists the flow parameters for three subsonic cases. Note that the Mach numbers and angles represent tangentially (y direction) flux-averaged quantities. The steady-state and time-averaged results of computations performed with inlet vortex and radial temperature gradient are given in the first two columns. For comparison, the third column lists the results of a computation with uniform inlet conditions, i.e. no vortex and constant temperature. The ratio of uniform to vortex velocity was chosen in accordance with the experimental observations of Moore and Adhye [79] and Langston et al. [71]. The inlet temperature profile consists of a linear variation from hub to tip with its lowest value at the tip. The midspan value matches the temperature of the uniform flow. The inlet uniform Mach number, inflow angle and the rotor wheel Mach number were chosen to achieve the design rotor-relative inflow Mach number and angle in the absence of vortex and temperature variation. Since the uniform inlet conditions solution represents a 2-D flow, any radial flow induced by the vortex-temperature disturbance is considered a secondary flow.

The steady-state results are discussed first. The flow in the stator frame of reference is similar to a swirling flow in a duct. As a result of the helical type shape of the streamlines, the surfaces of constant stagnation temperature are gradually distorted from the inlet to the interface, see Figures 8.6 and 8.7.

As discussed in Chapter 5, tangentially flux-averaged values are transferred through

the steady-state stator/rotor interface. Thus, in the rotor frame of reference the vortex is represented only in an average sense. For instance, the rotor-relative inflow stagnation pressure, tangential angle and Mach number are plotted versus span in Figures 8.8, 8.9 and 8.10, respectively. The vortex-temperature disturbance produces a change up to 2.4% of the stagnation pressure, which represents 27.5% of the vane exit dynamic head (based on a Mach number of 0.37). The variations in tangential angles from hub to tip are very large (up to 20^0 relative to the uniform flow solution), which is a striking result, considering the fact that the ratio of uniform flow to maximum vortex velocity is almost 3. Hence, the vortex-temperature disturbance is severe. Notice however that the rotor-relative midspan inflow angle is close to the value calculated in the case of uniform conditions. Figure 8.9 indicates that the hot hub fluid is oriented more towards the pressure side of the rotor, whereas the cold tip fluid moves towards the suction side as it flows through the rotor. Thus, in general, one would expect to see hot hub fluid moving across the channel and then up along the blade pressure side and tip fluid cooling the blade suction side. This type of segregation effect is similar to that observed in Chapter 7, though the resulting secondary flow is quite different. Stagnation temperature contours on several blade-to-blade and hub-to-tip grid surfaces are represented in Fig. 8.11 for different axial locations.

The introduction of the vortex and the radial temperature variation induces a non-uniform stagnation pressure distribution in both the stator and the rotor frame of reference. The vortex core region located at midspan shows up as a deficit in total pressure, see Figure 8.8. The radial temperature variation introduces a spanwise asymmetry in the total pressure distribution. The higher density of the cold tip fluid contributes to the increase of rotor-relative stagnation pressure at the tip compared to the hub. As a consequence of this, a radial flow that was non-existent in the case of uniform inlet conditions occurs in the rotor. As in Section 7.3, the results can be best understood by utilizing the secondary flow theory and in particular the relations for the growth of streamwise vorticity derived by Hawthorne [49] and Horlock et al. [69]. In Reference [68] Lakshminarayana used those relations to derive an approximate method to calculate the rotation of isothermal surfaces in a turbine nozzle and in a rotor.

In the absence of body forces, the Helmholtz equation that governs the vorticity $\vec{\omega}$, $\vec{\omega} = \nabla \times \vec{V}$, for an inviscid compressible flow is given by

$$\frac{D}{Dt}\left(\frac{\vec{\omega}}{\rho}\right) = \left(\frac{\vec{\omega}}{\rho} \cdot \nabla\right) \vec{V} - \frac{1}{\rho}\nabla\left(\frac{1}{\rho}\right) \times \nabla p, \tag{8.20}$$

where D/Dt stands for the particular derivative. The first term on the right-hand side of Equation (8.20) represents the tilting and the stretching of the vortex filaments. The second term involving the density and pressure gradients arises in non-barotropic situations. It represents the production of vorticity due to the moment of pressure forces about the center of mass of a fluid particle. In this particular application both terms are important, as discussed later on.

To explain the rotor-relative secondary flow it is useful to write down the steady-state streamwise component of Equation (8.20) in generalized coordinates.

$$\begin{aligned} \frac{\partial}{\partial s}\left(\frac{\omega_s}{\rho W}\right) &= \frac{2\omega_n}{\rho W \sigma} + \frac{1}{\rho^2 W^2 T}\frac{\partial T}{\partial b}\frac{\partial p}{\partial n} \\ &= \frac{2\omega_n}{\rho W \sigma} - \frac{1}{\rho T \sigma}\frac{\partial T}{\partial b} \end{aligned} \tag{8.21}$$

Notice that for the 3-D spanwise linear partial-vane/rotor geometry tested here, the wheel speed is uniform, hence the relative vorticity equals the absolute vorticity. Equation (8.21), taken from Reference [55] provides an expression for the development of secondary vorticity along the relative streamline. Using intrinsic coordinates, the vorticity is written as

$$\vec{\omega} = \hat{s}\omega_s + \hat{n}\omega_n + \hat{b}\omega_b, \tag{8.22}$$

where ω_s, ω_n and ω_b are the components of vorticity in the streamwise ($\hat{s}$), principal normal ($\hat{n}$) and binormal ($\hat{b}$) directions, respectively, see Figure 8.12. Using these coordinates it can be shown that

$$\omega_n = \frac{\partial W}{\partial b}, \tag{8.23}$$

and

$$\omega_b = -\frac{\partial W}{\partial n} + \frac{W}{\sigma}, \tag{8.24}$$

where σ is the radius of curvature of the streamline. Equation (8.21) can also be written as a function of stagnation pressure variation only, [49, 55].

$$\frac{\partial}{\partial s}\left(\frac{\omega_s}{\rho W}\right) = \frac{2}{\rho \rho_t W^2 \sigma}\frac{\partial p_t}{\partial b}. \tag{8.25}$$

As seen in Figure 8.5, the vane inlet vorticity is aligned with the freestream, i.e. $\omega_n = 0$, and is essentially concentrated at midspan. Notice the contrast with the case of Chapter 7, where the vorticity in the stator frame is directed along the principal normal. In the rotor frame of reference, the inlet vorticity can be decomposed into a streamwise (ω_s) and a normal (ω_n) component, see Fig. 8.13. Then, as indicated by Equation (8.21), the streamwise vorticity is intensified (or weakened) by two terms.[2] The first contribution arises from the turning of the inlet normal vorticity through the rotor and is related to the classical Squire and Winter [102] expression for secondary vorticity in a duct. The second contribution is due to the radial temperature gradient which has been introduced without significantly affecting the pressure. Hence, the last term of Equations (8.20) and (8.21) contributes to the generation of vorticity, and secondary flow in particular.

However, as noticed by Hawthorne [49, 50, 51] and illustrated by Equation (8.25), the essential quantity to be considered for secondary flow is the gradient in stagnation pressure. This means that thermally driven secondary flows occur only when associated by gradients in Mach number and entropy such that the stagnation pressure is not constant.

The rotor-relative stagnation pressure on both the suction and the pressure side of the blade is plotted in Figures 8.14 and 8.15, respectively. Relative to the case of uniform flow conditions, the blade stagnation pressure gradient is relevant because it produces a pressure gradient which forces fluid of different stagnation temperatures to move radially. From Figures 8.14 and 8.15 the following trends are obtained. On the

[2] In the stator frame, absolute velocity V and absolute stagnation pressure are implied in the above equations.

suction side $\frac{\partial p_t}{\partial z} > 0$ from the leading edge to the crown and then stays mostly constant. On the suction side $\frac{\partial p_t}{\partial z} \approx 0$ from leading edge to midchord. Then, in the aft part of the blade $\frac{\partial p_t}{\partial z} < 0$ from hub to midspan whereas $\frac{\partial p_t}{\partial z} > 0$ from midspan to tip. Consequently, on the suction side midspan flow is expected to move towards the hub. On the pressure side however, radial flow occurs mainly in the second part of the blade and consists of hot hub fluid and cold tip fluid moving towards midspan. This is illustrated in Figures 8.16 and 8.17 for the suction and the pressure side of the blade, respectively.

From the midspan blade-to-blade pressure contours plotted in Figure 8.18 one can infer that the pressure gradients are very small in magnitude in the first part of blade pressure side and in the aft part of the suction side. Thus, the contribution of the temperature-pressure term (of Eq. (8.21)) to the secondary flow is likely to be small in these regions. Also, as a consequence of the velocity/vorticity triangle plotted in Figure 8.13, where the absolute vorticity is aligned with the freestream, the rotor inlet normal vorticity component is small and so the growth of secondary vorticity in the first 40 %, say, of the blade pressure side in small too. As seen in Figure 8.17 and compared to the radial flow in the second part of the blade, the secondary flow is very weak in this area (a factor 6 in the velocity magnitude).

The secondary radial flow on the blade is best represented by the streamlines, see Figures 8.19 and 8.20. Secondary flow does affect both heat transfer and growth of boundary-layer. For instance the surface contours of total temperature are important in assessing the heat loads. Figure 8.21 indicates that large temperature gradients occur at the root of the blade on the suction side. On the pressure side, see Fig. 8.22, the temperature gradients are large in the aft portion of the blade at midspan and at the trailing edge. Sharma and Graziani [95] analyzed the effect of endwall flow on the blade suction surface midheight boundary-layer development in a turbine cascade. The secondary flow vortex associated with the endwall flow generates cross-flow that drives endwall gas towards midspan. In particular they showed that the penetration height of the separation streamline can be used to estimate the cross-flow velocity profiles on the blade surface. As the strength of the secondary vortex increases, the penetration

height of the separation line gets larger. This information is then used to assess the influence of the secondary flow on the aerodynamics and heat transfer at midspan. For instance, they showed that the cross-flow increases the thickness of the boundary-layer, thus increasing the midheight losses, decreases the Reynolds shear stress, skin friction and Stanton number.

The distortion of the isothermal surfaces, as seen in Fig. 8.11, can be explained from the cross-flow pattern. Under the influence of the initial streamwise vorticity and high incidence angle, hot hub fluid is gradually shifted across the channel from suction to pressure side. It then moves up along the blade pressure side towards midspan. This allows colder midspan-tip fluid to migrate down the blade suction side. In addition, non-barotropic effects cause cold tip gas to also move towards midspan on the blade pressure side. As the two streams converge they are deflected normal to the blade and roll-up into a secondary vortex which is then convected down the rotor passage. Its formation occurs in a region close to the trailing edge and is highlighted by the circular stagnation temperature contours plotted in Fig. 8.11.

Another numerical simulation involving only the vortex but no stagnation temperature variation was actually performed, see Figures 8.23 and 8.24. The results indicate that the same secondary flow pattern occurs because the shape of the stagnation pressure distribution is similar to the one of Figure 8.8. Because of the lack of non-barotropic effect in the contribution of streamwise vorticity, the separation line on the pressure side is moved above midspan, instead of below as in Figure 8.20. In this case, the magnitude of the radial variation in rotor-relative inlet stagnation pressure is decreased. For a combined vortex-temperature disturbance it represents a maximum of 48% of the rotor inlet dynamic head (based on a Mach number of 0.28), which compares to 36% for the vortex alone. Hence, the vortex is responsible for most of the rotor-relative secondary flow.

Figure 8.25 is a 3-D representation of the vane/rotor blade passage with five near wall streamtubes. The expansion of the streamtubes close to the stagnation point on

the pressure side of the leading edge is clearly visible, as well as the rapid contraction as they concentrate towards midspan and the flow accelerates. Notice that the merging of the two streams does occur slightly below midspan. As mentioned earlier, the strengths of the upper and lower half radial flows depends on the stagnation pressure distribution, which is not symmetric about midspan. The 3-D views of Figures 8.26 and 8.27 represent the rotor passage with hub and pressure side density and pressure contours, respectively. Also represented on theses figures is a particular cutting plane which intersects a near wall streamline. Hence, this plane is essentially normal to the primary flow direction. The projection of tufts on the cutting plane allows to clearly visualize the secondary flow vortex, see Figure 8.28.[3]

Another interesting feature to notice about this flow is that the spanwise mass flow distribution is not uniform, see Figure 8.29. This means that the work output is non-uniform along the span. At the inlet, tip streamtubes carry more mass flow than their hub counterparts. This is a direct consequence of the choice for the sense of rotation of the inlet vortex, its strength, and the radial temperature (density) distribution. At the rotor exit, however, due to the mixing created by the secondary flow, the mass flow distribution along the span is more uniform, see Fig. 8.30. The mixing is significant since the spanwise variation in mass flow is reduced by a factor 2.

The flow around the leading edge of the rotor blade is interesting to analyze. Due to the large difference in incidence angles from hub to tip, the stagnation line is skewed as illustrated in Figures 8.17 and 8.20. The hub stagnation point is located farther back on the pressure side than the tip stagnation region. Hence as the flow deflects round the leading edge towards the suction side, and for a given rotor-relative stagnation pressure, the pressure drop is expected to be larger in the hub region. This sets a radial pressure gradient that forces a cross-flow to move from the tip to the hub, see Figures 8.16 and 8.17. Also, this radial flow is a consequence of the spanwise total pressure gradient at the local stagnation point, see Figs 8.14 and 8.15.

[3]Figures 8.19, 8.20, 8.25, 8.26, 8.27 and 8.28 were generated using VISUAL3 [40].

The pressure distributions around the blade at hub, midspan and tip are plotted in Figures 8.31, 8.32 and 8.33, respectively. On each figure four curves are drawn which represent the steady-state, the time-averaged, the minimum unsteady and the maximum unsteady pressure, respectively. The difference between the maximum and the minimum pressure for a given axial location highlights the importance of the unsteady effects. Clearly these are small in this application[4]. For instance, the maximum periodic tangential force perturbation, with respect to the time-averaged solution, represents only 2%. Hence, the loading is not significantly affected. Another indication of the weakness of the unsteady effects is that the steady-state pressure distribution matches almost perfectly the time-averaged values.

The major difference between the steady and the unsteady vortex interaction is that in the unsteady solution, the rate of rotation is transmitted across the vane/rotor interface. One of the consequences is that the time-averaged stagnation temperature contours will not match those of the steady-state flow, see Figures 8.11 and 8.34. The difference between the two cases in terms of temperature distribution in the flow field is small. However, in terms of magnitude the differences are more important. For instance in Figure 8.35, the rotor-relative surface stagnation temperature is plotted at midspan for the steady, time-averaged, minimum unsteady and maximum unsteady. Clearly the steady-state solution tends to underestimate the level of temperature occurring on the rotor blade. Differences between the magnitude of steady and time-averaged temperatures may increase if the strength of the vortex is intensified 'sufficiently' or/and if the flow becomes transonic and vortex/shock interactions occur.

[4]The reduced frequency of this case is about five times smaller than the reduced frequency of the transonic flow treated in Chapter 9.

8.5 Conclusions and discussion

In this chapter, the secondary flow produced by a combined vortex-temperature disturbance introduced at the vane trailing edge upstream of a moving rotor row has been analyzed. The strength of the disturbance, with a ratio of vane exit velocity to maximum vortex velocity of 2.8 and a spanwise temperature variation of 20% (with respect to uniform flow conditions), is realistic, though the local features of the secondary flow might be quite different due to the presence of a second vortex in an actual turbine environment. The design of the rotor, with a turning of 125^0 and untwisted blades is typical of a high-turning, linear subsonic cascade. The generic configuration chosen here allows the inlet conditions to be viewed 'in reverse' due to the arbitrary definition of the hub and the tip endwall. From one viewpoint the inlet conditions consist in a clockwise vortex combined with a decrease in temperature from hub to tip. The other viewpoint, found by inverting hub and tip, represents a counter-clockwise inlet vortex combined with an increase in temperature from hub to tip.

The rotor-relative radial mixing is driven by two basic mechanisms. The first mechanism is related to the steady-state axisymmetric streamwise vorticity, which produces a secondary (radial) velocity. The second mechanism, due to the discrete vortex, enhances an unsteady radial velocity component. The comparison between the steady and the time-averaged unsteady solution shows that the steady result captures the essential features of the secondary flow with nearly identical blade pressure distributions. This suggests that the first mechanism is more important, and that the steady-state stator/rotor interface tangential averaging procedure, by allowing for radial variations to be accounted for, retains the streamwise vorticity introduced by the vortex. However, differences appear in the blade temperature distributions. The steady solution underestimates the level of blade temperature, i.e. differences with the time-averaged solution up to 2.5% the inlet stagnation value are recorded. This is not really significant since it represents only 12% of the inlet radial temperature disturbance.

The unsteady pressure fluctuations are limited to 3% (peak-to-peak local variation)

of the inlet stagnation pressure, which represents 60% of the rotor inlet dynamic head (with an inlet Mach number of 0.28) a value which is comparable to the stagnation pressure variation introduced by the vortex-temperature disturbance. These unsteady fluctuations represent only 13% of the rotor pressure drop, which means that unsteadiness is not significant. The maximum unsteady stagnation temperature fluctuation (peak-to-peak value) reaches 11% of the inlet reference stagnation value, which also corresponds to about half of the inlet disturbance.

By comparing the result with an inlet disturbance formed by the vortex but no temperature variation and the flow with a combined vortex-temperature disturbance, it is possible to separate the shear flow effects from the non-barotropic effects. The latter ones account only for 25% of the stagnation pressure gradient, which indicates that it is mainly the deficit in the stagnation pressure in the vortex core that is responsible for the secondary flow.

In conclusion, the introduction of a combined velocity-thermal disturbance whose strength represents about 50% of the rotor inlet dynamic head, produces a significant secondary flow. The good agreement between the steady and time-averaged results indicates that the steady-state solution captures most of the secondary flow features. Surprisingly, the unsteadiness has only a small effect on the mean flow, with the steady-state matching the pressure distribution, providing trends for the temperature distribution but underestimating the local values.

parameter		*steady*	*time-averaged*	*uniform*
Ratio of inlet velocities $\left(\frac{u_\infty}{V_{vmax}}\right)$		2.8	2.8	∞
Vortex core size $\left(\frac{2a}{L}\right)$		≈ 0.17	≈ 0.17	0.00
Ratio of inlet temperatures $\left(\frac{T_{tip}}{T_{mid}}\right)$		0.9 (linear)	0.9 (linear)	1.0 (cst)
Inlet freestream tangential angle		63.0^0	63.0^0	63.0^0
Inlet freestream Mach number		0.37	0.37	0.37
Vane outlet tangential angle	hub	76.1^0	76.1^0	63.0^0
	mid	61.9^0	61.8^0	63.0^0
	tip	51.8^0	51.5^0	63.0^0
Vane outlet Mach number	hub	0.37	0.37	0.37
	mid	0.36	0.36	0.37
	tip	0.40	0.40	0.37
Rotor-relative inlet tangential angle	hub	70.6^0	70.7^0	52.4^0
	mid	50.6^0	50.6^0	52.4^0
	tip	38.3^0	37.9^0	52.4^0
Rotor-relative outlet tangential angle	hub	-66.7^0	-66.7^0	-72.7^0
	mid	-75.6^0	-75.7^0	-72.7^0
	tip	-69.6^0	-68.8^0	-72.7^0
Rotor-relative inlet Mach number	hub	0.27	0.27	0.28
	mid	0.27	0.27	0.28
	tip	0.31	0.31	0.28
Rotor-relative outlet Mach number	hub	0.75	0.75	0.74
	mid	0.75	0.75	0.74
	tip	0.77	0.78	0.74
Rotor Mach number	hub	0.11	0.11	0.11
	mid	0.11	0.11	0.11
	tip	0.12	0.12	0.11
Ratio of specific heats γ		1.4	1.4	1.4

Table 8.1: Flow parameters for vortex-temperature interaction in a 3-D linear subsonic stage. The third column indicates results for steady uniform inlet conditions.

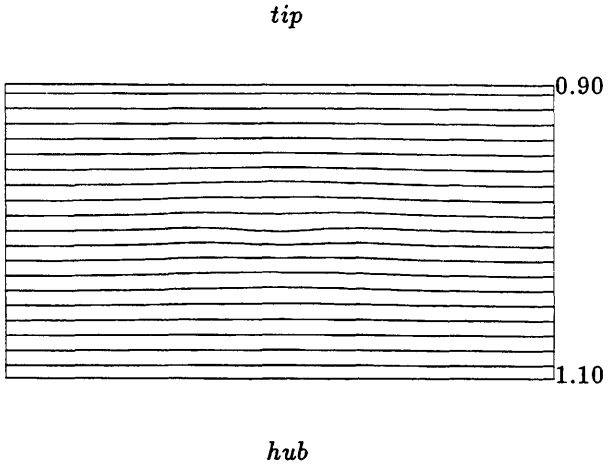

Figure 8.6: Inlet stagnation temperature contours ($T_{t\,inl}/T_{t\,\infty}$).

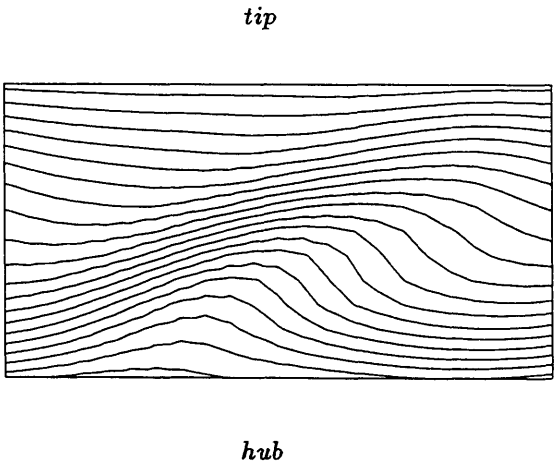

Figure 8.7: Vane exit stagnation temperature contours ($T_t/T_{t\,\infty}$). Increments = 0.01.

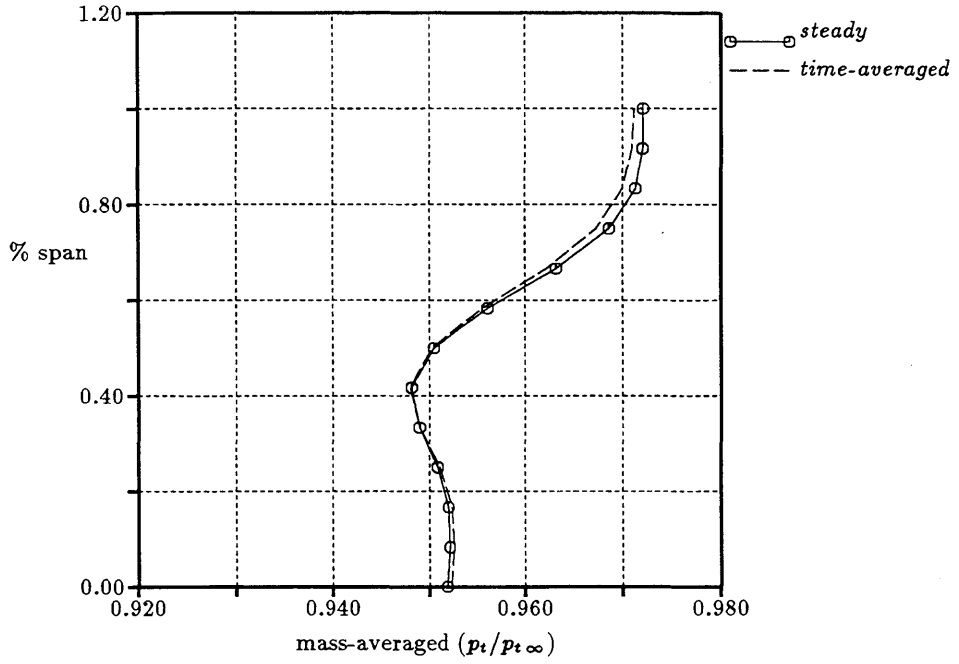

Figure 8.8: Rotor-relative inlet stagnation pressure.

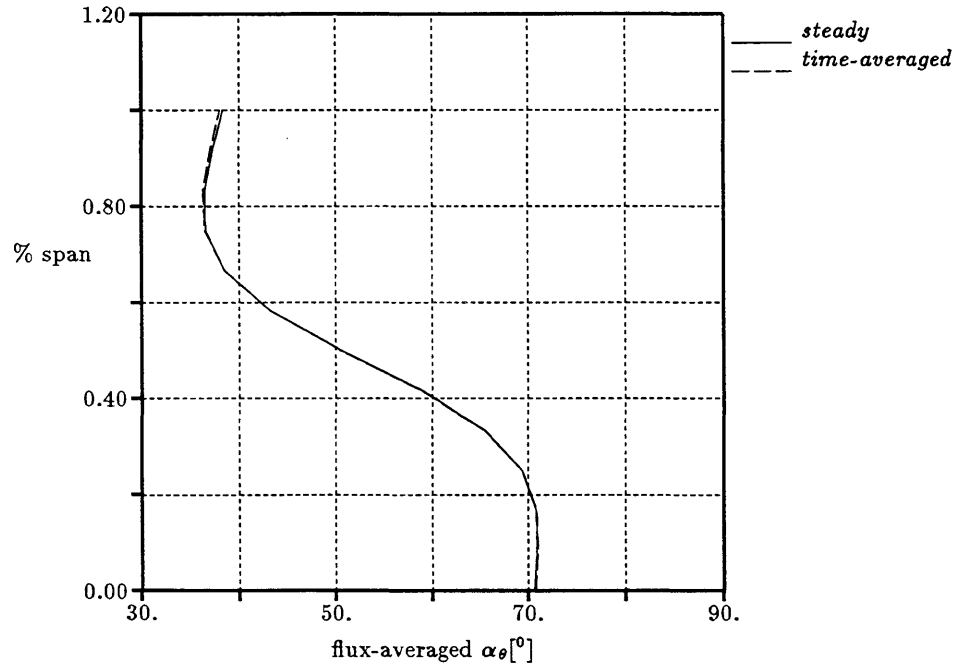

Figure 8.9: Rotor-relative inlet tangential angle.

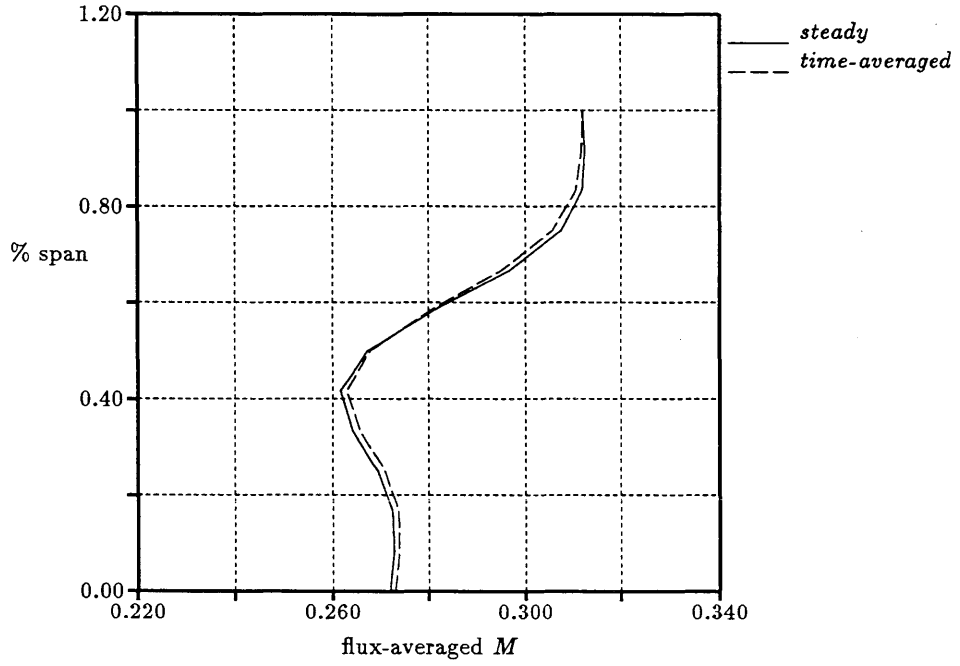

Figure 8.10: Rotor-relative inlet Mach number.

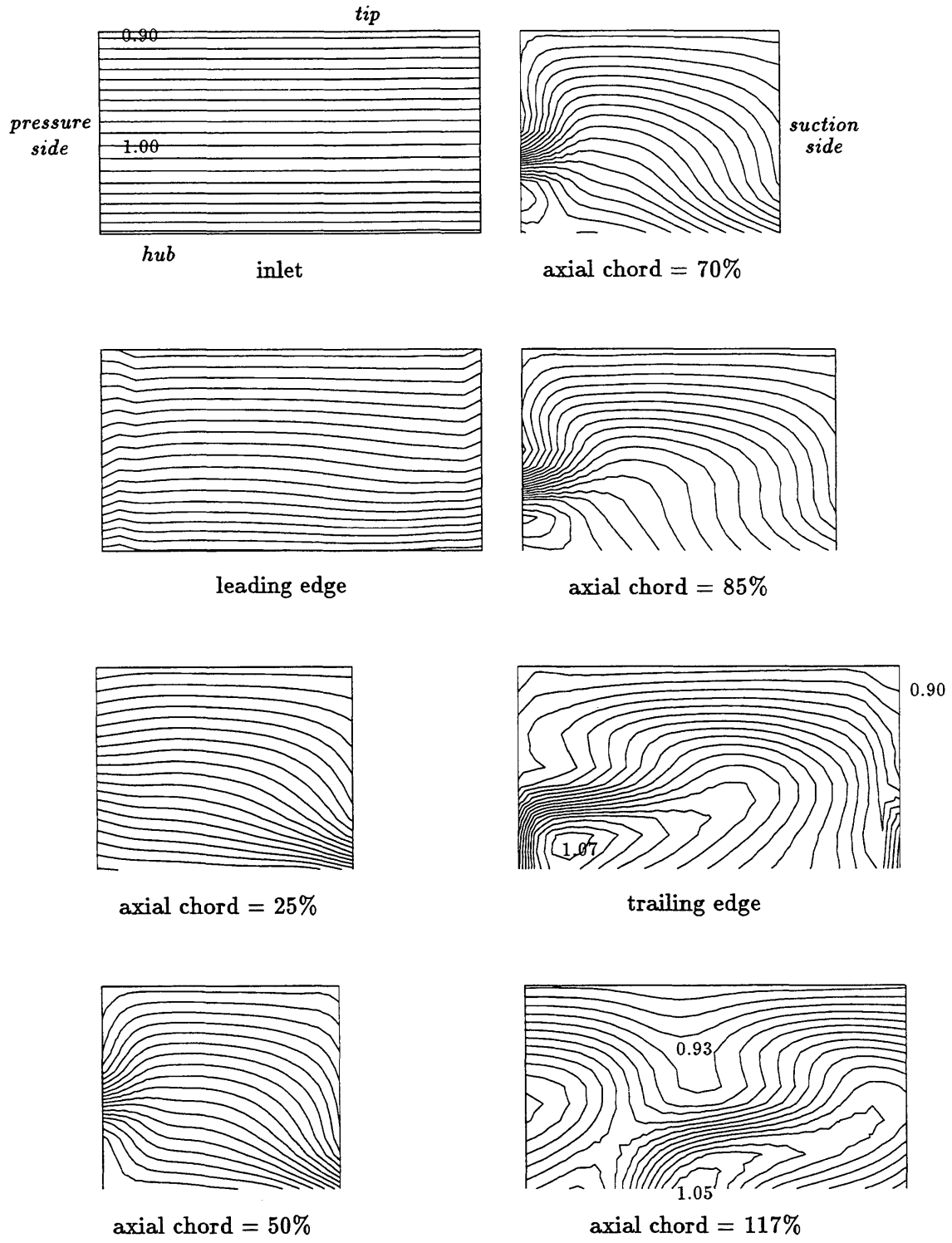

Figure 8.11: Steady-state rotor-relative stagnation temperature contours ($T_t/T_{t\infty}$) on eight blade-to-blade mesh surfaces along the passage. Increments = 0.01.

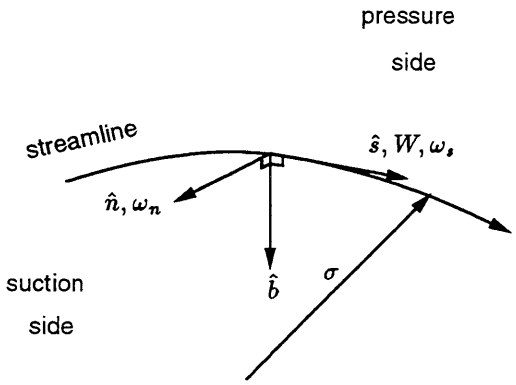

Figure 8.12: Intrinsic coordinates.

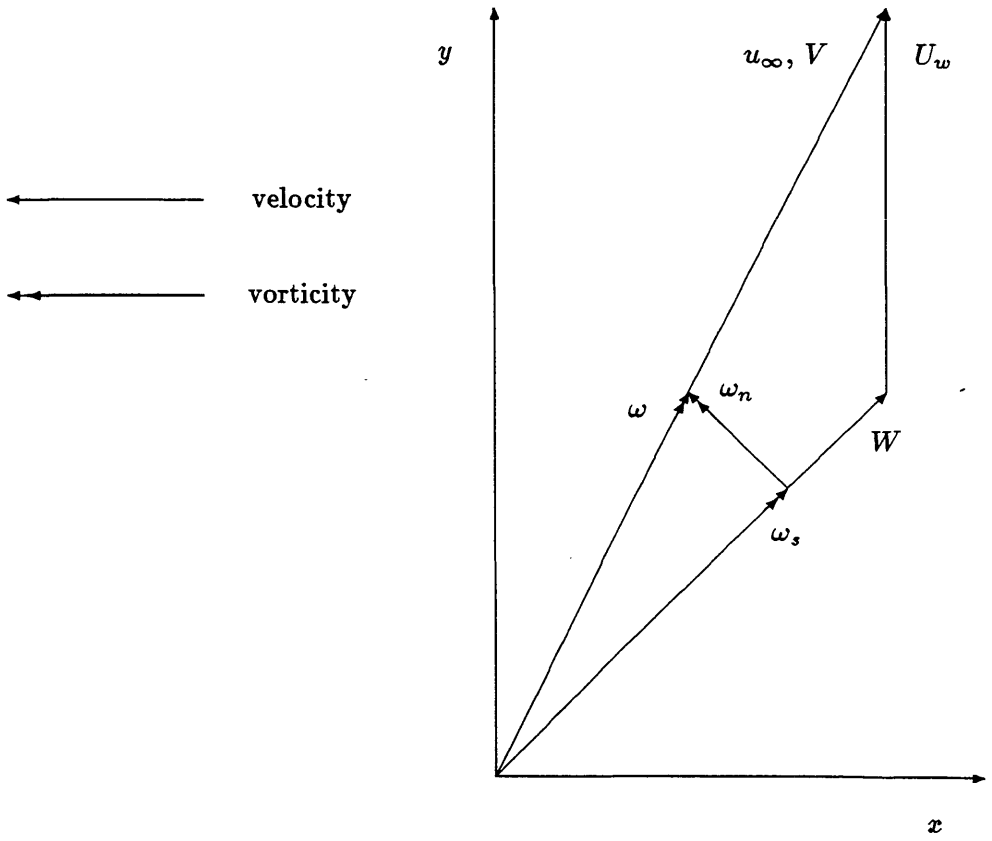

Figure 8.13: Velocity and vorticity triangles at vane/rotor interface (midspan region).

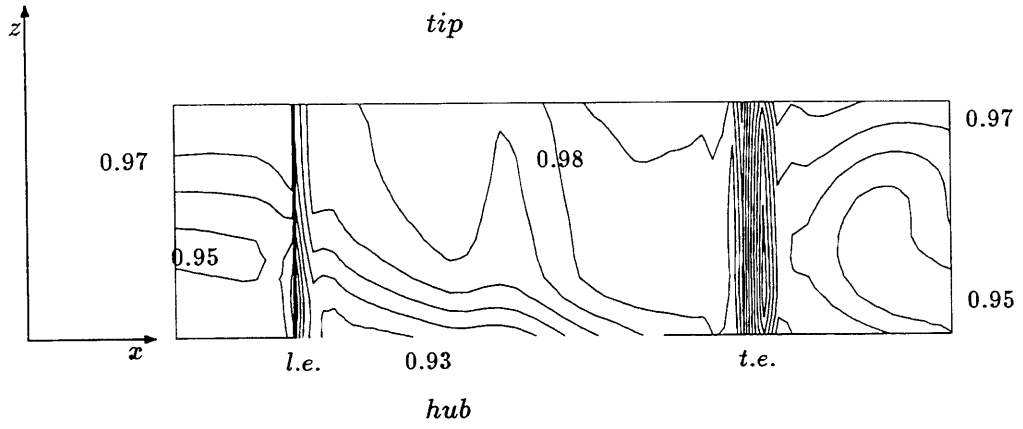

Figure 8.14: Rotor-relative stagnation pressure contours ($p_t/p_{t\infty}$) on suction side and periodic surfaces ahead of leading edge and downstream of trailing edge. Increments = 0.01.

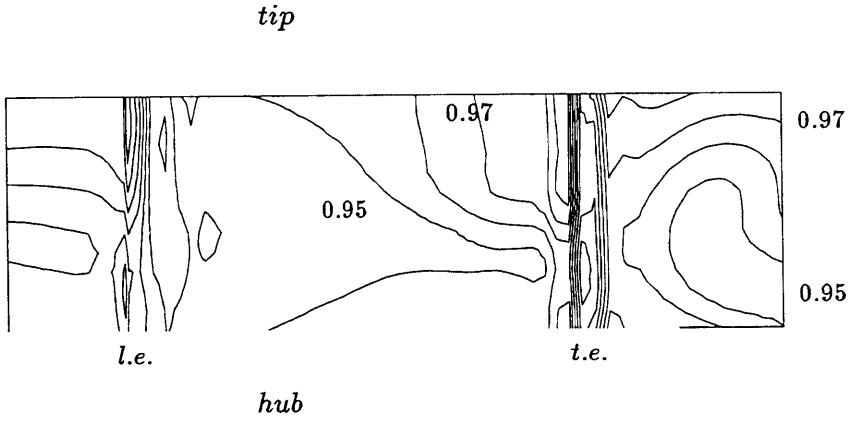

Figure 8.15: Rotor-relative stagnation pressure contours ($p_t/p_{t\infty}$) on pressure side and periodic surfaces ahead of leading edge and downstream of trailing edge. Increments = 0.01.

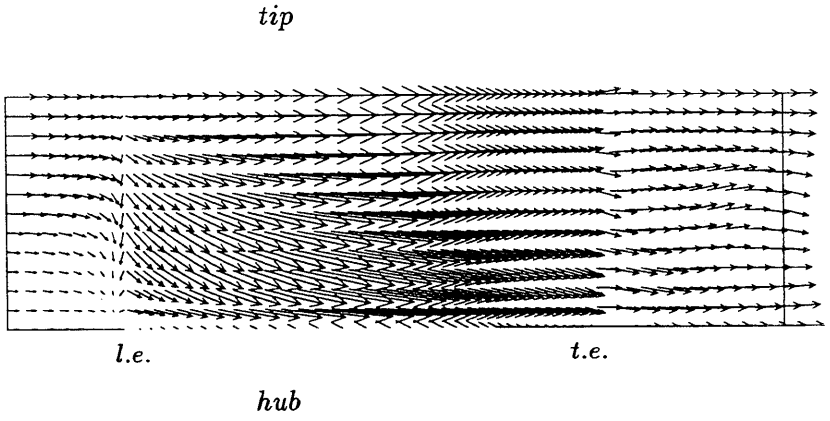

Figure 8.16: Vortex-temperature disturbance: rotor-relative velocity vectors on suction side and periodic surfaces ahead of leading edge and downstream of trailing edge.

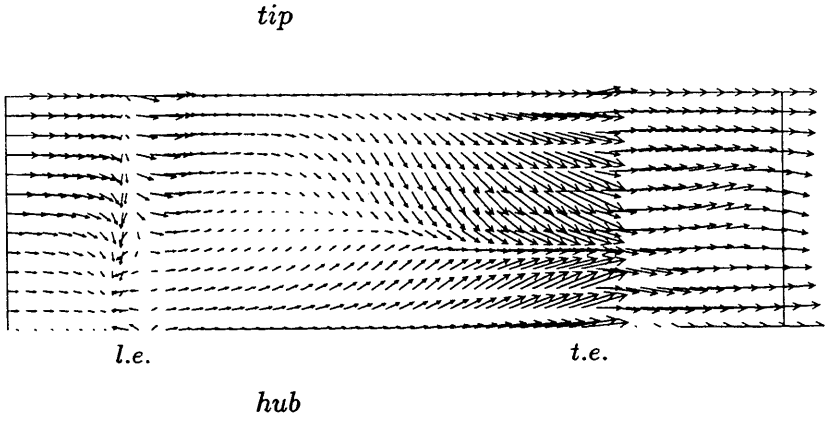

Figure 8.17: Vortex-temperature disturbance: rotor-relative velocity vectors on pressure side and periodic surfaces ahead of leading edge and downstream of trailing edge.

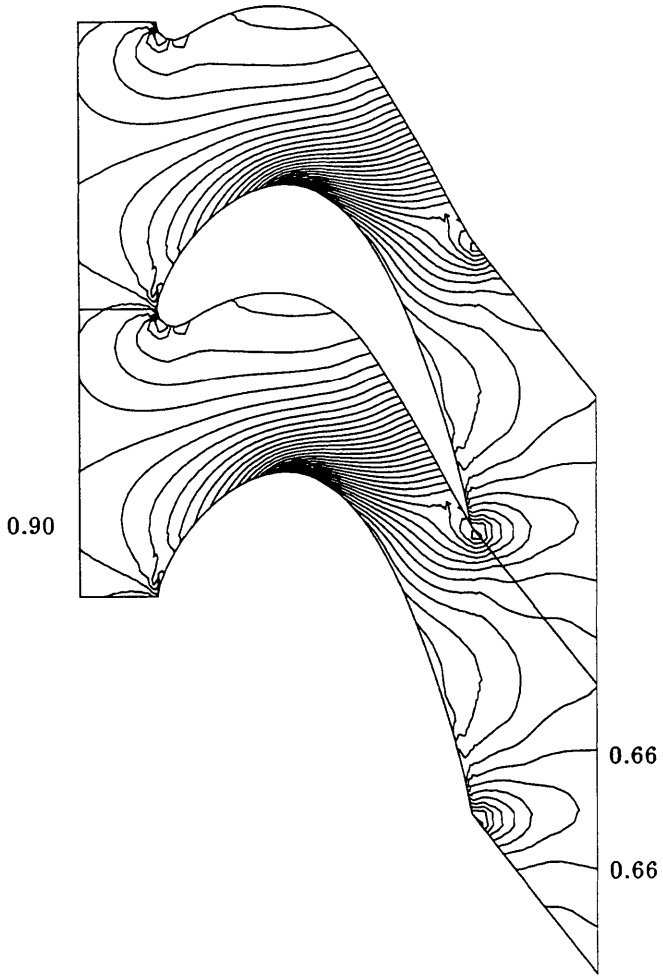

Figure 8.18: Rotor-relative pressure contours ($p/p_{t\infty}$) at midspan. Increments = 0.01.

tip

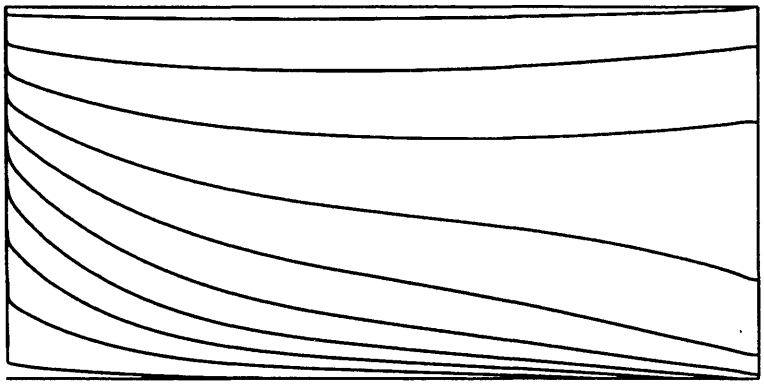

hub

Figure 8.19: Streamlines on rotor suction side.

tip

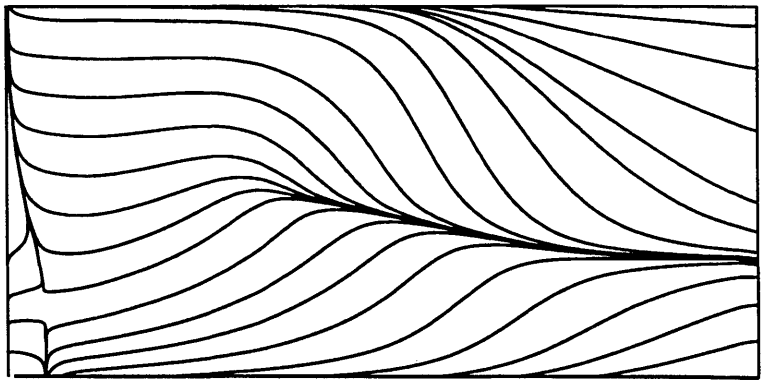

hub

Figure 8.20: Streamlines on rotor pressure side.

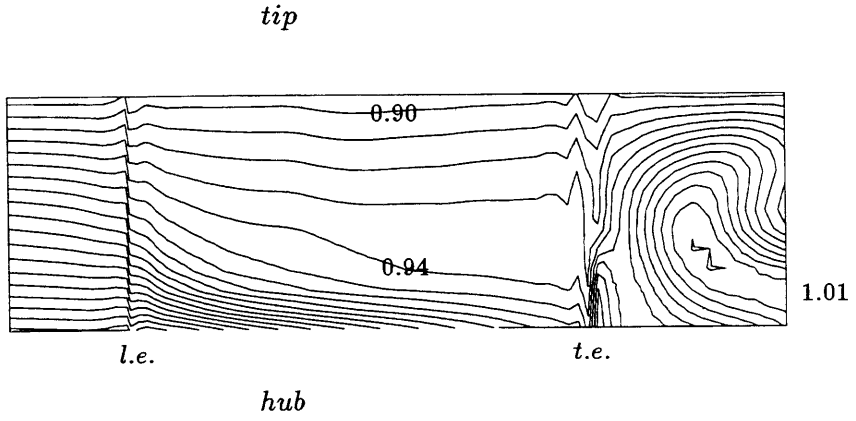

Figure 8.21: Rotor-relative stagnation temperature contours ($T_t/T_{t\infty}$) on suction side and periodic surfaces ahead of leading edge and downstream of trailing edge. Increments = 0.01.

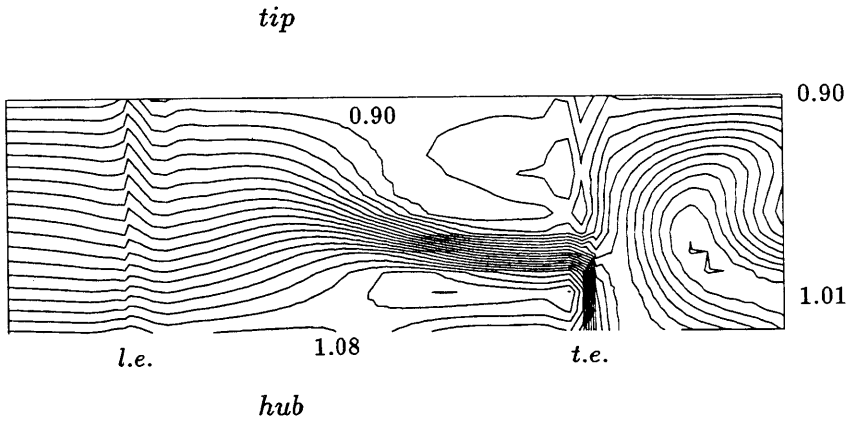

Figure 8.22: Rotor-relative stagnation temperature contours ($T_t/T_{t\infty}$) on pressure side and periodic surfaces ahead of leading edge and downstream of trailing edge. Increments = 0.01.

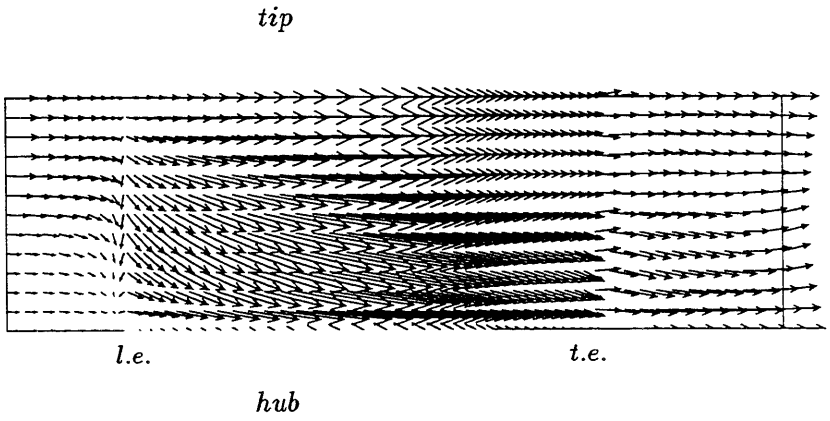

Figure 8.23: Vortex alone: rotor-relative velocity vectors on suction side and periodic surfaces ahead of leading edge and downstream of trailing edge.

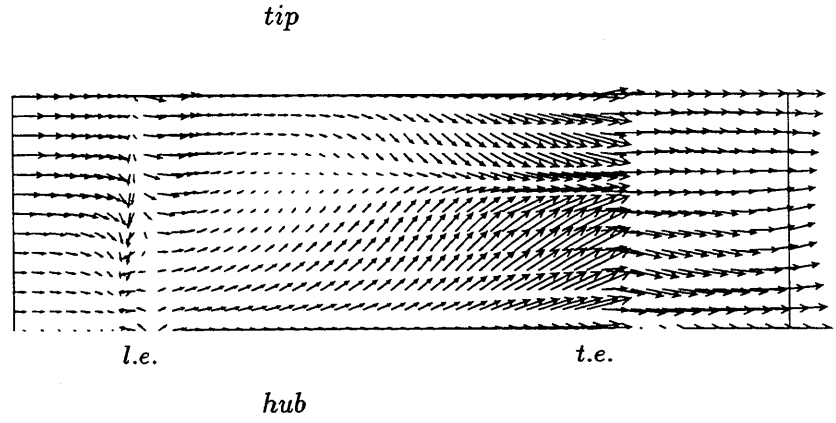

Figure 8.24: Vortex alone: rotor-relative velocity vectors on pressure side and periodic surfaces ahead of leading edge and downstream of trailing edge.

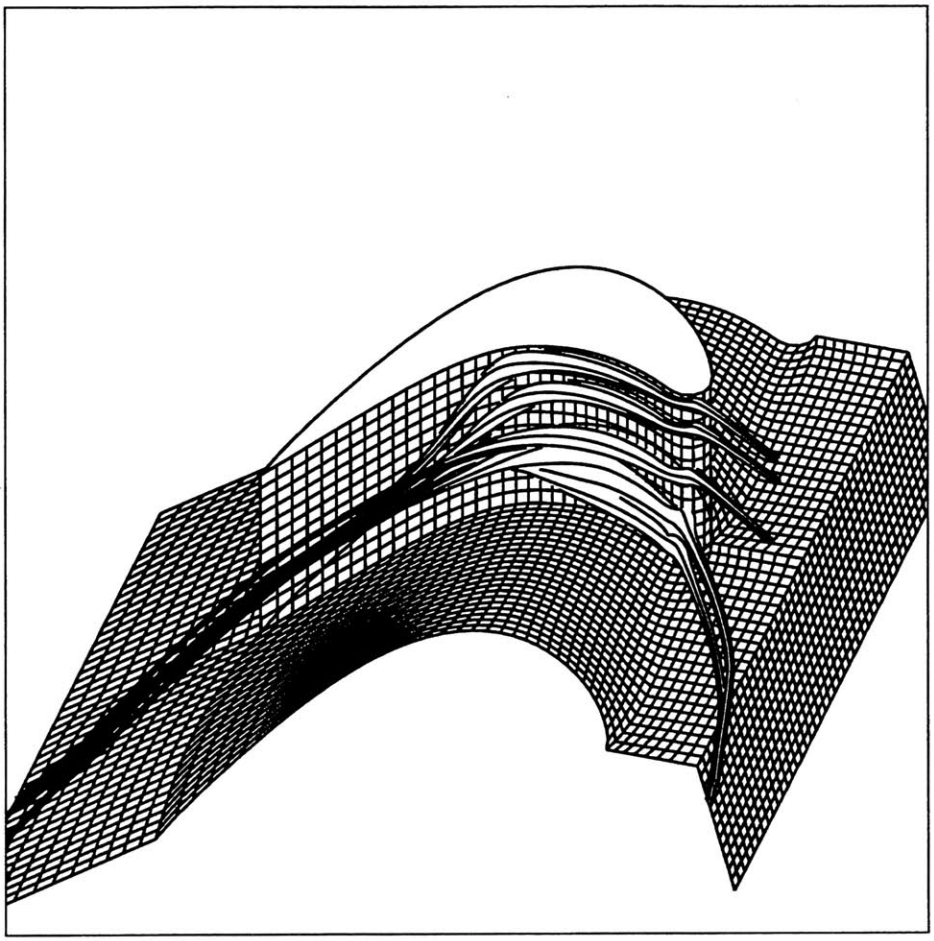

Figure 8.25: Five near-blade streamtubes with blade and hub mesh.

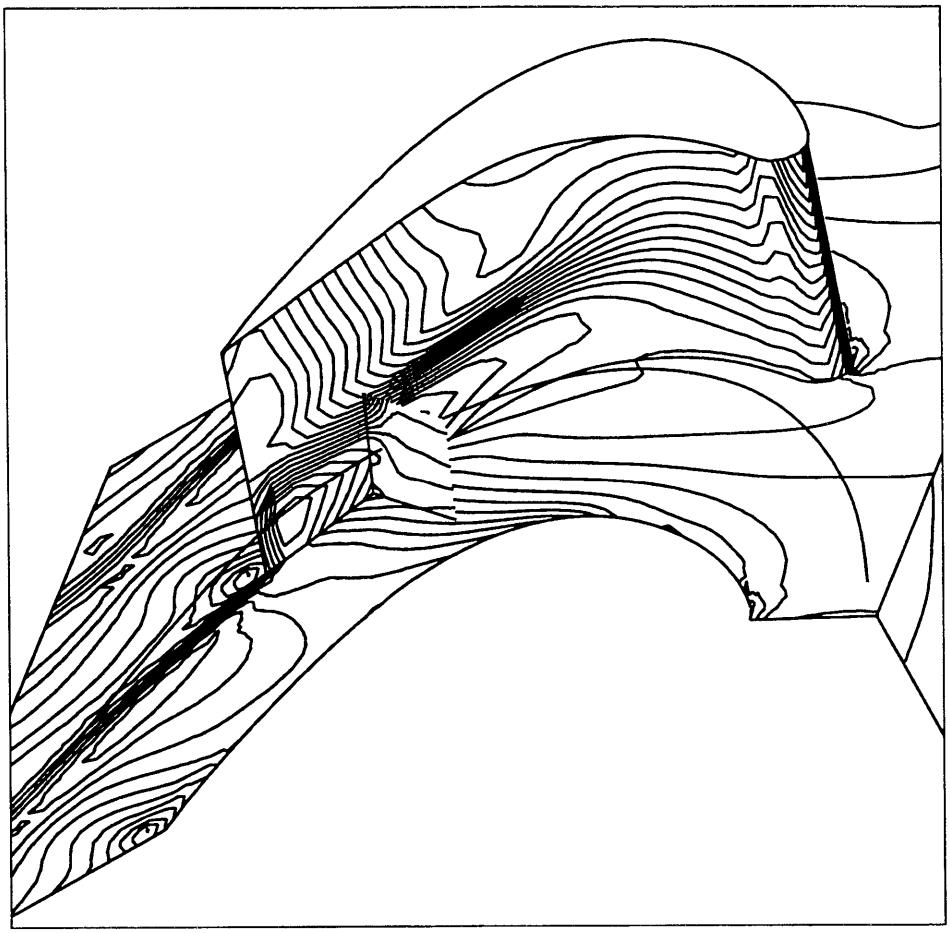

Figure 8.26: Density on hub, blade pressure side and cutting plane normal to streamline.

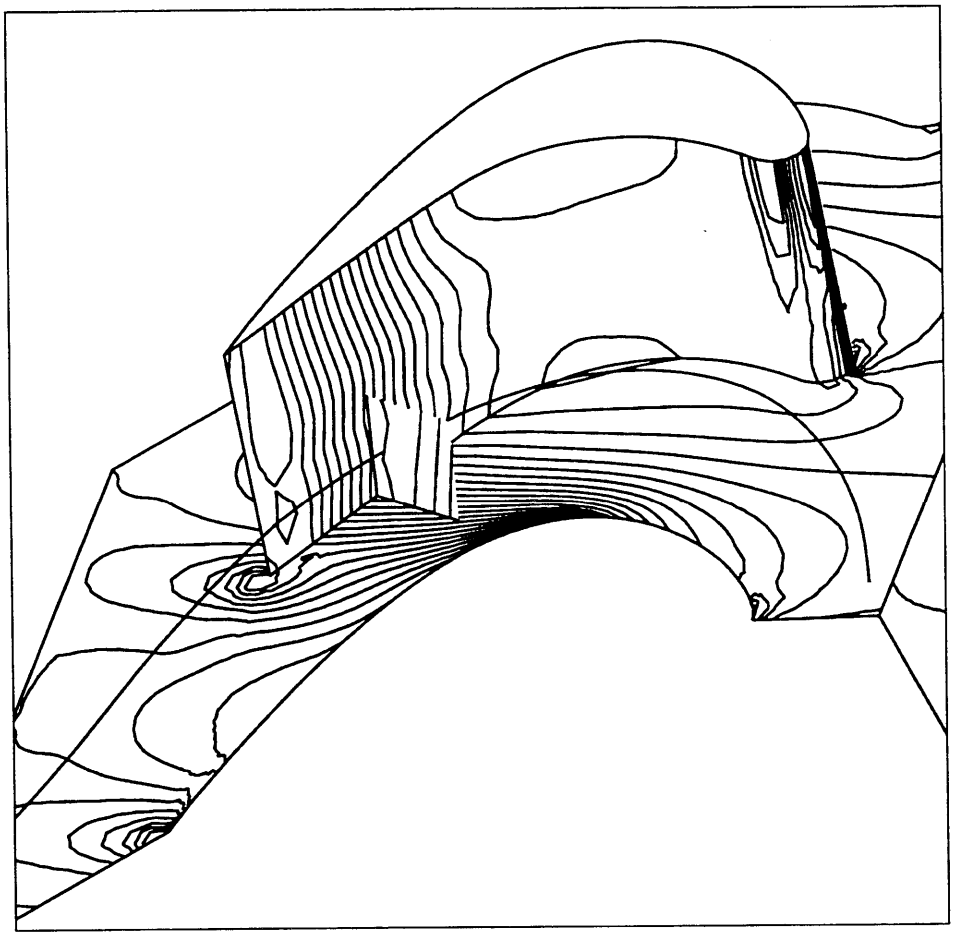

Figure 8.27: Pressure on hub, blade pressure side and cutting plane normal to streamline.

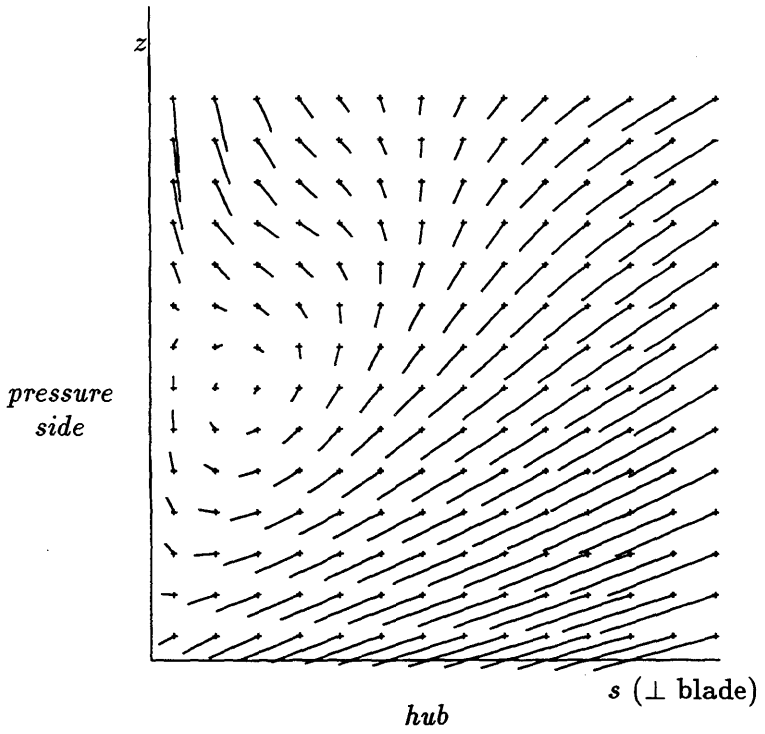

Figure 8.28: Tufts projected on cutting plane normal to streamline of Figures 8.26 and 8.27.

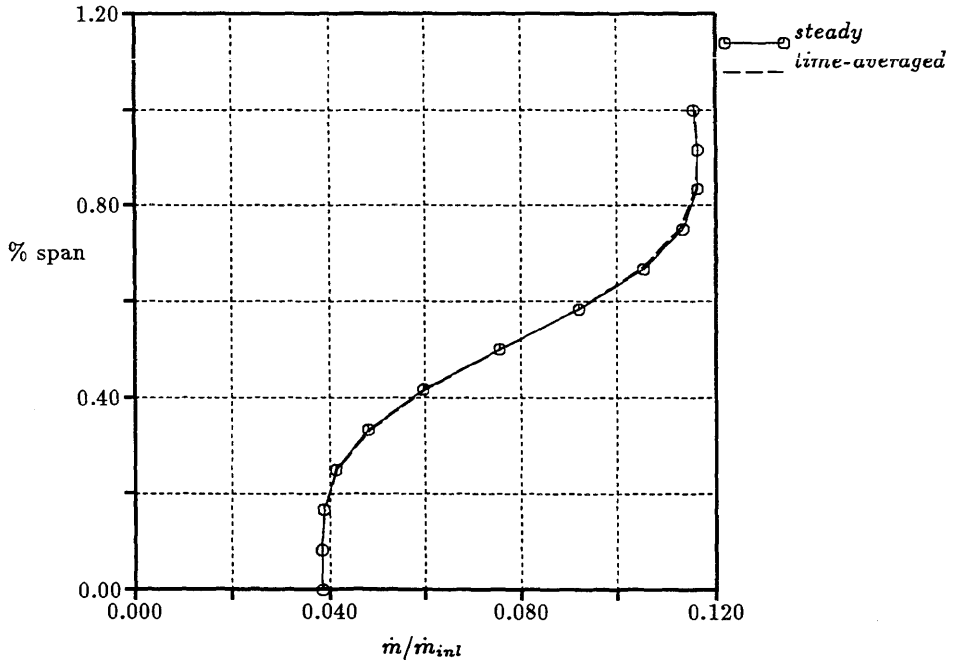

Figure 8.29: Rotor inlet mass flow distribution along span.

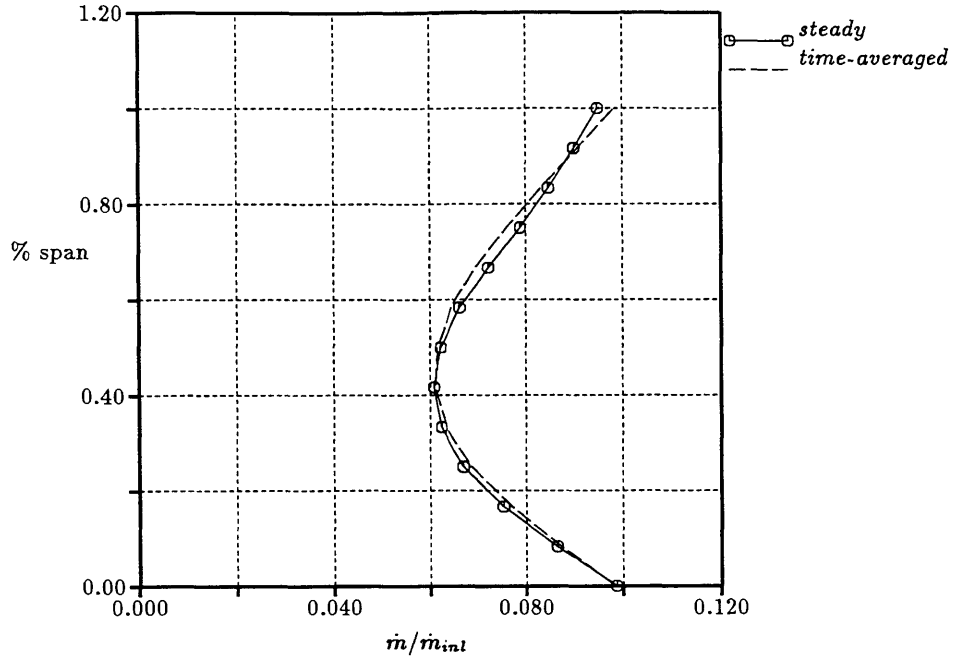

Figure 8.30: Outlet mass flow distribution along span.

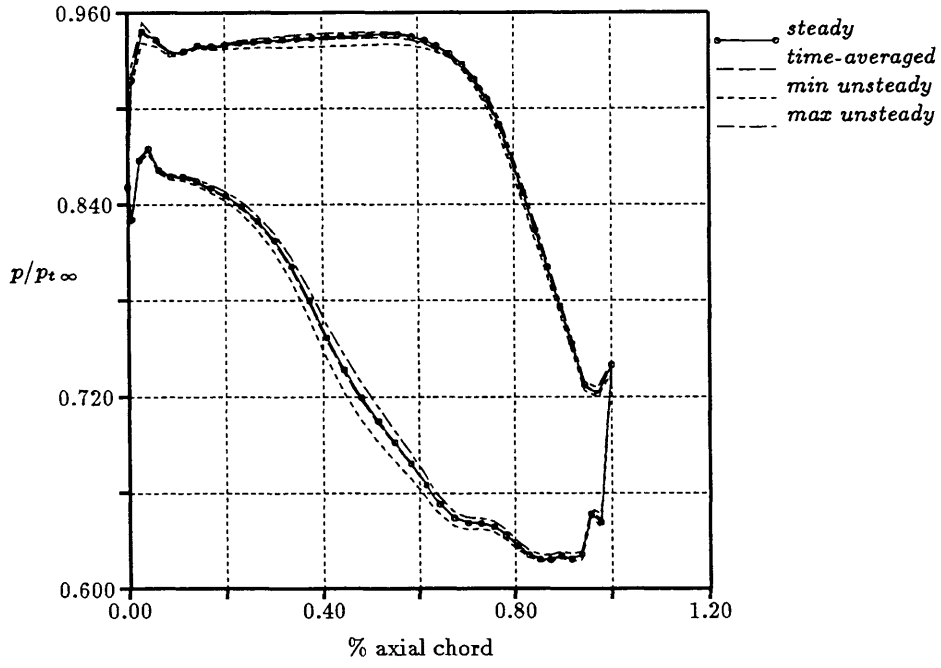

Figure 8.31: Rotor-relative pressure around the blade root.

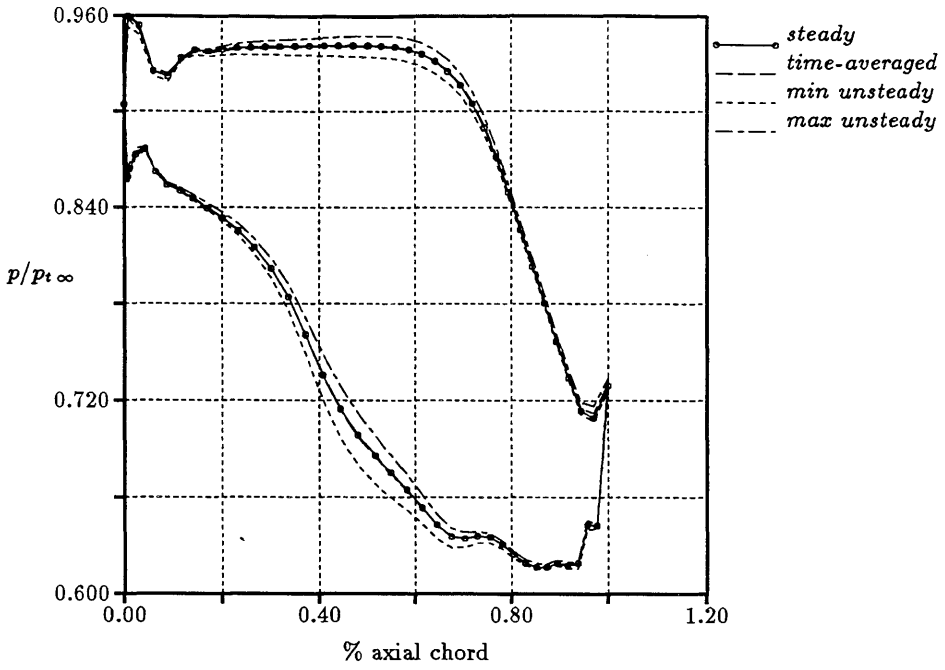

Figure 8.32: Rotor-relative pressure around the blade at midspan.

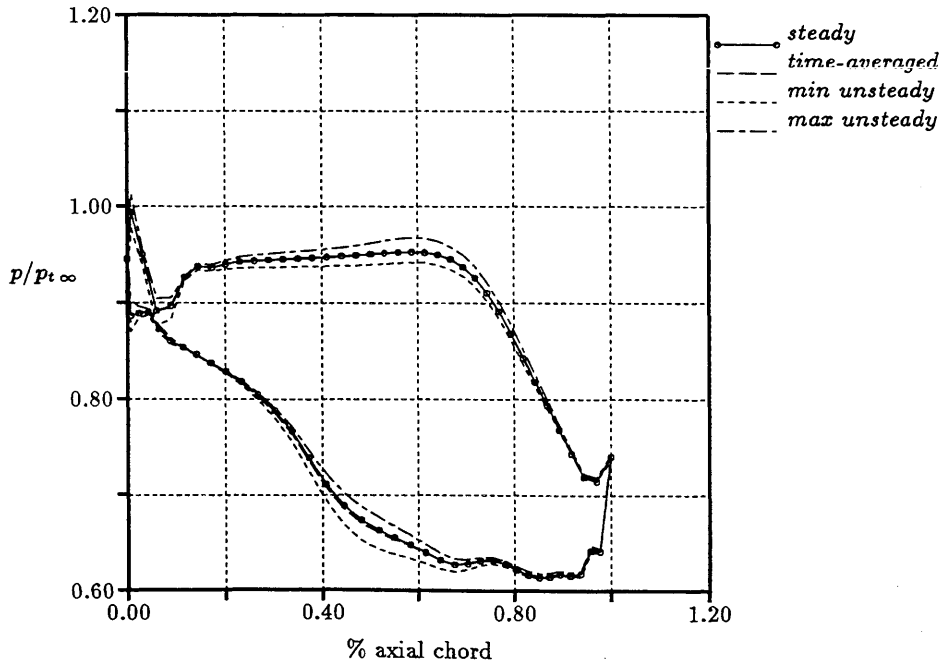

Figure 8.33: Rotor-relative pressure around the blade tip.

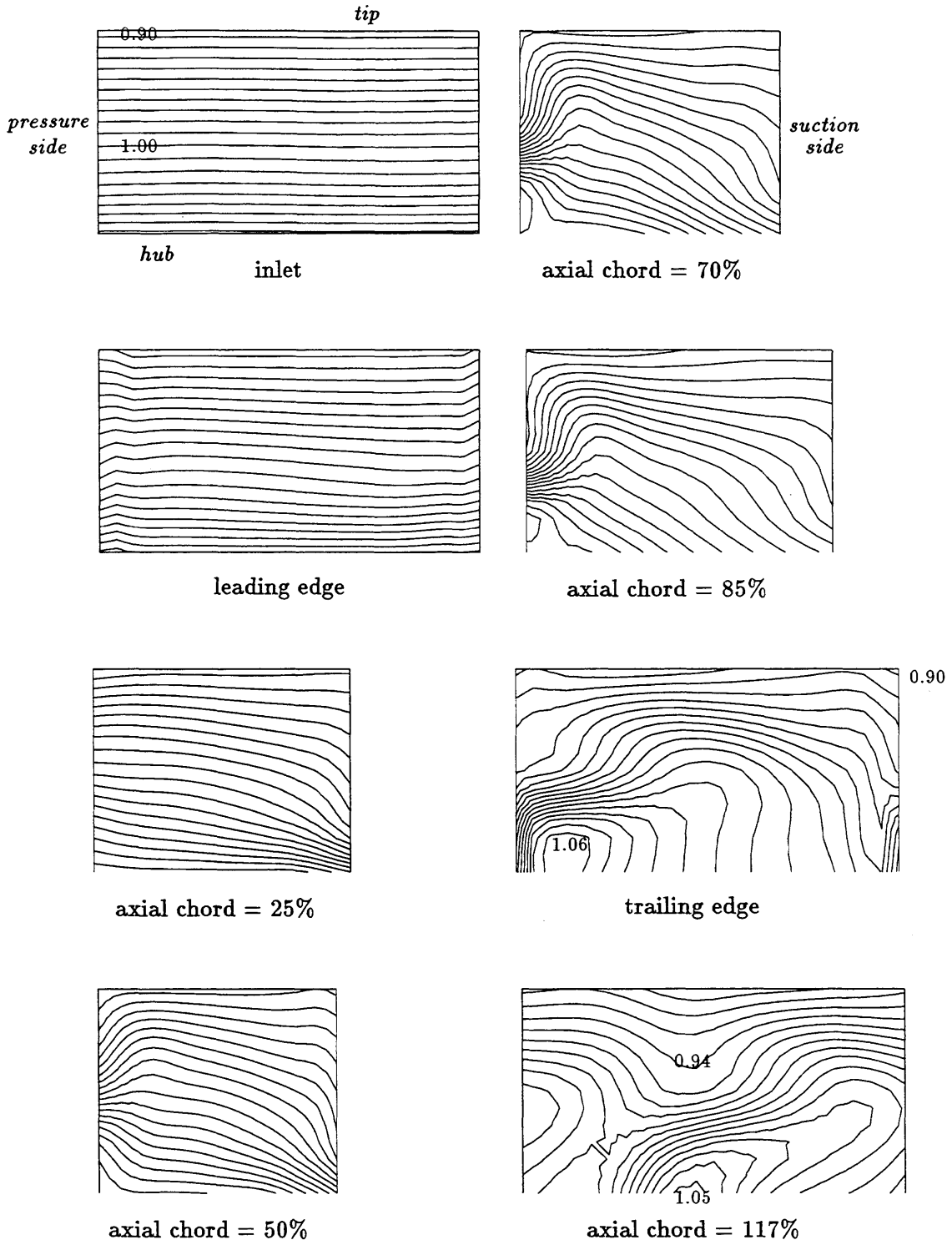

Figure 8.34: Time-averaged rotor-relative stagnation temperature contours ($T_t/T_{t\infty}$) on eight blade-to-blade mesh surfaces along the passage. Increments = 0.01.

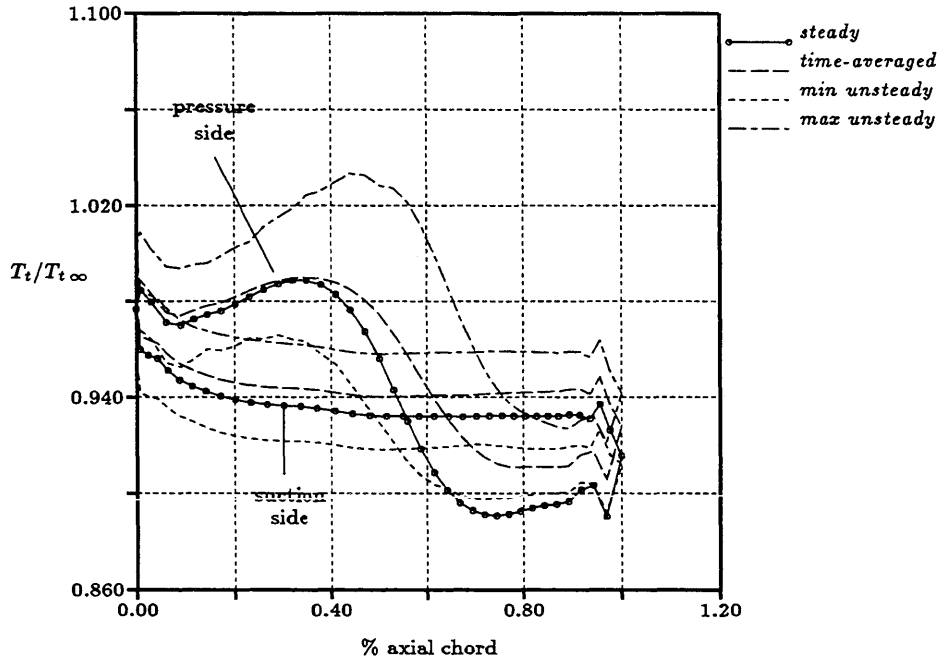

Figure 8.35: Rotor-relative stagnation temperature at midspan.

Chapter 9

Analysis of steady, unsteady and time-averaged flow fields in a turbine stage with strong shock interaction.

In this chapter, the present method is applied to investigate both the steady and unsteady flow fields occurring in a highly loaded transonic first turbine stage. In addition a comparison is made between the steady and the time-averaged result. Of particular importance in this study is the correct capturing of the motion of the shocks that is produced by the impact of the oblique shock wave extending from the stator trailing edge off the downstream rotor. Considering the fact that turbine blading design is usually based upon steady-state flow analysis (streamline curvature for instance), it is important to assess the variations from steady-state due to non-linear unsteady processes as well as their influence on the time-averaged solution.

In the last fifteen years several numerical analyses of unsteady stator/rotor interactions have been performed. For instance, in two dimensions Erdos et al. [22] were among the first to propose a numerical method for solving periodic inviscid and compressible flow in a stage using an algorithm to treat unequal pitches. In 1986 Fourmaux [27] presented a 2-D simulation of Euler flow in a compressor stage with unequal numbers of stator and rotor blades. Lewis et al. [72] for subsonic flow and Giles [33] for transonic flow presented quasi-three-dimensional turbine stator/rotor calculations using the Euler equations. In 1985 Koya and Kotake [64] extended Erdos' work to three dimensions.

Navier-Stokes solutions of unsteady subsonic stator/rotor interactions were published by Jorgenson and Chima [60], and Rai [86] for two-dimensional flow, and Rai [87] and and Chen [12] for three-dimensional flow. In these subsonic flow studies, the maximum unsteady pressure fluctuations represent less than 5% of the inlet stagnation pressure[1]. As seen later in this chapter, the unsteady static pressure envelope for transonic flow is one order of magnitude larger.

The steady-state results are discussed in Appendix E. The configuration of the transonic first turbine stage is shown in Figures 9.1 and 9.2. It is similar to the stage shown in Figures 7.2 and 7.3 which was used to assess the effects of non-uniform inlet temperature, see Chapter 7. The difference lies in the scaling of the rotor blading. Indeed, the unsteady stator/rotor interface boundary condition used here is designed for equal stator and rotor pitches. Thus, a scaling of the rotor blades by a factor 61/36 with respect to the real turbine stage is required. This has been done while keeping the annulus (hub and tip walls) unchanged and in particular the channel height and the axial location of the rotor leading edge have not been altered. The procedure of scaling a row of blades such that the stator/rotor pitch ratio is 1:1 or some simple ratio such as 2:3 or 3:4 is quite common, see for instance References [22, 64, 87, 72], because it greatly simplifies the handling of the periodic boundary conditions. Since this is not the main thrust of this chapter, the effects of scaling, with respect to the original configuration, are discussed in Appendix E together with the steady-state flow features occurring in the stage.

In Section 9.1, the unsteady shock motion occurring in the stage is discussed. In particular, the impact of the upstream stator oblique shock on the downstream rotor suction surface which produces reflected waves on both the adjacent rotor and on the upstream stator is presented. Then, in Section 9.2 a comparison between the steady and the time-averaged result is presented, together with an analysis of the differences between the two cases. Finally, a brief discussion of some of the consequences of the unsteadiness followed by some conclusions are presented in Section 9.3.

[1]This represents about 50% of the stator inlet dynamic head.

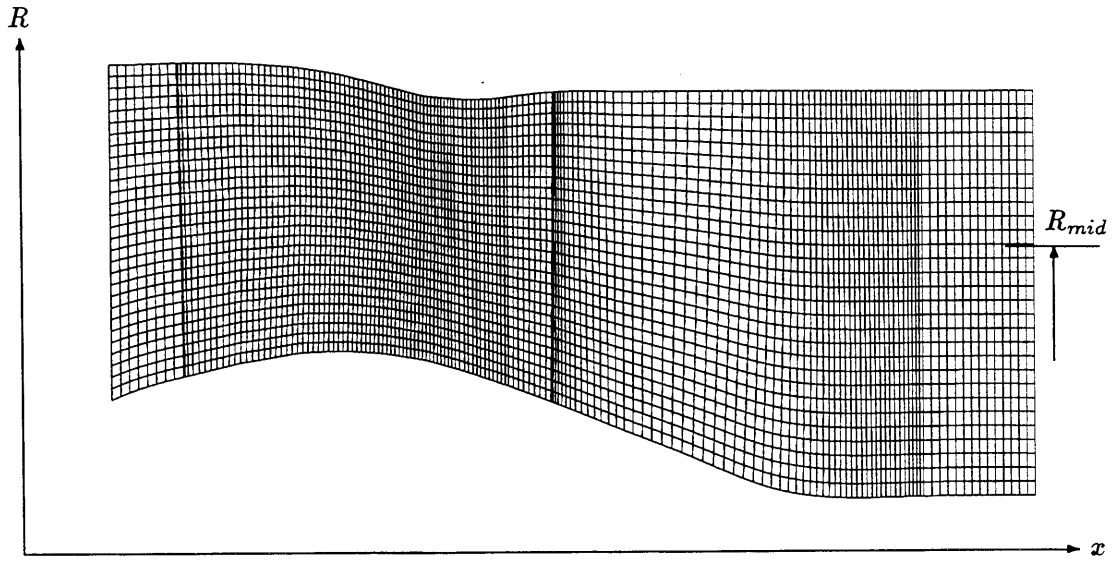

Figure 9.1: Side view of the scaled transonic first turbine stage including stator pressure and rotor suction sides.

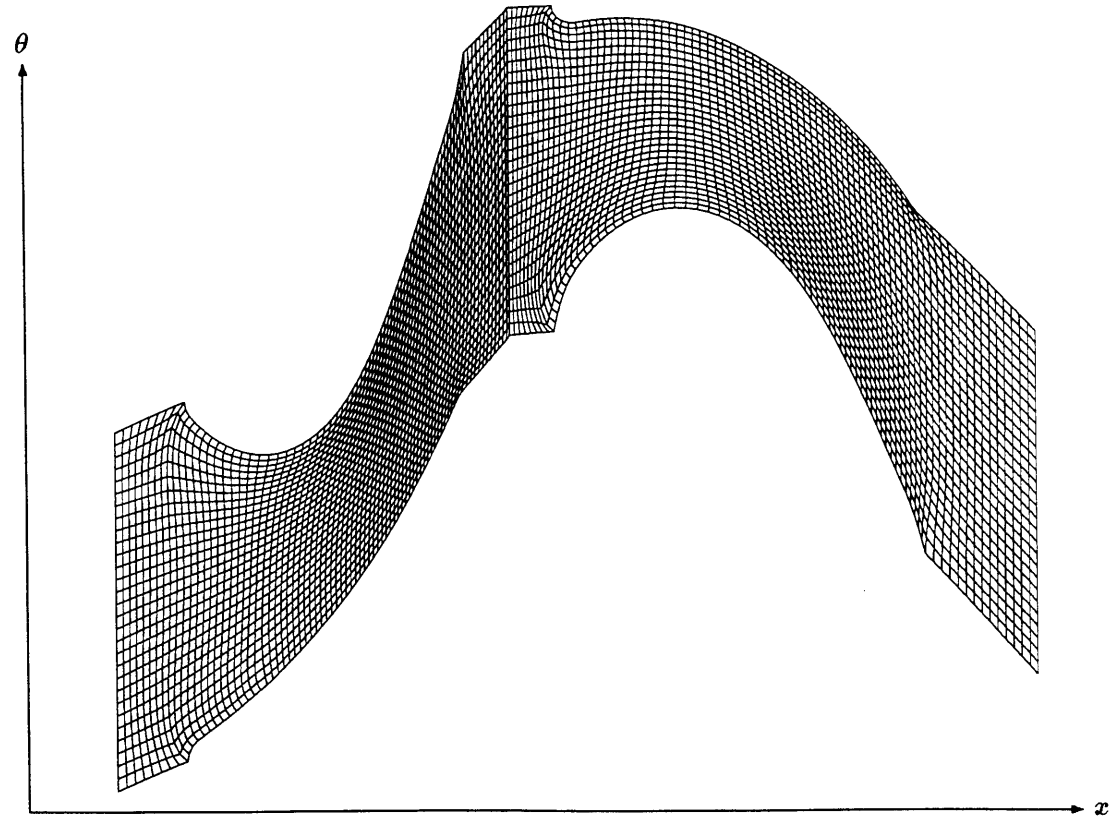

Figure 9.2: Mean height blade-to-blade mesh (stator: $80 \times 30 \times 30$, rotor: $80 \times 30 \times 30$ nodes).

9.1 Unsteady shock motion

The unsteady computation took 12 blade-passing periods to converge to a periodic solution, using 400 iterations/period. Figure 9.3 displays the pressure history for two particular rotor nodes during the last two periods.

In the axial flow turbine stage considered here, the unsteady stator/rotor shock interaction is principally a two-dimensional process driven by the oblique shock leaving the stator trailing edge which impacts on the moving rotor blade. Although shock surfaces interact, unsteady pressure contours at a representative radius in the axial-tangential plane are considered first. Figure 9.4 shows pressure contours at a constant radius $R = R_{mid}$ for the unsteady stator/rotor interaction at eight intervals during one blade-passing period. The contour plots are defined for a given non-dimensional time $t = const$, where t varies from $t = 0$, the beginning of the period, to $t = 1$, the end of the period, which also corresponds to $t = 0$ by periodicity. Notice that although a very simple interface algorithm using characteristics theory has been used, the unsteady pressure contours match well across the stator/rotor boundary.

At the beginning of the period at $t = 0$, the oblique shock extending downstream from the stator trailing edge has hit the crown of the rotor suction surface. At $t = 0.125$ the location of impingement has moved forward towards the leading edge as the rotor blade moves upward. A weak reflection is visible. At $t = 0.25$ the reflected wave is still growing and the reflection point continues to move closer to the rotor leading edge. At $t = 0.375$ the same process continues. However, in addition the portion of the reflected wave which moves towards the pressure surface of the adjacent rotor has now reflected a second time and is moving back towards the original rotor. This phenomenon is not clearly visible on the pressure contours, but can better be seen and analyzed using VISUAL3 [40]. Using the gray-scale animation option of this visualization package, it is possible to see the motions of both the primary reflection and the secondary reflection on the adjacent rotor pressure side. At $t = 0.5$ the primary shock wave reflection has reached the rotor leading edge and the secondary reflected wave has crossed back to

the original rotor. It has sufficiently intensified that it is now visible on the pressure contours.

At $t = 0.625$ the stator oblique shock no longer impacts on the rotor. At the same time the primary reflected wave has left the rotor and is propagating upstream towards the stator suction surface. The direction of propagation of the moving primary reflected wave is indicated in Figure 9.5, which represents a schematic of velocity triangles for a moving and a stationary shock. The velocity of a very weak shock is defined as the sum of the gas local convection velocity, plus a velocity of magnitude c, the speed of sound, normal to the shock. Also at $t = 0.625$ the secondary reflected shock has strengthened further and moved upstream. It actually appears to have moved upstream, but since the flow on the rotor suction surface is supersonic it does not permit disturbances to move upstream. Thus the upstream motion of the shock surface is achieved by the pressure wave moving upstream through the subsonic flow near the pressure surface of the adjacent rotor, and then moving across the channel towards the original rotor. As the pressure wave moves into the higher Mach number flow region, the strength of the shock increases. The dynamics of the primary oblique shock which has left the rotor can be understood using the simplified shock motion theory illustrated in Figure 9.5. It is a good approximation to assume that the straight part of the oblique shock is a stationary shock in the stator frame of reference, and so propagates along the shock front with the speed $\sqrt{V^2 - c^2}$. This velocity tends to increase the length of the straight portion of the shock from $t = 0.625$ to $t = 0.875$ until it refracts with the secondary reflected shock.

At $t = 0.75$ the primary reflected shock has just struck the suction side of the upstream stator in a region close to the trailing edge. The secondary reflected shock wave is still moving upstream towards the crown of the rotor.

At $t = 0.875$ the primary oblique shock has almost regained its maximum strength. The primary reflected shock is reflecting from the upstream stator suction surface and moves back to the adjacent rotor. This reflection is also visible at $t = 0$, but then

disappears as it strikes the rotor leading edge at $t = 0.125$. However this effect is recorded in the history of the rotor leading edge pressure in Figure 9.3. In addition, this figure clearly illustrates the impact of the stator oblique shock on the rotor leading edge at $t = 0$ and $t = 1$.

This unsteady shock interaction is similar in nature to the result presented by Giles [33] in a 2-D time-accurate numerical simulation which included quasi-three-dimensional source terms. However, some differences appear in the timing of the events because Giles' computation was performed on the actual configuration with a stator-to-rotor pitch ratio equal to 1.69.

Some 3-D effects can be extracted from the unsteady pressure and the unsteady Mach number distributions on the rotor suction surface shown in Figures 9.6 and 9.7, respectively. At $t = 0$ the impact of the stator oblique shock surface is clearly visible and extends along the entire span of the rotor suction side. Also some dispersion is visible. Notice that at the hub and the tip wall the shock strikes normally in order to satisfy the flow tangency condition and that the strength is higher at the root than at midspan. At $t = 0.25$ the reflection has moved upstream closer to the leading edge, and at $t = 0.5$ the primary oblique shock strikes the rotor leading edge. In addition, the secondary reflection off the neighboring rotor has come back across the channel and is visible at $x/L \approx 70\%$ from midspan to the tip. At the root, the reflected wave has not yet crossed back to the original rotor. At $t = 0.75$ the entire span is under the influence of the secondary reflected shock which has strengthened and moved upstream.

Figure 9.8 shows the instantaneous tufts distribution on the rotor suction for one blade-passing period. A secondary flow is visible in the aft part of the blade that drives fluid from hub towards midspan. Reverse flow occurs behind the secondary reflected wave as it moves forward towards the leading edge and strengthens. However, recirculation occurs only partially during the cycle.

Figure 9.9 is a schematic of the 3-D shock structure at $t = 0.625$. The stage is seen

from the hub (not drawn) towards the tip. The labels point out the different shock waves; i.e. A) and B) the stator and rotor trailing edge oblique shocks, respectively; C) the primary reflection moving upstream and D) the secondary reflection moving across the channel from the adjacent rotor pressure side. The shock surfaces are not much skewed from hub to tip, which suggests that the shock interaction is essentially a 2-D process. Not represented in this figure is the strength of the different shocks. At this particular time, the strength of the primary reflection is fairly uniform in the spanwise direction, wihle the secondary reflected wave is stronger at the tip than at the hub. Also, shocks A) C) and D) are one order of magnitude stronger than the rotor trailing edge shock B).

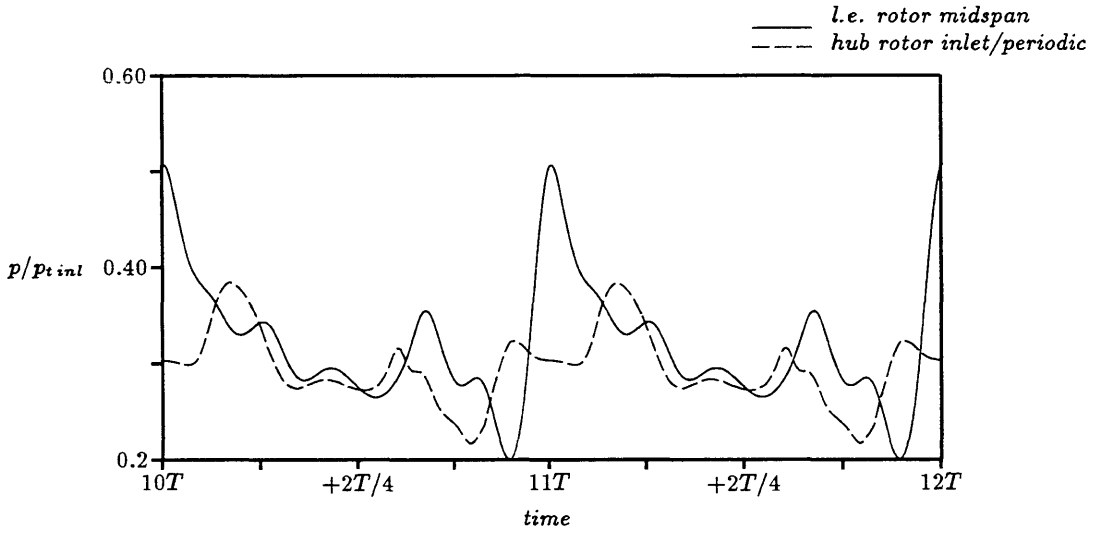

Figure 9.3: Pressure history for the last two periods.

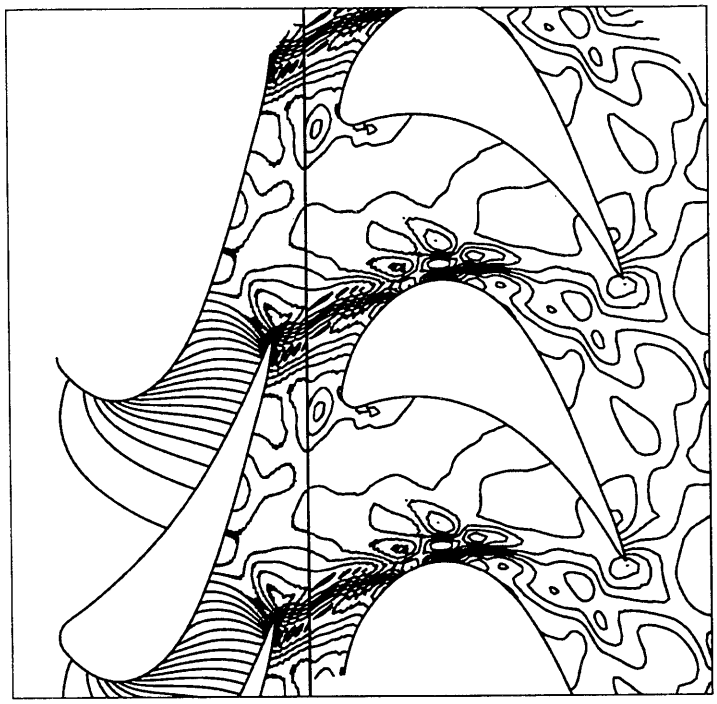

$t = 0.125$

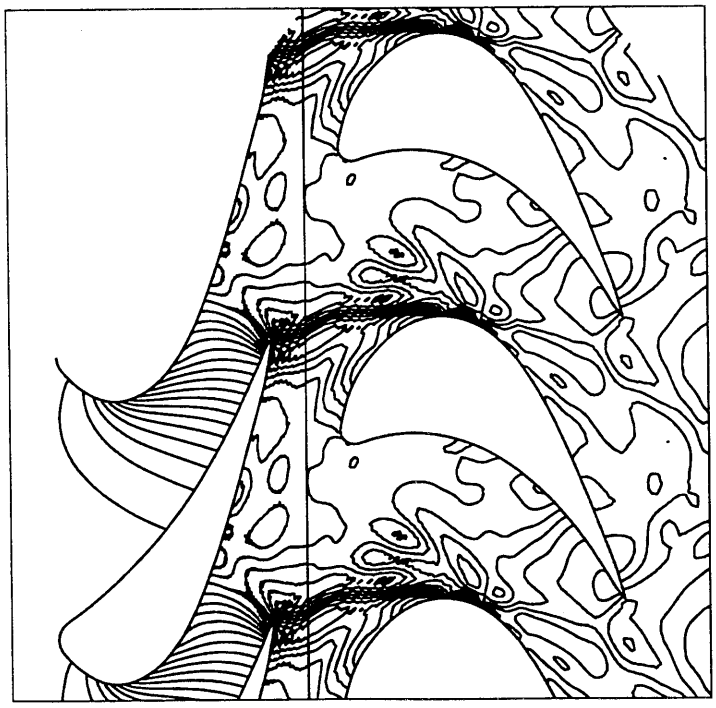

$t = 0.0$

Figure 9.4: Unsteady pressure contours at $R = R_{mid}$.

$t = 0.375$

$t = 0.250$

Figure 9.4 (contd.).

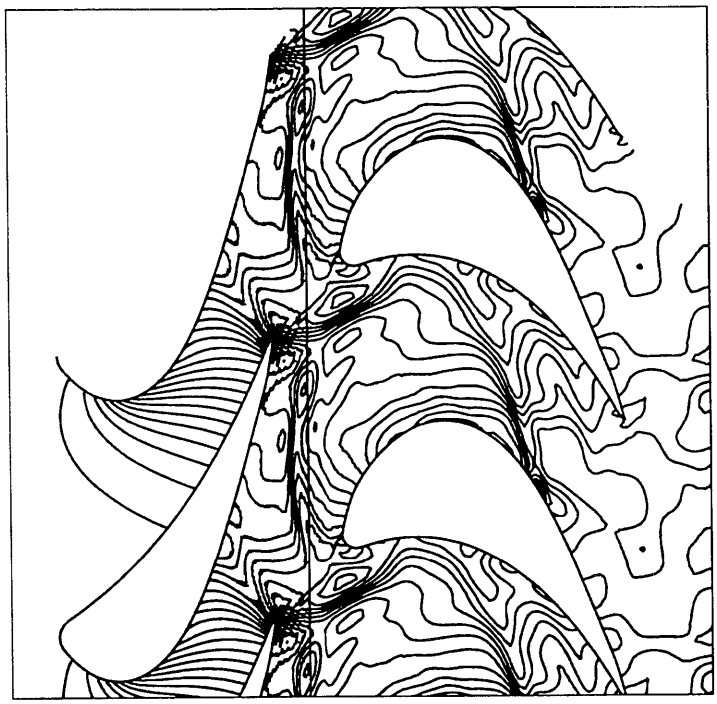

$t = 0.625$

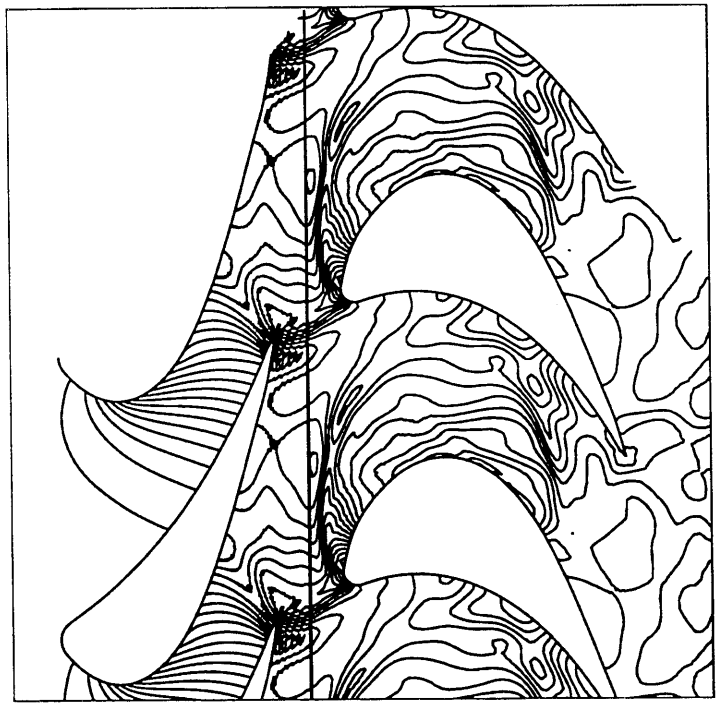

$t = 0.500$

Figure 9.4 (contd.).

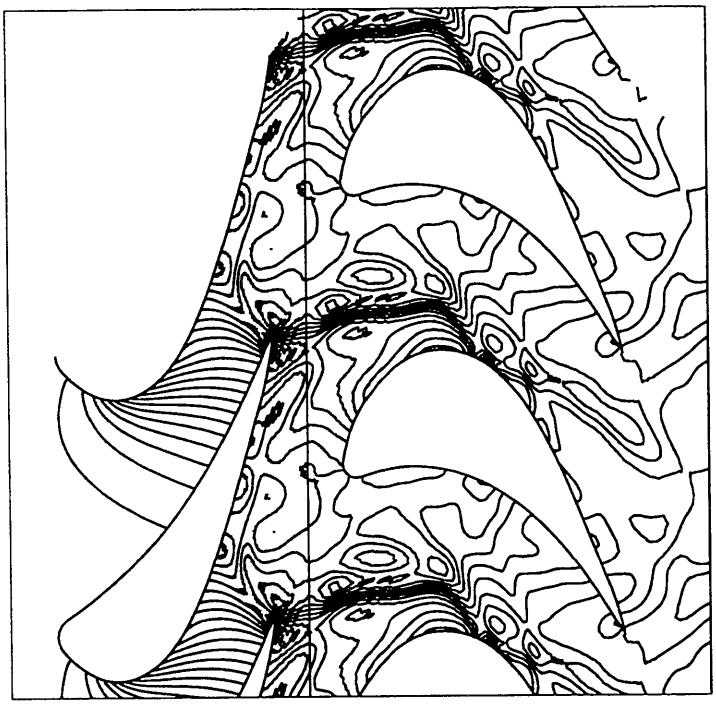

$t = 0.875$

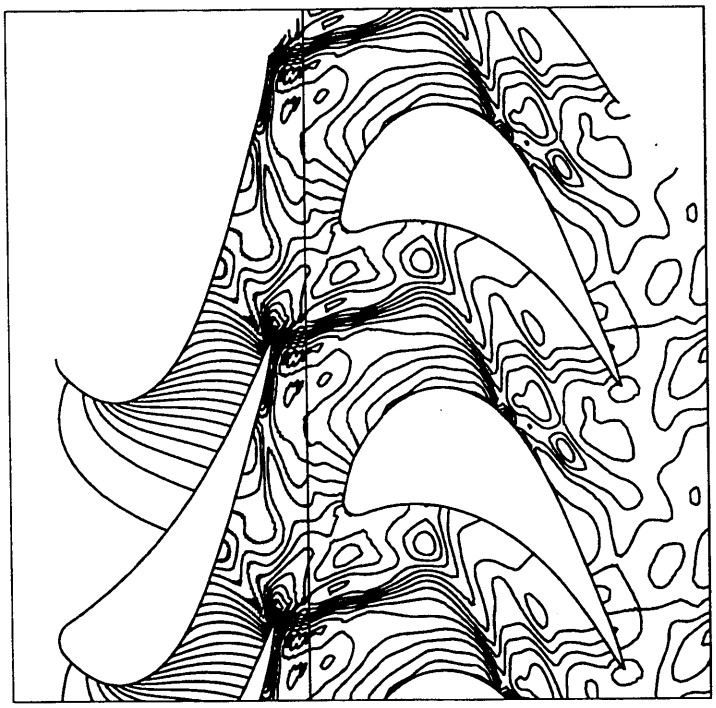

$t = 0.750$

Figure 9.4 (contd.).

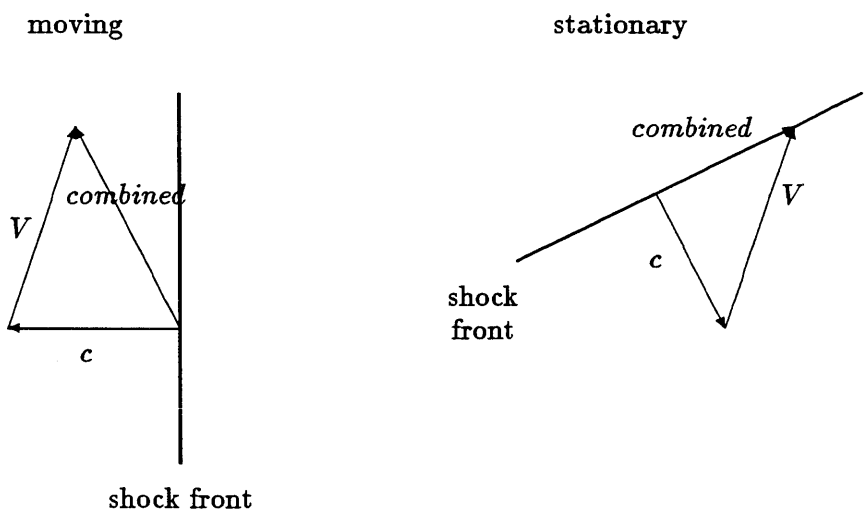

Figure 9.5: Shock velocity triangles.

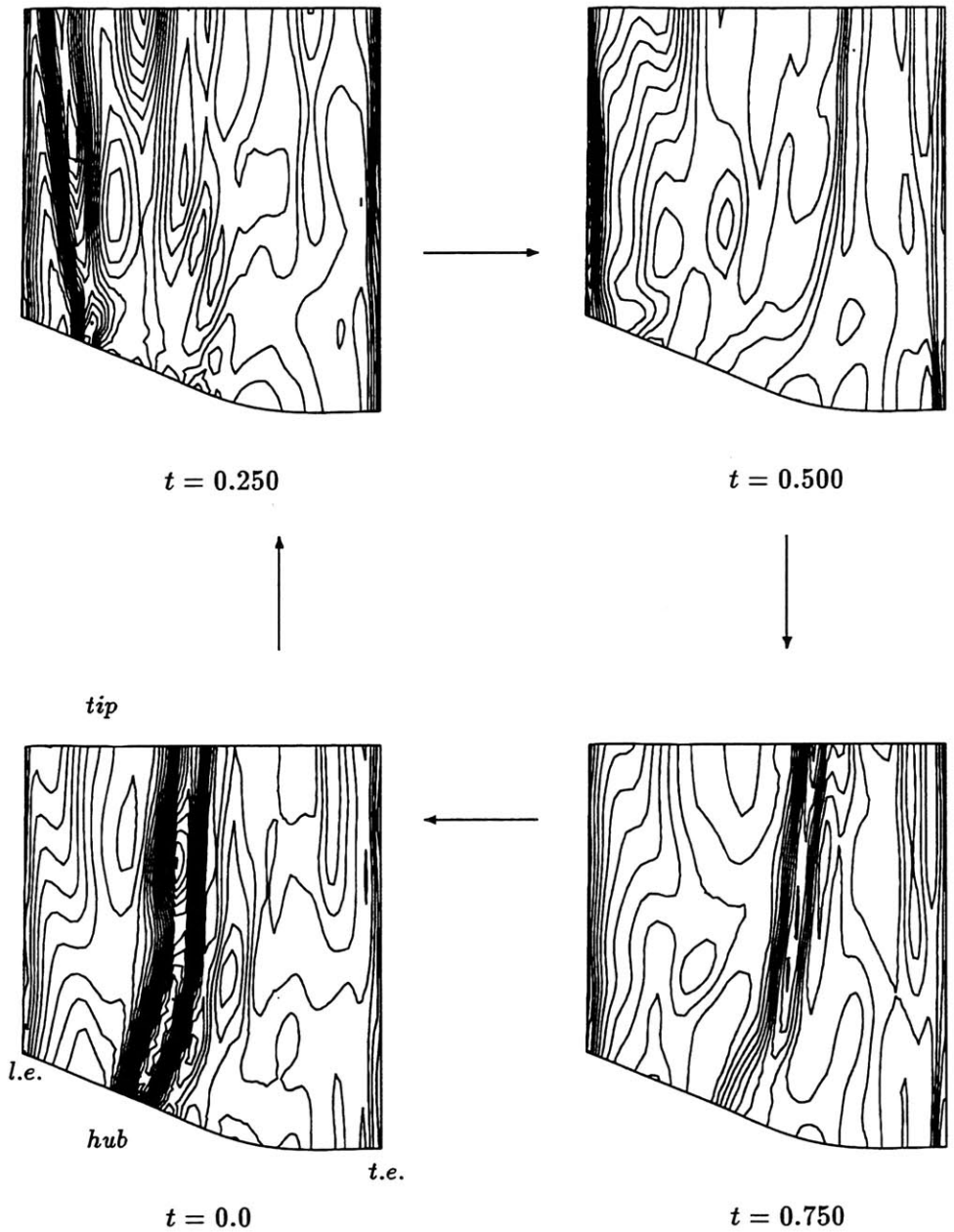

Figure 9.6: Unsteady pressure contours on rotor suction side.

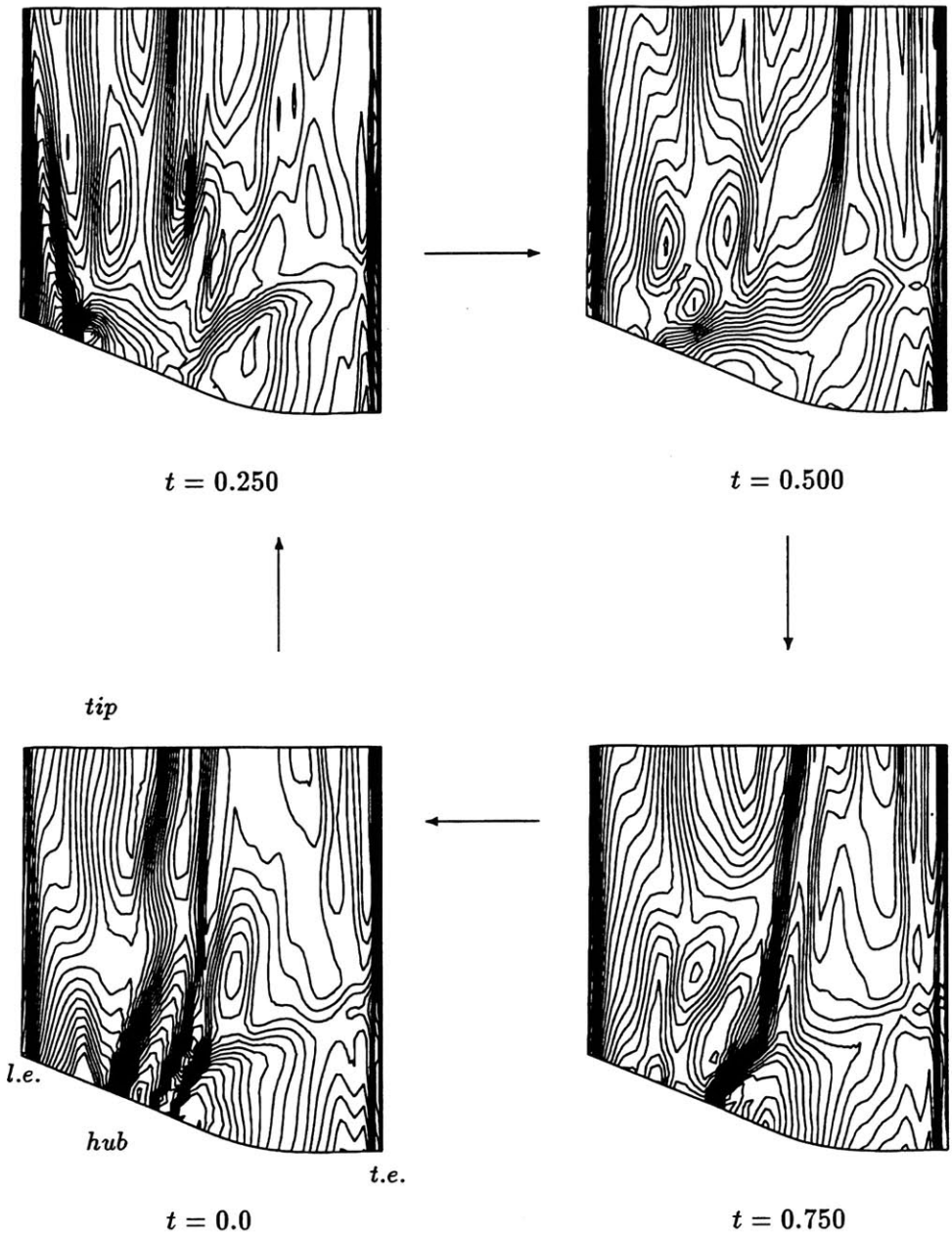

Figure 9.7: Unsteady Mach number contours on rotor suction side.

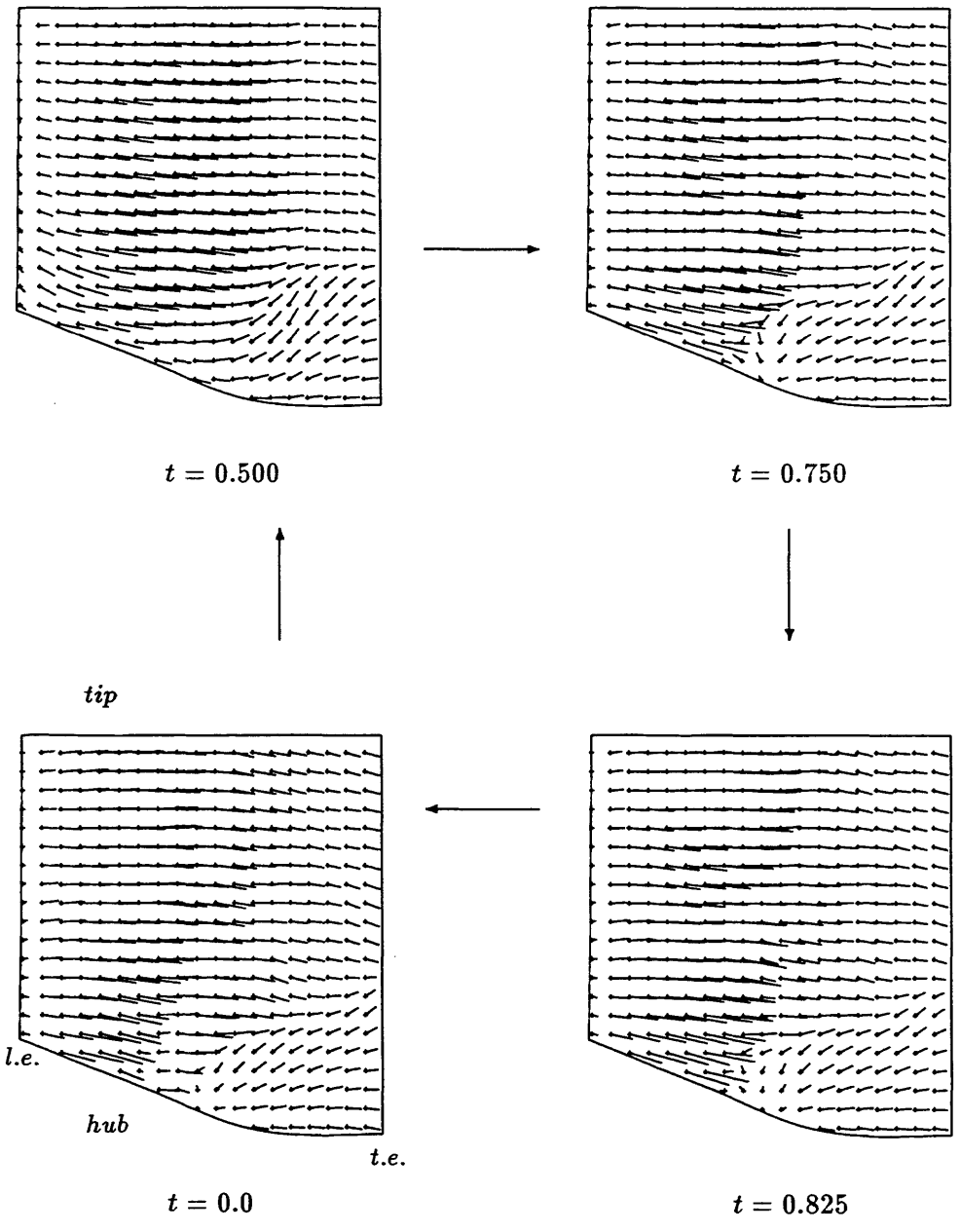

Figure 9.8: Tufts on rotor suction side at different times.

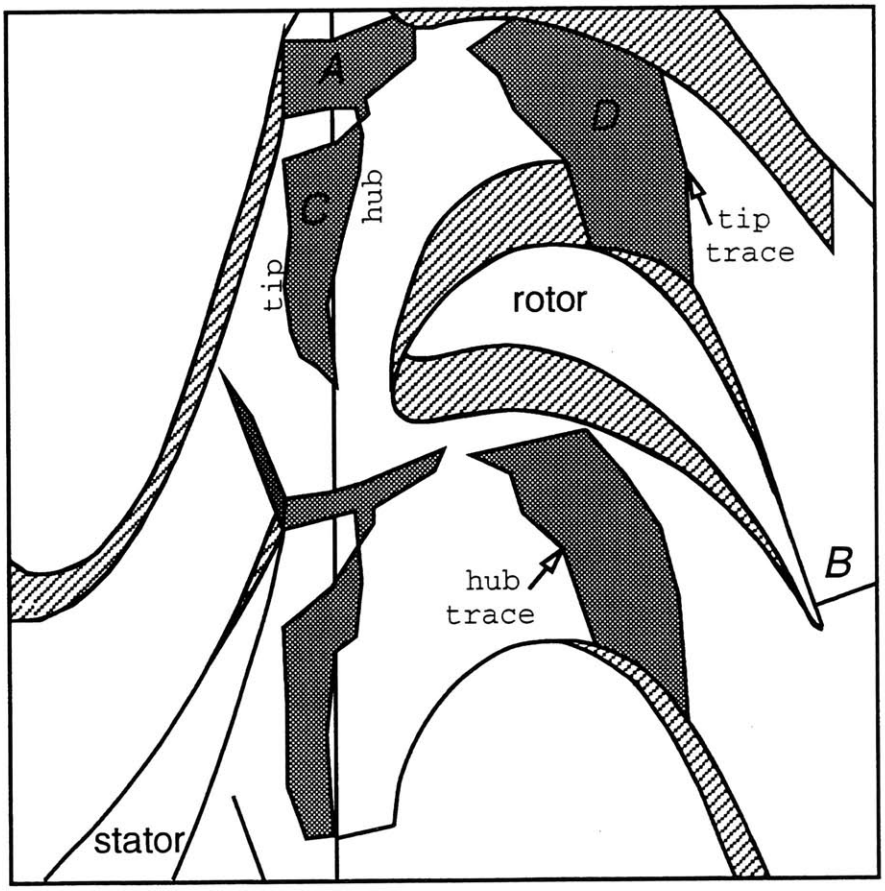

Figure 9.9: Schematic of shock structure at $t = 0.625$.

9.2 Comparison of steady and time-averaged results

The material presented in this section provides an opportunity to compare the steady-state solution with the time-averaged result. The flow conditions for the steady-state and the time-averaged computation are listed in Table 9.1. The Mach and angle values represent average quantities calculated by the flux-averaging procedure described in Section 5.5.

The stator static pressure and Mach number distributions around the blade root are given in Figures 9.10 and 9.11, respectively. The corresponding results at midspan and tip sections are shown in Figures 9.12, 9.13, 9.14 and 9.15. Also shown in these figures are the maximum and minimum unsteady pressures and Mach numbers on both the suction and the pressure sides. These maxima and minima values were extracted from eight unsteady snapshots during the final blade-passing period. Because the flow is choked at the throat, and since the stator inlet conditions are steady, no unsteadiness is present upstream of that area and so the mass flow is the same in both cases. Notice that the time-averaged solution almost matches the steady-state result over the entire stator span.

The rotor blade pressure and Mach number distributions are presented in Figures 9.16, 9.17, 9.18, 9.19, 9.20 and 9.21. Here the unsteadiness is much more intense, especially on the suction side of the blade due to the unsteady shock motion and shock reflection described in the previous section. At the hub, the steady-state shock located at the front part of the suction side is intensified during a portion of the period, which results in a Mach number as high as 2.1. Also, for certain axial locations on the rotor suction side near the leading edge, the peak-to-peak pressure variation accounts for up to 60% of the (stator) inlet stagnation pressure. It is surprising to notice that although the variations in pressure and Mach number are large, the time-averaged solution is similar to the steady-state result over all but the root section of the blade. However, on the suction side lower Mach numbers are generally observed in the time-averaged solution compared to the steady-state result, which can be explained by higher entropy

and rotor-relative stagnation pressure losses occurring during the unsteady flow process.

It should be pointed out that the time-averaged solutions presented in this chapter (and also Chapter 8) were computed during the blade-passing period from *all* the time-steps, i.e. it is a true discrete representation of the following integral.

$$\bar{\bar{\varphi}}(x,y,z) = \frac{1}{T}\int_0^T \varphi(x,y,z,t)dt, \tag{9.1}$$

with $\bar{\bar{()}}$ representing a quantity that has been time-averaged over a period T. On the other hand, the minimum and maximum unsteady values at a certain location were sorted out from eight stored instantaneous solutions, i.e. every 50 time-steps, during the last blade-passing period. This is why a certain amount of discreteness in those quantities is present in the plots of Figures 9.16 through 9.21, in particular.

As described in the previous section, there is a rotor-relative unsteady secondary flow driving hub fluid towards midspan on the aft portion of the suction surface. In the rotor frame of reference, Crocco's equation relating the thermodynamics and fluid kinematics of an inviscid, compressible flow is

$$\frac{\partial \vec{W}}{\partial t} - \vec{W} \times \vec{\omega} = -\nabla I + T\nabla S, \tag{9.2}$$

where $\vec{W}$, I and S represent the relative velocity vector, rothalpy and specific entropy, respectively and $\vec{\omega}$ is the absolute vorticity vector. Equation (9.2) has an important physical interpretation. It shows that when a flow field has gradients of rothalpy (stagnation enthalpy in the absolute frame of reference) and/or entropy it is likely to be rotational[2]. In this application, the rothalpy is almost constant at the rotor inlet. However, as indicated in Figure 9.22 for the rotor suction surface, the entropy production during the unsteady shock motion and symbolized in the time-averaged solution is almost one order of magnitude larger than in the steady-state result. As a consequence of the strong shocks occurring at the rotor root, the entropy gradients are very large in this area. As mentioned earlier, the primary reflection of the stator oblique shock off

[2]Except for the case where $\nabla I = T\nabla S$, which, for transonic flow does not occur. For example, for steady-state flow the rothalpy is constant along a streamline, but not the entropy due to the shock losses.

the rotor suction surface is stronger at the root than at midspan. This also means that the secondary reflection off the adjacent rotor which then moves back towards the original rotor is stronger. The resulting strength of the upstream moving shock is therefore larger at the hub. It seems that the vorticity production is large enough to generate a secondary flow during the entire blade-passing period, see Figure 9.23.

Using secondary flow theory , it is possible to be precise in the explanation for the cross-flow seen in Fig. 9.23. For instance, in the work of Smith [100], Hawthorne [48, 50, 51], Lakshminarayana and Horlock [69], and Johnson [59], the equation for the generation of a streamwise component ω_s of vorticity is derived. For incompressible inviscid flow this equation has the following form.

$$\frac{\partial}{\partial s}\left(\frac{\omega_s}{\rho W}\right) = \frac{2}{\rho W^2}\left(\underbrace{\frac{1}{\sigma}\hat{b}\cdot\nabla p_t^\star}_{\text{curvature}} + \underbrace{\frac{1}{W}\vec{\Omega}\cdot\nabla p_t^\star}_{\text{rotation}}\right). \tag{9.3}$$

Equation (9.3), is written in intrinsic coordinates where $\hat{s}, \hat{n}, \hat{b}$ represent the unit vectors in the direction of relative streamline, inward of principal normal and in the binormal direction, respectively. σ is the principal radius of curvature of the relative streamline and $p_t^\star$ is the rotary stagnation pressure defined in Eq. (7.24). In the above equation, two terms contribute to the generation of streamwise vorticity, one due to the curvature of the streamline with radius σ, and one due to the rotation Ω around the x axis. These contributions are due to the gradients of rotary stagnation pressure in the binormal and axial directions, respectively.

As seen in Figure 9.17, the Mach number and hence velocity field behind the shocks occuring on the rotor suction side is smaller than in the steady-state case. Thus, assuming locally incompressible flow streamwise vorticity can be generated if a gradient of rotary stagnation pressure exist in the direction of the axis of rotation. In Figure 9.24 the steady and time-averaged rotary stagnation pressure on the rotor suction surface are compared. In the steady-state calculation $p_t^\star$ is almost constant over the entire blade except behind the hub shock. In the time-averaged solution however, gradients of rotary stagnation pressure show up not only near the location of the steady-state shock but

over the entire near-hub suction surface. Hence, the comparison clearly shows that a strong axial p_t^* gradient exists in the time-averaged solution which, when dot-producted with the rotation vector, produces a positive component of streamwise vorticity. This tends to develop a radially outward component of velocity.

It is interesting to notice that the rotor-relative secondary flow creates a slight blockage of the annulus passage. This becomes apparent when comparing the spanwise mass flow distributions at the rotor inlet for the steady and the time-averaged solution, see Figure 9.25. In order to compensate for the lack of mass flow at the lower radii, an increased amount of fluid streams through the rotor from midspan to the tip.

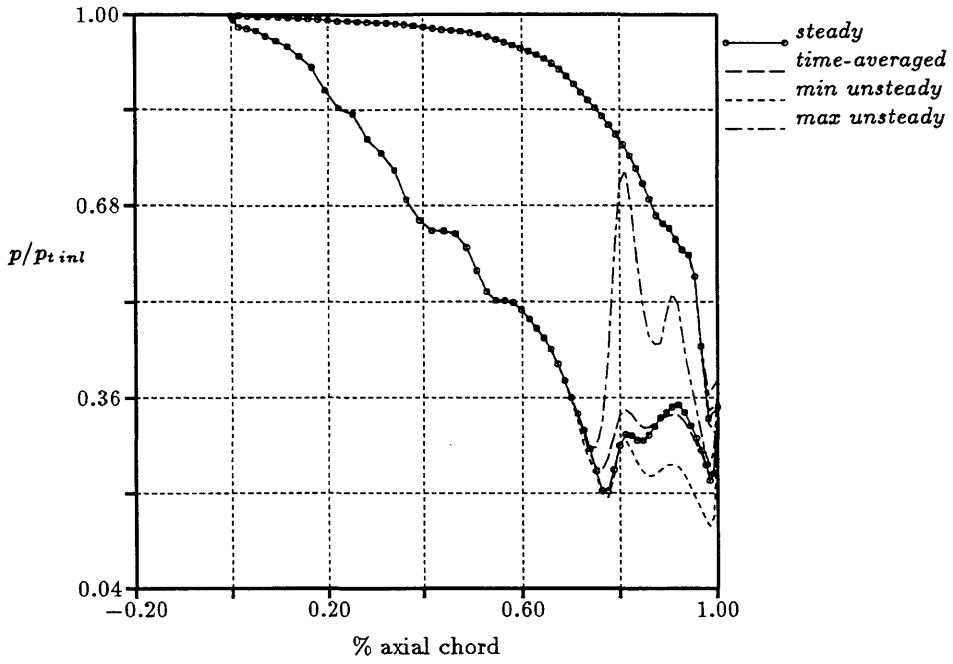

Figure 9.10: Steady and unsteady stator blade pressure at the hub.

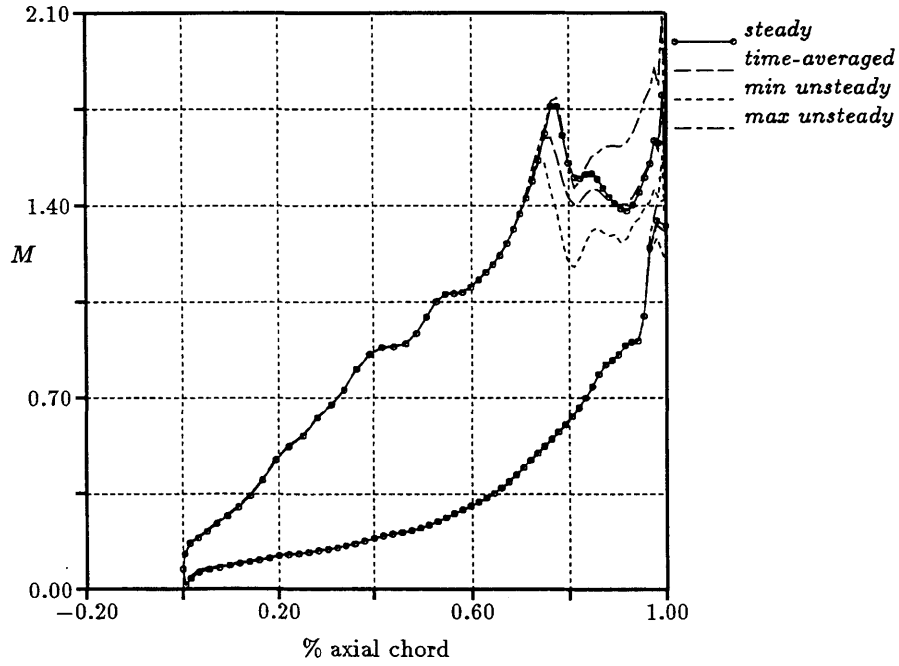

Figure 9.11: Steady and unsteady stator blade Mach number distribution at the hub.

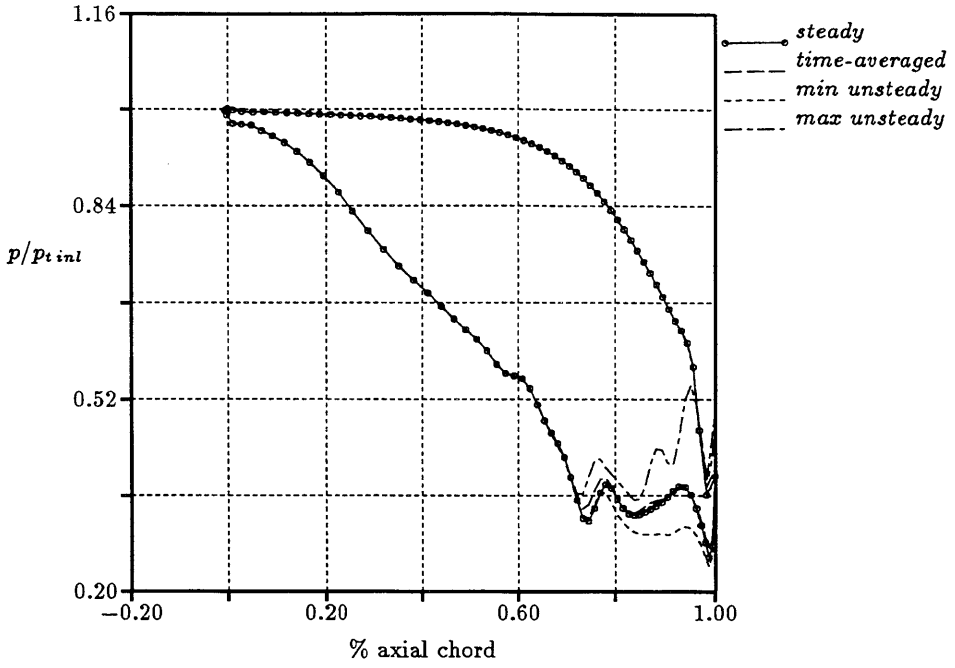

Figure 9.12: Steady and unsteady stator blade pressure at midspan.

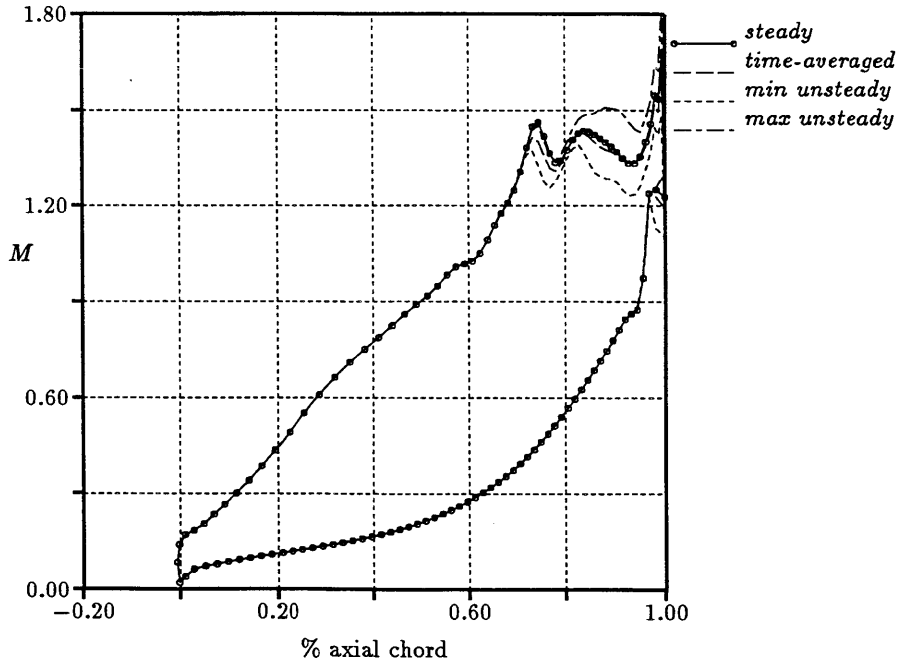

Figure 9.13: Steady and unsteady stator blade Mach number distribution at midspan.

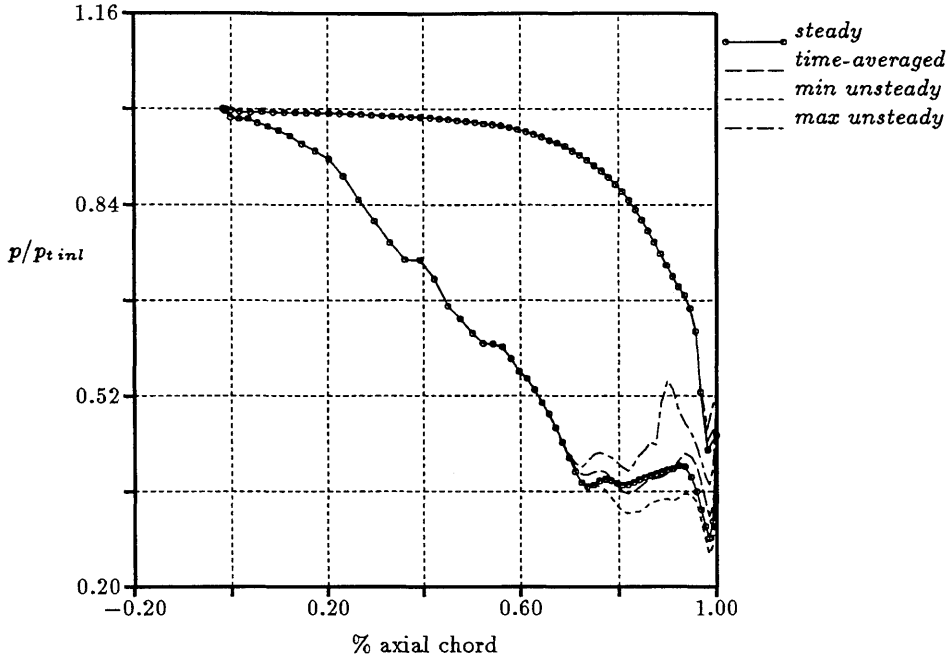

Figure 9.14: Steady and unsteady stator blade pressure at the tip.

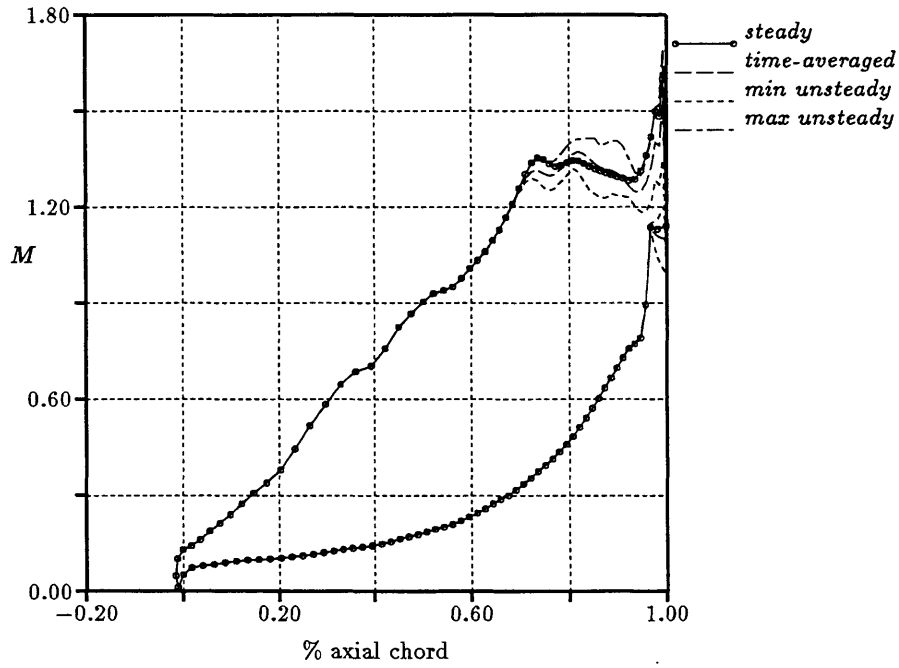

Figure 9.15: Steady and unsteady stator blade Mach number distribution at the tip.

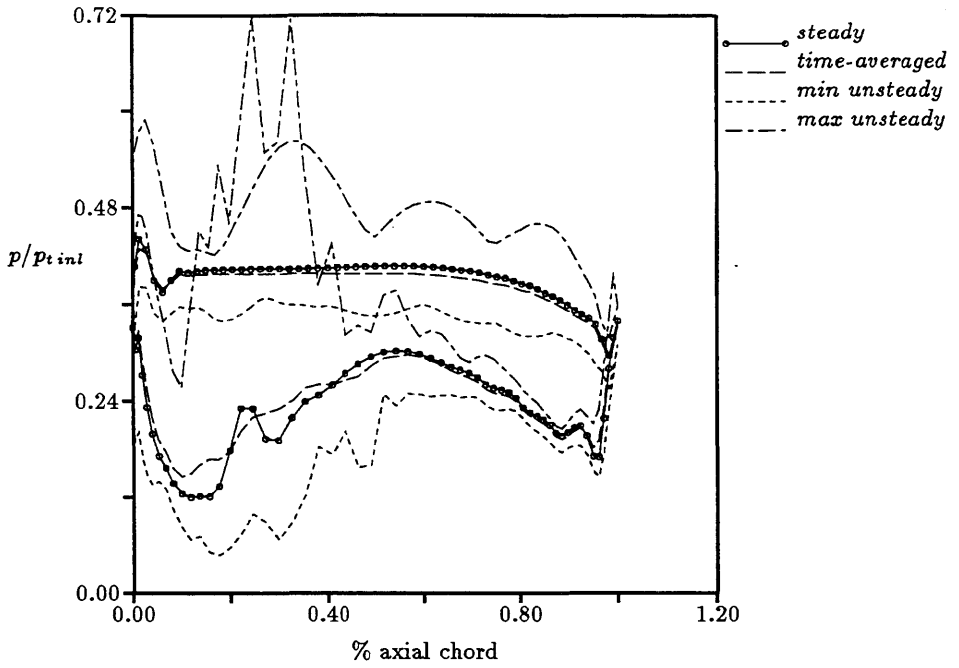

Figure 9.16: Steady and unsteady rotor blade pressure at the hub.

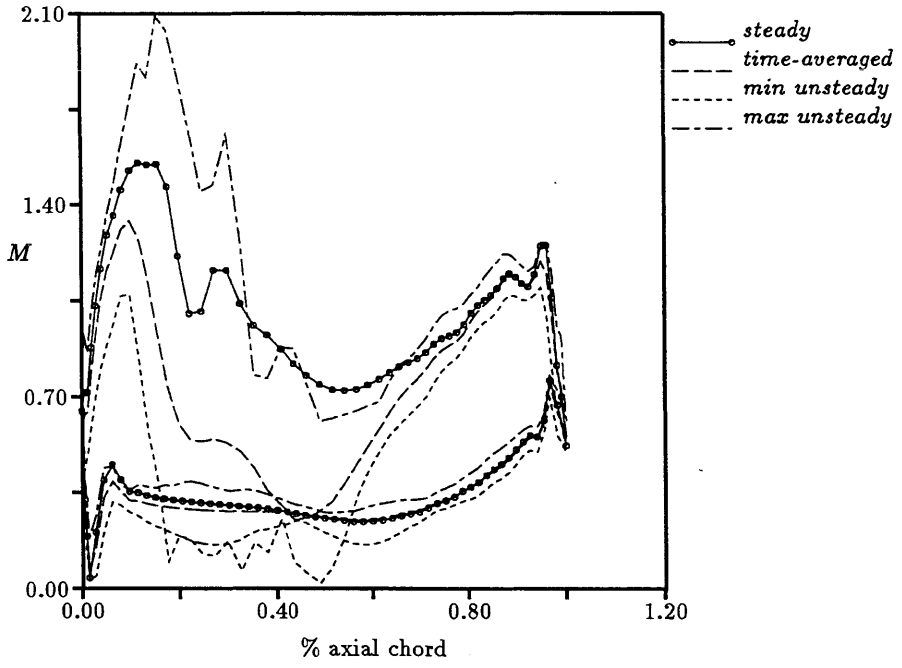

Figure 9.17: Steady and unsteady rotor blade Mach number distribution at the hub.

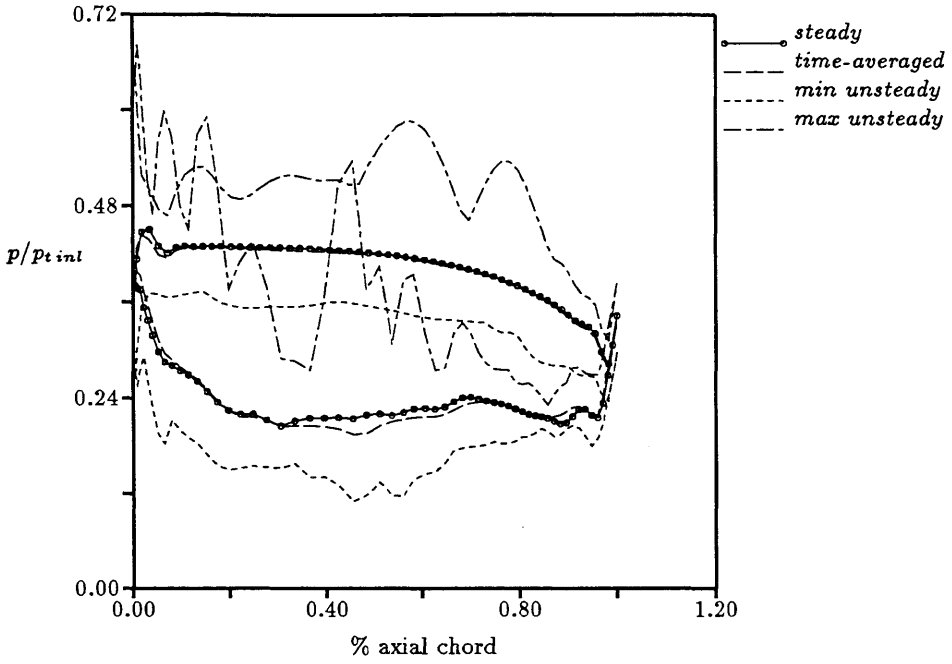

Figure 9.18: Steady and unsteady rotor blade pressure at midspan.

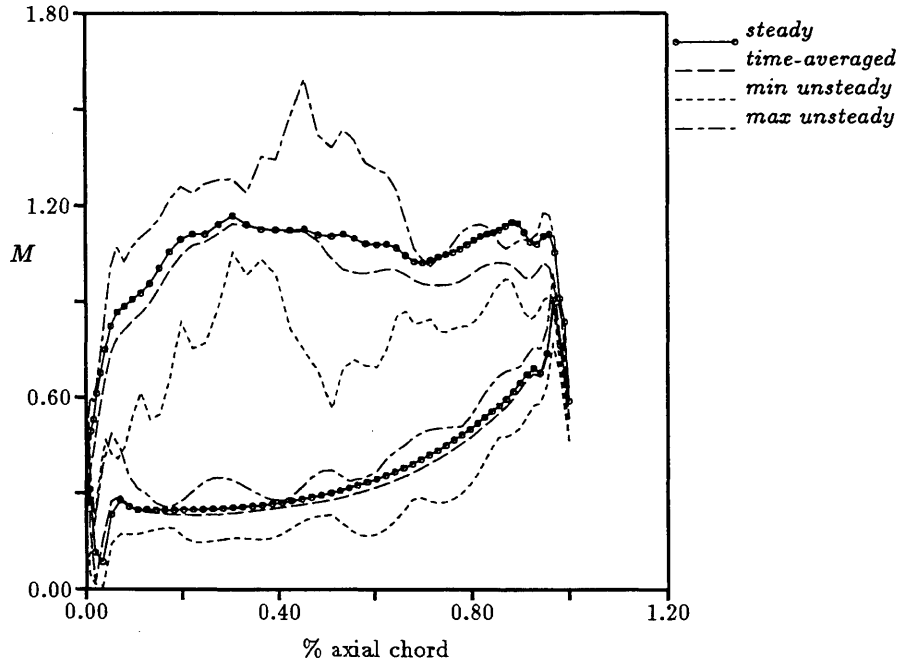

Figure 9.19: Steady and unsteady rotor blade Mach number distribution at midspan.

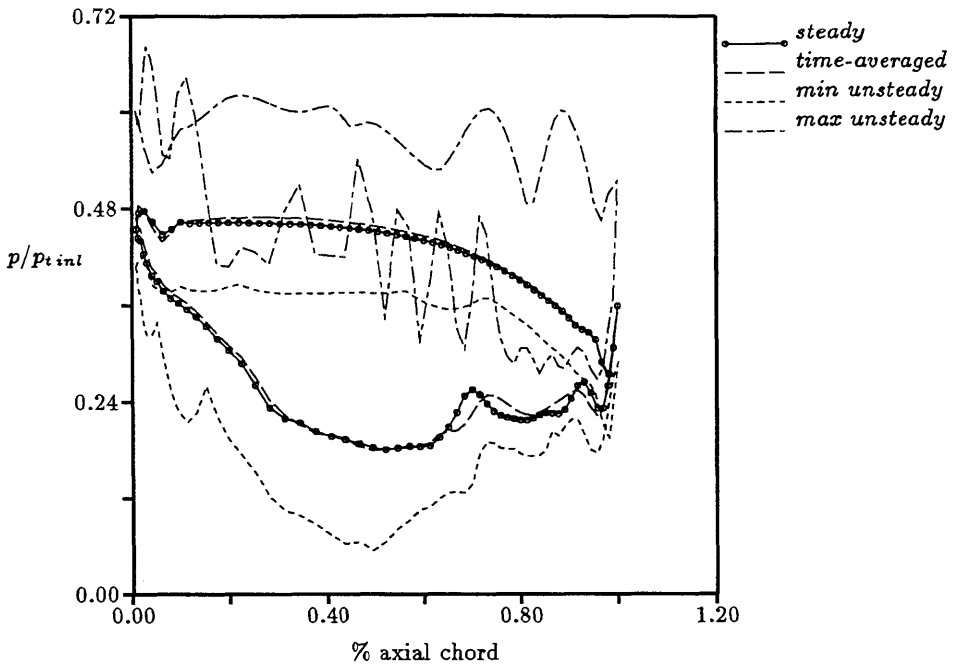

Figure 9.20: Steady and unsteady rotor blade pressure at the tip.

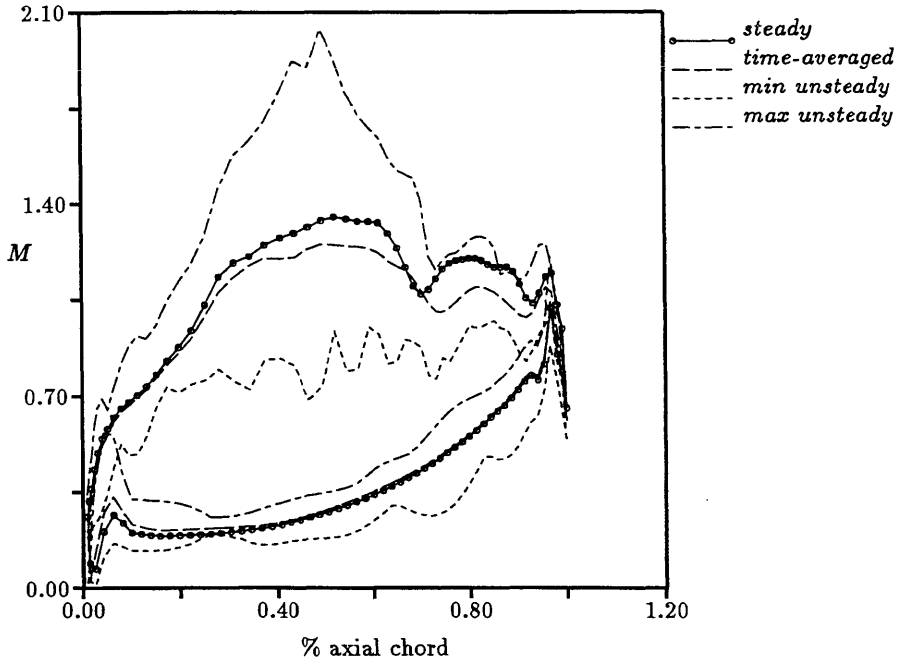

Figure 9.21: Steady and unsteady rotor blade Mach number distribution at the tip.

b)

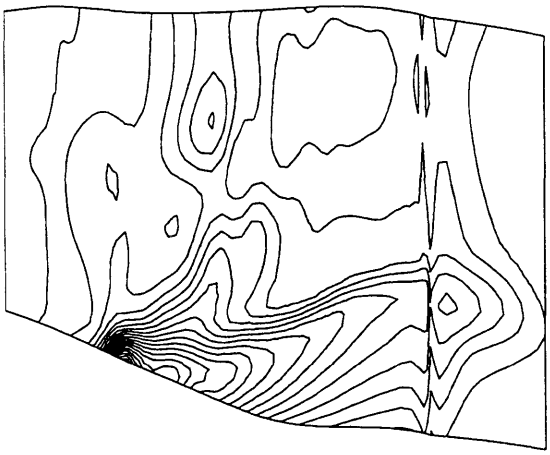

a)

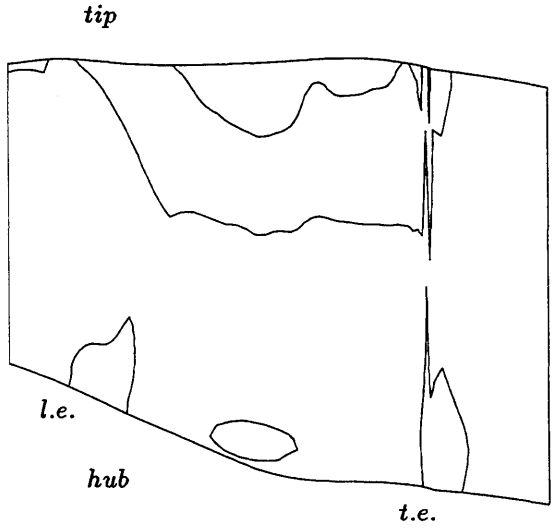

Figure 9.22: Entropy contours on rotor suction side: a) steady-state and b) time-averaged.

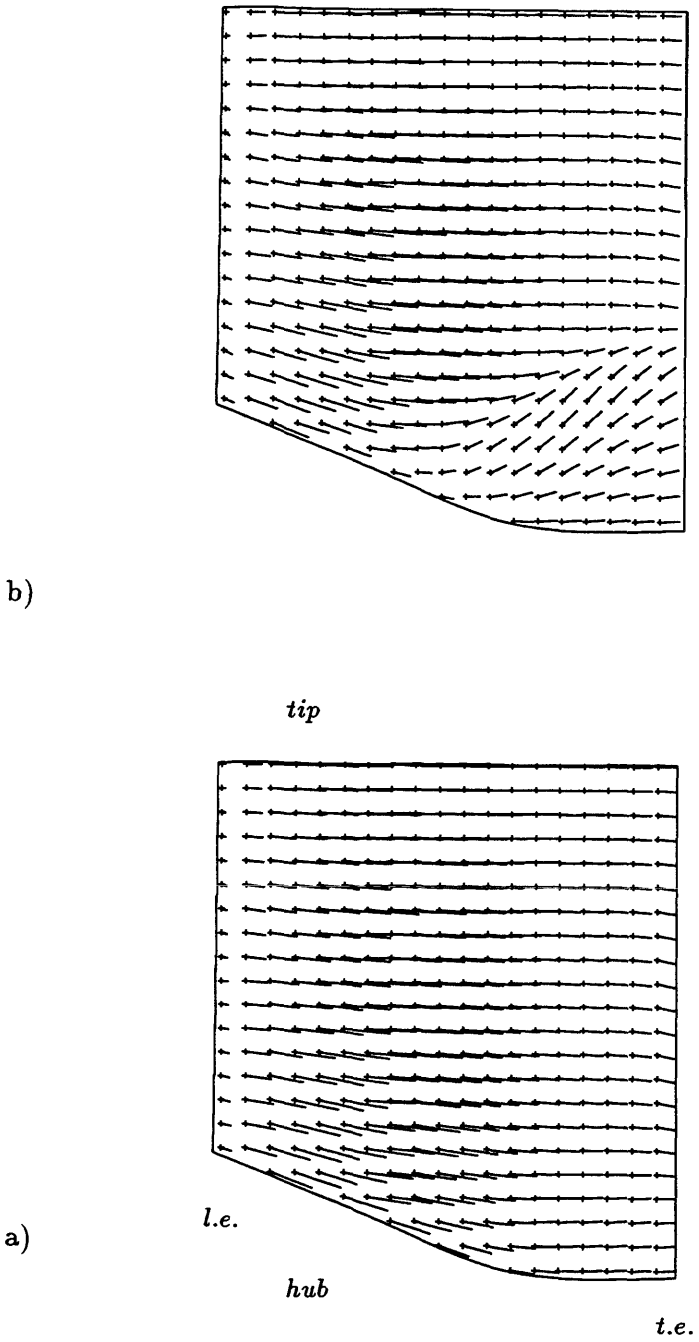

Figure 9.23: Tufts on rotor suction side: a) steady-state and b) time-averaged.

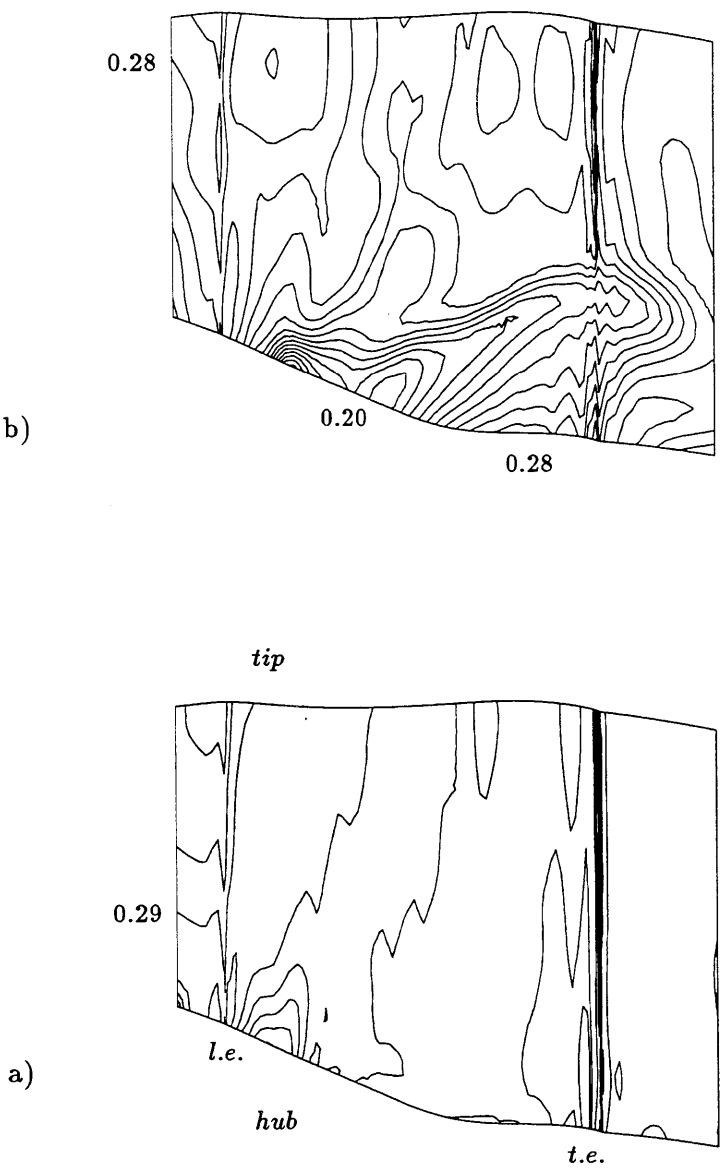

Figure 9.24: Rotary stagnation pressure ($p_t^*/p_{t\,inl}$) contours on rotor suction side: a) steady-state and b) time-averaged. Increments = 0.01.

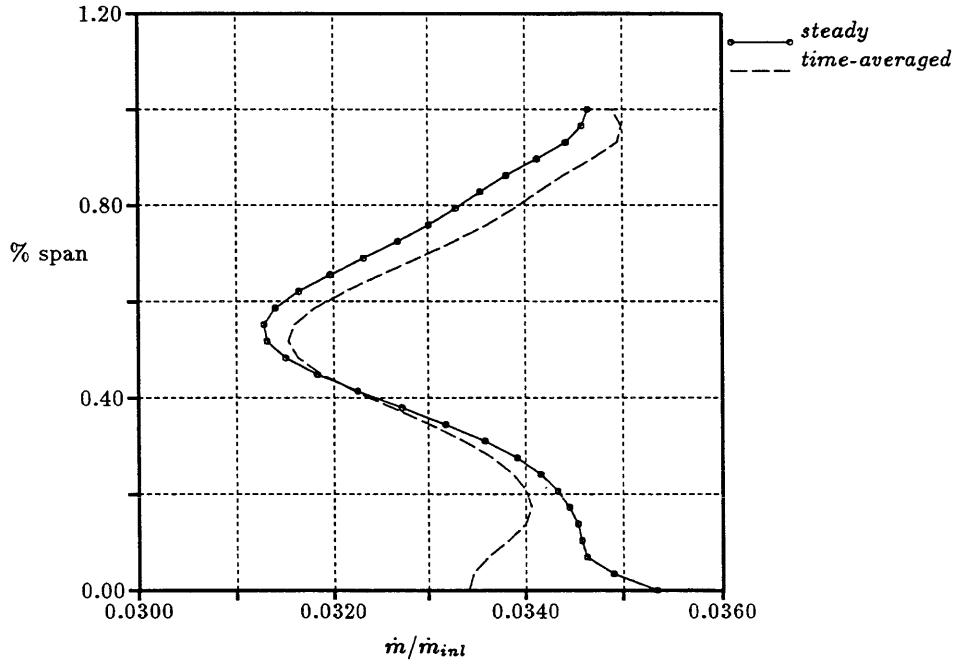

Figure 9.25: Spanwise mass flow distribution at the rotor inlet.

9.3 Consequences and conclusions

The unsteady non-dimensional torque acting on the stator and the rotor during one blade-passing period is shown in Figures 9.26 and 9.27, respectively. The distribution is found from eight intermediate unsteady solutions that were stored during the computation. Also, represented on those figures is the corresponding steady and time-averaged torques. On the stator, there is a 6% peak-to-peak variation in torque, despite the fact that the pressure field is steady on all but a small portion of the suction (and also pressure) side near the trailing edge. The variation is essentially caused by the primary rotor-reflected shock moving upstream and striking the stator suction side. The strong unsteady shock motion described earlier causes the rotor torque to vary 66% peak-to-peak. Notice that in the 2-D simulation [33] the unsteady stator lift has a peak-to-peak variation of 6%, which compares well to the 3-D case. However, as opposed to the 66%, 'only' 40% peak-to-peak variation in lift is experienced by the rotor in the 2-D case. Indeed, in the 3-D simulation larger unsteady variations occur at the tip and especially at the root compared to midspan.

There are several consequences associated with the unsteady shock motion and hence unsteady torque. These are discussed in Reference [33]. Experimental work has been done in order to predict the effects of shock waves passing on a turbine rotor blade, see for instance References [93, 58, 18]. It has been observed that the shock striking the rotor suction surface does cause a temporary boundary-layer separation. These separation bubbles convect downstream along the blade surface and subsequently collapse into turbulent flow which increases the heat transfer rate and the viscous losses. Also, the unsteady shock reflections produce an adiabatic compression of the boundary-layer which in turn gives rise to transients in the heat transfer. Other consequences involve structural excitations and amplified vortex shedding at the blunt trailing edge leading to increased base losses. In addition, associated with the unsteady torque there must be an unsteady vortex sheet shed at the trailing edge, whose energy is eventually dissipated, thus contributing to increase the overall losses.

However, an important conclusion from these results is that in many aspects the the steady-state results are extremely close to the time-averaged values. For instance, the maximum variation in the blade static pressure[3] between the steady-state and the time-averaged solution is less than 4% of the stator inlet stagnation pressure, a value 15 times smaller than the maximum local unsteady fluctuation (peak-to-peak value). The agreement is even better for integral values such as the axial torque, with a difference less than 0.5% of the time-averaged value.

The results presented by Jorgenson [60] and Chen [12] for subsonic flow indicate that the effect of changing the periodicity, i.e. ratio of stator-to-rotor pitch, on the time-averaged solution is small. For instance, in Ref. [60] less than one percent difference is observed in the time-averaged rotor lift for a change in stator-to-rotor pitch ratio from 1:1 to 2:3, although the magnitude of the unsteady lift (envelope) increases from 4% to 20% of the time-averaged value. The comparison between the present 3-D shock interaction with the 2-D simulation of Giles [33] indicates that the rotor blade experiences similar shock reflections, although the difference in pitch ratios shows up in the pattern of the unsteady lift during the blade-passing period. This suggests that although the time-averaged solution is affected by the blades pitch ratio, the match between the time-averaged and the steady-state solution is not dependent from the stator-to-rotor pitch ratio.

[3]The maximum discrepancy between the two solutions is located at the rotor root on the suction side.

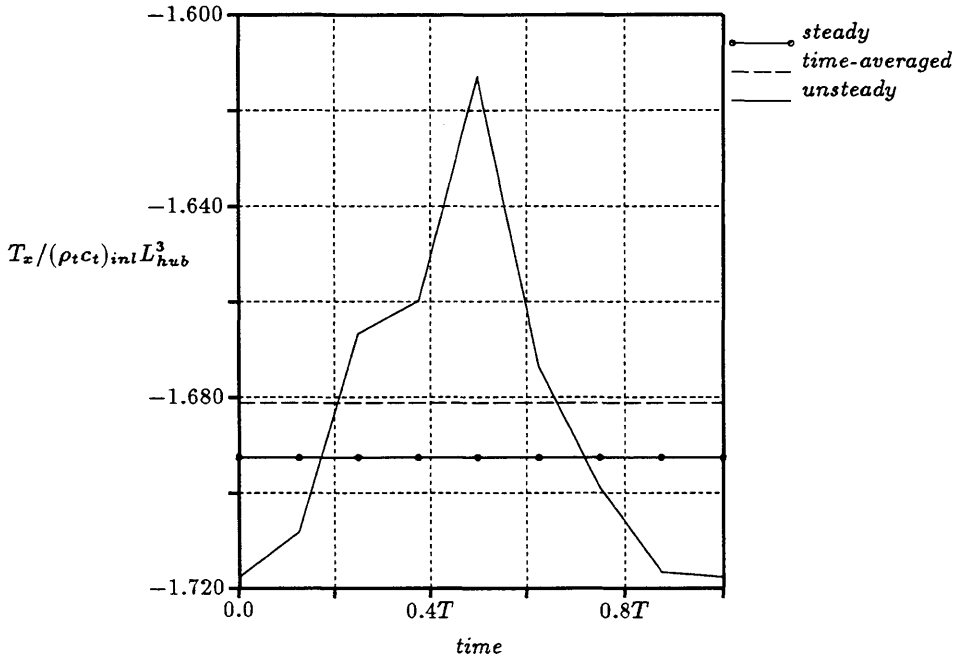

Figure 9.26: Unsteady stator torque.

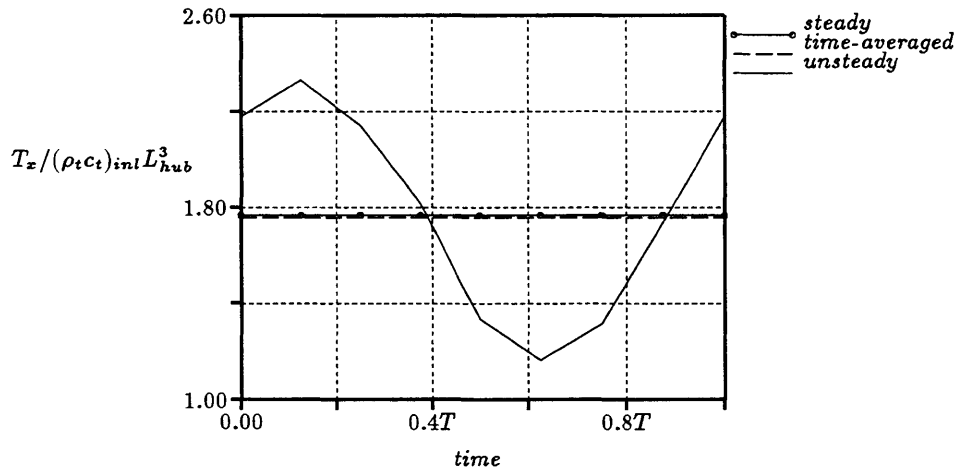

Figure 9.27: Unsteady rotor torque.

parameter		*steady*	*time-averaged*
Stator inlet tangential angle	hub	0.0^0	0.0^0
	mid	0.0^0	0.0^0
	tip	0.0^0	0.0^0
Stator outlet tangential angle	hub	72.1^0	72.6^0
	mid	74.8^0	74.6^0
	tip	73.9^0	73.8^0
Rotor-relative inlet tangential angle	hub	51.3^0	53.4^0
	mid	50.2^0	51.0^0
	tip	40.6^0	41.1^0
Rotor-relative outlet tangential angle	hub	-57.1^0	-60.6^0
	mid	-67.8^0	-67.0^0
	tip	-76.3^0	-76.8^0
Stator inlet Mach number	hub	0.15	0.15
	mid	0.13	0.13
	tip	0.13	0.13
Stator outlet Mach number	hub	1.37	1.33
	mid	1.25	1.24
	tip	1.19	1.18
Rotor-relative inlet Mach number	hub	0.69	0.67
	mid	0.52	0.52
	tip	0.44	0.44
Rotor-relative outlet Mach number	hub	1.00	0.99
	mid	0.96	0.97
	tip	0.95	0.93
Rotor Mach number	hub	0.76	0.73
	mid	0.81	0.79
	tip	0.86	0.84
Rotor wheel speed $\left(\frac{\Omega}{c_{t\,inl}/L_{hub}}\right)$		0.097	0.097
Stator axial torque $\left(\frac{T_x}{(\rho_t c_t)_{inl} L_{hub}^3}\right)$		-1.6926	-1.6812
Rotor axial torque $\left(\frac{T_x}{(\rho_t c_t)_{inl} L_{hub}^3}\right)$		1.7678	1.7579
Ratio of specific heats γ		1.27	1.27

Table 9.1: Steady and time-averaged flow parameters for scaled transonic turbine stage.

Chapter 10

Concluding Remarks

If winning is not important, why count points? Lt. Worf, Star Trek the Next Generation.

A summary of the thesis is presented in Section 10.1, followed in Sections 10.2 and 10.3 by the major contributions and essential conclusions, respectively. Finally some extensions and recommendations for future research are discussed in Section 10.4.

10.1 Summary

This thesis has presented a numerical method for solving the equations of motion of a 3-D, inviscid, compressible steady and/or unsteady flow within an axial turbine stage. The material has been divided into two distinct parts. The numerical methodology is described in the first part, which includes both the discretization procedure and the handling of the boundary conditions. In particular, the main endeavor has been put towards the development of novel *quasi-3-D non-reflecting boundary conditions* for steady-state inviscid flow fields. In the second part of the work, the numerical method is applied to three major cases involving subsonic and transonic flow with inlet distortions.

The governing Euler equations are solved in conservation form which allows for the correct representation of the Rankine-Hugoniot shock jump relations. The numerical

methodology uses a node-based, explicit Ni-Lax-Wendroff discretization scheme implemented on an unstructured grid composed of hexahedral cells. Relative flow variables attached to each individual blade row are used. The mesh itself is generated in a structured fashion by iteratively solving a 3-D Poisson system, in which the source terms are automatically evaluated in order to provide a control of the cell size and skewness at the blade boundary. The Euler algorithm presented here requires the addition of a fourth-difference numerical smoothing in order to prevent unwanted high frequency oscillations in the solution. The formulation of this smoothing, which exploits the advantages of a pseudo-Laplacian, and its accuracy were discussed. The shocks are captured using a non-linear second-difference operator acting on the state vector. For the cases presented in this study, a CPU time of the order of 385×10^{-6} seconds/iteration/grid point was required on a Stardent GS-2000 in vector mode.

A significant portion of the thesis, i.e. Chapter 5, Appendix D and Section 8.3, is devoted to the analysis and the implementation of the inlet, outlet and stator/rotor interface boundary conditions. In particular, a theory for the construction of steady-state quasi-3-D non-reflecting boundary conditions was introduced and applied to the Euler equations. Eigenmode solutions of the linearized equations which vary sinusoidally in the pitchwise direction were derived according to Fourier analysis. These were then used to obtain linear relationships between the steady-state perturbations in density, velocity and pressure at inflow and outflow boundaries which produce no incoming modes. The treatment of the interface plane between a stator and a rotor was also presented. For steady-state flow, a circumferential stream-thrust flux-averaging technique is used to conserve mass, momentum and energy across the mixing plane. The coupling between this technique and the non-reflecting boundary condition formulation was discussed. To illustrate the benefit of the non-reflecting boundary conditions, solutions using the novel formulation were presented and compared to the solutions obtained using the standard 1-D boundary condition approach. This was done for several 3-D cases including a transonic flow in a vane, a transonic stator/rotor combination and a 3-D linear subsonic cascade flow. The effect of placing the boundaries at different axial locations was also discussed. For unsteady flow, i.e. time-accurate calculations of stator/rotor flow fields,

a simple interface model based upon the 1-D characteristics theory was presented.

The validation of the code as a research tool for internal, steady and time-accurate fluid flow problems was accomplished by comparing the numerical solution with analytical and experimental data, by evaluating errors in stagnation properties (for subsonic uniform inlet conditions) and by assessing the errors in mass flow, angular momentum and axial torque.

Three cases directly related to flow phenomena occurring in a typical transonic first turbine stage were examined. The first, discussed in Chapter 7, concerned the steady-state secondary flow occurring in a rotor due to a spanwise non-uniform stage inlet stagnation temperature distribution. A comparison was made between the resulting flow field and the solution obtained with uniform inlet conditions. The analysis showed that rotor-relative secondary flow occurred as a consequence of both rotor-relative radial total pressure and inlet angle distributions. The results were also explained in terms of rotor inlet streamwise vorticity distribution. In addition, the analysis showed that the stator flow field was also affected by the introduction of the total temperature variation.

The second case involved the combined effects of a velocity shear flow and a spanwise temperature gradient on a rotor flow field (Chapter 8). The inlet vortical disturbance was modelled using potential theory. Steady as well as unsteady results were presented and discussed in terms of rotor-relative stagnation temperature, stagnation pressure and static pressure distributions. The features of the rotor flow field, and in particular the mechanisms for creating the radial flow, were discussed using secondary flow theory.

The final case, presented in Chapter 9, consisted of an analysis of steady, unsteady and time-averaged flow fields occurring in a typical highly loaded transonic first turbine stage. The sequencing of the unsteady events and in particular the unsteady shock motion was explained. Compared to the steady-state result, a rotor-relative secondary flow was observed during the unsteady process as well as in the time-averaged solution. The analysis also focussed on comparing the steady to the time-averaged solution for

both the stator and the rotor flow field. Unsteady deviations from the time-averaged result were assessed. The analysis concluded by addressing some of the consequences of the strong unsteady shock motion in terms of blade loading, boundary-layer behavior and heat transfer.

10.2 Contributions

One of the most significant contribution of this thesis to CFD is the introduction of the *quasi-3-D non-reflecting boundary conditions* discussed from a theoretical point of view in Chapter 5. A fundamental approximation is that radial effects are accounted for in the average mode only. With this procedure, the computations can be performed on truncated domains where the inlet and outlet boundaries can be located close to the blades. Also, this procedure can be used in conjunction with the flux-averaging technique for transferring information across the stator/rotor interface in a manner that conserves fluxes of mass, momentum and energy and avoids spurious reflections. From a practical point of view, this means that there is no need for 'human' intervention at the interface in order to match the stator and the rotor flow field. The results presented indicate that they are extremely effective in a typical industrial turbomachinery environment, even in the presence of shock waves crossing the boundaries. In particular, the second-order non-linear errors together with the error due to the uncoupling of the radial and tangential variations are much smaller than the ones introduced in the solution using the standard one-dimensional approach. Relative to the 1-D formulation, the increase in computational cost using the quasi-3-D technique is negligible. Also from a CFD point of view, the unsteady results presented here suggest that the use of a simple 1-D characteristics-based, linear interpolation procedure at a sliding stator/rotor interface is good enough for engineering applications.

The time-marching, cell-vertex, discretization procedure described in Chapter 3 does not represent by itself a significant contribution. In fact, the Ni-Lax-Wendroff algorithm

is rather widely used nowadays, though the formulation presented here may differ from others in specific details such as the arrangement and definition of the (volume/time-step) ratio and the discretization of the second-order source terms. It is the combination of this algorithm with the second- and fourth-difference numerical smoothing, implemented on an unstructured grid that, to the author's knowledge, represents an original contribution. In particular, the fourth-difference smoothing extended to 3-D from an original idea of Holmes and Connell [54] is very efficient in not corrupting linear functions on an irregular grid even with cells' aspect ratios well above 10.

10.3 Conclusions

From the application point of view, there are several conclusions that can be drawn from the three cases presented in Chapters 7, 8 and 9. One conclusion is that in many aspects, especially in the static pressure distribution, the steady-state flow solution agrees extremely well with the time-averaged result. It is believed that such good agreement between the two solutions is greatly due to the use of the non-reflecting boundary conditions in the steady-state calculation of the stator/rotor interface. By avoiding spurious reflections and by providing a relieving effect for the flow to account for the presence of the leading and the trailing edge of neighboring blades, these steady-state conditions represent, to a good approximation, the time-averaged physical phenomena.

For subsonic flow, the results of Chapter 8 indicate that the introduction of an inlet distortion combining a temperature gradient and a vortical velocity field of realistic strengths leads to unsteady fluctuations of similar magnitude. The steady and time-averaged solutions match extremely well in terms of static pressure distribution, hence loading, but not in terms of stagnation temperature distribution, for which the steady solution provides only trends. The vorticity introduced by the vortical disturbance is larger than that produced by the temperature gradient and contributes more to the generation of the secondary flow.

For steady-state transonic flow fields, the results of Chapter 7 indicate that the introduction of an inlet spanwise temperature distortion of realistic shape and strength leads to strong secondary flow in the rotor frame of reference, created from variations in the rotor-relative stagnation or rotary stagnation pressure. This results in a redistribution of the temperature with concentrated regions of high stagnation temperature gradients on the rotor blade pressure surface. Also, because of the transonic nature of the flow, the secondary flow can trigger the formation of shocks.

The robustness of the method was demonstrated through the computation of the unsteady transonic flow field of Chapter 9, where the unsteady fluctuations can be one order of magnitude larger than the subsonic ones. Due to the impact of the stator trailing edge shock wave off the downstream rotor, a strong unsteady shock motion in the stage was captured as part of the solution. The unsteady shock interaction includes a primary reflection off the rotor suction surface and a secondary reflection off the adjacent rotor pressure side. The primary reflection moves back towards the upstream stator striking it on the suction side close to the trailing edge. In addition, the secondary reflection crosses back towards the original rotor and intensifies into a strong shock. As a consequence of the unsteady interaction, a secondary radial flow from hub towards midspan is created and is strong enough to be present in the time-averaged solution. This secondary flow creates a slight flow blockage at the lower radii (hub), which is compensated by an increase in mass flow through the outer rotor radii streamtubes. Although the time-sequencing of the events are different, the motion of the shocks are consistent with the quasi-3-D numerical simulation of Giles [33]. On the rotor root suction surface, the level of unsteadiness in static pressure reached a peak-to-peak value of about 60% of the inlet stagnation pressure. In general, the level of unsteadiness was higher on the rotor suction side than on the pressure side, and also at the hub and tip compared to midspan. It is believed that, for the generic stator/rotor configuration chosen here, realistic levels of unsteadiness have been computed.

Regarding periodic unsteady effects, the following observations are inferred from this study. The time-accurate inviscid computations provide an estimate for the peak values

in the blade passage, in particular for the static pressure and the stagnation temperature which are two important quantities for work output, boundary-layer behavior and heat transfer. Typically for transonic flow, where the unsteady fluctuations in pressure are one order of magnitude larger than for subsonic flow, the unsteady static pressure envelope can exceed the level of the time-averaged local value. The unsteady stagnation temperature fluctuations are less than 25% of the time-averaged local value. Also for transonic flow, the unsteady interaction creates overall higher entropy losses than for steady-state flow, resulting in a different time-averaged distribution of Mach number. For the case examined here, the 3-D unsteady transonic stator/rotor interaction results in a periodic shock-induced secondary flow that is not present in the steady-state solution.

10.4 Recommendations for future work

Unless the unsteady interface boundary condition formulation is extended to handle non-equal numbers of stator and rotor blades, it is difficult to assess the influence of the scaled rotor during the unsteady process. This effect should be investigated, especially in the case of a non-uniform inlet stagnation temperature distribution combining both radial and tangential variations, i.e. different conditions per blade-passage.

The *quasi-3-D non-reflecting boundary conditions* should be extended to incompressible flow computations. The system of equations governing the motion of an incompressible flow is of the elliptic type, in which pressure waves propagate at infinite speed. However, the use of Chorin's artificial compressibility method [13, 11] which introduces a time-dependent pressure term in the continuity equation[1] results in a system of hyperbolic-type equations of motion very similar in nature to the actual Euler equations with waves of finite speed. Thus, the non-reflecting boundary condition procedure developed in this thesis could be applied to this modified system.

[1]The solution of the modified system is only physically meaningful for steady-state.

The source term of Equation (2.1) could be modified to include the effects of mass injection due to cooling, friction forces and heat addition. As shown in this work, 3-D steady and/or unsteady stator/rotor interactions can produce significant secondary flows (sometimes reverse flow) which may hamper the use of the current boundary-layer solvers if used in conjunction with an inviscid solver. Hence, the simulation of viscous effects through distributed body forces seems to be a promising area of research which would lead to an intermediate technique between a fully inviscid method such as the one proposed in this thesis and a coupled boundary-layer/inviscid one. This could be done at little extra computational cost compared to a 3-D boundary-layer/inviscid coupling for instance. A good starting point for this is to examine the method proposed by Denton [16].

Bibliography

[1] AGARD Working Group 12. Through Flow Calculations in Axial Turbomachines. AGARD AR-175, 1981.

[2] J. J. Adamczyk. Model Equation for Simulating Flows in Multistage Turbomachinery. ASME Paper 85-GT-226, 1985.

[3] D. Anderson, J. Tannehill, and R. Pletcher. *Computational Fluid Mechanics and Heat Tranfer.* McGraw-Hill, 1984.

[4] John D. Jr. Anderson. *Modern Compressible Flow: With Historical Perspective.* McGraw-Hill, 1982.

[5] D. A. Ashworth, J. E. LaGraff, D. L. Schultz, and K. J. Grindrod. Unsteady Aerodynamic and Heat Transfer Processes in a Transonic Turbine Stage. *Journal of Engineering for Gas Turbines and Power*, 107:1022–1030, 1985.

[6] T. J. Barber and L. S. Langston. Three Dimensional Modelling of Cascade Flows. AIAA Paper 79-0047, 1979.

[7] A. Bayliss and E. Turkel. Far-Field Boundary Conditions for Compressible flows. *Journal of Computational Physics*, 48:182–199, 1982.

[8] A. Binder, W. Forster, H. Kruse, and H. Rogge. An Experimental Investigation into the Effects of Wakes on the Unsteady Turbine Rotor Flow. ASME Paper 84-GT-178, 1984.

[9] T. L. Butler, O. P. Sharma, H. D. Joslyn, and R. P. Dring. Redistribution of an Inlet Temperature Distortion in an Axial Flow Turbine Stage. AIAA Paper 86-1468, 1986.

[10] L. N. Cattafesta. An Experimental Investigation of the Effects of Inlet Radial Temperature Profiles on the Aerodynamic Performance of a Transonic Turbine Stage. Master's thesis, MIT, August 1988.

[11] J. L. C. Chang and D. Kwak. On the Method of Pseudo-Compressibility for Numerically Solving Incompressible Flows. AIAA Paper 84-0252, 1984.

[12] Y. S. Chen. 3-D Stator-Rotor Interaction of the SSME. AIAA Paper 88-3095, 1988.

[13] A. J. Chorin. A Numerical Method for Solving Incompressible Viscous Flow Problems. *Journal of Computational Physics*, 2:12–26, 1967.

[14] W. N. Dawes. A Numerical Method for the Analysis of 3-D Viscous Compressible Flow in Turbine Cascades; Application to Secondary Flow Development in a Cascade With and Without Dihedral. ASME Paper 86-GT-145, 1986.

[15] W. N. Dawes. Towards Improved Throughflow Capability: The Use of 3-D Viscous Flow Solvers in a Multistage Environment. ASME Paper 90-GT-18, 1990.

[16] J. D. Denton. The Use of a Distributed Body Force to Simulate Viscous Effects in 3-D Flow Calculations. ASME Paper 86-GT-144, 1986.

[17] J. D. Denton. The Calculation of Three-Dimensional Viscous Flow Through Mulistage Turbomachines. ASME Paper 90-GT-19, 1990.

[18] D. J. Doorly and M. L. G. Oldfield. Simulation of the Effects of Shock Wave Passing on a Turbine Rotor Blade. *Transactions of the ASME, Journal of Engineering for Gas Turbines and Power*, 107, October 1985.

[19] D. J. Dorney, L. D. Roger, D. E. Edwards, and N. K. Madavan. Unsteady Analysis of Hot Streak Migration in a Turbine Stage. AIAA Paper 90-2354, 1990.

[20] B. Engquist and A. Majda. Absorbing Boundary Conditions for the Numerical Simulation of Waves. *Mathematics of Computation*, 31:629–651, July 1977.

[21] A. H. Epstein, G. R. Guenette, and R. J. G. Norton. The MIT Blowdown Turbine Facility. ASME Paper 84-GT-116, 1984.

[22] J. I. Erdos, E. Alzner, and W. McNally. Numerical Solution of Periodic Transonic Flow Through a Fan Stage. *AIAA Journal*, 15:1559–1568, Nov 1977.

[23] L. E. Eriksson. Practical Three-Dimensional Mesh Generation Using Transfinite Interpolation. Lectures series notes, Von Karman Institute for Fluid Dynamics, 1983.

[24] I. D. Faux and M. J. Pratt. *Computational Geometry for Design and Manufacture.* Mathematics and its Applications. Ellis Horwood Limited, Chichester, 1979. Chapters 5-6-7.

[25] L. Ferm. Open Boundary Conditions for External Flow Problems. Dept. of Computing Science Report 108, Uppsala University, February 1987.

[26] L. Ferm and B. Gustafsson. A Down-stream Boundary Procedure for the Euler Equations. *Computer and Fluids*, 10(4):261–276, 1982.

[27] A. Fourmaux. Unsteady Flow Calculation in Cascades. ASME Paper 86-GT-178, 1986.

[28] G. Fritsch. *An Analytical and Numerical Study of the Second-Order Effects of Unsteadiness on the Performance of Turbomachines.* PhD thesis, MIT, June 1992.

[29] M. B. Giles. Eigenmode Analysis of Unsteady One-Dimensional Euler Equations. ICASE Report No. 83-47, 1983.

[30] M. B. Giles. Newton Solution of Steady Two-Dimensional Transonic Flow. Gas Turbine Laboratory Report 186, Massachusetts Institute of Technology, October 1985.

[31] M. B. Giles. Accuracy of Node-Based Solutions on Irregular Meshes. Proceedings of 11th International Conference on Numerical Methods in Fluid Dynamics, 1988.

[32] M. B. Giles. Non-Reflecting Boundary Conditions for the Euler Equations. Technical Report TR-88-1, MIT Computational Fluid Dynamics Laboratory, 1988.

[33] M. B. Giles. Stator/Rotor Interaction in a Transonic Turbine. AIAA Paper 88-3093, 1988.

[34] M. B. Giles. UNSFLO: A Numerical Method for Unsteady Inviscid Flow in Turbomachinery. Technical Report 195, MIT Gas Turbine Laboratory, 1988.

[35] M. B. Giles. Non-Reflecting Boundary Conditions For Euler Equation Calculations. AIAA Paper 89-1942-CP, 1989.

[36] M. B. Giles. Numerical Methods for Unsteady Turbomachinery Flow, (VKI Lecture Series Notes). Technical Report TR-89-3, MIT Computational Fluid Dynamics Laboratory, 1989.

[37] M. B. Giles. UNSFLO: A Numerical Method for Unsteady Inviscid Flow in Turbomachinery. Technical Report 205, MIT Gas Turbine Laboratory, 1991.

[38] M. B. Giles. An Approach for Multi-Stage Calculations Incorporating Unsteadiness. ASME Paper, June 1992. 37^{th} IGTI Conference in Cologne, Germany.

[39] M. B. Giles. ANSI-3D: An Explicit Method for Solving the Steady-State Navier-Stokes Equations. MIT Contractor Report, January 1986.

[40] M. B. Giles and R. Haimes. Advanced Interactive Visualization for CFD. *Computing Systems in Engineering*, 1(1), 1990. pages 51-62.

[41] J. P. Gostelow. *Cascade Aerodynamics.* Pergamon Press, 1984.

[42] E. M. Greitzer. The Stability of Pumping Systems – The 1980 Freeman Scholar Lecture. *Journal of Fluids Engineering*, 103:193–242, 1981.

[43] E. M. Greitzer. An Introduction to Unsteady Flow in Turbomachines. Technical Report 2, NATO ASI Series, 1985.

[44] E. M. Greitzer, R. W. Paterson, and C. S. Tan. An approximate substitution principle for viscous heat conducting flows. *Proceedings of the Royal Society of London*, A 401:163–193, 1985.

[45] J. Haeuser and C. Taylor, editors. *Numerical Grid Generation in Computational Fluid Dynamics*, Swansea, 1986. Pineridge.

[46] M. G. Hall. Cell-Vertex Multigrid Schemes for Solution of the Euler Equations. Technical Report 2029, Royal Aircraft Establishment, March 1985.

[47] S. P. Harasgama. Combustor Exit Temperature Distortion Effects on Heat Transfer and Aerodynamics within a Rotating Turbine Blade Passage. ASME Paper 90-GT-174, 1990.

[48] W. R. Hawthorne. Secondary Circulation in Fluid Flow. *Proc. Roy. Soc.*, 206:374, 1951.

[49] W. R. Hawthorne. The Growth of Secondary Circulation in Frictionless Flow. *Proc. Camb. Phil. Soc.*, 51(4):737, 1955.

[50] W. R. Hawthorne. On the Theory of Shear Flow. Gas Turbine Lab report 88, Massachusetts Institute of Technology, Department of Aeronautics and Astronautics, 1966.

[51] W. R. Hawthorne. Secondary Vorticity in Stratified Compressible Fluids in Rotating Systems. CUED/A-Turbo/TR 63, University of Cambridge, Department of Engineering, 1974.

[52] F. B. Hildebrand. *Advanced Calculus For Applications.* Prentice-Hall, Englewood Cliffs, New Jersey, second edition, 1976.

[53] C. Hirsch and A. Verhoff. Far-field Numerical Boundary Conditions for Internal and Cascade Flow Computations. AIAA Paper 89-1943-CP, 1989.

[54] D. G. Holmes and S. D. Connell. Solution of the 2-D Navier-Stokes Equations on Unstructured Adaptive Grids. AIAA Paper 89-1932-CP, 1989.

[55] J. H. Horlock and B. Lakshminarayana. Secondary Flows: Theory, Experiment, and Application in Turbomachinery Aerodynamics. *Annual Review of Fluid Mechanics*, 5, 1973.

[56] A. Jameson, W. Schmidt, and E. Turkel. Numerical Solutions of the Euler Equations by Finite Volume Methods Using Runge-Kutta Time-Stepping Schemes. AIAA Paper 81-1259, 1981.

[57] A. B. Johnson, M. L. G. Oldfield, M. J. Rigby, and M. B. Giles. Nozzle Guide Vane Shock Wave Propagation and Bifurcation in a Transonic Turbine Rotor. ASME Paper 90-GT-310, 1990.

[58] A. B. Johnson, M. J. Rigby, M. L. G. Oldfield, R. W. Ainsworth, and M. J. Oliver. Surface Heat Transfer Fluctuations on a Turbine Rotor Blade due to Upstream Shock Wave Passing. ASME Paper 88-GT-172, 1988.

[59] M. W. Johnson. Secondary Flow in Rotating Bends. CUED/A-Turbo/TR 92, University of Cambridge, Department of Engineering, 1978.

[60] P. C. E. Jorgenson and R. V. Chima. An Explicit Runge-Kutta Method for Unsteady Rotor/Stator Interaction. AIAA Paper 88-0049, 1988.

[61] D. Joslyn and R. Dring. Three-Dimensional Flow in an Axial Turbine. ASME Paper 90-GT-56, 1990.

[62] H. D. Joslyn, R. P. Dring, and O. P. Sharma. Unsteady Three-Dimensional Turbine Aerodynamics. *Journal of Engineering for Power*, 105:322–331, 1983.

[63] J. L. Kerrebrock and A. A. Mikolajczak. Intra-Stator Transport of Rotor Wakes and its Effect on Compressor Performance. ASME Paper 70-GT-39, 1970.

[64] M. Koya and S. Kotake. Numerical Analysis of Fully Three-Dimensional Periodic Flows Through a Turbine Stage. ASME Paper 85-GT-57, 1985.

[65] H.-O. Kreiss. Initial Boundary Value Problems for Hyperbolic Systems. *Communications on Pure and Applied Mathematics*, 23:277–298, 1970.

[66] B. Krouthén and M. B. Giles. Numerical investigation of hot streaks in turbines. AIAA Paper 88-3015, 1988.

[67] A. M. Kuethe and C-Y. Chow. *Foundations of Aerodynamics.* John Wiley & Sons, Inc., fourth edition, 1986.

[68] B. Lakshminarayana. Effects of Inlet Temperature Gradients on Turbomachinery Performance. *Transactions of the ASME, Journal of Engineering for Power*, January 1975.

[69] B. Lakshminarayana and J. H. Horlock. Generalized expressions for secondary vorticity using intrinsic co-ordinates. *Journal of Fluid Mechanics*, 59:97–115, 1973.

[70] H. Lamb. *Hydrodynamics*, pages 591–592. Dover, 6th edition, 1945. New York.

[71] L. S. Langston, M. L. Nice, and R. M. Hooper. Three-Dimensional Flow Within a Turbine Cascade Passage. ASME Paper 76-GT-50, 1976.

[72] J. P. Lewis, R. A. Delaney, and E. J. Hall. Numerical Prediction of Turbine Vane-Blade Interaction. AIAA Paper 87-2149, 1987.

[73] H. W. Liepmann and A. Roshko. *Elements of Gasdynamics*. John Wiley & Sons, Inc., 1957.

[74] D. R. Lindquist. A Comparison of Numerical Schemes on Triangular and Quadrilateral Meshes. Master's thesis, MIT, May 1988.

[75] R. Löhner, K. Morgan, J. Peraire, and O. C. Zienkiewicz. Finite Element Methods for High Speed Flows. AIAA Paper 85-1531, 1985.

[76] P. Marchal and C. H. Sieverding. Secondary Flows within Turbomachinery Bladings. In *Secondary Flows in Turbomachines*, 1977. AGARD-CP-214.

[77] W. D. McNally and P. M. Sockol. Computational Methods for Internal Flows with Emphasis on Turbomachinery. NASA TM-82764, 1981.

[78] L. M. Milne-Thomson. *Theoretical Aerodynamics*. Dover Publications Inc., 4th edition, 1973.

[79] J. Moore and R. Y. Adhye. Secondary Flows and Losses Downstream of a Turbine Cascade. *Transactions of the ASME, Journal of Engineering for Gas Turbines and Power*, 107:961–968, 1985.

[80] M. Munk and R. C. Prim. On the Multiplicity of Steady Gas Flows Having the Same Streamline Pattern. *Proceedings of the National Academy of Sciences, U.S.*, 33:137–141, 1947.

[81] R.-H. Ni. A Multiple Grid Scheme for Solving the Euler Equations. *AIAA Journal*, 20:1565–1571, Nov 1981.

[82] R.-H. Ni and J. C. Bogoian. Prediction of 3-D Multi-Stage Turbine Flow Field Using a Multiple-Grid Euler Solver. AIAA Paper 89-0203, 1989.

[83] R.-H. Ni and O. Sharma. Using 3-D Euler Flow Simulations to Assess Effects of Periodic Unsteady Flow Trough Turbines. AIAA Paper 90-2357, 1990.

[84] G. Pappas. Influence of Inlet Radial Temperature Distribution on Turbine Rotor Heat Transfer. Master's thesis, MIT, August 1990.

[85] W. H. Press, B. P. Flannery, S. A. Teukolsky, and W. T. Vetterling. *Numerical Recipes.* Cambridge University Press, Cambridge, 1986. pages 86-89.

[86] M. M. Rai. Navier-Stokes Simulations of Rotor-Stator Interaction Using Patched and Overlaid Grids. AIAA Paper 85-1519, 1985.

[87] M. M. Rai. Unsteady Three-Dimensional Navier-Stokes Simulations of Turbine Rotor-Stator Interaction. AIAA Paper 87-2058, 1987.

[88] M. M. Rai and R. P. Dring. Navier-Stokes Analyses of the Redistribution of Inlet Temperature Distortions in a Turbine. AIAA Paper 87-2146, 1987.

[89] R. D. Richtmeyer and K. W. Morton. *Difference Methods for Initial-Value Problems.* John Wiley & Sons, second edition, 1967.

[90] A. Rizzi and L.-E. Eriksson. Computations of flow around wings based on the Euler Equations. *Journal of Fluid Mechanics*, 148:45–71, November 1984.

[91] I. L. Ryhming. *Dynamique des Fluides.* Presses Polytechniques Romandes, Lausanne, Switzerland, 1985.

[92] A. P. Saxer and M. B. Giles. Inlet Radial Temperature Redistribution in a Transonic Turbine Stage. AIAA Paper 90-1543, 1990.

[93] D. L. Schultz, D. A. Ashworth, J. E. LaGraff, M. J. Rigby, and A. B. Johnson. Wake and Shock Interactions in a Transonic Turbine Stage. AGARD PEP CP-401, 1986.

[94] O. P. Sharma and T. L. Butler. Predictions of Endwall Losses and Secondary Flows in Axial Flow Turbine Cascades. ASME Paper 86-GT-228, 1986.

[95] O. P. Sharma and R. A. Graziani. Influence of Endwall Flow on Airfoil Suction Surface Midheight Boundary Layer Development in a Turbine Cascade. *Transactions of the ASME, Journal of Engineering for Power*, 105, January 1983.

[96] O. P. Sharma, G. F. Pickett, and R. H. Ni. Assessment of Unsteady Flows in Turbines. ASME Paper 90-GT-150, 1990.

[97] O. P. Sharma, E. Renaud, T. L. Butler, K. Millsaps, R. P. Dring, and H. D. Joslyn. Rotor-Stator Interaction in Multi-Stage Axial-Flow Turbines. AIAA Paper 88-3013, 1988.

[98] C. H. Shieh. Three-Dimensional Grid Generation Using Poisson Equations. In Joe F. Thompson, editor, *Numerical Grid Generation*, pages 687–694. Elsevier Science Publishing Company, 1982.

[99] C. H. Sieverding. Recent Progress in the Understanding of Basic Aspects of Secondary Flows in Turbine Blade Passages. *Transactions of the ASME, Journal of Engineering for Gas Turbines and Power*, 107, April 1985.

[100] A. G. Smith. On the Generation of the Streamwise Component of Vorticity for Flows in Rotating Passages. *The Aeronautical Quarterly*, 8:369–383, 1957.

[101] R. L. Sorenson and J. L. Steger. Grid Generation in Three Dimensions by Poisson Equations with Control of Cell Size and Skewness at Boundary Surfaces. In *Advances in Grid Generation*, Houston, Texas, 1983. Applied Mechanics, Bioengineering, and Fluids Engineering Conference.

[102] H. B. Squire and K. G. Winter. The Secondary Flow in a Cascade of Airfoils in a Nonuniform Stream. *Journal of the Aeronautical Science*, 18:271–277, 1951.

[103] J. L. Steger and R. L. Sorenson. Automatic Mesh-Point Clustering Near a Boundary in Grid Generation with Elliptic Partial Differential Equations. *Journal of Computational Physics*, 33:405–410, 1979.

[104] J. C. Strikwerda. *Finite Differences Schemes and Partial Differential Equations.* Wadsworth & Brooks/Cole, Belmont, CA, 1989.

[105] R. K. Takahashi and R.-H. Ni. Unsteady Euler Analysis of the Redistribution of an Inlet Temperature Distortion in a Turbine. AIAA Paper 90-2262, 1990.

[106] P. D. Thomas. Numerical Grid Generation of Composite Three Dimensional Grids by Quasilinear Elliptic Systems. In Joe F. Thompson, editor, *Numerical Grid Generation*, pages 667–686. Elsevier Science Publishing Company, 1982.

[107] W.T. Thompkins, S.S. Tong, R.H. Bush, W.J. Usab, and R.J. Norton. Solution Procedures for Accurate Numerical Simulations of Flow in Turbomachinery Cascades. AIAA Paper 83-0257, 1983.

[108] J. F. Thompson, F. C. Thames, and C. W. Mastin. Automatic Numerical Generation of Body-Fitted Curvilinear Coordinate System for Field Containing Any Number of Arbitrary Two-Dimensional Bodies. *Journal of Computational Physics*, 15:299–319, 1974.

[109] L. N. Trefethen. Dispersion, Dissipation and Stability. In D. F. Griffiths and G. A. Watson, editors, *Numerical Analysis*. Longman, 1986.

[110] M. G. Turner. *Design and Analysis of Internal Flowfields Using a Two Stream Function Formulation*. PhD thesis, MIT, January 1991.

[111] F. M. White. *Viscous Fluid Flow*. McGraw-Hill, 1974. Chapter 3.

[112] G. B. Whitham. *Linear and Nonlinear Waves*. John Wiley & Sons, 1974.

[113] H. C. Yee, R. M. Beam, and R. F. Warming. Stable Boundary Approximations for the One-Dimensional Inviscid Equations of Gas Dynamics. AIAA Paper 81-1009, 1981.

Appendix A

Three-Dimensional Mesh Generation Technique for Euler Flows in Axial Turbines

In the process of numerical fluid dynamics analysis, the generation of efficient computational grids is generally required for the discrete solution of the governing flow equations. The mesh generation technique is a critical element for supporting the flow simulation, especially in three dimensions, since most of the discretization schemes currently in use are affected (either through numerical convergence and/or by the quality of the results) by the construction of the grid.

This report describes the three-dimensional (3-D) mesh generation technique used in connection to UNSFLO, a program developed for solving inviscid unsteady flows in a stator/rotor configuration. Specifically, a discrete approximation of Ni's type [81] of the Euler equations is performed at each of the nodal points defined by the mesh. The two-dimensional (2-D) version of this code has been developed by Giles [33], whereas Saxer extended it to 3-D steady flows [92]. For that type of flow solver two main numerical constraints should be considered in the mesh generation process, namely

- cell volumes as uniform as possible to ensure no severe CFL restrictions, and almost equal resolution everywhere in the flow field. This latter feature is desirable for unsteady calculations since the moving wakes can have large gradients in almost any part of the flow domain, and
- a definition of a sufficiently smooth mesh at the inlet and outlet in order to avoid

wakes distortions from one row of blades to the other.

A useful user "constraint" would be

- Few, but well defined parameters to control the mesh (spacing and clustering for instance), especially on the blade surface.

In recent years, different approaches have been used to generate grid systems for arbitrary two and three-dimensional flow regions, including conformal mapping, algebraic methods and partial differential equation (PDE) solutions [45]. In particular, one possible technique which satisfies the above mentioned criteria is to generate a boundary-conforming mesh, of H-H type, by solving a set of elliptic PDE. This procedure, first developed by Thompson [108], has been chosen in this work since it has the nice property of generating continuous and smooth meshes and since it has been successfully applied to several 3-D geometries, see for instance [106], [98] and [101]. Algebraic methods such as Eriksson's transfinite interpolation [23] have also been proven to be efficient in a number of three-dimensional applications. However, this kind of technique requires a certain amount of ingenuity to produce a nice smooth mesh with properly ordered points, especially for highly curved geometries.

Section A.1 describes the theoretical aspect of the elliptic mesh generation technique. Section A.2 deals with the numerical implementation of this method applied to industrial data.

A.1 Elliptic grid generation method

A.1.1 Governing equations

In the boundary-conforming procedure, the strategy consists of mapping the three-dimensional physical domain of Cartesian coordinates (x, y, z) onto a cubic computational domain of coordinates (ξ,η,τ). The first step in defining the transformation is to specify Dirichlet and/or Neumann conditions on the limiting surfaces of the physical region; those boundaries being represented by $\xi = const$, $\eta = const$ and $\tau = const$ in the computational domain. In the elliptic partial differential method, the distribution of the interior grid points is then governed by the following Poisson system

$$\begin{aligned} \xi_{xx} + \xi_{yy} + \xi_{zz} &= P(\xi, \eta, \tau) \\ \eta_{xx} + \eta_{yy} + \eta_{zz} &= Q(\xi, \eta, \tau) \\ \tau_{xx} + \tau_{yy} + \tau_{zz} &= R(\xi, \eta, \tau) \end{aligned} \tag{A.1}$$

where P, Q and R are source terms that can be selected to control the mesh points distribution. Since it is much easier to solve a system of PDE on the uniformly spaced grid of the computational domain, it is useful to transform system (A.1) on to the computational space. This is achieved by interchanging the roles of the dependent (ξ,η,τ) and independent (x, y, z) variables in Eqs. (A.1). This yields an elliptic system of quasi-linear equations that can be written in the vector form [98]

$$a_{11}(\vec{r}_{\xi\xi} + \phi\vec{r}_{\xi}) + a_{22}(\vec{r}_{\eta\eta} + \psi\vec{r}_{\eta}) + a_{33}(\vec{r}_{\tau\tau} + \lambda\vec{r}_{\tau}) + 2(a_{12}\vec{r}_{\xi\eta} + a_{13}\vec{r}_{\xi\tau} + a_{23}\vec{r}_{\eta\tau}) = 0, \tag{A.2}$$

where $\vec{r} = (x, y, z)$ is the position vector,

$$a_{ij} = \sum_{m=1}^{3} A_{mi} A_{mj}$$

and A_{mi} is the cofactor of the (m,i) element in the following matrix

$$M = \begin{bmatrix} x_\xi & x_\eta & x_\tau \\ y_\xi & y_\eta & y_\tau \\ z_\xi & z_\eta & z_\tau \end{bmatrix}$$

The forcing functions ϕ, ψ and λ serve to control the interior mesh points distribution,

$$\phi = \frac{J^2 P}{a_{11}}, \quad \psi = \frac{J^2 Q}{a_{22}}, \quad \lambda = \frac{J^2 R}{a_{33}}$$

where

$$J = \frac{\partial(x,y,z)}{\partial(\xi,\eta,\tau)} = det(\vec{r}_\xi, \vec{r}_\eta, \vec{r}_\tau)$$

Given a proper choice of the source terms P, Q and R, this transformation defines a one-to-one correspondence between the two spaces.

A.1.2 Problem specification

In the present method the meshes used for stator/rotor interactions are generated separately, then patched together. Each patch, composed of hexahedral cells, is representative of a single row of an axial turbine and, by using periodic boundary conditions at the pitch, can be reduced to one blade to blade control volume. This domain is composed of solid body surfaces (blade, hub and tip walls) and fluid surfaces (periodic and inlet/outlet surfaces). Since the mesh has to be developed for an Euler calculation the tip leakage can be neglected and, in the (ξ,η,τ) space, the region appears as a single block. For a rotor row of H-H mesh type the corresponding physical and computational domains are represented in Figures A.1 and A.2, respectively. The surface $\xi = 0$ is chosen as the inlet boundary and the surface $\xi = 1$ corresponds to the outlet boundary. The surface $\eta = 0$ defines the suction side together with the lower periodic surface stretching upstream from the leading edge line and downstream from the trailing edge line. The boundary $\eta = 1$ corresponds to the pressure side together with the upper periodic surfaces, which are the same as the lower periodic ones but displaced by one

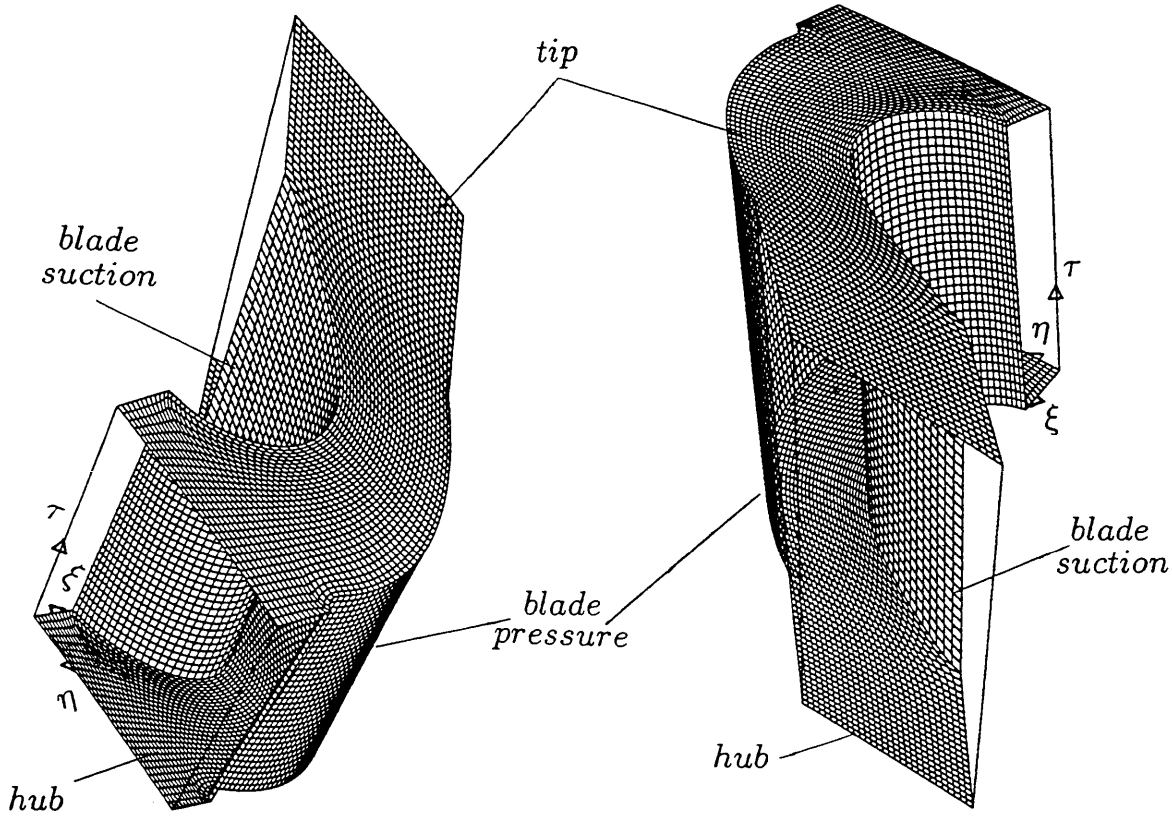

Figure A.1: Rotor interblade control volume in physical space ($80 \times 30 \times 35$ nodes). The fluid boundary surfaces (inlet/outlet/periodic) have been removed.

pitch angle. The surface $\tau = 0$ defines the hub wall, whereas $\tau = 1$ represents the tip wall.

A.1.3 Mesh control

Previous work

Usually, the non-homogeneous source terms are used for the stretching of coordinate lines toward other coordinate lines, whereas the grid spacing distribution is specified by the boundary coordinates. The forcing terms P, Q and R in Eqs. (A.1) improve the

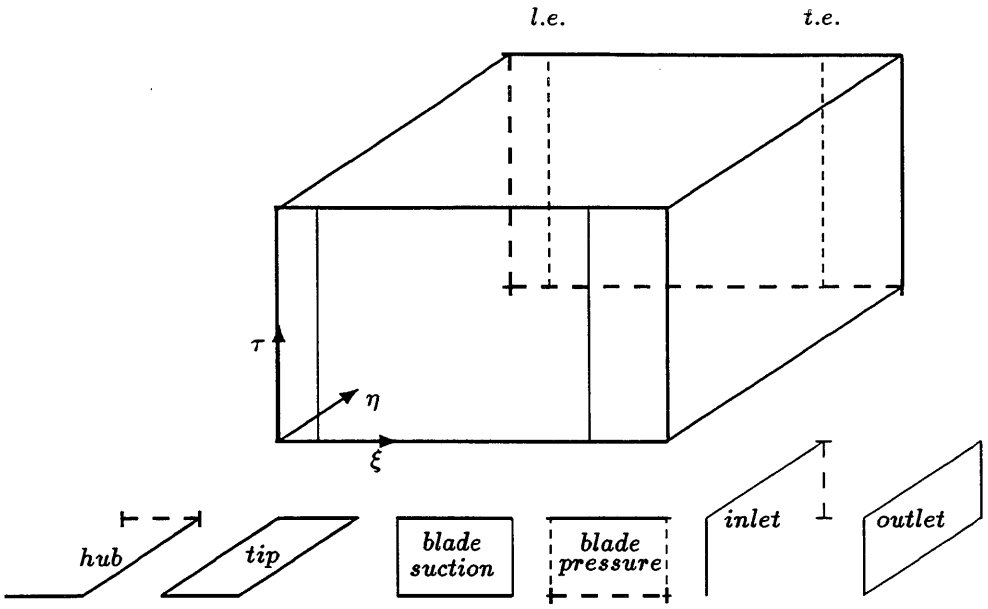

Figure A.2: Computational space resulting from the H-H mapping of the rotor control volume. (*l.e.* and *t.e.* refer to the leading and the trailing edges, respectively.)

flexibility of the method, but their choice is not a trivial task.

In 3-D, one method consists of choosing exponential functions for ϕ, ψ and λ which include appropriate "tuning" parameters [98]. However, a more rational way to control the mesh propagation using exponential functions for the inhomogeneous terms has been proposed by Sorenson and Steger [101], [103]. Their method, valid in 2-D and 3-D, allows the user to have some control of the mesh cell size and skewness at a boundary by including in the source terms a normal grid spacing parameter and the orthogonality condition at the considered boundary. A different approach has been suggested by Thomas [106]. In Thomas' 3-D method, the grid control parameters are defined in terms of Dirichlet type boundary values. Then, the forcing functions are interpolated linearly into the interior to obtain a continuous representation. By including these parameters in the solution of the elliptic system, this method constitutes an indirect interpolation mechanism (whereas algebraic methods generally use direct interpolation procedures) for projecting the boundary mesh surfaces into the interior of the region. Giles' [30] grid control is based on algebraic manipulations directly on the computational grid, which

is no longer uniform. His PDE system is of Laplace's type (source terms set to zero) instead of Poisson's type but has not yet been extended to 3-D.

As opposed to a viscous calculation, a mesh for an inviscid computation does not necessarily require to be (nearly) orthogonal at the body. Specifying orthogonality at boundaries may induce highly skewed cells in the rest of the flow domain, especially in the case of small blade pitch combined with highly cambered airfoils. This decreases the accuracy of numbers of discretization algorithms. However, some kind of grid clustering technique is needed, especially around the leading edge. By considering these aspects and the mesh properties defined in the introduction, the grid control is based on the following premises:

- Define mixed boundary conditions on the different limiting surfaces instead of the usual Dirichlet conditions on every boundary.
- Use one or combine the following two options.
    1. Solve system (A.2) with the forcing terms set to zero. Then, redistribute the nodes along each blade to blade or periodic to periodic surfaces such that a relatively uniform grid is obtained.
    2. Solve system (A.2) with the forcing terms evaluated according to the theory described in the next section. This allows the user to control the mesh cell size and the skewness at the blade surface.

Present approach

In the present application the inhomogeneous terms P, Q and R control grid spacing and skewness for mesh cells adjacent to the blade surface only. This is achieved by controlling the orthogonality of the grid lines intersecting the surfaces $\eta = 0$ and $\eta = 1$ (less the part defining the periodic surfaces ahead and downstream of the leading and the trailing edges, respectively), and by regulating the volume of the cells connected to the

blade. This approach follows the work of Sorenson and Steger [101] and is summarized here. Consider for instance the suction side of the blade which is part of $\eta = 0$, then, according to [101] the forcing terms are chosen to be

$$\begin{aligned} P(\xi,\eta,\tau) &= \tilde{P}(\xi,\tau)\exp^{-a\eta} \\ Q(\xi,\eta,\tau) &= \tilde{Q}(\xi,\tau)\exp^{-b\eta} \\ R(\xi,\eta,\tau) &= \tilde{R}(\xi,\tau)\exp^{-c\eta} \end{aligned} \tag{A.3}$$

where the exponential factors cause the control to relax with distance from the boundary $\eta = 0$ and the positive constants a, b, c influence the rate of decay of the boundary control.

The points on the blade surface are specified by the user, i.e. the ξ, τ points distribution on $\eta = 0$ is known and can be used to set the orthogonality condition of the grid lines intersecting the $\eta = 0$ boundary surface. This condition is represented by the following two vector dot products,

$$\vec{r}_\eta \cdot \vec{r}_\xi = 0 \tag{A.4}$$

$$\vec{r}_\eta \cdot \vec{r}_\tau = 0 \tag{A.5}$$

Relations (A.4) and (A.5) express the fact that the unit vectors in the η and ξ directions and in the η and τ directions be mutually normal. The control of the cell size at $\eta = 0$ is achieved by regulating the cell "height" S, which is the distance along a line of increasing η. Consequently, the specification of $\Delta S/\Delta\eta$ at $\eta = 0$ allows the user to control the volume of the blade surface cells. Expressed in differential form the third boundary control equation is

$$\vec{r}_\eta \cdot \vec{r}_\eta = \left(\frac{\partial S}{\partial \eta}\right)^2 \tag{A.6}$$

The numerical procedure described in the Section A.2.7 requires that Equations (A.4), (A.5) and (A.6) be solved for the derivatives with respect to η at the blade surface,

giving

$$
\begin{aligned}
z_\eta &= \frac{\partial S/\partial \eta}{((A_{12}/A_{32})^2 + (A_{22}/A_{32})^2 + 1)^{1/2}} \\
y_\eta &= \frac{A_{22} z_\eta}{A_{32}} \\
x_\eta &= \frac{A_{12} z_\eta}{A_{32}}
\end{aligned}
\tag{A.7}
$$

Since $\vec{r}$ is specified on the blade, the surface control equations expressed by Equations (A.4), (A.5) and (A.6) or by the system (A.7) provide three additional relations that can be used to determine the unknowns values of $\tilde{P}$, $\tilde{Q}$ and $\tilde{R}$ and hence P, Q and R in the entire field. The boundary control equations are solved simultaneously with the interior mesh generation equations given by system (A.2) using an iterative solution procedure described in Section A.2.7.

A.2 Numerical procedure

A.2.1 Mesh generation path

The numerical generation of the mesh is based upon the following steps.

- Set the user input parameters.
- Process the industrial data, i.e. blade sections (2-D profiles), upper and lower annulus walls, in order to create a structure suitable for numerical grid generation.
- Define the root and the tip parts of the blade by intersecting the blade cuts and the lower and upper annulus walls, respectively.
- Define the blade surface by bicubic spline.

- Define the periodic surfaces ahead and downstream of the leading and trailing edge lines, respectively.
- Define the inlet and outlet mesh surfaces.
- Generate the interior mesh points by solving iteratively a Poisson's type PDE system; the hub and tip walls grid points distribution are included in this process by defining Neumann type conditions on these surfaces.
- If needed, redistribute nodes to obtain a uniform grid.
- Plot and store the computed mesh.

The relevant stages of this procedure are described in the next sections.

A.2.2 User parameters

The user has access to the following parameters to define the mesh:

- IL, JL, KL: number of points in the ξ, η, τ directions, respectively.
- $CHINL$, $CHOUT$: grid lengths (measured in axial chords) upstream and downstream of the leading and the trailing edges, respectively.
- $SGINL$, $SGOUT$: slopes of the periodic lines (at the root of the blade) extending from the leading and the trailing edges to the inlet and the outlet surfaces, respectively. (Measured in $x - y$ plane, see Section A.2.3).
- $SLEP$, $SLES$: grid spacing parameters for points distribution around the blade (see Section A.2.3). Typical range of values 0.005 - 0.015.
- AP, AS: positive constants influencing the rate of decay of the blade surface control source terms, see Section A.2.7. Typical value 0.5.

A.2.3 Input data processing

Data supplied by industry generally need to be altered to a form suitable for numerical treatment. For instance, curve and/or surface splines provide the necessary smoothness and flexibility (in terms of number of points and spacing) to the geometry. In this work, the input data for a stator or rotor geometry are of the following form:

- Two sets of points for the upper and lower annulus walls, each of them of the type $R = R(x)$, where x lies along the axis of rotation and r is the radius.
- N blade sections at N radii along the span. The value of N depends on the blade twisting, typically $N = 3$. Each blade cut is represented in local 2-D Cartesian coordinates (x, y) by a discrete number of points. Specifically the 2-D profile is defined by a suction side and a pressure side set of points, which are connected by circles at the leading and trailing edges.
- Number of blades, trailing edge location expressed in the annulus frame of reference, leading and trailing edge circle centers and radii.

An example is shown in Figure A.3.

The first step in smoothing the geometry is to define each of the 2-D blade cuts as a closed curve. Once a sharp trailing edge has been defined, a standard cubic spline interpolation is used to parameterize each profile. This allows a continuous curvature around the blade section, except at the trailing edge. The total number of points along $\eta = 0$, which includes the suction side, is IL. For a periodic geometry of H-H type this value has to equal the number of points along $\eta = 1$ (containing the pressure side). Then, the number of points (ILB) around each 2-D blade is defined as

$$ILB = 2\,IL\,(1 - \frac{c_{inl}}{c} - \frac{c_{out}}{c})$$

where c_{inl} and c_{out} are the lengths between the leading edge to the inlet and the trailing edge to the outlet, respectively. c_{inl} and c_{out} are functions of the input parameters

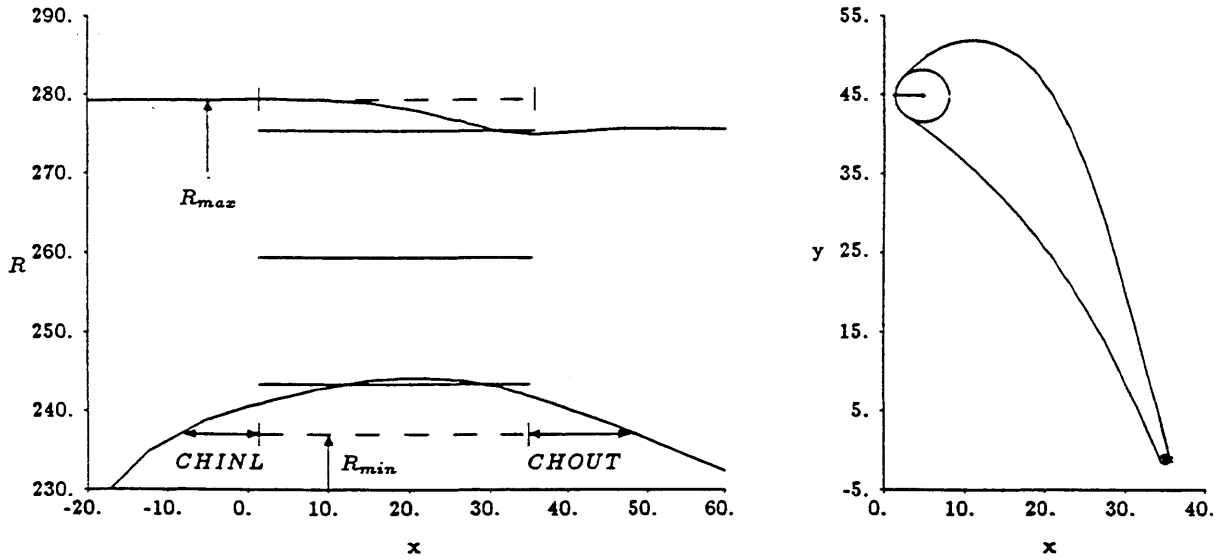

Figure A.3: Typical stator row data: a) Upper and lower annulus walls with 3 blade sections (solid lines). At local R_{max} and R_{min}, the dashed lines represent two extrapolated blade sections. b) Mean height blade profile with leading and trailing edge circles.

($CHINL$, $SGINL$) and ($CHOUT$, $SGOUT$), respectively. c is the distance from the inlet to the outlet surface. The axial location of the inlet (outlet) surface is assumed to be constant over the height of the channel.

The mesh points distribution along each blade curve is specified by a continuous collocation function $u(i)$, which is found by connecting at the leading edge two 2nd degree polynomials. This procedure allows only two free parameters ($SLEP$, $SLES$), which are the slopes of the collocation function on the pressure and suction side part of the leading edge, respectively, see Figure A.4.

In the examples presented in this appendix, the axial location of the trailing edge line (connecting the trailing edges of the blade sections) is constant over the height of the channel. However, this is not assumed to be true in general. The lower and upper annulus walls are simply fitted by natural cubic splines.

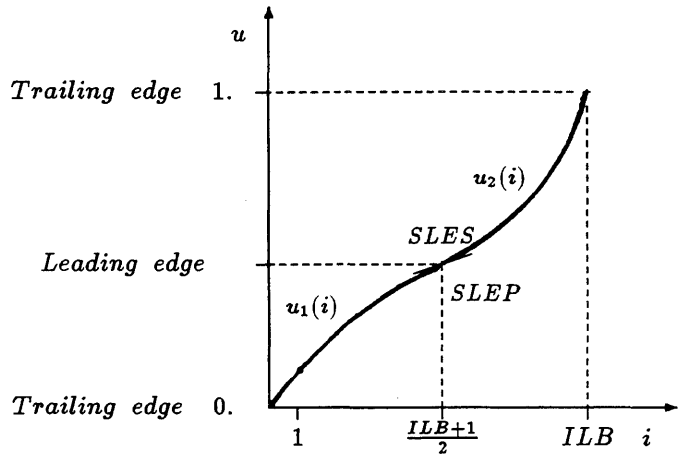

Figure A.4: Collocation function for mesh points distribution around the blade. u: normalized curvilinear coordinate, i: number of points. Free parameters: slopes $SLEP$ and $SLES$ on the pressure and suction part of the leading edge, respectively.

A.2.4 Blade root and blade tip construction

At this stage, the blade surface is not smooth but composed of a bunch of 2-D profiles, some of them cutting the annulus walls, see Figure A.3 (solid lines). The root (tip) of the blade is defined by intersecting the 2-D cuts with the lower (upper) annulus walls. In practice, it may be necessary to define a profile at $R = R_{min}$ (on the lower wall) and at $R = R_{max}$ (on the upper wall) in order to perform these interpolations, see Figure A.3 (dashed lines). If these extra profiles are required, then N, the total number of profiles, is adjusted accordingly. In that case, R_{min} and R_{max} are the maximum and minimum radii locally defined from the inlet to the outlet surface. The new sections are linearly extrapolated from the two nearest provided blade cuts. Then, at each i location ($1 \leq i < ILB$) around the profile, a cubic spline of the form $x = x(R)$ and $y = y(R)$ interpolates the N points along the span corresponding to the N blade cuts.

Finally, the trace of the blade on the hub (tip) wall is constructed by intersecting the lower (upper) wall spline with each of these spanwise fitting curves. This procedure, schematically represented in Figures A.5 and A.6, is allowed since every 2-D profile is

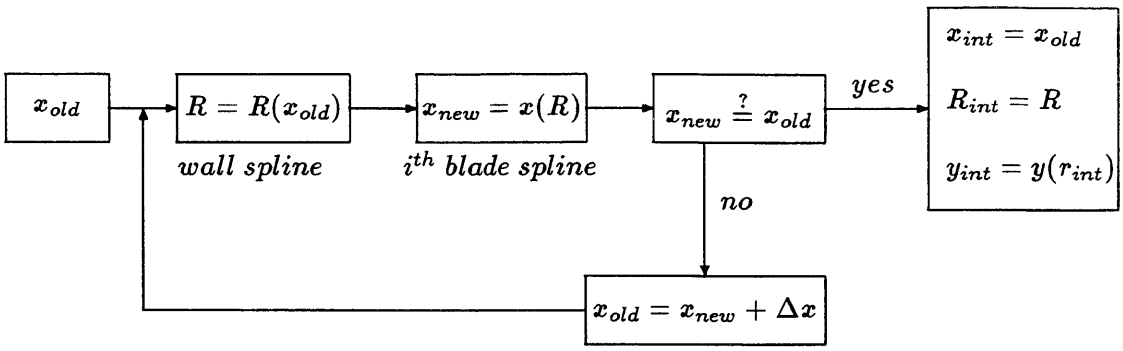

Figure A.5: Blade - annulus walls intersecting map. Subscript $_{int}$ stands for the interpolated root (tip) coordinates. $\Delta x = 0.5(x_{old} - x_{new})$.

described by the same number of points. Note that the spanwise cubic splines are used only to intersect the hub and the tip walls.

A.2.5 Blade surface definition

Bicubic spline fundamentals

The method for defining the blade as a parametric smooth surface is based on a framework built up of two intersecting families of curves. The u-curves run around the blade, whereas the w-curves extend along the span from the (newly defined) root to the tip. It is assumed that $0 \leq u, w \leq 1$ and $u = u(x, y, z)$, $w = w(x, y, z)$. Clearly the blade surface may be represented by the vector $\vec{s}(u, w) = \vec{r}(\xi, 0, \tau)$ and $\vec{r}(\xi, 1, \tau)$ for ξ varying from the leading edge to the trailing edge and τ from the root to the tip. The network of curves divides the surface into an assembly of topologically rectangular patches, each of which has as its boundaries two u-curves and two w-curves, defined by $w_k \leq w \leq w_{k+1}$ and $u_i \leq u \leq u_{i+1}$. To provide the necessary flexibility and smoothness to the geometry each patch boundary is chosen to be one span of a cubic spline. Then the patch surface

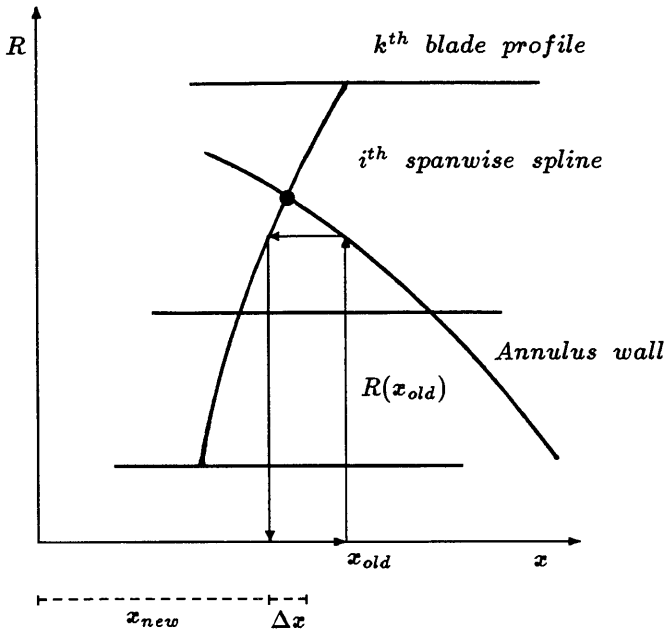

Figure A.6: Schematic of the blade root/tip construction.

may be represented by a bicubic of the form

$$\vec{s}(u,w) = \sum_{m=0}^{3}\sum_{n=0}^{3} \vec{b}_{m,n} \left(\frac{u-u_i}{g_i}\right)^m \left(\frac{w-w_k}{h_k}\right)^n \tag{A.8}$$

where $g_i = u_{i+1} - u_i$ and $h_k = w_{k+1} - w_k$. This type of surface representation is known as the Ferguson bicubic formula. It can be shown [24] that the coefficients $\vec{b}_{m,n}$ are linear combinations of position and derivative vectors at the patch corners, i.e. of the following matrix

$$\vec{Q} = \begin{bmatrix} \vec{s}(u_i,w_k) & \vec{s}(u_i,w_{k+1}) & \vec{s}_w(u_i,w_k) & \vec{s}_w(u_i,w_{k+1}) \\ \vec{s}(u_{i+1},w_k) & \vec{s}(u_{i+1},w_{k+1}) & \vec{s}_w(u_{i+1},w_k) & \vec{s}_w(u_{i+1},w_{k+1}) \\ \vec{s}_u(u_i,w_k) & \vec{s}_u(u_i,w_{k+1}) & \vec{s}_{uw}(u_i,w_k) & \vec{s}_{uw}(u_i,w_{k+1}) \\ \vec{s}_u(u_{i+1},w_k) & \vec{s}_u(u_{i+1},w_{k+1}) & \vec{s}_{uw}(u_{i+1},w_k) & \vec{s}_{uw}(u_{i+1},w_{k+1}) \end{bmatrix}.$$

The vectors $\vec{s}_u(u_i,w_k)$ and $\vec{s}_w(u_i,w_k)$ are proportional to the tangent vectors to the parametric curves u = const and w = const at the patch boundary points (i,k). The cross-derivative vector $\vec{s}_{uw}$ is called the "twist" vector.

For now on, the shorthand notation $\vec{s}(u_i, w_k) = \vec{s}_{ik}$, $\vec{s}_u(u_i, w_k) = \vec{s}_{u,ik}$ etc. is adopted. Note that a patch completely defined in terms of the vectors $\vec{s}$, $\vec{s}_u$, $\vec{s}_w$ and $\vec{s}_{uw}$ at its four corners is called a tensor-product (or Cartesian product) patch. Since the blade is regarded as a composite surface, there must be some constraints on the elements of $\vec{Q}$ in order to achieve the curvature continuity over the entire blade. Here the positions of the patch corners ($\vec{s}_{ik}$, $\vec{s}_{i+1k}$, $\vec{s}_{ik+1}$, $\vec{s}_{i+1k+1}$, $1 \leq i < ILB$, $1 \leq k < N$) are known at the outset from the framework based on the root, the tip and the inbetween blade sections. When first derivatives are matched in both direction and magnitude at the data points, the u-curves will have second derivative continuity if the tangent vectors $\vec{s}_{u,ik}$ are calculated from the system of recurrent equations

$$\vec{s}_{u,i-1k} + 4\vec{s}_{u,ik} + \vec{s}_{u,i+1k} = 3(\vec{s}_{i+1k} - \vec{s}_{i-1k}), \quad i = 2, ..., ILB - 1. \tag{A.9}$$

Similarly, the w-curves will have second-order continuity if

$$\vec{s}_{w,ik-1} + 4\vec{s}_{w,ik} + \vec{s}_{w,ik+1} = 3(\vec{s}_{ik+1} - \vec{s}_{ik-1}), \quad k = 2, ..., N - 1. \tag{A.10}$$

At this point, the relations (A.9) and (A.10) simply express the requirements for two composite curves to be piecewise cubic with continuous first and second derivatives at the data points. However, from an implementation point of view, the systems (A.9) and (A.10) are generally written in terms of recurrent relations involving the second derivatives instead of the first ones, see for instance [85]. The extra conditions to be met for second-order continuity of $\vec{s}_{uu}$ across all the w-boundaries of the blade composite surface can be summarized as

$$\vec{s}_{uw,i-1k} + 4\vec{s}_{uw,ik} + \vec{s}_{uw,i+1k} = 3(\vec{s}_{w,i+1k} - \vec{s}_{w,i-1k}), \quad i = 2, ..., ILB - 1. \tag{A.11}$$

Here the gradients $\vec{s}_w$ on the right-hand side may be considered known from Eq. (A.10). Alternatively, continuity of $\vec{s}_{ww}$ in the w-direction over the entire blade may be achieved by satisfying the analogous equation

$$\vec{s}_{wu,ik-1} + 4\vec{s}_{wu,ik} + \vec{s}_{wu,ik+1} = 3(\vec{s}_{u,ik+1} - \vec{s}_{u,ik-1}), \quad k = 2, ..., N - 1, \tag{A.12}$$

where the gradients $\vec{s}_u$ are known from Eq. (A.9).

Since the formulation of the tensor-product patch assumes that $\vec{s}_{uw} = \vec{s}_{wu}$ (at patch corners) and that cross-boundary gradients are specified in terms of $\vec{s}_u$, $\vec{s}_w$ and $\vec{s}_{uw}$ also at patch corners, it can be shown [24] that the solutions $\vec{s}_{uw}$ of Eq. (A.11) are going to be the same as the solutions $\vec{s}_{wu}$ of Eq. (A.12). Consequently, overall second-order continuity is attainable.

Note that the entire surface is uniquely determined in terms of

- the points $\vec{s}_{ik}$ $(1 \leq i \leq ILB, 1 \leq k \leq N)$,
- the tangent vectors $\vec{s}_{u,ik}$ along the w-boundaries $(i = 1, ILB, 1 \leq k \leq N)$ and $\vec{s}_{w,ik}$ along the u-boundaries $(1 \leq i \leq ILB, k = 1, N)$ of the composite surface as a whole, and
- the twist vectors $\vec{s}_{uw,ik}$ at its corners $(i = 1, ILB, k = 1, N)$, which are taken to be zero.

Bicubic spline implementation

The numerical procedure to implement the bicubic spline differs slightly from the theory in the sense that it is based on a sequence of one-dimensional splines. Since ILB represents the number of points around the blade and $KLB = KL$ the number of points along the span, a table of $ILB \times KLB$ functional values of the form (A.8) is to be interpolated through the bicubic spline. This is accomplished by performing KLB one-dimensional splines across the rows of the table, followed by ILB additional one-dimensional splines down the newly created columns. Subroutines of reference [85] are used in this procedure. First ILB splines over N points (corresponding to the root, the tip and the inbetween blade sections) are *constructed.* Then ILB spline *evaluations* are performed at KLB linearly distributed spanwise locations. Each of these new sets of data are used to *construct* KLB splines over ILB points around the blade. Finally KLB spline *evaluations* performed over the blade points distribution complete

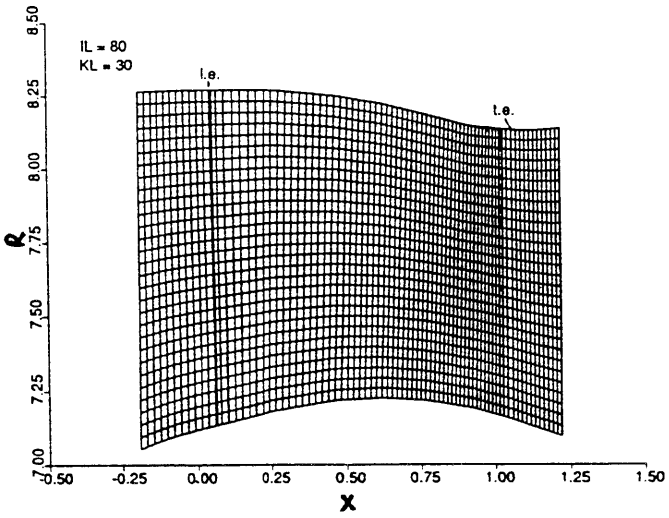

Figure A.7: Stator mesh, $80 \times 30 \times 30$ nodes. Pressure and periodic surfaces (side view).

the bicubic interpolation. For this last process, the points are distributed around the blade according to the same type of collocation function as the one described in Section A.2.3 (2nd degree polynomial points distribution). Examples are given in Figures A.7 and A.8, where $ILB = 115$, $KLB = 30$ for the stator, and $ILB = 93$, $KLB = 35$ for the rotor.

A.2.6 Periodic and inlet/outlet mesh surfaces

The upstream (downstream) part of the periodic mesh surface at $\eta = 0$ is constructed in three steps, namely

- The x value is found by linear interpolation between the axial locations of the inlet (outlet) surface and the leading edge (trailing edge).
- The radial component r corresponding to each axial location is also defined by linear interpolation, between the hub and tip wall radii.
- The third component (y or θ) is defined such that

$$\frac{d\theta}{dR} = 0, \quad \xi = 0, 1, \quad \eta = 0, \quad 0 < \tau < 1.$$

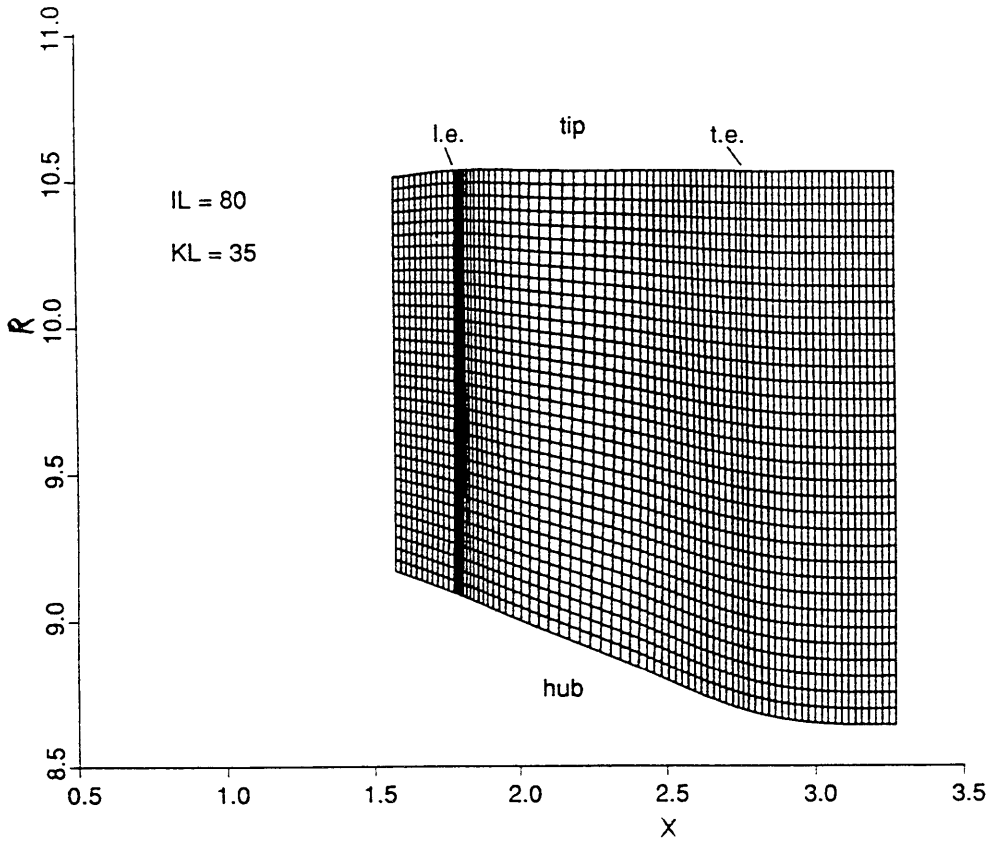

Figure A.8: Rotor mesh, $80 \times 30 \times 35$ nodes. Suction and periodic surfaces (side view).

The last condition is introduced in order to match the boundary conditions at the hub and the tip walls in the solution of the Poisson equations (see Section A.2.7). The periodic mesh surface at $\eta = 1$ is defined by a one pitch angle rotation of the surface $\eta = 0$. Examples of periodic mesh surfaces are shown in Figures A.7 and A.8.

As for the periodic surfaces, the radial component of the inlet and outlet mesh surface ($\xi = 0, 1,\ 0 < \eta < 1$), is defined linearly from the hub to the tip. Then, since the inlet (outlet) axial location is specified at the outset, only one condition remains to be set for a unique definition of these surfaces. It is chosen to be

$$\frac{d\theta}{dR} = 0, \quad \xi = 0, 1, \quad 0 < \eta < 1, \quad 0 \leq \tau \leq 1.$$

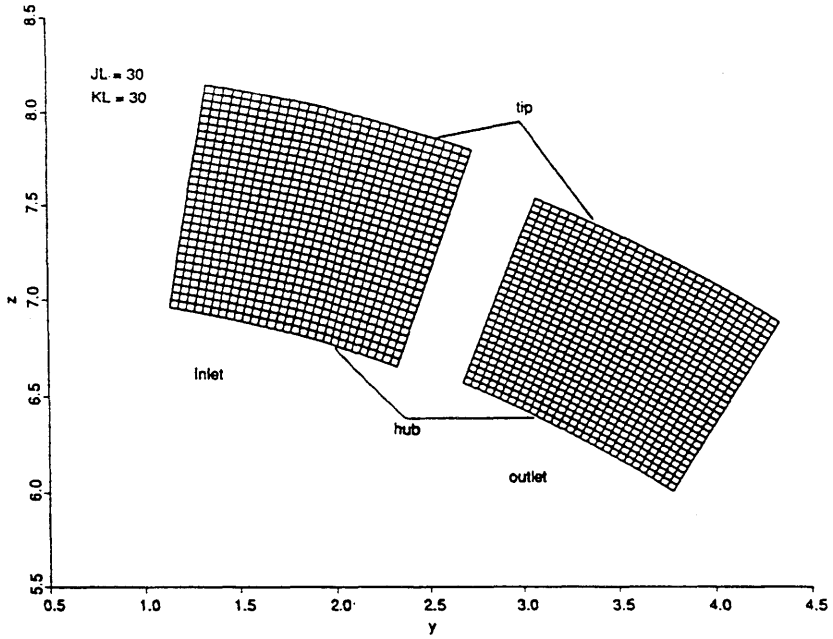

Figure A.9: Stator mesh, $80 \times 30 \times 30$ nodes. Front view of the inlet and the outlet surfaces. See Figures A.3 and A.7 for corresponding geometry.

The above relation together with the condition that the same (not necessarily linear[1]) radial interpolation function holds for $0 \leq \eta \leq 1$ yields a uniform and smooth mesh at the inlet and the outlet, see Figure A.9.

A.2.7 Poisson solver and hub/tip mesh points distribution

In the present study an iterative procedure of Successive Line Over Relaxation (SOR) is used to solve Equations (A.2), see [3] for instance.

The (x, y, z) coordinates are known at the boundaries $\xi = 0, 1$ (inlet/outlet surfaces) and $\eta = 0, 1$ (periodic, suction and pressure surfaces). The boundary conditions on $\tau = 0, 1$ corresponding to the hub and the tip walls are specified in the iterative procedure as follows

[1]The radial points distribution function as well as the points distribution function around the blade may be easily replaced in the code since these two functions depend only on one parameter.

- The axial component x is defined such that $x_\tau = 0$.
- The y coordinate results from the condition $\frac{d\theta}{dR} = 0$.
- The z value is found by using the wall spline $R = R(x)$ and the relation $z = \sqrt{R^2 - y^2}$ (the mesh being defined in the first quadrant).

The part of $\eta = 0, 1$ corresponding to the points distribution on the blade surface is used to calculate the boundary source terms $\tilde{P}$, $\tilde{Q}$ and $\tilde{R}$.

Each iteration consists of two distinct parts. In the first part the values of $\tilde{P}$, $\tilde{Q}$ and $\tilde{R}$ are updated using the (x, y, z) coordinates of the initial solution or the values of the previous iteration. Specifically, the derivatives in Eqs. (A.7) together with finite difference approximations for the first and second partial derivatives of $\vec{r}$ with respect to ξ, η, τ are substituted into Eqs. (A.2) which are solved for $\tilde{P}$, $\tilde{Q}$ and $\tilde{R}$ at the boundaries $\eta = 0, 1$. Note that in this part the user may specify $\partial S/\partial \eta$ on the blade surface. Non central differences using the current interior mesh solution are used for evaluating second partial derivatives on the blade surface in the η direction. Hence, for each $\eta = 0, 1$ node on the blade Eqs. (A.2) provide three relations which can be solved for the three unknowns $\tilde{P}$, $\tilde{Q}$ and $\tilde{R}$ to give

$$\begin{bmatrix} \tilde{P} \\ \tilde{Q} \\ \tilde{R} \end{bmatrix} = -M^{-1}J^{-2}\left[a_{11}\vec{r}_{\xi\xi} + a_{22}\vec{r}_{\eta\eta} + a_{33}\vec{r}_{\tau\tau} + 2(a_{12}\vec{r}_{\xi\eta} + a_{13}\vec{r}_{\xi\tau} + a_{23}\vec{r}_{\eta\tau})\right] \quad \text{(A.13)}$$

To avoid highly skewed cells in the control volume mid-passage of high turning turbine cascades, it is actually preferable not to impose the orthogonality conditions (A.4) and (A.5) on the entire blade surface. In the present application the surface control system of Equations (A.7) (orthogonality and spacing) is applied on the entire pressure side, but only from the leading edge to the crown on the suction side. Then, from the suction side crown to the trailing edge just the cell size control Equation (A.6) is used. The discrete version of $(\partial S/\partial \eta)$ in Eq. (A.6) is currently defined as

$$\Delta S_{ik} = f_{ik}\left(\frac{\sum_{j=1}^{JL-1} \|\vec{r}_{j+1} - \vec{r}_j\|}{JL-1}\right), \quad f_{ik} \equiv min(i = 1, ..., IL-1,\ k = 1, ..., KL-1).$$

ΔS_{ik} is actually implemented as an array, so it may vary along the blade and can easily be set by the user to some particular values. As already noticed by Steger [103] the corrections of the source terms from one iteration to another may be quite large so that under-relaxation of the order of 1% is used to update $\tilde{P}$, $\tilde{Q}$ and $\tilde{R}$.

In the second part of the each iteration step the source terms P, Q and R for the whole field are evaluated using the relations (A.3). Then, the new values of (x, y, z) are calculated everywhere in the interior domain according to the line SOR iterative scheme using Thomas' algorithm [3]. Examples of stator and rotor row meshes using this procedure are given in Figures A.10 and A.11. The CPU time needed on a Microvax station II is $O(10^{-3})$ sec./iteration/mesh point.

As mentioned in Section A.1.3, a computationally less expensive procedure, but valid only to generate a uniform mesh, is to calculate a few SOR iterations with the source terms set to zero, and then redistribute the grid points from blade to blade or periodic to periodic surface. This is achieved according to

$$\vec{r}_{new} = \vec{r}_{old} + \alpha_j(\vec{r}_{old\,j+1} - \vec{r}_{old\,j}), \quad j = 1, ..., JL-1,$$

where the subscripts $_{old}$ and $_{new}$ refer to the mesh before and after redistribution. α_j is a redistribution factor defined by

$$\alpha_j = \frac{LU_j - L_j}{L_{j+1} - L_j}, \quad LU_j = \frac{j}{JL-1} L_{JL}, \quad j = 1, ..., JL-1,$$

where L_j is the measures the length along an η line from $j = 1$ to j. The above redistribution relations hold for $i = 2, ..., IL-1$ and $k = 1, ..., KL$. This redistribution procedure destroys the smoothness of the mesh and does not allow for any direct control of the grid lines along the boundary surfaces.

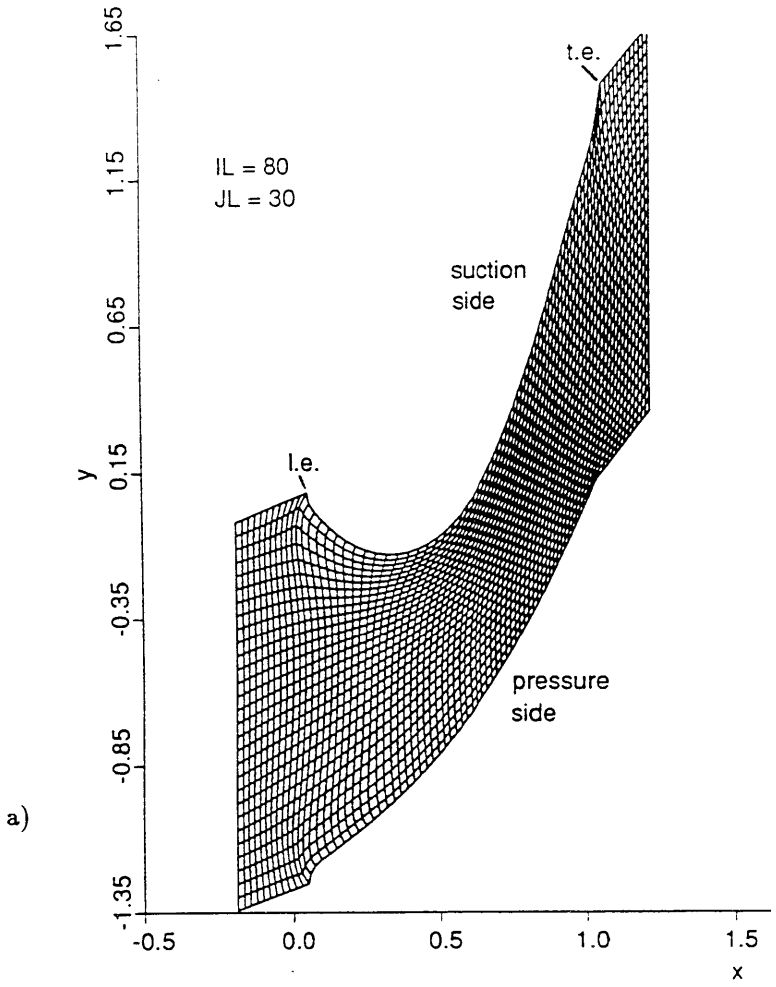

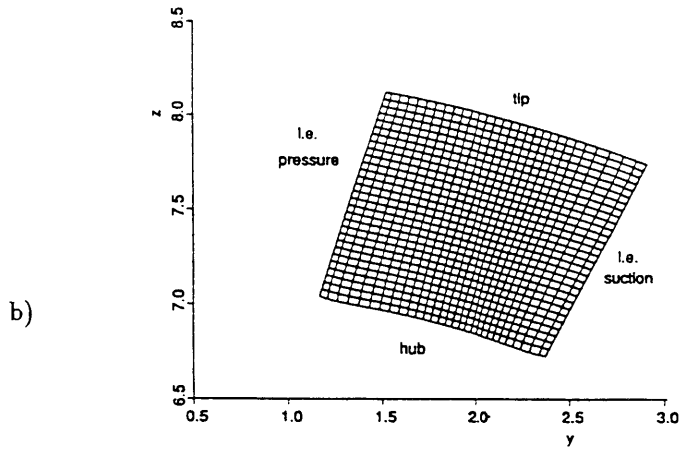

Figure A.10: Stator mesh, $80 \times 30 \times 30$ nodes. a) Quasi top view of the mean height surface $k = 15$. b) Front view of the leading edge interblade surface. See Figures A.3, A.7 and A.9 for corresponding geometry.

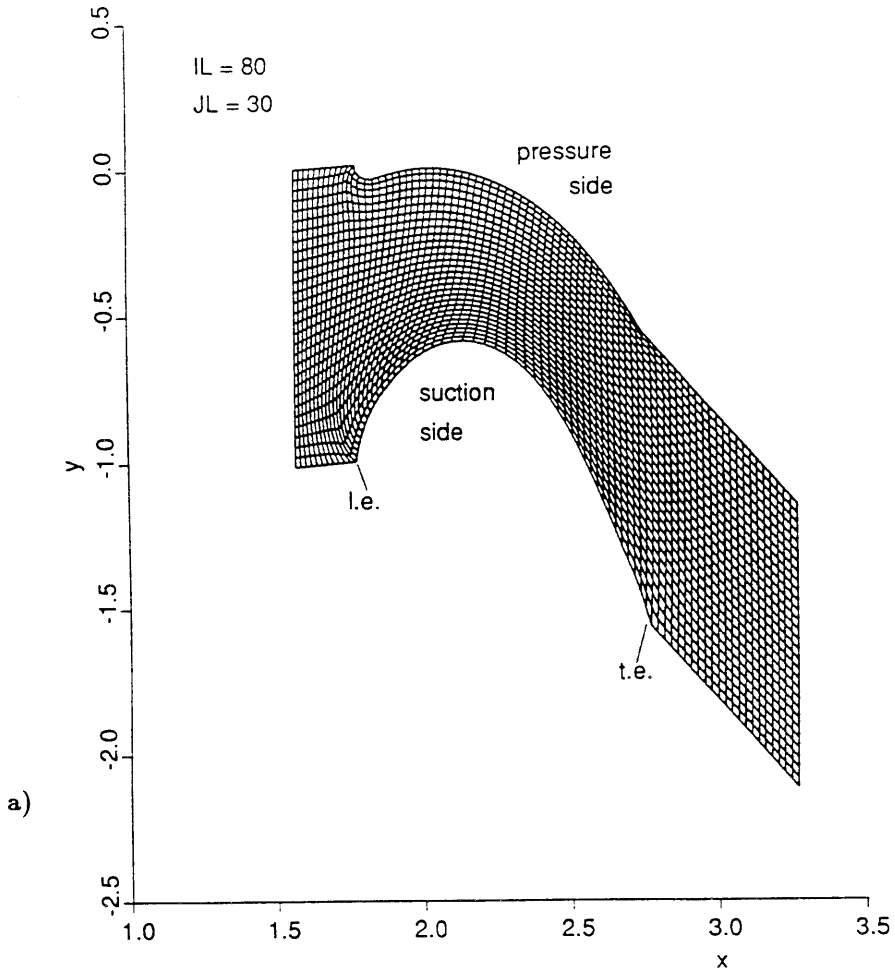

a)

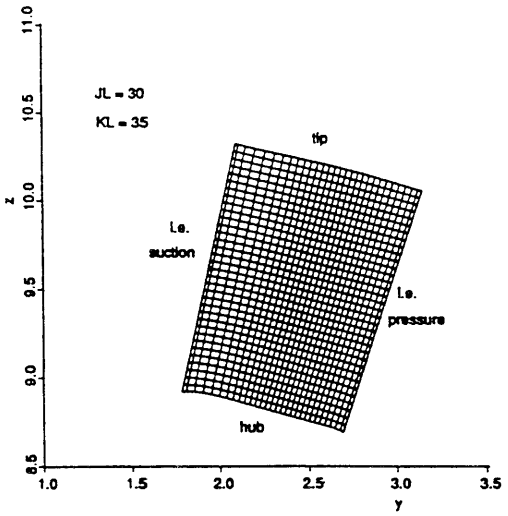

b)

Figure A.11: Rotor mesh, $80 \times 30 \times 35$ nodes. a) Quasi top view of the mean height surface $k = 17$. b) Front view of the leading edge interblade surface. See Figure A.8 for corresponding geometry.

Appendix B

Cell Volume and Face Area

The derivation of the cell volume and the projected surface areas of the cell faces is presented in this appendix.

The volume of an hexahedral cell can be decomposed into five constituent tetrahedra. For instance, with reference to Fig. B.1, the volume V_{1236} of the tetrahedron defined by the corner nodes $1, 2, 3, 6$ is given by

$$V_{1236} = \frac{1}{6} \begin{vmatrix} x_1 & y_1 & z_1 & 1 \\ x_2 & y_2 & z_2 & 1 \\ x_3 & y_3 & z_3 & 1 \\ x_6 & y_6 & z_6 & 1 \end{vmatrix}. \tag{B.1}$$

Thus, the volume of the cell is defined as

$$V = V_{1236} + V_{3867} + V_{1685} + V_{3816} + V_{1384}. \tag{B.2}$$

The edges of a cell face are straight lines. Thus, the area of the face is given by the half cross-product of its line diagonals. The following projected areas, $\vec{S} = (S_x, S_y, S_z)$ can be derived for the six faces defining the cell, see Figure B.1.

$$\begin{aligned} (S_x)_1 &= \frac{1}{2}((y_3 - y_6)(z_7 - z_2) - (y_7 - y_2)(z_3 - z_6)) \\ (S_y)_1 &= \frac{1}{2}((z_3 - z_6)(x_7 - x_2) - (z_7 - z_2)(x_3 - x_6)) \end{aligned}$$

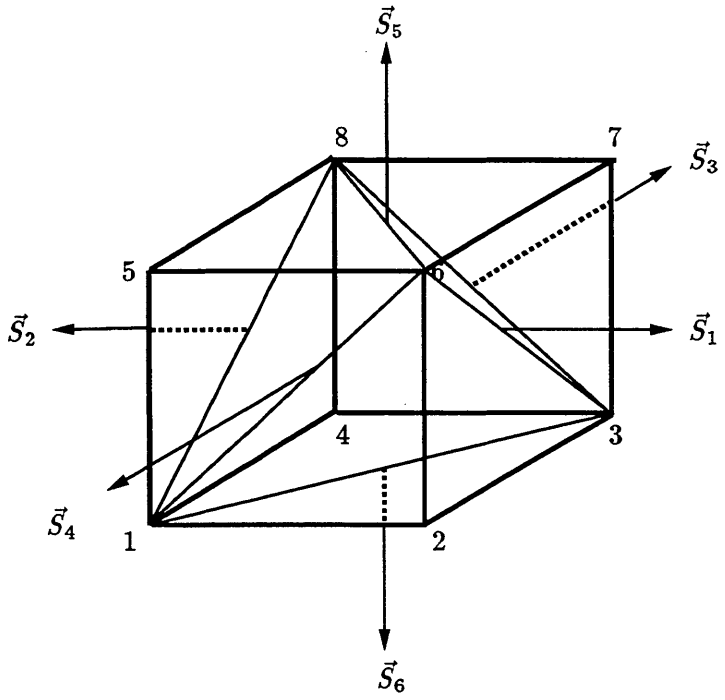

Figure B.1: Hexahedral cell is formed by five tetrahedra.

$$
\begin{aligned}
(S_z)_1 &= \frac{1}{2}\left((x_3-x_6)(y_7-y_2)-(x_7-x_2)(y_3-y_6)\right)\\
(S_x)_2 &= \frac{1}{2}\left((y_8-y_1)(z_4-z_5)-(y_4-y_5)(z_8-z_1)\right)\\
(S_y)_2 &= \frac{1}{2}\left((z_8-z_1)(x_4-x_5)-(z_4-z_5)(x_8-x_1)\right)\\
(S_z)_2 &= \frac{1}{2}\left((x_8-x_1)(y_4-y_5)-(x_4-x_5)(y_8-y_1)\right)\\
(S_x)_3 &= \frac{1}{2}\left((y_7-y_4)(z_3-z_8)-(y_3-y_8)(z_7-z_4)\right)\\
(S_y)_3 &= \frac{1}{2}\left((z_7-z_4)(x_3-x_8)-(z_3-z_8)(x_7-x_4)\right)\\
(S_z)_3 &= \frac{1}{2}\left((x_7-x_4)(y_3-y_8)-(x_3-x_8)(y_7-y_4)\right)\\
(S_x)_4 &= \frac{1}{2}\left((y_6-y_1)(z_5-z_2)-(y_5-y_2)(z_6-z_1)\right)\\
(S_y)_4 &= \frac{1}{2}\left((z_6-z_1)(x_5-x_2)-(z_5-z_2)(x_6-x_1)\right)\\
(S_z)_4 &= \frac{1}{2}\left((x_6-x_1)(y_5-y_2)-(x_5-x_2)(y_6-y_1)\right)\\
(S_x)_5 &= \frac{1}{2}\left((y_7-y_5)(z_8-z_6)-(y_8-y_6)(z_7-z_5)\right)\\
(S_y)_5 &= \frac{1}{2}\left((z_7-z_5)(x_8-x_6)-(z_8-z_6)(x_7-x_5)\right)\\
(S_z)_5 &= \frac{1}{2}\left((x_7-x_5)(y_8-y_6)-(x_8-x_6)(y_7-y_5)\right)\\
(S_x)_6 &= \frac{1}{2}\left((y_3-y_1)(z_2-z_4)-(y_2-y_4)(z_3-z_1)\right)\\
(S_y)_6 &= \frac{1}{2}\left((z_3-z_1)(x_2-x_4)-(z_2-z_4)(x_3-x_1)\right)\\
(S_z)_6 &= \frac{1}{2}\left((x_3-x_1)(y_2-y_4)-(x_2-x_4)(y_3-y_1)\right).
\end{aligned}
\tag{B.3}
$$

With these definitions, all the cell faces surface vectors are pointing outward.

Appendix C

Stability Analysis

The stability analysis of the Ni-Lax-Wendroff method is performed on the Euler equations written in primitive variables and computational coordinates, and is valid for a 3-D skewed mesh. Section C.1 describes the transformation from conservative variables in Cartesian space to conservative variables in computational coordinates leading to the so-called weak conservation law form of the Euler equations. Then the Euler equations are written in primitive variables in Section C.2. Finally, the stability criterion is derived from the primitive form in Section C.3.

C.1 3-D Euler equations in conservative variables and computational coordinates

In the absolute frame of reference the Euler equations expressed in conservative form and Cartesian coordinates are

$$\frac{\partial U}{\partial t} + \frac{\partial F}{\partial x} + \frac{\partial G}{\partial y} + \frac{\partial H}{\partial z} = 0, \tag{C.1}$$

where

$$U = \begin{pmatrix} \rho \\ \rho u \\ \rho v \\ \rho w \\ \rho e_t \end{pmatrix}, \; F = \begin{pmatrix} \rho u \\ \rho u^2+p \\ \rho uv \\ \rho uw \\ \rho u h_t \end{pmatrix}, \; G = \begin{pmatrix} \rho v \\ \rho uv \\ \rho v^2+p \\ \rho vw \\ \rho v h_t \end{pmatrix}, \; H = \begin{pmatrix} \rho w \\ \rho uw \\ \rho vw \\ \rho w^2+p \\ \rho w h_t \end{pmatrix}. \tag{C.2}$$

The pressure p, and stagnation enthalpy h_t, are related to the density ρ, velocity components (u, v, w), and stagnation energy per unit mass e_t by the following two equations which assume a perfect gas with a constant specific heat ratio γ.

$$p = (\gamma-1)\rho\left(e_t - \frac{1}{2}(u^2+v^2+w^2)\right) \tag{C.3}$$

$$h_t = e_t + \frac{p}{\rho}. \tag{C.4}$$

The transformation from Cartesian (x, y, z) to computational (ξ, η, τ) coordinates is accomplished using the chain rule derivative. Thus,

$$\frac{\partial U}{\partial t}+\frac{\partial F}{\partial \xi}\xi_x+\frac{\partial F}{\partial \eta}\eta_x+\frac{\partial F}{\partial \tau}\tau_x+\frac{\partial G}{\partial \xi}\xi_y+\frac{\partial G}{\partial \eta}\eta_y+\frac{\partial G}{\partial \tau}\tau_y+\frac{\partial H}{\partial \xi}\xi_z+\frac{\partial H}{\partial \eta}\eta_z+\frac{\partial H}{\partial \tau}\tau_z = 0, \tag{C.5}$$

where the subscripts indicate partial derivatives. The Jacobian J of the transformation from the physical space to the computational space is written as

$$J = x_\xi(y_\eta z_\tau - y_\tau z_\eta) - x_\eta(y_\xi z_\tau - y_\tau z_\xi) + x_\tau(y_\xi z_\eta - y_\eta z_\xi). \tag{C.6}$$

The metrics are

$$\begin{aligned}
\xi_x &= \frac{y_\eta z_\tau - y_\tau z_\eta}{J}, \quad \xi_y = -\frac{x_\eta z_\tau - x_\tau z_\eta}{J}, \quad \xi_z = \frac{x_\eta y_\tau - x_\tau y_\eta}{J}, \\
\eta_x &= \frac{y_\xi z_\tau - y_\tau z_\xi}{J}, \quad \eta_y = -\frac{x_\xi z_\tau - x_\tau z_\xi}{J}, \quad \eta_z = \frac{x_\xi y_\tau - x_\tau y_\xi}{J}, \\
\tau_x &= \frac{y_\xi z_\eta - y_\eta z_\xi}{J}, \quad \tau_y = -\frac{x_\xi z_\eta - x_\eta z_\xi}{J}, \quad \tau_z = \frac{x_\xi y_\eta - x_\eta y_\xi}{J}.
\end{aligned} \tag{C.7}$$

The following three relations are easy to demonstrate.

$$\begin{aligned}
\frac{\partial}{\partial\xi}(y_\eta z_\tau - y_\tau z_\eta) &- \frac{\partial}{\partial\eta}(y_\xi z_\tau - y_\tau z_\xi) &- \frac{\partial}{\partial\tau}(y_\xi z_\eta - y_\eta z_\xi) &= 0,\\
\frac{\partial}{\partial\xi}(x_\eta z_\tau - x_\tau z_\eta) &- \frac{\partial}{\partial\eta}(x_\xi z_\tau - x_\tau z_\xi) &- \frac{\partial}{\partial\tau}(x_\xi z_\eta - x_\eta z_\xi) &= 0,\\
\frac{\partial}{\partial\xi}(x_\eta y_\tau - x_\tau y_\eta) &- \frac{\partial}{\partial\eta}(x_\xi y_\tau - x_\tau y_\xi) &- \frac{\partial}{\partial\tau}(x_\xi y_\eta - x_\eta y_\xi) &= 0.
\end{aligned} \tag{C.8}$$

Using the above relations the Euler equations are rewritten in computational coordinates as

$$\begin{aligned}
&J\frac{\partial U}{\partial t} + \frac{\partial F'}{\partial\xi} + \frac{\partial G'}{\partial\eta} + \frac{\partial H'}{\partial\tau}\\
&- F\underbrace{\left[\frac{\partial}{\partial\xi}(y_\eta z_\tau - y_\tau z_\eta) - \frac{\partial}{\partial\eta}(y_\xi z_\tau - y_\tau z_\xi) - \frac{\partial}{\partial\tau}(y_\xi z_\eta - y_\eta z_\xi)\right]}_{=0}\\
&- G\underbrace{\left[\frac{\partial}{\partial\xi}(x_\eta z_\tau - x_\tau z_\eta) - \frac{\partial}{\partial\eta}(x_\xi z_\tau - x_\tau z_\xi) - \frac{\partial}{\partial\tau}(x_\xi z_\eta - x_\eta z_\xi)\right]}_{=0}\\
&- H\underbrace{\left[\frac{\partial}{\partial\xi}(x_\eta y_\tau - x_\tau y_\eta) - \frac{\partial}{\partial\eta}(x_\xi y_\tau - x_\tau y_\xi) - \frac{\partial}{\partial\tau}(x_\xi y_\eta - x_\eta y_\xi)\right]}_{=0} = 0.
\end{aligned} \tag{C.9}$$

F', G', H' are the contravariant fluxes defined as

$$\begin{aligned}
F' &= (y_\eta z_\tau - y_\tau z_\eta)F - (x_\eta z_\tau - x_\tau z_\eta)G + (x_\eta y_\tau - x_\tau y_\eta)H,\\
G' &= -(y_\xi z_\tau - y_\tau z_\xi)F + (x_\xi z_\tau - x_\tau z_\xi)G - (x_\xi y_\tau - x_\tau y_\xi)H,\\
H' &= (y_\xi z_\eta - y_\eta z_\xi)F - (x_\xi z_\eta - x_\eta z_\xi)G + (x_\xi y_\eta - x_\eta y_\xi)H.
\end{aligned} \tag{C.10}$$

Moreover let

$$\begin{aligned}
r_1 &= u(y_\eta z_\tau - y_\tau z_\eta) - v(x_\eta z_\tau - x_\tau z_\eta) + w(x_\eta y_\tau - x_\tau y_\eta),\\
r_2 &= -u(y_\xi z_\tau - y_\tau z_\xi) + v(x_\xi z_\tau - x_\tau z_\xi) - w(x_\xi y_\tau - x_\tau y_\xi),\\
r_3 &= u(y_\xi z_\eta - y_\eta z_\xi) - v(x_\xi z_\eta - x_\eta z_\xi) + w(x_\xi y_\eta - x_\eta y_\xi).
\end{aligned} \tag{C.11}$$

Using the above definitions it follows that

$$J\frac{\partial U}{\partial t} + \frac{\partial F'}{\partial\xi} + \frac{\partial G'}{\partial\eta} + \frac{\partial H'}{\partial\tau} = 0, \tag{C.12}$$

where

$$U = \begin{pmatrix} \rho \\ \rho u \\ \rho v \\ \rho w \\ \rho E \end{pmatrix}, \quad F' = \begin{pmatrix} \rho r_1 \\ \rho r_1 u + p(y_\eta z_\tau - y_\tau z_\eta) \\ \rho r_1 v - p(x_\eta z_\tau - x_\tau z_\eta) \\ \rho r_1 w + p(x_\eta y_\tau - x_\tau y_\eta) \\ r_1(\rho E + p) \end{pmatrix}, \quad G' = \begin{pmatrix} \rho r_2 \\ \rho r_2 u - p(y_\xi z_\tau - y_\tau z_\xi) \\ \rho r_2 v + p(x_\xi z_\tau - x_\tau z_\xi) \\ \rho r_2 w - p(x_\xi y_\tau - x_\tau y_\xi) \\ r_2(\rho E + p) \end{pmatrix},$$

$$H' = \begin{pmatrix} \rho r_3 \\ \rho r_3 u + p(y_\xi z_\eta - y_\eta z_\xi) \\ \rho r_3 v - p(x_\xi z_\eta - x_\eta z_\xi) \\ \rho r_3 w + p(x_\xi y_\eta - x_\eta y_\xi) \\ r_3(\rho E + p) \end{pmatrix}. \tag{C.13}$$

C.2 3-D Euler equations in primitive variables and computational coordinates

The continuity equation of System (C.13) is

$$\begin{aligned} J\frac{\partial \rho}{\partial t} &= -\frac{\partial}{\partial \xi}(\rho r_1) - \frac{\partial}{\partial \eta}(\rho r_2) - \frac{\partial}{\partial \tau}(\rho r_3) \\ &= -r_1\frac{\partial \rho}{\partial \xi} - r_2\frac{\partial \rho}{\partial \eta} - r_3\frac{\partial \rho}{\partial \tau} - \rho\left(\frac{\partial r_1}{\partial \xi} + \frac{\partial r_2}{\partial \eta} + \frac{\partial r_3}{\partial \tau}\right), \end{aligned} \tag{C.14}$$

where

$$\begin{aligned} \frac{\partial r_1}{\partial \xi} + \frac{\partial r_2}{\partial \eta} + \frac{\partial r_3}{\partial \tau} &= \\ \frac{\partial u}{\partial \xi}(y_\eta z_\tau - y_\tau z_\eta) &- \frac{\partial v}{\partial \xi}(x_\eta z_\tau - x_\tau z_\eta) + \frac{\partial w}{\partial \xi}(x_\eta y_\tau - x_\tau y_\eta) \\ -\frac{\partial u}{\partial \eta}(y_\xi z_\tau - y_\tau z_\xi) &+ \frac{\partial v}{\partial \eta}(x_\xi z_\tau - x_\tau z_\xi) - \frac{\partial w}{\partial \eta}(x_\xi y_\tau - x_\tau y_\xi) \\ \frac{\partial u}{\partial \tau}(y_\xi z_\eta - y_\eta z_\xi) &- \frac{\partial v}{\partial \tau}(x_\xi z_\eta - x_\eta z_\xi) + \frac{\partial w}{\partial \tau}(x_\xi y_\eta - x_\eta y_\xi). \end{aligned} \tag{C.15}$$

The time derivative of the u component in the momentum equation is written as

$$J\rho\frac{\partial u}{\partial t} = J\left(\frac{\partial}{\partial t}(\rho u) - u\frac{\partial \rho}{\partial t}\right). \tag{C.16}$$

The time derivatives of the two terms on the right-hand side of Equation (C.16) are replaced by their spatial derivatives using Equations (C.13) and (C.14), respectively. Hence, Eq. (C.16) becomes

$$J\rho\frac{\partial u}{\partial t} = -\rho r_1\frac{\partial u}{\partial \xi} - \rho r_2\frac{\partial u}{\partial \eta} - \rho r_3\frac{\partial u}{\partial \tau} - \frac{\partial p}{\partial \xi}(y_\eta z_\tau - y_\tau z_\eta) + \frac{\partial p}{\partial \eta}(y_\xi z_\tau - y_\tau z_\xi) - \frac{\partial p}{\partial \tau}(y_\xi z_\eta - y_\eta z_\xi). \tag{C.17}$$

The y and z components for the conservation of momentum are found in a similar way.

$$J\rho\frac{\partial v}{\partial t} = -\rho r_1\frac{\partial v}{\partial \xi} - \rho r_2\frac{\partial v}{\partial \eta} - \rho r_3\frac{\partial v}{\partial \tau} + \frac{\partial p}{\partial \xi}(x_\eta z_\tau - x_\tau z_\eta) - \frac{\partial p}{\partial \eta}(x_\xi z_\tau - x_\tau z_\xi) + \frac{\partial p}{\partial \tau}(x_\xi z_\eta - x_\eta z_\xi). \tag{C.18}$$

$$J\rho\frac{\partial w}{\partial t} = -\rho r_1\frac{\partial w}{\partial \xi} - \rho r_2\frac{\partial w}{\partial \eta} - \rho r_3\frac{\partial w}{\partial \tau} - \frac{\partial p}{\partial \xi}(x_\eta y_\tau - x_\tau y_\eta) + \frac{\partial p}{\partial \eta}(x_\xi y_\tau - x_\tau y_\xi) - \frac{\partial p}{\partial \tau}(x_\xi y_\eta - x_\eta y_\xi). \tag{C.19}$$

The time derivative of Equation (C.3) is

$$J\frac{1}{\gamma - 1}\frac{\partial p}{\partial t} = J\left(\frac{\partial}{\partial t}(\rho E) - \frac{1}{2}(u^2 + v^2 + w^2)\frac{\partial \rho}{\partial t} - \rho u\frac{\partial u}{\partial t} - \rho v\frac{\partial v}{\partial t} - \rho w\frac{\partial w}{\partial t}\right). \tag{C.20}$$

Again, the right-hand side time derivative terms are replaced by spatial derivatives using Equations (C.13), (C.14) (C.17), (C.18) and (C.19). Thus, the energy equation becomes

$$J\frac{\partial p}{\partial t} = -r_1\frac{\partial p}{\partial \xi} - r_2\frac{\partial p}{\partial \eta} - r_3\frac{\partial p}{\partial \tau} - \gamma p\left(\frac{\partial r_1}{\partial \xi} + \frac{\partial r_2}{\partial \eta} + \frac{\partial r_3}{\partial \tau}\right). \tag{C.21}$$

Finally, the Euler equations in primitive form and in computational coordinates are

$$\frac{\partial U_p}{\partial t} + J^{-1}\left(A\frac{\partial U_p}{\partial \xi} + B\frac{\partial U_p}{\partial \eta} + C\frac{\partial U_p}{\partial \tau}\right) = 0, \qquad \text{where} \qquad U_p = \begin{pmatrix} \rho \\ u \\ v \\ w \\ p \end{pmatrix}, \tag{C.22}$$

$$A = \begin{pmatrix} r_1 & \rho(y_\eta z_\tau - y_\tau z_\eta) & -\rho(x_\eta z_\tau - x_\tau z_\eta) & \rho(x_\eta y_\tau - x_\tau y_\eta) & 0 \\ 0 & r_1 & 0 & 0 & \frac{1}{\rho}(y_\eta z_\tau - y_\tau z_\eta) \\ 0 & 0 & r_1 & 0 & -\frac{1}{\rho}(x_\eta z_\tau - x_\tau z_\eta) \\ 0 & 0 & 0 & r_1 & \frac{1}{\rho}(x_\eta y_\tau - x_\tau y_\eta) \\ 0 & \gamma p(y_\eta z_\tau - y_\tau z_\eta) & -\gamma p(x_\eta z_\tau - x_\tau z_\eta) & \gamma p(x_\eta y_\tau - x_\tau y_\eta) & r_1 \end{pmatrix},$$

$$B = \begin{pmatrix} r_2 & -\rho(y_\xi z_\tau - y_\tau z_\xi) & \rho(x_\xi z_\tau - x_\tau z_\xi) & -\rho(x_\xi y_\tau - x_\tau y_\xi) & 0 \\ 0 & r_2 & 0 & 0 & -\frac{1}{\rho}(y_\xi z_\tau - y_\tau z_\xi) \\ 0 & 0 & r_2 & 0 & \frac{1}{\rho}(x_\xi z_\tau - x_\tau z_\xi) \\ 0 & 0 & 0 & r_2 & -\frac{1}{\rho}(x_\xi y_\tau - x_\tau y_\xi) \\ 0 & -\gamma p(y_\xi z_\tau - y_\tau z_\xi) & \gamma p(x_\xi z_\tau - x_\tau z_\xi) & -\gamma p(x_\xi y_\tau - x_\tau y_\xi) & r_2 \end{pmatrix},$$

$$C = \begin{pmatrix} r_3 & \rho(y_\xi z_\eta - y_\eta z_\xi) & -\rho(x_\xi z_\eta - x_\eta z_\xi) & \rho(x_\xi y_\eta - x_\eta y_\xi) & 0 \\ 0 & r_3 & 0 & 0 & \frac{1}{\rho}(y_\xi z_\eta - y_\eta z_\xi) \\ 0 & 0 & r_3 & 0 & -\frac{1}{\rho}(x_\xi z_\eta - x_\eta z_\xi) \\ 0 & 0 & 0 & r_3 & \frac{1}{\rho}(x_\xi y_\eta - x_\eta y_\xi) \\ 0 & \gamma p(y_\xi z_\eta - y_\eta z_\xi) & -\gamma p(x_\xi z_\eta - x_\eta z_\xi) & \gamma p(x_\xi y_\eta - x_\eta y_\xi) & r_3 \end{pmatrix}.$$

C.3 Stability criterion

The discretization following Ni's method gives

$$U_p^{n+1} = U_p^n + \Delta t \mu_\tau \mu_\eta \mu_\xi \ (A\mu_\tau \mu_\eta \delta_\xi + B\mu_\tau \mu_\xi \delta_\eta + C\mu_\eta \mu_\xi \delta_\tau) \ U_p^n + \frac{1}{2}\Delta t^2 \ (A\mu_\tau \mu_\eta \delta_\xi + B\mu_\tau \mu_\xi \delta_\eta + C\mu_\eta \mu_\xi \delta_\tau)^2 \ U_p^n, \tag{C.23}$$

where the operators δ and μ are defined by

$$\delta_\xi (U_p)_{ijk} = (U_p)_{i+\frac{1}{2}jk} - (U_p)_{i-\frac{1}{2}jk}, \quad \delta_\eta (U_p)_{ijk} = (U_p)_{ij+\frac{1}{2}k} - (U_p)_{ij-\frac{1}{2}k},$$

$$\delta_\tau (U_p)_{ijk} = (U_p)_{ijk+\frac{1}{2}} - (U_p)_{ijk-\frac{1}{2}},$$

$$\mu_\xi(U_p)_{ijk} = \frac{1}{2}((U_p)_{i+\frac{1}{2}jk} + (U_p)_{i-\frac{1}{2}jk}), \quad \mu_\eta(U_p)_{ijk} = \frac{1}{2}((U_p)_{ij+\frac{1}{2}k} + (U_p)_{ij-\frac{1}{2}k}),$$

$$\mu_\tau(U_p)_{ijk} = \frac{1}{2}((U_p)_{ijk+\frac{1}{2}} + (U_p)_{ijk-\frac{1}{2}}). \tag{C.24}$$

Stability analysis is performed upon the linearized discretized equations and considers wave-like solutions of the form $U_p^n = \bar{U}_p^n e^{i(i\psi_1 + j\psi_2 + k\psi_3)}$, where ψ_1, ψ_2, ψ_3 are the wave numbers in the three computational directions (ξ, η, τ). The amplification matrix is

$$G(\psi_1, \psi_2, \psi_3) = I - 2i \cos\frac{\psi_1}{2}\cos\frac{\psi_2}{2}\cos\frac{\psi_3}{2}M + 2\Delta t^2 M^2, \tag{C.25}$$

where

$$M = A \sin\frac{\psi_1}{2}\cos\frac{\psi_2}{2}\cos\frac{\psi_3}{2} + B \sin\frac{\psi_2}{2}\cos\frac{\psi_1}{2}\cos\frac{\psi_3}{2} + C \sin\frac{\psi_3}{2}\cos\frac{\psi_1}{2}\cos\frac{\psi_2}{2}. \tag{C.26}$$

Let

$$D = \Delta t\,(s_1 A + s_2 B + s_3 C)$$

$$s = \sqrt{(\sin\frac{\psi_1}{2}\cos\frac{\psi_2}{2}\cos\frac{\psi_3}{2})^2 + (\cos\frac{\psi_1}{2}\sin\frac{\psi_2}{2}\cos\frac{\psi_3}{2})^2 + (\cos\frac{\psi_1}{2}\cos\frac{\psi_2}{2}\sin\frac{\psi_3}{2})^2}$$

$$s_1 = \frac{\sin\frac{\psi_1}{2}\cos\frac{\psi_2}{2}\cos\frac{\psi_3}{2}}{s}, \quad s_2 = \frac{\cos\frac{\psi_1}{2}\sin\frac{\psi_2}{2}\cos\frac{\psi_3}{2}}{s}, \quad s_3 = \frac{\cos\frac{\psi_1}{2}\cos\frac{\psi_2}{2}\sin\frac{\psi_3}{2}}{s}$$

Then noticing that $s_1^2 + s_2^2 + s_3^2 = 1$, the amplification matrix G can be written as

$$G(\psi_1, \psi_2, \psi_3) = I - 2i\, s \cos\frac{\psi_1}{2}\cos\frac{\psi_2}{2}\cos\frac{\psi_3}{2}\, D - 2\, s^2\, D^2. \tag{C.27}$$

If λ_D is an eigenvalue of D, the corresponding eigenvector is also an eigenvector of G with an associated eigenvalue

$$\lambda_G = 1 - 2i\, s \cos\frac{\psi_1}{2}\cos\frac{\psi_2}{2}\cos\frac{\psi_3}{2}\lambda_D - 2s^2{\lambda_D}^2. \tag{C.28}$$

If λ_D is real and $|\lambda_D| \leq 1$, then

$$|\lambda_G|^2 = 1 - 4s^2\lambda_D^2\left(1 - s^2\lambda_D^2 - \cos\frac{\psi_1}{2}^2\cos\frac{\psi_2}{2}^2\cos\frac{\psi_3}{2}^2\right)$$

$$\leq 1 - 4s^2\lambda_D^2\left(1 - s^2 - \cos\frac{\psi_1}{2}^2\cos\frac{\psi_2}{2}^2\cos\frac{\psi_3}{2}^2\right)$$

$$= 1 - 4s^2\lambda_D^2 \left(\sin\frac{\psi_1}{2}^2 \sin\frac{\psi_2}{2}^2 \cos\frac{\psi_3}{2}^2 + \cos\frac{\psi_1}{2}^2 \sin\frac{\psi_2}{2}^2 \sin\frac{\psi_3}{2}^2 + \sin\frac{\psi_1}{2}^2 \cos\frac{\psi_2}{2}^2 \text{ s} \right.$$

$$\leq 1$$

Thus the condition $\lambda_D \leq 1$ is sufficient (but may be not necessary) for stability. Let

$$r = r_1 s_1 + r_2 s_2 + r_3 s_3 \tag{C.29}$$

$$a = (y_\eta z_\tau - y_\tau z_\eta)s_1 - (y_\xi z_\tau - y_\tau z_\xi)s_2 + (y_\xi z_\eta - y_\eta z_\xi)s_3 \tag{C.30}$$

$$b = -(x_\eta z_\tau - x_\tau z_\eta)s_1 + (x_\xi z_\tau - x_\tau z_\xi)s_2 - (x_\xi z_\eta - x_\eta z_\xi)s_3 \tag{C.31}$$

$$d = (x_\eta y_\tau - x_\tau y_\xi)s_1 - (x_\xi y_\tau - x_\tau y_\xi)s_2 + (x_\xi y_\eta - x_\eta y_\xi)s_3 \tag{C.32}$$

With these definitions, the matrix D becomes

$$D = \begin{pmatrix} r & \rho a & \rho b & \rho d & 0 \\ 0 & r & 0 & 0 & a/\rho \\ 0 & 0 & r & 0 & b/\rho \\ 0 & 0 & 0 & r & d/\rho \\ 0 & \gamma p a & \gamma p b & \gamma p d & r \end{pmatrix}. \tag{C.33}$$

The eigenvalues of D are

$$\frac{\Delta t}{J}\left(r,\ r,\ r,\ r + c\sqrt{a^2+b^2+d^2},\ r - c\sqrt{a^2+b^2+d^2}\right), \tag{C.34}$$

where c is the speed of sound, $c = \sqrt{\gamma p/\rho}$. A conservative estimate for the maximum eigenvalue is

$$\lambda_{D_{max}} \leq \frac{\Delta t}{J}\left(\sqrt{r_1^2+r_2^2+r_3^2} + c\sqrt{a^2+b^2+d^2}\right), \tag{C.35}$$

where the value of r has been maximized by $\sqrt{r_1^2 + r_2^2 + r_3^2}$ since $s_1^2 + s_2^2 + s_3^2 = 1$. Thus a sufficient criterion for stability is

$$\Delta t \leq \frac{J}{\sqrt{r_1^2+r_2^2+r_3^2} + c\sqrt{a^2+b^2+d^2}}. \tag{C.36}$$

From the implementation point of view, it turns out that the Jacobian represents

the volume of the cell and all quantities in Eq. (C.36) are cell-averaged defined. Hence, the time-step is defined locally on a cell-by-cell basis. For steady-state calculations, local time-steps are used to accelerate the convergence, i.e.

$$\Delta t_{max} = CFL \frac{J}{\sqrt{\bar{r}_1^2+\bar{r}_2^2+\bar{r}_3^2} + \bar{c}\sqrt{\bar{a}^2+\bar{b}^2+\bar{d}^2}}, \tag{C.37}$$

where CFL is a 'safety' factor typically taken to be 0.9.

For unsteady calculations, the uniform global time-step is defined as

$$\Delta t = \min\left(\Delta t_{max}\right)_{all\ cells}. \tag{C.38}$$

The volume/time-step ratio associated with a grid node surrounded by its eight neighboring cells is defined by

$$\left(\frac{V}{\Delta t}\right)_{node} = \frac{1}{8}\sum_{i=1}^{8\,cells}\left(\frac{V}{\Delta t}\right)_i. \tag{C.39}$$

Appendix D

Implementation of the Non-Reflecting Boundary Conditions

The numerical implementation of the quasi-3-D non-reflecting boundary conditions presented in Chapter 5 is described in this appendix. This implementation procedure is an extension of the one used for 2-D steady-state flows in Reference [34].

The boundary conditions are implemented at the point in the overall numerical scheme at which the Lax-Wendroff algorithm has distributed changes δU to all of the nodes, including nodes on the boundaries, but the nodal values have not yet been updated. The characteristic variables are used to define the changes in the boundary values from the time level n to the time level $n+1$. In doing so, the characteristics are defined in terms of perturbations to the average inflow or outflow field at the time level n. The one-dimensional characteristic variables are related to the perturbations in the primitive variables according to Equations (5.5) and (5.6). For the changes δU, the transformation from conservation variables to primitive variables is given by Eq. (3.16).

At an inflow and an outflow boundary node, the changes in the outgoing characteristics are obtained from the changes distributed by the Lax-Wendroff algorithm according to the direction of propagation of the characteristic waves. Assuming the axial Mach number is subsonic, the only exiting mode at an inflow is the upstream running pressure wave. Thus, only the change in the fifth characteristic variable is extrapolated from the

flow field according to

$$(\delta\phi_5)_{LW} = \begin{pmatrix} 0 & -\bar{\rho}\bar{c} & 0 & 0 & 1 \end{pmatrix} \begin{pmatrix} \delta\rho \\ \delta u \\ \delta v \\ \delta w \\ \delta p \end{pmatrix}_{LW} . \tag{D.1}$$

At an outflow, the first four characteristic variables representing the linearized entropy, the two vorticity and the downstream running pressure waves are outgoing and so are obtained from the interior flow field.

$$\begin{pmatrix} \delta\phi_1 \\ \delta\phi_2 \\ \delta\phi_3 \\ \delta\phi_4 \end{pmatrix}_{LW} = \begin{pmatrix} -\bar{c}^2 & 0 & 0 & 0 & 1 \\ 0 & 0 & \bar{\rho}\bar{c} & 0 & 0 \\ 0 & 0 & 0 & \bar{\rho}\bar{c} & 0 \\ 0 & \bar{\rho}\bar{c} & 0 & 0 & 1 \end{pmatrix} \begin{pmatrix} \delta\rho \\ \delta u \\ \delta v \\ \delta w \\ \delta p \end{pmatrix}_{LW} . \tag{D.2}$$

Indeed, the Lax-Wendroff algorithm should accurately model the outgoing characteristic waves, and thus correctly distribute the changes associated with those modes. However, for incoming modes, the Lax-Wendroff changes in the incoming characteristic variables are discarded, since these are the changes which are to be defined by the user-specified average flow quantities and the non-reflecting theory. This is discussed in Sections D.1 and D.2 for inflows and in Sections D.3 and D.4 for outflows. Once the changes for ingoing and outgoing waves have all been specified, the combined changes in the five characteristic variables at the boundary nodes can be converted back into changes in the primitive variables according to

$$\begin{pmatrix} \delta\rho \\ \delta u \\ \delta v \\ \delta w \\ \delta p \end{pmatrix} = \begin{pmatrix} \frac{-1}{\bar{c}^2} & 0 & 0 & \frac{1}{2\bar{c}^2} & \frac{1}{2\bar{c}^2} \\ 0 & 0 & 0 & \frac{1}{2\bar{\rho}\bar{c}} & \frac{-1}{2\bar{\rho}\bar{c}} \\ 0 & \frac{1}{\bar{\rho}\bar{c}} & 0 & 0 & 0 \\ 0 & 0 & \frac{1}{\bar{\rho}\bar{c}} & 0 & 0 \\ 0 & 0 & 0 & \frac{1}{2} & \frac{1}{2} \end{pmatrix} \begin{pmatrix} \delta\phi_1 \\ \delta\phi_2 \\ \delta\phi_3 \\ \delta\phi_4 \\ \delta\phi_5 \end{pmatrix} . \tag{D.3}$$

These can then easily be transformed into changes in the conservation variables using the following relation and the entire flow field can be updated.

$$\begin{pmatrix} \delta\rho \\ \delta(\rho u) \\ \delta(\rho v) \\ \delta(\rho w) \\ \delta(\rho E) \end{pmatrix} = \begin{pmatrix} 1 & 0 & 0 & 0 & 0 \\ \bar{u} & \bar{\rho} & 0 & 0 & 0 \\ \bar{v} & 0 & \bar{\rho} & 0 & 0 \\ \bar{w} & 0 & 0 & \bar{\rho} & 0 \\ \frac{1}{2}(\bar{u}^2+\bar{v}^2+\bar{w}^2-\Omega^2R^2) & \bar{\rho}\bar{u} & \bar{\rho}\bar{v} & \bar{\rho}\bar{w} & \frac{1}{\gamma-1} \end{pmatrix} \begin{pmatrix} \delta\rho \\ \delta u \\ \delta v \\ \delta w \\ \delta p \end{pmatrix}. \quad \text{(D.4)}$$

D.1 Subsonic inflow

As explained in Chapter 5, for a given radius, the changes in the incoming characteristic variables at each point along the circumferential direction on the inflow boundary is split into two components. The first part represents an average change along the boundary, which is defined to achieve certain physical quantities. The second part is due to the harmonic variations in the characteristic variables along the boundary, which is designed to achieve non-reflecting boundary conditions. These are then added to the average changes to give the global changes.

The average characteristic changes in the incoming four characteristics are calculated from the requirement that the average entropy, radial and tangential flow angles, and stagnation enthalpy have the values specified by the user at the inlet, see Equations (5.9). An equivalent specification of the average inlet conditions is to drive to zero the following four residuals.

$$\begin{aligned} R_1^n &= \bar{p}^n(\bar{s}^n - \bar{s}_{inl}), \\ R_2^n &= \bar{\rho}^n\bar{c}^n\left(u_{\theta F}^n - |\vec{V}_F^n|\sin(\alpha_{\theta\,inl})\sin(\alpha_{R\,inl})\right), \\ R_3^n &= \bar{\rho}^n\bar{c}^n\left(u_{RF}^n - |\vec{V}_F^n|\cos(\alpha_{R\,inl})\right), \\ R_4^n &= \bar{\rho}^n(\bar{h}_t^n - \bar{h}_{t\,inl}). \end{aligned} \quad \text{(D.5)}$$

$u^n_{\theta F}$, u^n_{RF} and $|\vec{V}^n_F|$ are the tangential, the radial and the absolute value of the average flow velocity. The inlet tangential and radial flow angles $\alpha_{\theta inl}$ and α_{Rinl} are defined in Section 2.3 and the remaining quantities in Section 5.3. Notice that in defining R^n_2 and R^n_3 the flux-averaged values of the velocities have been used, see Section 5.5. The required average changes in the incoming characteristic variables are obtained by linearizing the residuals from the current time level, and by using a one-step Newton-Raphson procedure.

$$\begin{pmatrix} R_1 \\ R_2 \\ R_3 \\ R_4 \end{pmatrix}^{n+1} \simeq \begin{pmatrix} R_1 \\ R_2 \\ R_3 \\ R_4 \end{pmatrix}^{n} + \left(\frac{\partial(R_1,R_2,R_3,R_4)}{\partial(\phi_1,\phi_2,\phi_3,\phi_4)}\right)^n \begin{pmatrix} \delta\bar{\phi}_1 \\ \delta\bar{\phi}_2 \\ \delta\bar{\phi}_3 \\ \delta\bar{\phi}_4 \end{pmatrix} = 0. \tag{D.6}$$

Dropping the n, the Jacobian matrix is obtained as the product of two other matrices.

$$J = \frac{\partial(R_1,R_2,R_3,R_4)}{\partial(\phi_1,\phi_2,\phi_3,\phi_4)} = \frac{\partial(R_1,R_2,R_3,R_4)}{\partial(\bar{\rho},\bar{u},\bar{v},\bar{w},\bar{p})}\frac{\partial(\bar{\rho},\bar{u},\bar{v},\bar{w},\bar{p})}{\partial(\phi_1,\phi_2,\phi_3,\phi_4)}, \tag{D.7}$$

where

$$\frac{\partial(R_1,R_2,R_3,R_4)}{\partial(\bar{\rho},\bar{u},\bar{v},\bar{w},\bar{p})} = \begin{pmatrix} -\bar{c}^2 & 0 & 0 & 0 & 1 \\ 0 & -\bar{\rho}\bar{c}\tan(\alpha_{\theta inl}) & \bar{\rho}\bar{c} & 0 & 0 \\ 0 & -\frac{\bar{\rho}\bar{c}}{\tan(\alpha_{Rinl})\cos(\alpha_{\theta inl})} & 0 & \bar{\rho}\bar{c} & 0 \\ -\frac{\bar{c}^2}{\gamma-1} & \bar{\rho}\bar{u} & \bar{\rho}\bar{u}_\theta & \bar{\rho}\bar{u}_R & \frac{\gamma}{\gamma-1} \end{pmatrix}, \tag{D.8}$$

and

$$\frac{\partial(\bar{\rho},\bar{u},\bar{v},\bar{w},\bar{p})}{\partial(\phi_1,\phi_2,\phi_3,\phi_4)}, = \begin{pmatrix} -\frac{1}{\bar{c}^2} & 0 & 0 & \frac{1}{2\bar{c}^2} \\ 0 & 0 & 0 & \frac{1}{2\bar{c}^2} \\ 0 & \frac{1}{\bar{\rho}\bar{c}} & 0 & 0 \\ 0 & 0 & \frac{1}{\bar{\rho}\bar{c}} & 0 \\ 0 & 0 & 0 & \frac{1}{2} \end{pmatrix}. \tag{D.9}$$

Thus,

$$\frac{\partial(R_1,R_2,R_3,R_4)}{\partial(\phi_1,\phi_2,\phi_3,\phi_4)} = \begin{pmatrix} 1 & 0 & 0 & 0 \\ 0 & 1 & 0 & -\frac{\tan(\alpha_{\theta\,inl})}{2} \\ 0 & 0 & 1 & -\frac{1}{2\cos(\alpha_{\theta\,inl})\tan(\alpha_{R\,inl})} \\ \frac{1}{\gamma-1} & \frac{\bar{u}_\theta}{\bar{c}} & \frac{\bar{u}_R}{\bar{c}} & \frac{1}{2}\left(1+\frac{\bar{u}}{\bar{c}}\right) \end{pmatrix}. \tag{D.10}$$

In forming the Jacobian matrix several terms which are proportional to the residuals have been neglected since these are zero in the converged limit. The elements J_{lc}^{-1} of the inverted Jacobian matrix denoted J^{-1} are found according to

$$J_{lc}^{-1} = \frac{(-1)^{l+c} det(J_{cl})}{det(J)}, \quad l = 1,\ldots,4, \;\; c = 1,\ldots,4, \tag{D.11}$$

where the determinant $det(J_{cl})$ is formed by crossing the l^{th} line and the c^{th} column of J. Thus, the following average changes in the incoming characteristics are found.

$$\begin{pmatrix} \delta\bar{\phi}_1 \\ \delta\bar{\phi}_2 \\ \delta\bar{\phi}_3 \\ \delta\bar{\phi}_4 \end{pmatrix} = -J^{-1} \begin{pmatrix} R_1 \\ R_2 \\ R_3 \\ R_4 \end{pmatrix}. \tag{D.12}$$

The local changes in the characteristic variables at each circumferential point on the inflow due to the variation in the characteristic variables along the boundary are found as follows. Firstly, a discrete Fourier transform of the outgoing characteristic $\widehat{\phi}_5$ is performed which enables the steady-state amplitude of the Fourier transform of the desired incoming characteristics to be calculated according to Eqs. (5.56). The fifth characteristic variable is evaluated at each point, and its discrete Fourier transform is calculated for a range of values of k from $-N/2+1$ to $+N/2-1$, where N is the number of nodes in the circumferential direction, including the periodic node only once.

$$\widehat{\phi}_{5k} = \frac{1}{N}\sum_{j=1}^{N} \phi_{4j} \exp\left(-\frac{i2\pi jk}{N}\right). \tag{D.13}$$

According to the quasi-3-D non-reflecting boundary condition theory presented in Section 5.4.5, the steady-state amplitude of the Fourier transform of the second character-

istic is

$$\widehat{\phi}_{2ks} = -\frac{\beta+\bar{v}}{\bar{c}+\bar{u}}\,\widehat{\phi}_{5k}, \tag{D.14}$$

where

$$\beta = i\,\mathrm{sign}(k)\sqrt{\bar{c}^2-(\bar{u}^2+\bar{v}^2)}\,, \quad (\bar{u}^2+\bar{v}^2) < \bar{c}^2. \tag{D.15}$$

The steady-state amplitude of the local second incoming characteristic in the physical domain is recovered using the inverse discrete Fourier transform

$$\phi_{2js} = \sum_{k=-N/2+1}^{N/2-1} \widehat{\phi}_{2ks} \exp\left(\frac{i2\pi jk}{N}\right). \tag{D.16}$$

Because terms corresponding to $\pm k$ form complex conjugate pairs, this expression can be rewritten as

$$\phi_{2js} = 2\Re\left\{\sum_{k=1}^{N/2-1} \widehat{\phi}_{2ks} \exp\left(\frac{i2\pi jk}{N}\right)\right\}, \tag{D.17}$$

reducing the amount of computational required. Since the characteristic variables are defined as perturbations from the current average state, the Fourier components $\widehat{\phi}_{2ks}$ and $\widehat{\phi}_{5ks}$ are zero for $k = 0$.

For each node j along the boundary, the ideal (in a 2-D sense) steady-state correction to the local second characteristic variable is the difference between the correct steady-state value and the current value.

$$\delta\phi_{2js} = \phi_{2js} - \phi_{2j}. \tag{D.18}$$

Since the harmonics of the incoming third characteristic variable are zero, the correction to the local third characteristic variable is simply

$$\delta\phi_{3js} = \phi_{3js} - \phi_{3j} = -\phi_{3j}. \tag{D.19}$$

As mentioned in [34] by Giles, a straightforward implementation of the non-reflecting

boundary condition theory would result in a flow field which to first-order would have uniform entropy and stagnation enthalpy at each radius. However, the neglected second-order effects would introduce variations in entropy and total enthalpy. The standard implementation of the 1-D boundary conditions can be found in References [29] and [74]. To avoid this, the steady-state corrections to the local first and fourth characteristic variables are obtained from the conditions that the local entropy and stagnation enthalpy should match the average values. This is achieved by the same Newton-Raphson procedure used earlier to obtain the average changes. This time, the residuals are given by perturbations from the average entropy and stagnation enthalpy values.

$$R_{1j} = \bar{p}(S_j - \bar{S}), \tag{D.20}$$

$$R_{4j} = \bar{\rho}(h_{tj} - \bar{h}_t). \tag{D.21}$$

Thus the Newton-Raphson equation becomes

$$\begin{pmatrix} R_{1j} \\ R_{4j} \end{pmatrix}^n + \begin{pmatrix} 1 & 0 & 0 & 0 \\ \frac{1}{\gamma-1} & \frac{\bar{u}_\theta}{\bar{c}} & \frac{\bar{u}_R}{\bar{c}} & \frac{1}{2}(1+\frac{\bar{u}}{\bar{c}}) \end{pmatrix} \begin{pmatrix} \delta\phi_{1js} \\ \delta\phi_{2js} \\ \delta\phi_{3js} \\ \delta\phi_{4js} \end{pmatrix} = 0. \tag{D.22}$$

The solution is given by

$$\begin{aligned} \delta\phi_{1js} &= -R_{1j} \\ \delta\phi_{4js} &= -\frac{2}{1+\bar{u}/\bar{c}} \left(\frac{1}{\gamma-1}\delta\phi_{1js} + \frac{\bar{u}_\theta}{\bar{c}}\delta\phi_{2js} + \frac{\bar{u}_R}{\bar{c}}\delta\phi_{3js} + R_{4j} \right). \end{aligned} \tag{D.23}$$

Now that the local changes in the characteristic variables have been established, these are added to the average changes, and multiplied by an under-relaxation factor, σ.

$$\begin{aligned} \delta\phi_{1j} &= \sigma(\delta\bar{\phi}_1 + \delta\phi_{1js}) \\ \delta\phi_{2j} &= \sigma(\delta\bar{\phi}_2 + \delta\phi_{2js}) \\ \delta\phi_{3j} &= \sigma(\delta\bar{\phi}_3 + \delta\phi_{3js}) \end{aligned}$$

$$\delta\phi_{4j} = \sigma(\delta\bar{\phi}_4 + \delta\phi_{4js}) \tag{D.24}$$

The change in the outgoing fifth characteristic variable is given by the Lax-Wendroff algorithm,

$$\delta\phi_{5j} = \delta\phi_{5jLW}. \tag{D.25}$$

The combined five characteristic changes calculated in physical space are then transformed into changes in the primitive variables, and hence in conservation variables. This is done for all nodes along the circumferential direction of the boundary, i.e. $j = 1, \ldots, N$. This procedure is then repeated for another radius until all radii have been treated and the flow field can be updated.

D.2 Supersonic inflow

The boundary conditions for a supersonic inflow, but still axially subsonic, are implemented similarly to the subsonic inflow case. The difference lies in the definition of the parameter β, which is

$$\beta = -\text{sign}(\bar{v})\sqrt{(\bar{u}^2+\bar{v}^2)-\bar{c}^2}\ , \quad (\bar{u}^2+\bar{v}^2) > \bar{c}^2. \tag{D.26}$$

For this case, it is not necessary to perform the discrete Fourier transforms since β is now independent of the Fourier mode k. Hence, the correct steady-state values for the local incoming second characteristic are given by

$$\phi_{2js} = -\frac{\beta+\bar{v}}{\bar{c}+\bar{u}}\,\phi_5, \quad j = 1, \ldots, N \tag{D.27}$$

The remainder of the boundary condition treatment is exactly the same as for subsonic inflow.

D.3 Subsonic outflow

The implementation of the non-reflecting boundary conditions at outflow is easier than at inflow because only one characteristic needs to be set. As for the inlet this is done in two parts.

The first part allows the user to specify an average exit pressure at a certain radius.

$$\bar{p}^{n+1} = \bar{p}_{out}. \tag{D.28}$$

Using the residual $R_5^n = \bar{p}^n - \bar{p}_{out}$ and linearizing from the current time level gives

$$R_5^n + \frac{\partial R_5}{\partial \phi_5}\delta\bar{\phi}_5 = 0. \tag{D.29}$$

As mentioned in Section 5.3, the first four characteristics for a subsonic outflow represent outgoing waves, so only the fifth characteristic variable representing the upstream running pressure wave needs to be set. The derivative of pressure with respect to variations in the fifth characteristic is

$$\frac{\partial p}{\partial \phi_5} = \frac{1}{2}, \tag{D.30}$$

and so the equation for the average change in the fifth characteristic variable is

$$\delta\bar{\phi}_5 = -2(p_F - \bar{p}_{out}). \tag{D.31}$$

p_F is the current flow field flux-averaged pressure, and $\bar{p}_{out}$ is given by the radial equilibrium relation

$$\frac{\partial \bar{p}_{out}}{\partial R} = \bar{\rho}\frac{\bar{u}_\theta^2}{R}, \tag{D.32}$$

together with the specification of $\bar{p}_{out}$ at some particular radius. Notice that radial equilibrium of the flow is not required, but this condition usually represents a good physical assumption outside the blade row.

The second part consists of calculating the local changes. This is accomplished by first evaluating the outgoing local second and fourth characteristic variables, and then

calculating their discrete Fourier transforms.

$$\widehat{\phi}_{2k} = \frac{1}{N}\sum_{j=1}^{N}\phi_{2j}\exp\left(-\frac{i2\pi jk}{N}\right) \tag{D.33}$$

$$\widehat{\phi}_{4k} = \frac{1}{N}\sum_{j=1}^{N}\phi_{4j}\exp\left(-\frac{i2\pi jk}{N}\right). \tag{D.34}$$

According to Section 5.4.5, the correct steady-state amplitude of the Fourier transform of the incoming fifth characteristic variable is

$$\widehat{\phi}_{5ks} = \left(\frac{2\bar{u}}{\beta-\bar{v}}\right)\widehat{\phi}_{2k} - \left(\frac{\beta+\bar{v}}{\beta-\bar{v}}\right)\widehat{\phi}_{4k}. \tag{D.35}$$

Using the simplification due to the complex conjugate pairs allows the non-reflecting steady-state values for the incoming fifth characteristic variables to be rewritten as

$$\phi_{5js} = 2\Re\left\{\sum_{k=1}^{N/2-1}\widehat{\phi}_{5ks}\exp\left(\frac{i2\pi jk}{N}\right)\right\}. \tag{D.36}$$

The ideal local change is then

$$\delta\phi_{5js} = \phi_{5js} - \phi_{5j}, \quad j = 1,\ldots,N \tag{D.37}$$

where ϕ_{5j} is the current flow field value of the characteristic amplitude. As before, the global change in the incoming characteristics is formed by summing the average change to the local change and under-relaxing it to ensure well-posedness.

$$\delta\phi_{5j} = \sigma(\delta\bar{\phi}_5 + \delta\phi_{5js}). \tag{D.38}$$

The changes in the outgoing remaining four characteristics are again taken from the Lax-Wendroff algorithm.

$$\delta\phi_{1j} = \delta\phi_{1jLW}$$

$$\delta\phi_{2j} = \delta\phi_{2jLW}$$

$$\delta\phi_{3j} = \delta\phi_{3jLW}$$

$$\delta\phi_{4j} = \delta\phi_{4jLW} \tag{D.39}$$

As for the inflow boundary condition, the above procedure is repeated for all radii before updating the flow field.

D.4 Supersonic outflow

The supersonic outflow boundary condition (but still axially subsonic) is identical to the subsonic outflow condition, except for the definition of β which is

$$\beta = -\text{sign}(\bar{v})\sqrt{(\bar{u}^2+\bar{v}^2)-\bar{c}^2}\ , \quad (\bar{u}^2+\bar{v}^2) > \bar{c}^2. \tag{D.40}$$

Since β is again independent of the Fourier mode k, the computation can be simplified by not performing the discrete Fourier transforms of the second and fourth characteristic variables. The steady-state values for the amplitude of the incoming fifth characteristic variables is given by

$$\phi_{5js} = \left(\frac{2\bar{u}}{\beta-\bar{v}}\right)\phi_{2js} - \left(\frac{\beta+\bar{v}}{\beta-\bar{v}}\right)\phi_{4js}. \tag{D.41}$$

The remainder of the boundary condition treatment is exactly the same as for subsonic outflow.

D.5 Stator/rotor interface

To a large extend the steady-state stator/rotor interface boundary conditions formulation has been discussed in Section 5.5. Both the stator and the rotor flow fields are calculated simultaneously but with boundary conditions implemented to couple the two domains together.

As mentioned in Section 5.5, the objectives of the steady stator/rotor interface treatment is to conserve fluxes of mass momentum and energy according to the definition given by Eqs. (5.60) and (5.61). Their discrete counterparts are

$$\bar{F}(U_j) = F(U_F), \tag{D.42}$$

and

$$\bar{F} = \frac{1}{N}\sum_{j=1}^{N} F_j = \frac{1}{N}\sum_{j=1}^{N} F(U_j), \tag{D.43}$$

where N is the number of nodes in the circumferential direction, the periodic node taken into account only once.

At each radius along the span, the average characteristic changes at the stator outflow and the rotor inflow are set to eliminate the characteristic jumps defined by Equation (5.66). Assuming that the stator is upstream of the rotor, the stator outflow characteristic change is

$$\delta\bar{\phi}_5 = -\sigma\Delta\bar{\phi}_5, \tag{D.44}$$

while at the rotor inlet the average changes are

$$\begin{aligned}
\delta\bar{\phi}_1 &= \sigma\Delta\bar{\phi}_1 \\
\delta\bar{\phi}_2 &= \sigma\Delta\bar{\phi}_2 \\
\delta\bar{\phi}_3 &= \sigma\Delta\bar{\phi}_3 \\
\delta\bar{\phi}_4 &= \sigma\Delta\bar{\phi}_4.
\end{aligned} \tag{D.45}$$

Again the under-relaxation parameter σ is introduced to ensure well-posedness and convergence. Now that the average characteristic changes have been calculated for both sides of the interface, the local changes are treated exactly in the same manner as for inflow and outflow boundary. Also the outgoing characteristic changes are taken from the Lax-Wendroff algorithm.

In the case of non-equal number of nodes along the span a simple algorithm for

transferring flux-averaged quantities from one row to another has been developed. The tangential nodes distribution on either side of the interface does not matter because for steady-state calculations only circumferentially averaged quantities are interpolated across the mixing plane. The interpolation procedure is divided into two similar parts. One part consists of interpolating flux-averaged quantities from the stator frame to the rotor frame, while the other does just the opposite. The stator to rotor interpolation scheme is sketched in Figure D.1. A rotor relative flux-averaged quantity is linearly interpolated from the two radially closest stator nodes.

The rotor interpolated fluxes, subscripted $_r$, are given by the following formulae.

$$\begin{aligned}
\bar{F}_{1r} &= (\frac{\Delta R_r}{\Delta R_s})(\frac{R_s^-}{R_r})\bar{F}_1^- + (1 - \frac{\Delta R_r}{\Delta R_s})(\frac{R_s^+}{R_r})\bar{F}_1^+ \\
\bar{F}_{2r} &= (\frac{\Delta R_r}{\Delta R_s})(\frac{R_s^-}{R_r})\bar{F}_2^- + (1 - \frac{\Delta R_r}{\Delta R_s})(\frac{R_s^+}{R_r})\bar{F}_2^+ \\
\bar{F}_{3r} &= (\frac{\Delta R_r}{\Delta R_s})(\frac{R_s^-}{R_r})\bar{F}_3^- + (1 - \frac{\Delta R_r}{\Delta R_s})(\frac{R_s^+}{R_r})\bar{F}_3^+ \\
\bar{F}_{4r} &= (\frac{\Delta R_r}{\Delta R_s})(\frac{R_s^-}{R_r})\bar{F}_4^- + (1 - \frac{\Delta R_r}{\Delta R_s})(\frac{R_s^+}{R_r})\bar{F}_4^+ \\
\bar{F}_{5r} &= (\frac{\Delta R_r}{\Delta R_s})(\frac{R_s^-}{R_r})\bar{F}_5^- + (1 - \frac{\Delta R_r}{\Delta R_s})(\frac{R_s^+}{R_r})\bar{F}_5^+.
\end{aligned} \tag{D.46}$$

With reference to Figure D.1, the meaning of ΔR_r, ΔR_s, R_r, R_s^+ and R_s^- are self-explanatory. The reason for introducing radius dependency in Eqs. (D.46) is that formally one wishes to balance the integrated fluxes across the interface, i.e.

$$\int_{R_{hub}}^{R_{tip}} \bar{F}_s \, R \, dR = \int_{R_{hub}}^{R_{tip}} \bar{F}_r \, R \, dR. \tag{D.47}$$

Note that when converting the interpolated flux-averaged values into primitive values needed for the non-reflecting part of the boundary condition, the rotor wheel speed has to be added to the tangential velocity.

Stator-relative interpolated fluxes are calculated using the same procedure as above.

Once this is accomplished for all radii on both sides of the interface, the interpolated

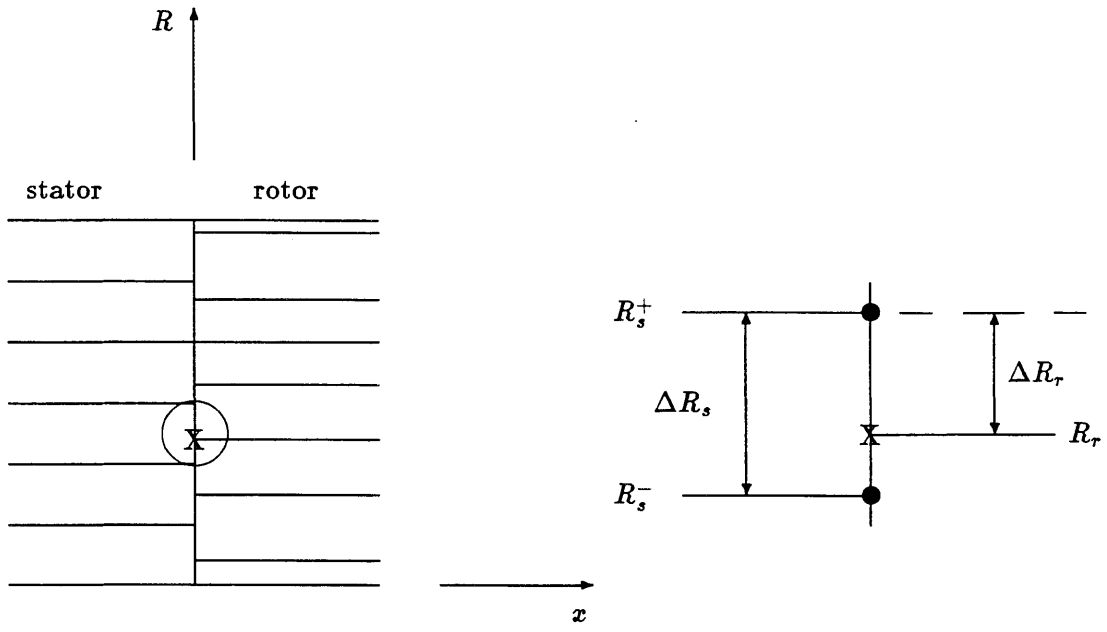

Figure D.1: Interpolation procedure for spanwise non-equal number of nodes at stator/rotor interface. The circled area is enlarged on the right.

flux-averaged values are plugged into Equation (5.66) to calculate the characteristic jumps, and the remainder of the boundary condition treatment is exactly the same as for inflow and outflow.

Finally note that this interpolation procedure is second-order accurate and thus consistent with the interior scheme.

Appendix E

Steady-State Transonic Results and Effect of Rotor Scaling

The features of the steady-state transonic flow in the turbine stage represented in Figures 7.2 and 7.3 are discussed in this appendix. In addition, the effects of an axial and a tangential direction scaling of the rotor geometry in order to get a stator-to-rotor pitch ratio equal to 1 are assessed with respect to the original configuration of 36 stators and 61 rotors. The steady-state results presented in this chapter were computed by using uniform inlet conditions and by imposing a radial equilibrium of the pressure at the rotor exit.

The pressure fields at the hub and at midspan for the actual configuration are shown in Figures 7.8 and 7.9, respectively, and ought to be compared to the pressure contours of Figures E.1 and E.2 for the scaled geometry. The tip pressure contours for the scaled version are displayed in Figure E.3. The flow parameters can be compared from Tables 7.1 ('*cold*' case column) and 9.1. Some of the flow features are identical, for instance both flows are choked at the stator throat and have trailing edge shocks. However, as discussed later on significant differences appear in the rotor flow field. Notice that in these steady-state results the flux-averaged pressure matches at the stator/rotor interface, while the local values are allowed to evolve to values which are consistent with the existence of an infinite annular duct upstream and downstream, see Chapter 5.

Figures E.1, E.2 and E.3 display the steady-state pressure field at the hub, at a

constant radius close to midheight and at the tip, respectively. The stator outlet and part of the rotor outflows are supersonic, producing weak oblique shocks at the trailing edges, which can be seen in Figures E.1, E.2 and E.3.

Figure E.4 is a schematic representing the variation of the streamtube height obtained from the streamline curvature analysis and used to design the 3-D turbine stage. The streamtube thickness decreases linearly through the stator and then increases linearly from the rotor leading edge to the trailing edge, while it is constant upstream, downstream and between the blade rows.

From the conservation of mass for a one-dimensional flow and using perfect gas relations, the mass flow $\dot{m}$, stagnation temperature T_t, stagnation pressure p_t and area S are related to the Mach number M by the following equation.

$$\frac{\dot{m}\sqrt{T_t}}{S\,p_t} = D(\gamma, M), \tag{E.1}$$

where

$$D(\gamma, M) = \sqrt{\frac{\gamma}{R_g}} \frac{M}{\left(1+\frac{\gamma-1}{2}M^2\right)^{\frac{\gamma+1}{2(\gamma-1)}}}. \tag{E.2}$$

R_g represents the gas constant.

Equation (E.1) which represents the corrected flow per unit area can be used, together with Figure E.4, to explain some of the flow features occurring in the stage.

Given $\dot{m}$, T_t and p_t, the area ratio between the inlet and the choked throat (denoted *) is

$$\frac{S_{inl}}{S^*} = \frac{D(\gamma, 1)}{D(\gamma, M_{inl})} > 1. \tag{E.3}$$

From this it follows that the decrease of the streamtube height through the stator together with the contraction of the blade-to-blade passage, decreases the inlet Mach number by increasing the ratio of the inlet area to the throat area. Hence, a large pressure drop and a high exit Mach number are expected in the stator row, see Figs. E.1,

E.2, E.3 and E.5. Similarly, the large increase in the streamtube thickness through the rotor produces the large rotor-relative inflow Mach number, and the high Mach numbers along almost the entire suction surface, see Fig. E.6.

A cusp has been used to close the finite thickness trailing edge of both the stator and the rotor blade. This produces sharp pressure rises at the trailing edges, see Figs. E.7 and E.8. On the stator suction side, the drop in pressure and rise in Mach number at $x/L \approx 0.75$ is due to the supersonic expansion wave leaving the trailing edge on the pressure side.

One important consequence of scaling the rotor geometry is to increase the effective throat area. Indeed in the scaled configuration, as seen in Figure 9.1 and sketched in Fig. E.4, the rotor trailing edge is located farther down the annulus, where the height is constant. For equal mass flows in the real and the scaled geometry, the rotor-relative stagnation temperature and stagnation pressure are related by

$$\sqrt{\frac{(T_t)_{scaled}}{(T_t)_{real}}}\frac{(p_t)_{real}}{(p_t)_{scaled}} = \frac{(S^*)_{scaled}}{(S^*)_{real}} > 1. \tag{E.4}$$

This leads to a lower rotor-relative stagnation pressure in the computation of the scaled configuration. For instance at the rotor inlet,

$$\frac{((p_t)_{real} - (p_t)_{scaled})_{rotor\ inl\ midspan}}{p_{t\,inl}} \approx 0.024. \tag{E.5}$$

In particular, the stator/rotor interface pressure is decreased. This means that relative to the flow in the real geometry, higher stator exit velocities and Mach numbers occur. Figures E.7 and E.5 show the pressure and the Mach number distribution around the stator blade at midspan for the two configurations, respectively. Note that the two solutions coincide ahead of the choked throat because the upstream conditions are the same. The flow behavior after the throat towards the stator exit is similar for the two configurations. However, the reduced exit pressure in the scaled version produces higher Mach numbers.

Then, by subtracting the rotor wheel speed, higher angles and Mach numbers arise

at the rotor inlet, see Figs. E.9 and E.10. Notice however, that the tangential angle and Mach number distributions are similar in shape for the two cases.

The combined effects of higher rotor-relative inflow angle and Mach number produce a shock at the root of the scaled blade that is not present otherwise, see Figures 7.8, E.1, E.11 and E.12. Relative to the real geometry calculation, the blade pressure distributions of the scaled version are 'shifted' to a lower value, see Figs. E.12, E.8 and E.13 which results in a lower lift. For instance the power delivered is reduced by approximately 4%. The corresponding Mach number distributions for the real and the scaled rotor are given in Figures E.11, E.6 and E.14. Notice that almost the entire rotor suction surface is supersonic due to the high inflow Mach number. Also a significant difference appears between the two flows at the rotor root. At about 50% chord the scaled configuration bends back to a constant radius. The curvature of the streamlines results in 'circular' type pressure contours in this area, see Figure E.15. This effect does not occur in the actual configuration, since in that case the bending occurs after the trailing edge.

At the rotor tip, a weak oblique shock is present at $x/L \approx 0.70$ in both the real and scaled configurations. This corresponds to the impingement on the suction surface of the oblique shock leaving the trailing edge on the pressure side. In the computation of the scaled rotor, a very low level of numerical smoothing was used, i.e. $\nu_4 = 0.002$, whereas ν_4 was set to 0.005 in the calculation of the actual geometry. This causes the strength of the trailing edge shocks to be different.

Notice that because of the imposition of the same exit pressure in both cases, the reduced rotor-relative stagnation pressure in the scaled geometry implies lower Mach numbers at the rotor exit.

The design of the transonic first turbine stage of Figure 7.2, with an increase of the rotor frontal area of 20% from the leading to the trailing edge (reference downstream cross-section), is fairly general for an axial flow first turbine stage. Hence, the

conclusions from the scaling study apply to a whole class of engines, and provide an upper limit for the magnitude of the changes to be expected for turbines with less three-dimensionality. Compared to the original configuration the scaling of the rotor geometry produces flow changes that are decomposed into an average and local changes. The average effects are linked to the alteration of the throat area, which for a given mass flow and exit pressure modifies the average rotor inlet and outlet flow conditions such as Mach number and angles (in the present study the rotor-relative inlet incidence is increased by 2^0). In a steady-state calculation, circumferentially-averaged flow conditions are imposed at the boundaries of the domain, with the stator-to-rotor pitch ratio and the blade number affecting the solution through the blockage factor. However, the axial and circumferential directions scaling, by forcing a stator-to-rotor pitch ratio of 1, does not necessarily guaranty the same blockage effect. Consequently, the scaling should also include the radial direction in a manner that keeps the same throat area. By producing pressure variations up to 75% of the rotor inlet dynamic head relative to the original flow (this is three times more than the average change in the rotor inlet stagnation pressure) the local alterations of the geometry can have significant consequences, especially if shock waves are involved.

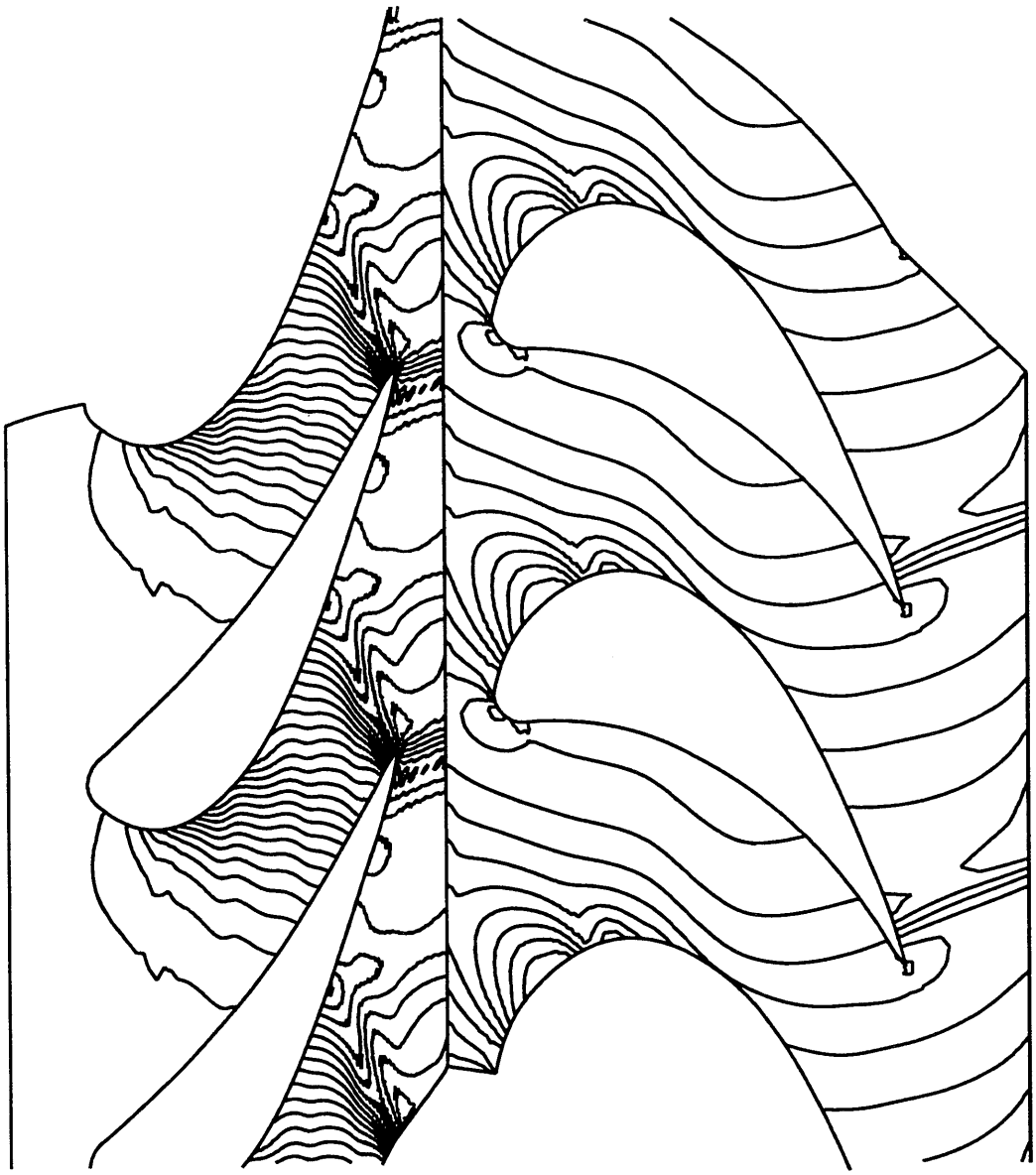

Figure E.1: Steady-state pressure contours at the hub (scaled rotor).

Figure E.2: Steady-state pressure contours at radius $R = R_{mid}$ (scaled rotor).

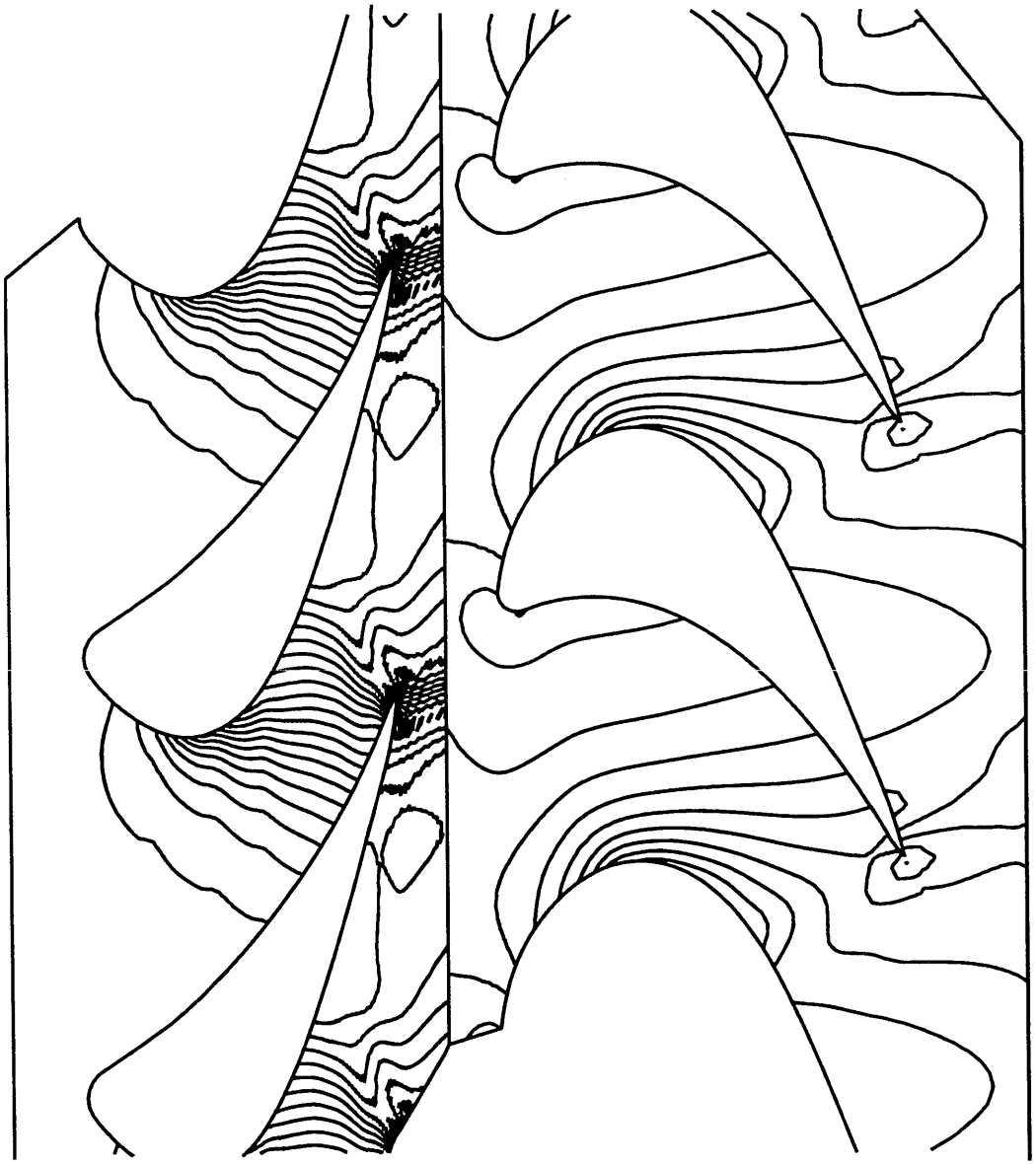

Figure E.3: Steady-state pressure contours at the tip (scaled rotor).

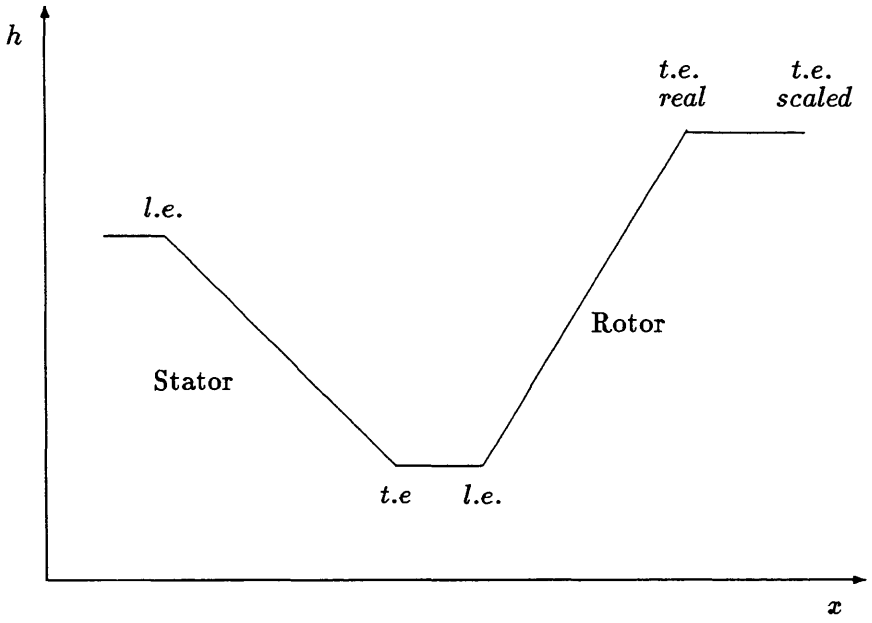

Figure E.4: Schematic of streamtube height for scaled and real turbine stage.

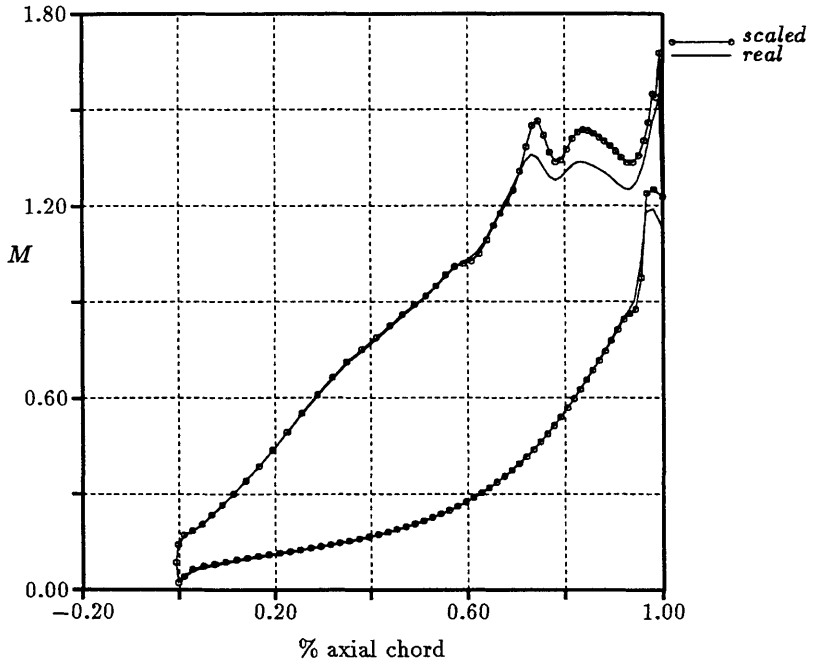

Figure E.5: Stator blade Mach number at midspan.

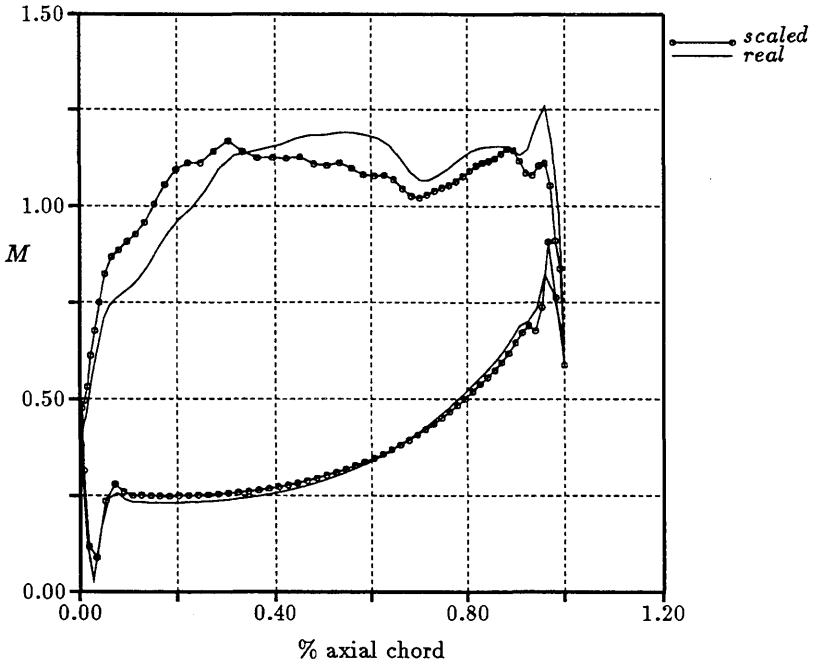

Figure E.6: Rotor blade Mach number at midspan.

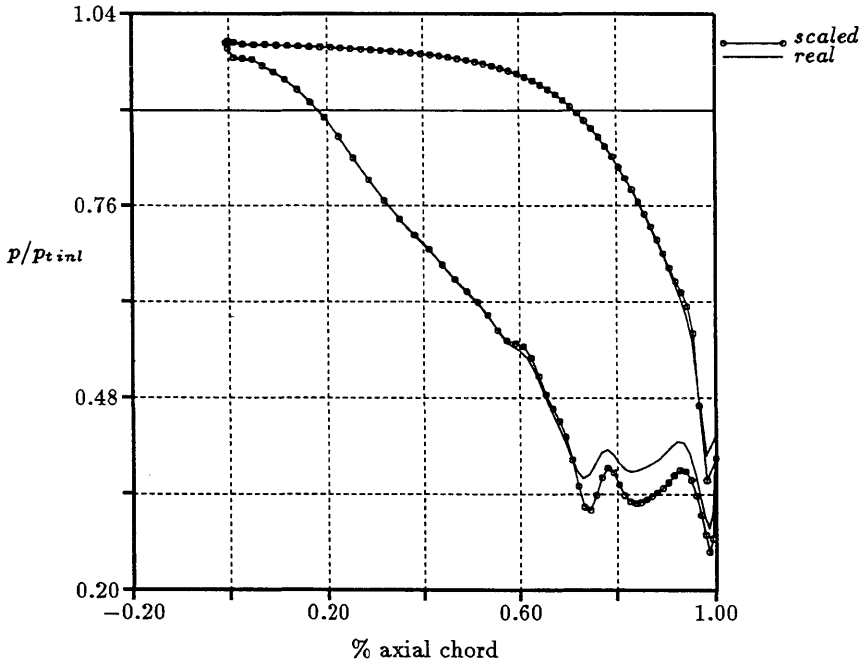

Figure E.7: Stator blade pressure at midspan.

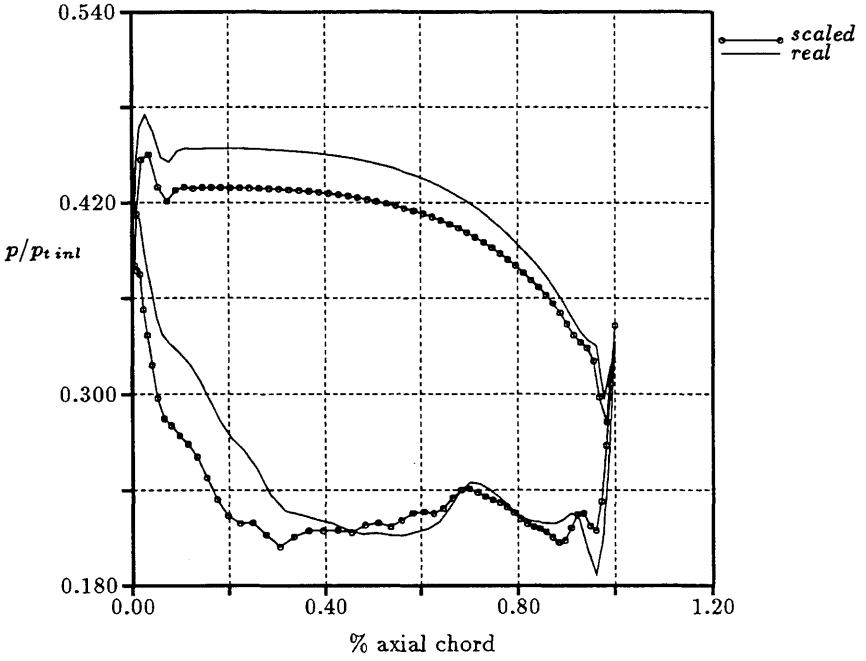

Figure E.8: Rotor blade pressure at midspan.

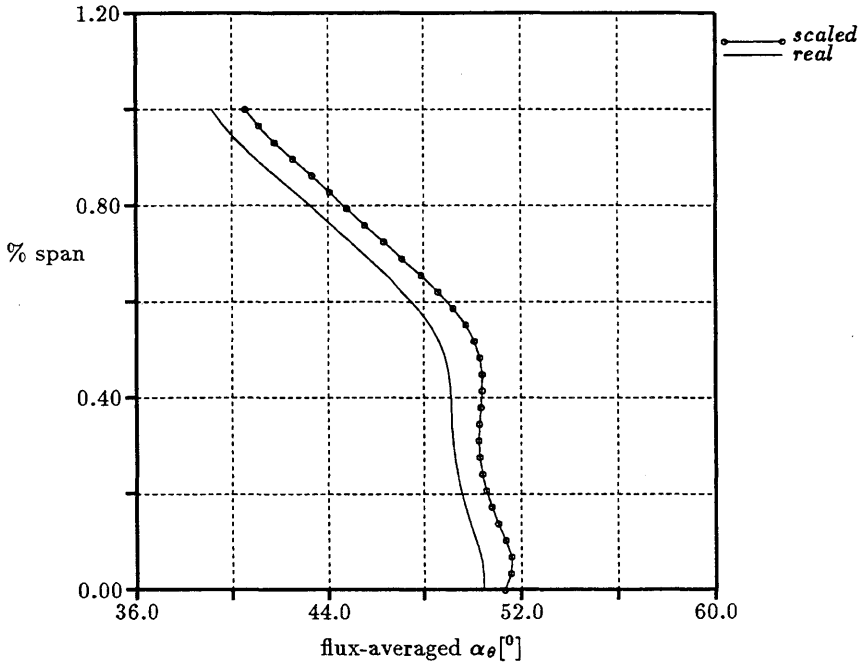

Figure E.9: Rotor-relative inlet angles.

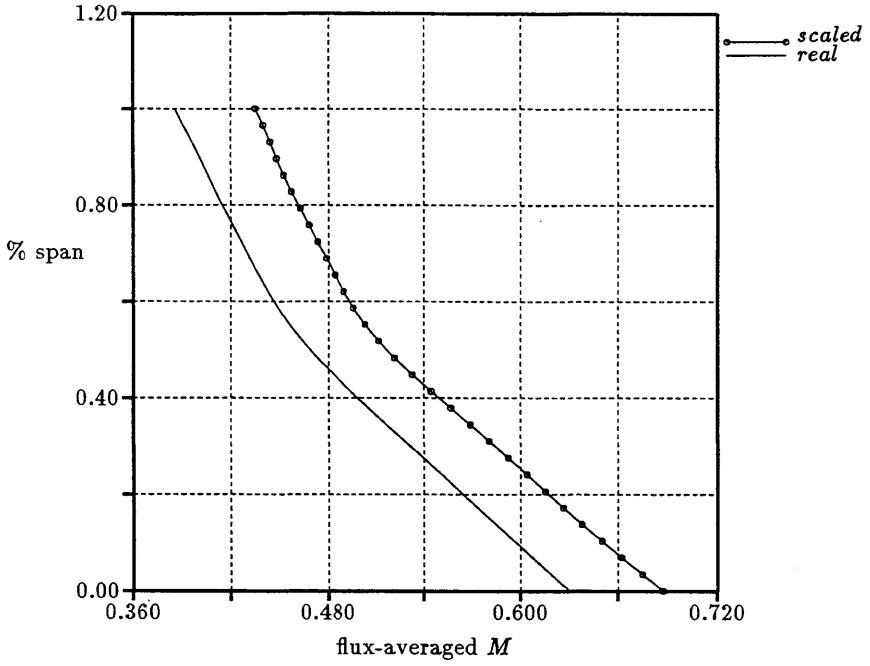

Figure E.10: Rotor-relative inlet Mach number distribution.

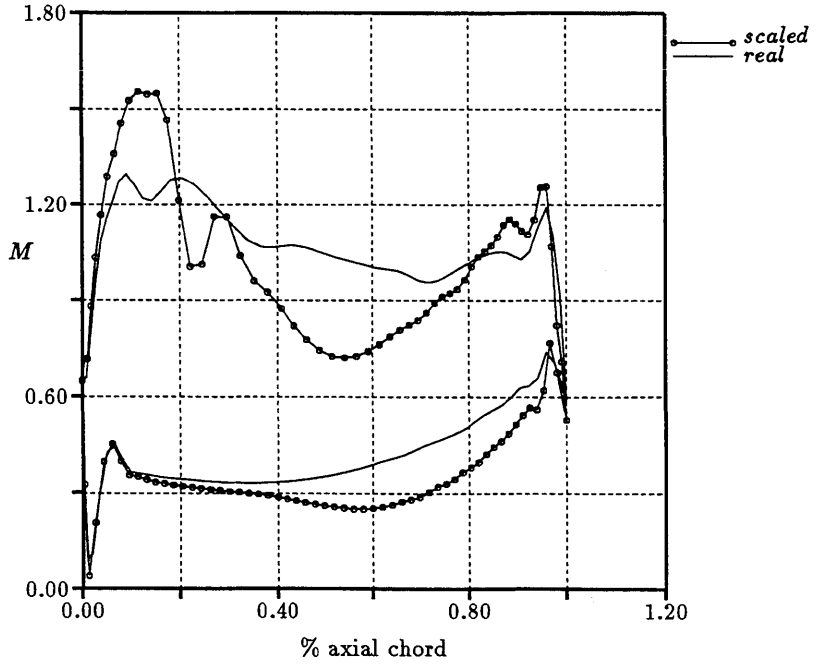

Figure E.11: Rotor blade Mach number at the hub.

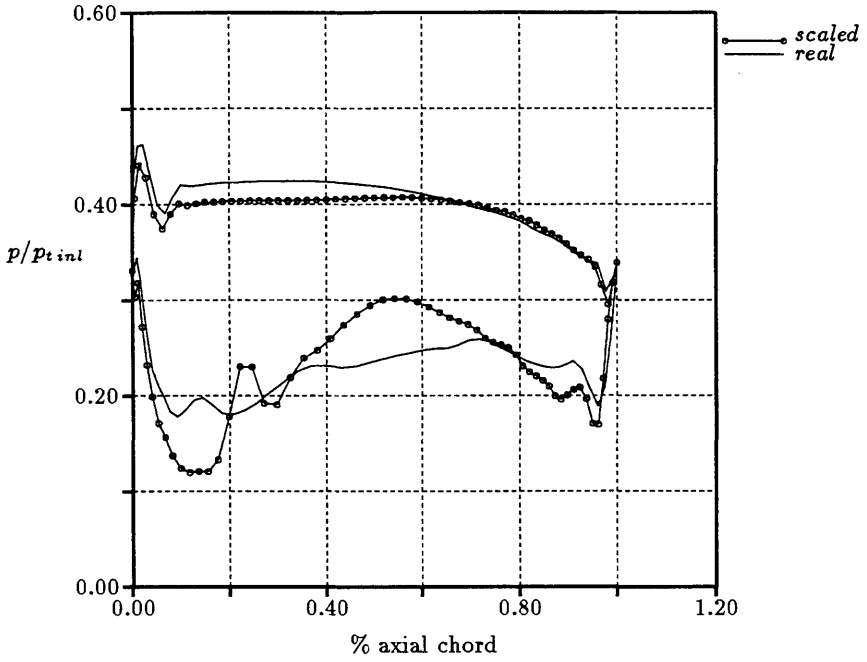

Figure E.12: Rotor blade pressure at the hub.

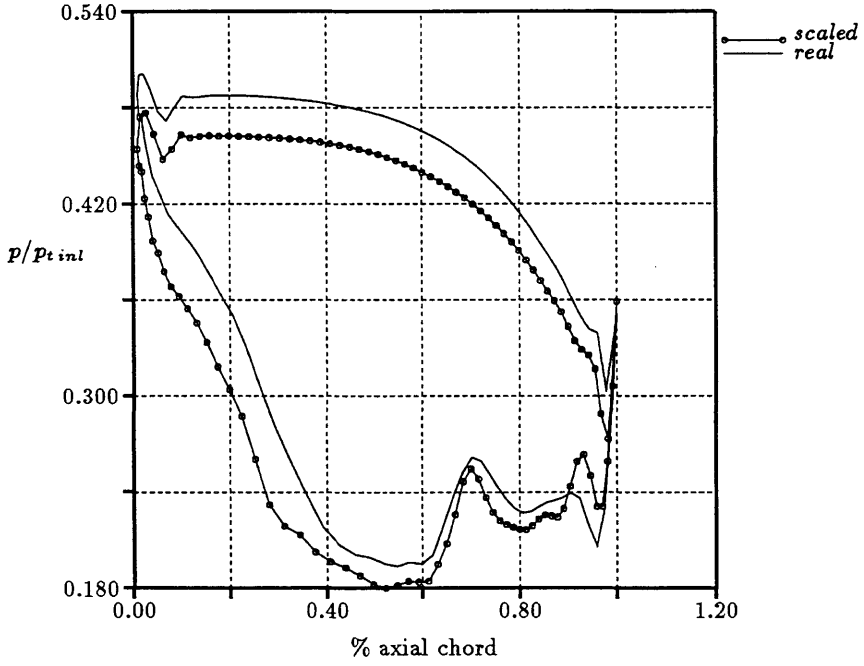

Figure E.13: Rotor blade pressure at the tip.

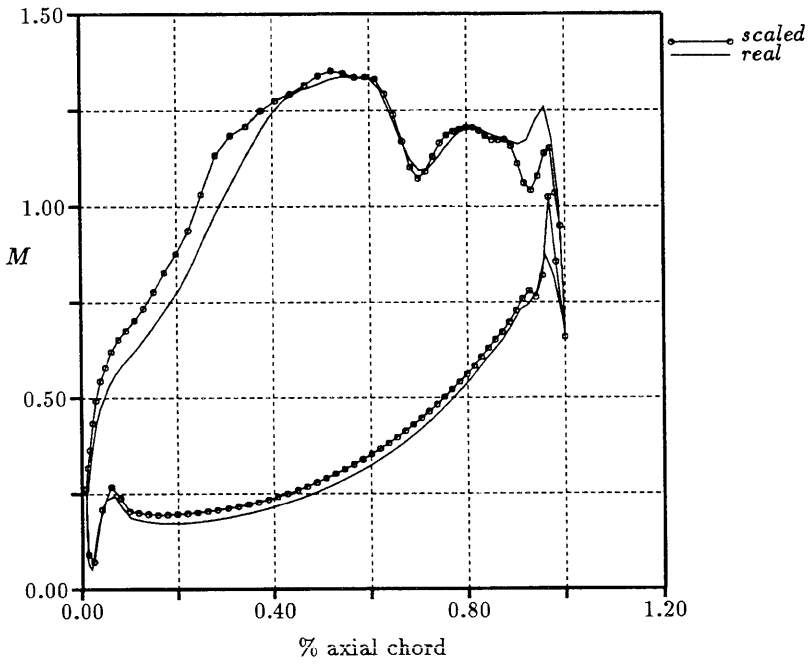

Figure E.14: Rotor blade Mach number at the tip.

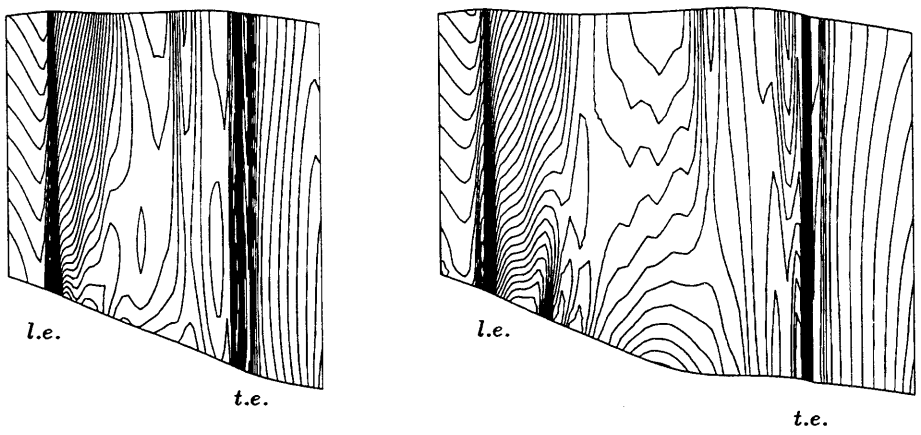

a) b)

Figure E.15: Rotor blade suction side pressure: a) real and b) scaled.